DESIGN AND FABRICATION OF OPTIMIZED MAGNETIC ROLLER FOR PERMANENT ROLL MAGNETIC SEPARATOR FOR THE PROCESSING OF LOW GRADE IRON ORE

Thesis

Submitted in partial fulfilment of the requirements for the degree of

DOCTOR OF PHILOSOPHY

by

MOHANRAJ G T

(Registration Number: 165045MT16F04)

DEPARTMENT OF METALLURGICAL AND MATERIALS ENGINEERING

NATIONAL INSTITUTE OF TECHNOLOGY KARNATAKA,

SURATHKAL, MANGALORE – 575 025

JUNE, 2022

DESIGN AND FABRICATION OF OPTIMIZED MAGNETIC ROLLER FOR PERMANENT ROLL MAGNETIC SEPARATOR FOR THE PROCESSING OF LOW GRADE IRON ORE

Thesis

Submitted in partial fulfilment of the requirements for the degree of

DOCTOR OF PHILOSOPHY

by

MOHANRAJ G T

(Registration Number: 165045MT16F04)

Under the Guidance of

Dr. MOHAMMAD RIZWANUR RAHMAN

DEPARTMENT OF METALLURGICAL AND MATERIALS ENGINEERING

NATIONAL INSTITUTE OF TECHNOLOGY KARNATAKA,

SURATHKAL, MANGALORE – 575 025

JUNE, 2022

DECLARATION

By the Ph.D. Research Scholar

I hereby declare that the Research Thesis entitled **"Design and Fabrication of Optimized Magnetic Roller for Permanent Roll Magnetic Separator for the Processing of Low Grade Iron Ore"** which is being submitted to the **National Institute of Technology Karnataka, Surathkal** in partial fulfillment of the requirements for the award of the Degree of **Doctor of Philosophy** in **Metallurgical and Materials Engineering,** is a bonafide report of the research work carried out by me. The material contained in this Research Thesis has not been submitted to any university or Institution for the award of any degree.

MOHANRAJ G T

Reg. NO.: 165045MT16F04

Department of Metallurgical and Materials Engineering

Place: **NITK - Surathkal**

Date: 10 – 06 – 2022

CERTIFICATE

This is to certify that the Research Thesis entitled **"Design and Fabrication of Optimized Magnetic Roller for Permanent Roll Magnetic Separator for the Processing of Low Grade Iron Ore"** submitted by **Mr. MOHANRAJ G T (Register Number: 165045MT16F04),** as the record of the research work carried out by him, is accepted as the Research Thesis submission in partial fulfillment of the requirements for the award of the **Degree of Doctor of Philosophy** in **Metallurgical and Materials Engineering.**

Research Guide

Dr. Mohammad Rizwanur Rahman

Associate professor

Department of Metallurgical and Materials Engineering

NITK, Surathkal

Chairman-DRPC

Department of Metallurgical and Materials Engineering

NITK, Surathkal

ACKNOWLEDGEMENT

ABSTRACT

The quality of iron ore in terms of high iron content is a critical parameter in iron and steel-making processes. So, it is necessary to take step towards the utilization of low grade iron ores, since, the higher-grade ores (non-renewable natural resource) become depleted. Whereas, the economics of low grade iron ore requires a process that can perform beneficiation at a low price and environmentally friendly way. Also, the effective utilization of these low grade iron ores depends upon the selection of suitable processing techniques which in turn mainly relies on the ore's compositional features.

Therefore, in the present work, the prior characterization studies on as-received ore sample followed by the design of Permanent Roll Magnetic Separator (PRMS) through Finite Element Method Magnetics (FEMM) analysis of magnetic roller (the active part of PRMS) was carried out. The FEMM analysis indicates that the optimized magnetic roller having a magnet-to-steel disk thickness ratio of 5 mm: 2.5 mm was proved to be gainful in beneficiating low grade hematite ore due to the efficient magnetic field value from the roller surface that is, 0.89 to 2.59 T. The obtained FEMM data was validated through prediction analysis using the Artificial Neural Network (ANN) modelling technique. Further, the design calculations of newly developed lab-scale PRMS in terms of power requirements and belt tensions were addressed.

In addition, the optimization of operating parameters of newly designed lab-scale PRMS has an impact on achieving the best performance in mineral processing, cost-effectively. So, the effect of feed rate (ton/h), roller speed (rpm), and belt thickness (mm) of PRMS on the processing of low grade hematite ore through the Design of Experiments (DOE) approach was addressed. The parametric optimization was carried out using Taguchi-based L_{27} orthogonal array design. The significance of the parameters on the overall quality of the product was evaluated quantitatively by the Analysis of Variance (ANOVA) method. It was found that the belt thickness was the most influential factor on the product of desired Fe grade and recovery %. The obtained regression coefficient (i.e., R^2 = 87.13 and 91.69 % for Fe grade and Fe recovery %, respectively) and normal probability plot show the highest correlation between the experimented and predicted data.

Also, the characterization study on optimized separated products endorse the enrichment of Fe content in magnetic products as compared to middling and non-magnetics. The obtained results suggest that the FEMM analysis is more suitable for designing of optimized magnetic roller for processing low grade iron ore. Moreover, the overall agenda of the present work was to find a positive solution towards the processing of low grade iron ore with reasonable expenditure.

Key words: PRMS, FEMM, Magnetic roller, ANN, Taguchi, ANOVA, Characterization study

TABLE OF CONTENTS

CONTENTS	PAGE NO.

LIST OF FIGURES

LIST OF TABLES

NOMENCLATURE

$(BH)_{max}$ Maximum energy product (MGOe)

N_P North pole

S_P South pole

F_m Magnetic force (N)

F_c Centrifugal force (N)

F_g Gravitational force (N)

μ_o Permeability of the free space/vacuum $= 4\pi \times 10^{-7}$ (Tm/A)

χ_p Mass magnetic susceptibility of the particle (m^3/kg)

χ_f Mass magnetic susceptibility of the fluid = Zero for air (m^3/kg)

m_p Mass of the particle (kg)

B Magnetic field/flux density (T)

∇B Magnetic field gradient (T/m)

$B\nabla B$ Force index [product of magnetic field and magnetic field gradient] (T^2/m)

F_m^{mag} Magnetic force acting on the magnetic particles (N)

$\sum C_F^{mag}$ Sum of competing forces acting on the magnetic particles (N)

$F_m^{non\ mag}$ Magnetic force acting on the non-magnetic particles (N)

$\sum C_F^{non\ mag}$ Sum of competing forces acting on the non-magnetic particles (N)

C_F Competing forces (N)

ρ_P Density of the particle (kg/m^3)

ρ_f Density of the fluid (kg/m^3)

V_P Volume of the particle (m^3)

g Acceleration due to gravity (ms^2)

ω Angular velocity (m/s)

r Distance from the origin (roller radius) (m or mm)

IRMS   Induced roll magnetic separator/separation

LRMS   Lift roll magnetic separator

CBMS   Cross belt magnetic separator

XRD	X-ray diffraction
OM	Optical microscopy
Y_{jk}	Output of the neuron
$X_{c(k-1)}$	Input of the neuron
W_{cjk}	Connection weight
b_{jk}	Bias weight
F_k	Transfer function
j	Neuron number
c	Node number
k	Layer number
τ	Target output value
α	Predicted output value
CAED	Computer Aided Engineering Drawing
A	Number of the experiment
j_r	Number of the replicate
n_r	Number of replication for each experiment
Y_{Aj_r}	Response for the j_r^{th} replicate of the Ath experiment
LIMS	Low intensity magnetic separation/separator
WHIMS	Wet high intensity magnetic separation/separator
SEM-EDS	Scanning electron microscopy-energy dispersive X-ray spectroscopy
VSM	Vibrating sample magnetometer
tph	Ton per hour
rpm	Revolutions per minute
RERMS	Rare earth roll magnetic separator/separation
RMS	Repulsive magnetic scavenger
AMR's	Active magnetic regenerators
FANN	Feed-forward artificial neural network
GA-ANN	Genetic algorithm-artificial neural network
BPA-ANN	Back propagation algorithm-artificial neural network

SQUID	Superconducting Quantum Interference Device
M	Magnet disc thickness (mm or m)
S	Steel disc thickness (mm or m)
B_1	Extended portion of magnetic roller for belt gripping (mm or m)
B_2	Distance from magnetic roller surface in radial direction (mm or m)
B_3	Effective width/length of magnetic roller (mm or m)
B_4	Overall width/length of magnetic roller (mm or m)
A_{14}	Solid steel rod diameter (mm or m)
A_4	Belt thickness (mm or m)
A_{16}	Belt surface
A_{10}	Magnetic roller surface
A_2	Magnetic roller diameter (mm or m)
P	Particle of different size/diameter (mm or μm)
H	Magnetic field strength (A/m)
B_o	Magnetic field/flux density on the surface of the magnetic roller (T)
z	Distance of the particle from the magnetic roller surface in radial/transverse direction (mm or m)
t	Thickness of the steel disks between the magnet disks (mm or m)
A_5	Diameter of the magnetic roller shaft (mm or m)
A_{13}	Grub screw (inserted through the magnetic roller shaft on either side to grip/tighten the stainless steel solid rod)
A_9	Welded joint [provided between the magnetic roller shaft and the extended portion of the magnetic roller (B_1) for rigid fixing]
A_8	Diameter of the support roller shaft (mm or m)
A_{15}	Overall length/width of the driven/support roller (mm or m)
A_3	Diameter/Size of the roller bearing (mm or m)
A_{11}	Centre distance (mm or m)
A_{12}	Extended portion of the slider bed beyond the belt width (mm or m)
A_6	Extended portion of the rollers beyond the belt width (mm or m)

A_7	Belt width (mm or m)
A_1	Diameter of the driven/support roller (mm or m)
A_{17}	Length of slider bed (mm or m)
M_d	Material density (kg/m^3)
W_1	Width of hopper opening (mm or m)
L_1	Length of hopper opening (mm or m)
T_1	Tension at the drive head or tight side tension (N)
T_2	Tension at the return side or slack side tension (N)
n	Roller speed (rpm)
f_o	Overall coefficient of friction
η	Overall efficiency of the motor
e	Naperian logarithm base
μ	Friction coefficient between the roller and the belt
θ	Belt wrap angle around the roller (rad)
VFD	Variable frequency drive

CHAPTER 1

INTRODUCTION

The present dissertation aims to study the development of an optimized magnetic roller for Permanent Roll Magnetic Separator (PRMS) for the processing of paramagnetic minerals. So, this chapter provides an overview of magnetism and innovation in magnetic separation, general aspects of magnetic separation, mechanism of magnetic separation, principles of magnetic separation, design aspects of PRMS including characterization studies of the ore sample, FEMM and ANN modelling technique followed by DOE approach.

1.1 Magnetism and magnetic separation innovation milestones

According to Thales of Miletus, the magnetic interaction among iron and lodestone/magnetite has been known since at least 600 B.C. Also, Socrates claimed that magnetite can cause iron to acquire attractive properties or become magnetic. Magnetic phenomena were studied and used for many years. Magnetite, the only naturally occurring magnetic substance, was used in earlier studies with magnetism. As a result, permanent and induced magnetism was among man's oldest scientific achievements. Whereas in 1792, W. Fullarton secured a patent for beneficiating iron ore by magnetic pull, demonstrating the real importance of magnetic attraction/pull as a preliminary type of magnetic separation (Dean and Davis 1941). Furthermore, several kinds of magnetic separators were changed over time, albeit the range of minerals that these separators could treat was limited to coarse and moderately strong magnetic minerals. However, at the end of the 19th century, both the equipment accessibility and the spectrum of mineral ores to which magnetic separation can be applied were steadily increased.

Magnetic separation innovation was fueled by the discovery of permanent magnetic materials and advancements in their magnetic characteristics. Fig. 1.1 (Svoboda 2004) depicts the evolution of permanent magnet's (BH)$_{max}$ over time. In Fig. 1.1, three innovation milestones were seen i.e., in the 1880s, 1940s, and late 1970s. At the end of the 19th century (tungsten and chromium steel) very weak magnets (steel-based) were used. While the permanent magnets that could contend with electromagnets were designed in the

1940s (CoPt, FePt, AlNi, and AlNiCo). Probably, the late 1970s (Sm_5Co and NdFeB) were a pivotal period in history since the magnets made of rare earth elements were available. These magnets provided new solutions to problems that electromagnets couldn't solve or weren't cost-effective to solve.
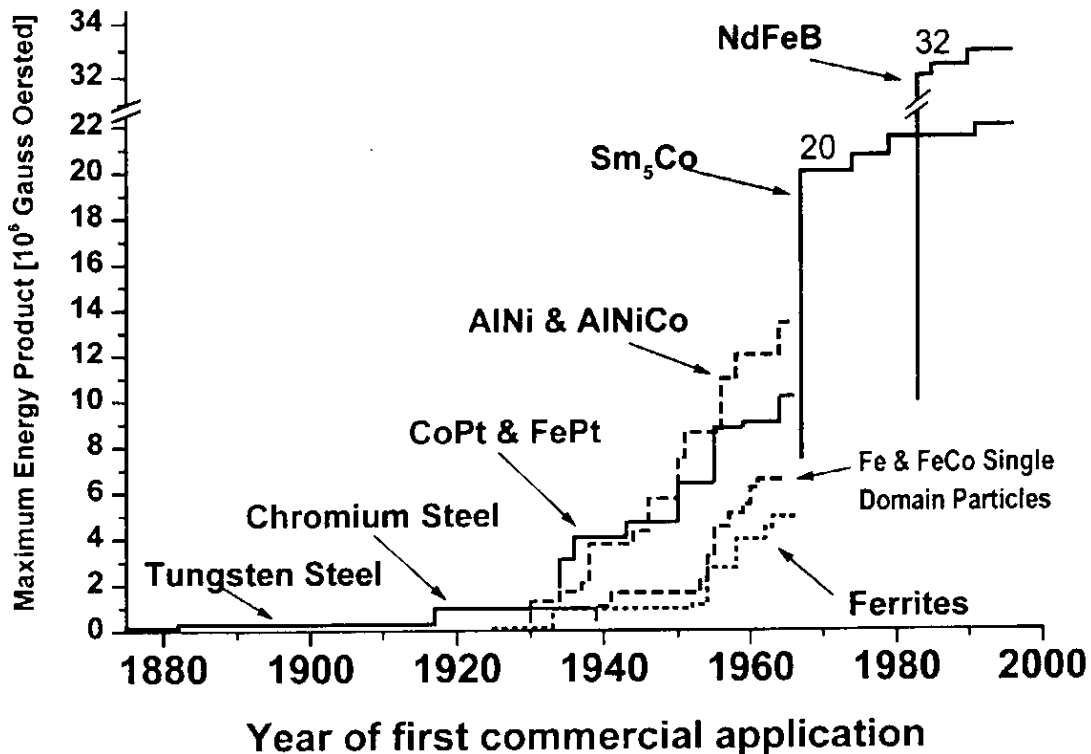
Fig. 1.1: Evolution of permanent magnetic materials (Svoboda 2004).

Another key driver of magnetic separation innovation was the insertion of ferromagnetic substances as matrix separators (mesh, wool, balls/grooved plates) into a separator's magnetic field (Fig. 1.2). In 1937, Frantz invented a magnetic separator that consisted of a solenoid (iron-bound) packed with ferromagnetic steel ribbons (Fraas 1973), and it was a significant step forward in the evolution of high-intensity magnetic separators. This innovation broadened the scope of magnetic separation to include a wide range of weakly magnetic and diamagnetic minerals down to the micrometer scale.
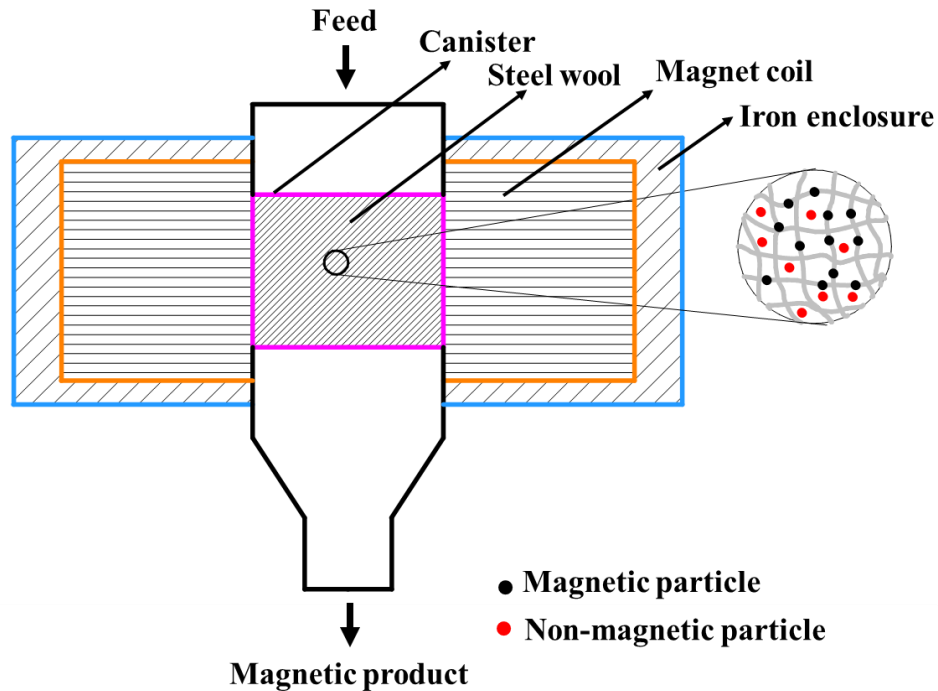
Fig. 1.2: Schematic representation of high-intensity magnetic separator (Ge et al. 2017)

1.2 General aspects of dry magnetic separation using high-intensity magnetic separator

In developing countries, industrialization has stimulated the growth of mining industries, as well as the search for technology that would transform mining into an environmentally friendly and cost-effective activity (Nunna et al. 2019; Yang et al. 2018). In addition, the global steel demand has been increasing the requirement of high-grade iron ore (IBM 2018). Whereas, the depleting nature of higher-grade iron ore calls for the efficient usage of lower-grade iron ores to meet the worldwide demand of the iron and steel industry (Suthers et al. 2019; Tang et al. 2016). However, the beneficiation/up-gradation of lower-grade iron ores includes a dry/wet processing technique. Where wet processing requires a large amount of water which leads to water contamination and creates environmental issues (Hanumanthappa et al. 2020; Nakai et al. 2010). Thus, to reduce water contamination and environmental issues dry processing technology (dry magnetic separation) can be adopted. Thus, the development of the dry mode of magnetic separation through PRMS (a type of

high-intensity magnetic separator) is an essential outcome, which is designed to utilize a high-intensity magnetic field for the separation of paramagnetic minerals (goethite, hematite, rutile, ilmenite, and garnet) (Ozcan and Celik 2016; Tripathy et al. 2014). Meanwhile, the PRMS was also used to separate magnetic impurities from glass and ceramic powder. Likewise, the recovery of valuable minerals and metals can be achieved from different waste streams (Norrgran and Mankosa 2006; Roe 1958; Russell 1992). Furthermore, the use of PRMS (dry magnetic separator) for the separation of paramagnetic minerals could prove to be a novel alternative as compared to other traditional dry high-intensity magnetic separators, such as IRMS, LRMS, and CBMS because of high magnetic field strength up to 1.6T can be produced with less energy consumption, low floor space (Tripathy et al. 2017). Also, the physicochemical methods which include gravity separation (jigging, spiral concentrator, heavy media separation) and froth flotation are used to segregate/separate the gangue from high density (hematite) minerals were considered as uneconomical and are not eco-friendly due to more power and water usage (Tripathy et al. 2017a).

1.3 Separation mechanism of PRMS

PRMS is a high-intensity permanent magnetic separator since it involves a permanent magnetic field for the separation process. It is the key source of innovation in dry paramagnetic mineral separation at a larger capacity and reduced operational cost. However, with the arrival of PRMS provided with permanent magnetic materials, now it is possible to build roll separators using an alternative magnet as well as steel disks (Fig. 1.3 (b)), which produce higher magnetic force compared to a high-intensity electromagnetic separator (Arvidson and Norrgran 2014). The feed to the PRMS is introduced onto the thin belt which rolls over the magnetic roll, and magnetic particles are attracted by the magnetic roll whereas non-magnetic particles are repelled off due to the resultant action of magnetic, centrifugal, and gravitational forces (Wills and Finch 2015). Fig. 1.3 (a) depicts the separation mechanism of PRMS.
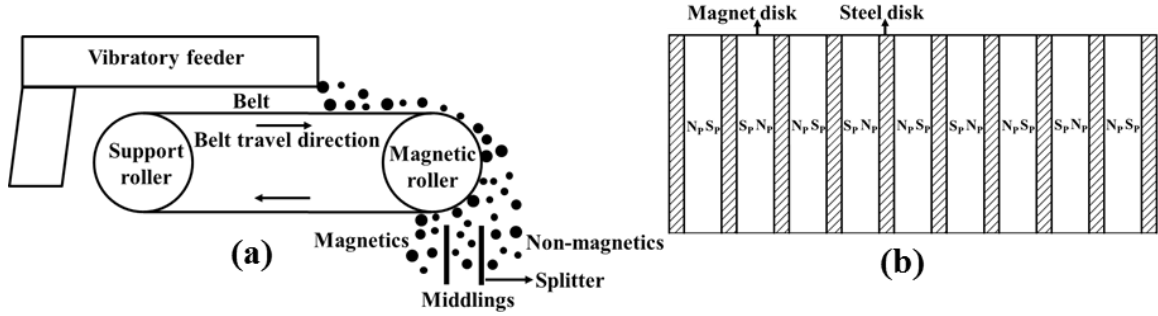
Fig. 1.3: (a) PRMS separation mechanism, and (b) Arrangement of magnet and steel disk in magnetic roller (the active part of PRMS)

1.4 Principle of PRMS

Magnetic separation is used to concentrate minerals by making use of discrepancies in magnetic susceptibility between magnetic minerals and gangue-containing components. The separation is accomplished by subjecting the particle mixtures to a magnetic field of non-homogeneous type, where the magnetizable particles are selectively retained or deflected as a result of the separation process. The mobility of magnetizable particles regarding magnetic force (F_m) and other competing forces (centrifugal force (F_c) and gravity force (F_g)) determines their separation from streams (Svoboda and Fujita 2003; Yamamoto 2013). In addition, the principle of separation of magnetizable particle retained in the magnetic field of non-homogeneous type, which is acted upon by F_m (Fig. 1.4) is given by equation (1.1)

$$F_m = \frac{1}{\mu_o}(\chi_p - \chi_f)m_p B\nabla B. \tag{1.1}$$

However, the efficient separation of magnetics from non-magnetics has taken place, if the following requirements were met:

$$F_m^{mag} > \sum C_F^{mag} \text{ and } F_m^{non\ mag} < \sum C_F^{non\ mag}. \tag{1.2}$$

To ensure high magnetic particle recovery, the magnetic separation force acting on the magnetic particles must thus be larger than the sum of the competing forces, as shown in equation (1.2) (Svoboda and Fujita 2003).

$$C_F = F_g + F_c. \tag{1.3}$$

The force of gravity can be written as $F_g = (\rho_P - \rho_f)V_P g.$ (1.4)

The centrifugal force can be written as $F_c = (\rho_P - \rho_f)\omega V_P r$. $\qquad$ (1.5)
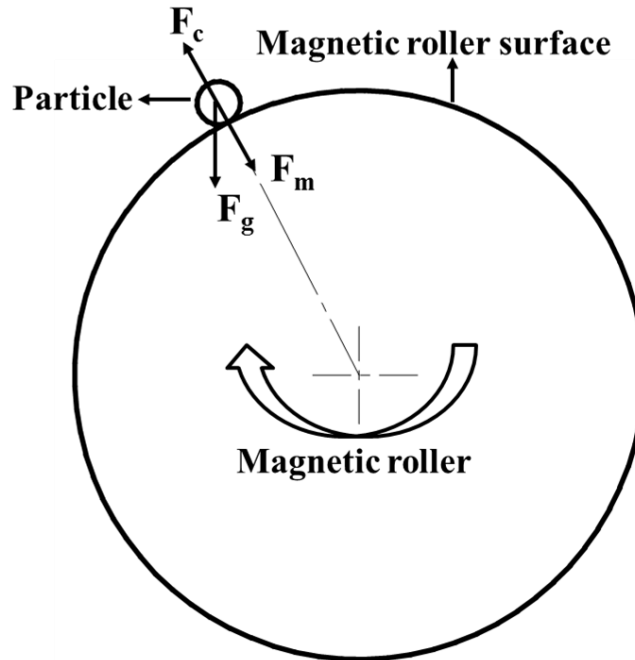
Fig. 1.4: Particle on the magnetic roller surface subjected to various combinations of forces

1.5 Design aspects of PRMS

In PRMS, the magnetic roller is the active part, comprising of permanent magnet disks interleaved with steel disks in such a way that like poles are facing each other (Fig. 1.3 (b)). The variation in magnet-to-steel disk thickness ratios affects the magnetic force value on the magnetic roller surface due to variation in magnetic flow lines. Thus, the use of FEMM software will provide a clear idea about the magnetic force value on the magnetic roller surface for different magnet-to-steel disk thickness ratios. Therefore, the FEMM analysis of magnetic roller for different magnet-to-steel disk thickness ratios has to be carried out by considering the properties of particles size fraction through prior characterization studies. Then, the obtained FEMM results can be validated through prediction analysis using ANN, to confirm that the obtained FEMM data was statistically accurate and valid.

1.5.1 Characterization studies

The ore (low grade) processing and its utilization mainly stem from their compositional features as well as ores' nature (Roy 2009). Therefore, the characterization of the ore sample was carried out with the aid of different approaches, including particle size analysis, wet chemical analysis, density measurement, X-ray diffraction (XRD) study, Optical microscopy (OM) study, and magnetic susceptibility study.

- Particle size analysis is a technique used for determining the distribution of various particle size fractions in the given sample using standard test sieves.
- The wet chemical analysis includes the methodology to dissociate sample with a reagent (acids) to solubilize in a solvent, then, identifies and quantifies the specific target elements by employing various measurement methods. If necessary, the sample will be separated and isolated.
- Density is a physical property that has a critical role to play. Moreover, density measurement provides information about a material's composition, purity, and concentration.
- XRD is a non-destructive way to analyze crystal structure, classify crystalline phases, and thereby reveal chemical composition data.
- Optical microscopy is a technique employed to closely view the mode of distribution of different phases in the given sample.
- Magnetic susceptibility study gives an insight into the extent where the particles could be magnetized in an applied magnetic field. Also, it shows how a particle is attracted to a magnetic field or repelled from it.

1.5.2 Finite Element Method Magnetics (FEMM)

FEMM is a collection of programs for solving planar and axisymmetric domains in two dimensions. Currently, the FEMM addresses magneto static problems of linear/nonlinear type, electrostatic problems of linear type, steady-state heat flow problems and magnetic problems with linear/nonlinear time harmonic (Baltzis 2010; David 2014).

FEMM is split into three sections:

1.5.2.1 Interactive shell (femm.exe): This program is a pre-processor (multiple document interface) and post-processor for the many kinds of problems that FEMM solves. It has a CAD-style interface for setting out the geometry of the problem to be solved, as well as defining material attributes and boundary constraints. Also, to make it easier to analyze existing geometries, DXF files from Autocad can be imported. In addition, contour and density plots are two ways to visualize field solutions. Moreover, the user can also analyze the field at any point, assess a variety of integrals, and plot various values of interest across user-defined contours using this program.

1.5.2.2 Triangle.exe.: This is an important feature of FEMM since it divides the solution region into a huge number of triangles. Also, it assigns points to the mesh to verify that there are no angles less than the desired angle. The triangulation algorithm is technically assured to terminate if a minimal angle is 20.7° or less. In fact, at minimal angles up to 33.8°, the algorithm frequently succeeds.

1.5.2.3 Solvers (**fkern.exe** for magnetics; **belasolv** for electrostatics; **hsolv** for heat flow problems; and **csolv** for current flow problems): Each solver starts with a set of data files that define the problem and solves the appropriate partial differential equations to produce results for the desired field over the solution domain. In addition, the solver automatically invokes the mesh generator to confirm that the mesh is updated.

Even though the FEMM addresses more number of problems, but the present concern is limited towards the magneto static problems. Magneto static problems have time-invariant fields.

In this scenario, the magnetic field intensity (H) and magnetic field/flux density (B) is required to obey the following condition:

$\nabla \times H = J$ (∇ with cross denotes curl, J denotes current density).   (1.6)

$\nabla \cdot B = 0$ (∇ with dot denotes divergence).   (1.7)

For any material, there is a constitutive link between B and H.

$B = \mu_n H.$ (1.8)

The permeability (μ_n) of a nonlinear material (e.g. saturating NdFeB, alnico or iron magnets) is essentially a function of B.

$$\mu_n = \frac{B}{H(B)}. \tag{1.9}$$

FEMM uses a magnetic vector potential technique to determine a field that meets the equation (1.6)-(1.8). The vector potential (A) is used to express the flux density as:

$$B = \nabla \times A. \tag{1.10}$$

Equation (1.7) is now satisfied by this notion of B. Then, rewrite equation (1.6) as:

$$\nabla \times \left(\frac{1}{\mu_n(B)} \nabla \times A \right) = J. \tag{1.11}$$

In the case of a linear isotropic material (with the assumption that, $\nabla \cdot A = 0$ for Coulomb gauge), equation (1.11) is reduced to:

$$-\frac{1}{\mu} \nabla^2 A = J. \tag{1.12}$$

To solve magneto-static problems with a nonlinear B-H relation, FEMM keeps the form of equation (1.11). In a generic 3D case, 'A' is a three-component vector. Whereas, two among those three components are zero in the 2D planar and axisymmetric scenarios, leaving only the "out of the page" component.

1.5.3 Artificial neural network (ANN)

ANN is a type of modelling tool that may be used to solve large nonlinear systems with challenges to establish relationships among input and output variables. The ANN system works similarly to the human brain's neuron system. The trained ANN predicts the unknown output from a given set of input data, similar to how a human brain does. The basic steps in ANN modelling are outlined here (Panda et al. 2014; Moghadassi et al. 2009; Sahoo and Roy 2007).

(a) Data is organized systematically;

(b) Identification of data sets for learning and testing;

(c) The ANN structure is being designed;

(d) The input data is used to train the ANN model;

(e) The trained ANN model is verified;

(f) Repeat steps (b) through (e) until an optimized ANN model has been prepared;

(g) To predict the output of a given input, use the ANN model.

The ANN serves as a link among input parameters and output values, and it may be either a feed-forward or feedback neural network. A Feed Forward Neural Network (FFNN) comprises of unlike types, i.e., radial-basis function nets, multi-layer perception (MLP), and single-layer perception. However, MLP is commonly employed for data analysis (Chaurasia and Nikkam 2017; Deosarkar and Sathe 2012).

In ANN modeling, MLP based FFNN is used for most of the non-linear systems (Fig. 1.5). Whereas, in an FFNN, the flow of information is in a forward direction (i.e., input to hidden to output). Also, MLP based FFNN consists of input, hidden, and output layers. However, depending on the intricacy of the problem to solve, the ANN structure may contain multiple hidden layers. As depicted in Fig. 1.5, neurons (connecting lines among nodes) connect nodes in one layer to nodes in other layers. These neurons are coupled with weights and are based on a weight adjustment-based learning algorithm (Panda et al. 2014; Moghadassi et al. 2009; Sahoo and Roy 2007). Fig. 1.5 and 1.6 depict the MLP neural network and general ANN model, respectively.
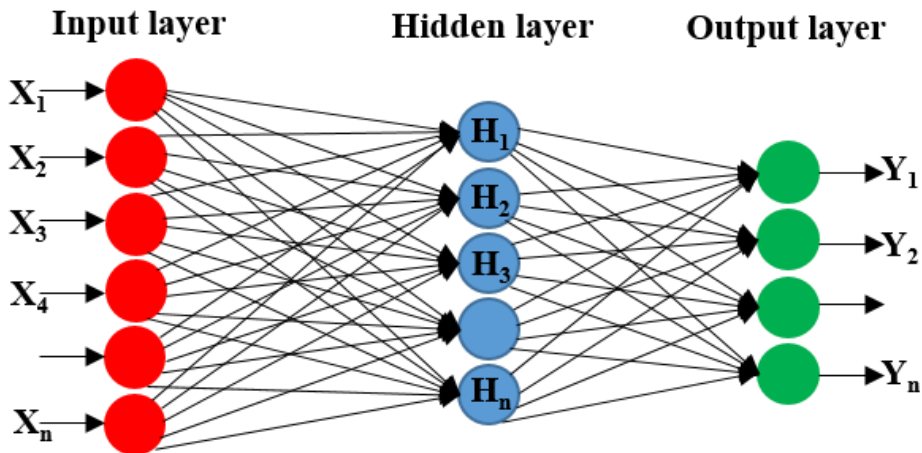
Fig. 1.5: Schematic representation of MLP neural network model (Panda et al. 2014).
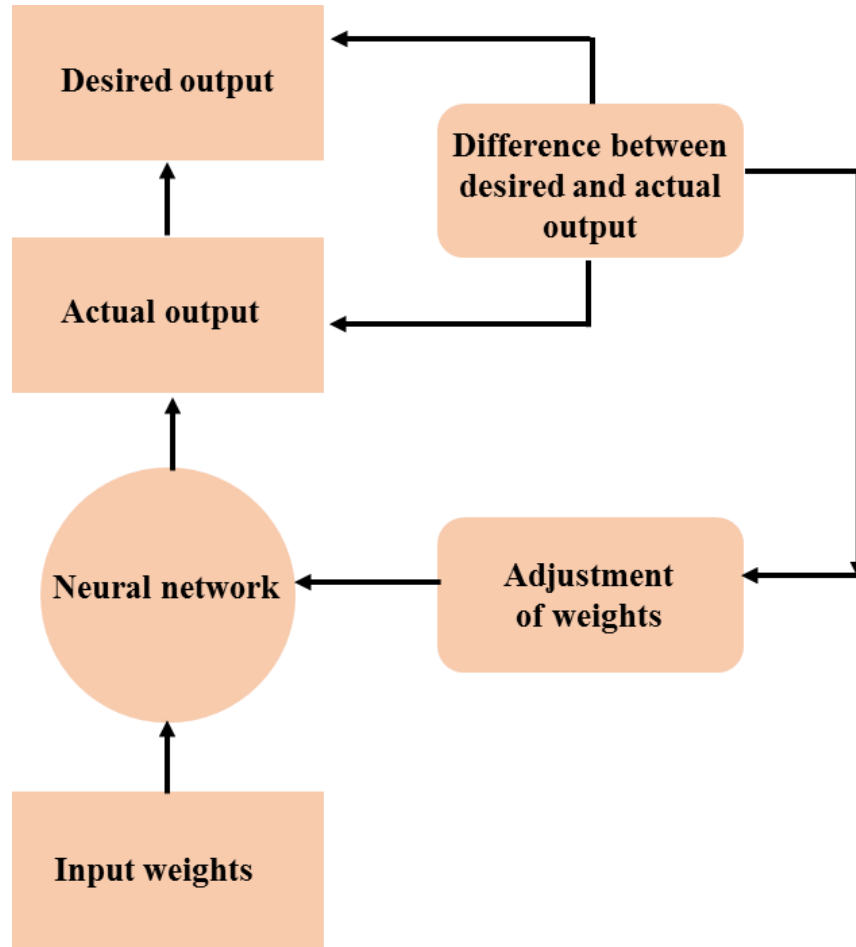
Fig. 1.6: Schematic diagram of ANN (Panda et al. 2014).

The following equation (1.13) is used to determine neuron's output (Panda et al. 2014):

$$Y_{jk} = F_k\left(\sum_{c=1}^{N} W_{cjk}X_{c(k-1)} + b_{jk}\right). \tag{1.13}$$

Linear and sigmoidal functions are often utilized transfer functions for non-linear systems. Mean squares error (MSE) is a common performance function for training FFNNs, which is expressed by the following equation (1.14)

$$MSE = \frac{1}{N}\sum_{c=1}^{N}(\tau_c - \alpha_c)^2. \tag{1.14}$$

1.6 Optimization approach

The completion of design aspects of PRMS paved the way for the evaluation of separation performance of PRMS followed by optimization of selected operating parameters using DOE. In DOE, a set of well-planned experiments comprises all the variables that are varied within a defined range and are a far more effective method of obtaining systematic data. Usually, Taguchi and Analysis of Variance (ANOVA) based experimental design and results processing methods, respectively were widely used (Naik et al., 2021; Yunus and Alsoufi, 2016).

1.6.1 Principle of Taguchi technique

The Taguchi technique is a scientifically disciplined mechanism for analyzing and improving product quality and process optimization. These improvements strive to improve the required qualities and simultaneously minimize the number of faults by examining the main variables affecting the process and optimizing the process or design to provide the best outcomes. This technique is used in a variety of engineering domains including the process responsible for production, fabrication, CAED, and service sectors (Taguchi and Konishi, 1987). However, in the overall case, the Taguchi approach can be used to 'tune' a process for achieving 'optimal' results.

Taguchi method employs orthogonal arrays from DOEs theory to study a wide number of parameters with a small number of tests. Orthogonal arrays considerably minimize the number of tests to be run. In the Taguchi method, three types of parameters (or noise factors) optimization are stated (Ranjit, 1990; Taguchi, 1987):

- Smaller is better: the purpose of this optimization type is to minimalize the response
- Larger is better: the purpose of this optimization type is to maximize the response
- Nominal is better: the purpose of this optimization type is to achieve the desired value

The Signal-to-Noise (S/N) ratio is calculated for each experiment and used to interpret experimental results, where, 'signal' refers to studied response and 'noise' refers to a set of variables for the given test. The definition of the S/N ratio relies on the optimization target (smaller is better, larger is better, or nominal is better). The equation

12

(1.15) defines the S/N ratio for the ''Larger is better'' optimization type. The equations for the other two types of optimization were found elsewhere (Ranjit, 1990; Taguchi, 1987).

$$\frac{S}{N_A} = -10\log_{10}\left[\frac{1}{n_r}\Sigma_{j_r=1}^{n_r}\frac{1}{Y_{Aj_r}{}^2}\right].$$ (1.15)

Using equation (1.15), the S/N ratio for each experimental condition was obtained. Further, the developed S/N ratios were utilized for result representation and interpretation in terms of the main effect plot and interaction plot.

1.6.2 Principle of ANOVA technique

Analysis of variance (ANOVA) is a statistical analytical technique that uses data sets into random and systematic factors. The systematic factor has statistical influence, whereas the random factors have no statistical influence. The ANOVA technique regression analysis provides the closeness of input and output variables (Corte et al. 2019).

ANOVA is also called the Fisher analysis of variance. The term became well-known in 1925 after appearing in Fisher's book, "Statistical Methods for Research Workers." ANOVA was initially utilized for experimental psychology, and later, it was utilized for wide application in resolving complex problems.

The formula for ANOVA is,

$$F = \frac{MST}{MSE}.$$ (1.16)

Where,

F= ANOVA coefficient

MST= Mean sum of squares due to treatment

MSE= Mean sum of squares due to errors

Moreover, the ANOVA test is a preliminary statistical procedure carried out to determine the influential factor affecting the data set. After completion, the additional confirmation test was carried out to determine the data set's consistency. The ANOVA results provide the F-test, which determines the influential and non-influential variables. (Youssef et al. 2014). It was also found that the ANOVA test provides the analysis of several factors simultaneously. This eliminates the utilization of one factor at a time analysis. The F-test provides the analysis of multiple factors affecting the variability

between samples and within samples and also provides whether a relationship exists between them (Makhula et al. 2016).

1.7 Outline of the thesis

In the present work, the prior characterization studies on as-received ore samples followed by FEMM analysis of magnetic roller for different magnet-to-steel disk thickness ratios was carried out. Then, the validation of obtained FEMM data was performed through prediction analysis using ANN modelling technique. However, based on the FEMM analysis results, the optimized magnet-to-steel disk thickness ratio was considered for the fabrication of the magnetic roller. In addition, the design calculation has been done on the power requirements and belt tensions of fabricated lab-scale PRMS. The experiments were conducted for different roller speeds and belt thicknesses to evaluate the separation performance of fabricated lab-scale PRMS.

The thesis has been presented in five chapters

**Chapter 1** introduces an overview of magnetism and magnetic separation innovation, general aspects, separation mechanism, and the principle of magnetic separation followed by design aspects involved in the development of new lab-scale PRMS and optimization approach.

**Chapter 2** gives a detailed review of the published literature relevant to the present study. The literature review presented mainly includes earlier research work carried out on the characterization studies, the concentration of different minerals, and improvement in the product grade by discarding the iron-bearing/magnetic minerals as a gangue from the valuables under different operating parameters. In addition, earlier work related to the wide application of FEMM, ANN, and DOE technique in the optimization were also reviewed. The broad objectives of the present research work are drawn based on the gaps observed in the available literature.

**Chapter 3** describes the methodology which includes material selection, characterization techniques/facilities, and parameters considered in FEMM and ANN approach followed by the experimental procedure for magnetic separation and optimization of selected operating parameters of PRMS through the DOE technique were discussed.

Chapter 4 comprises the results and discussion of characterization studies of as-received samples, design, and fabrication of optimized magnetic roller for PRMS through FEMM and ANN technique followed by DOE approach for parameters optimization and evaluation of separation performance.

Chapter 5 presents the conclusions drawn based on the results obtained in this research work and the future scope of work is also enlisted. The appendix and the list of references are shown at the end of the dissertation.

CHAPTER 2

LITERATURE REVIEW

A detailed literature review of published research articles related to characterization studies and magnetic separation under different operating parameters for different applications was reported. In addition, wide application of FEMM, ANN, Taguchi, and ANOVA methods in the parametric optimization were also reviewed from the available literature.

2.1 Characterization studies

The characterization studies are aimed at classifying the various phases to understand their distribution, phase morphology, and mineral behavior for recovering additional values. Analysis of previous research reveals that the up-gradation of iron ore of lower grade is not a challenging one, but the beneficiation procedure must be suited to the ore's quality and acceptable for different range products. The problem lies in assuming the effectiveness of a technique and economics associated with the quality of the ore. Therefore, before ore processing, adequate characterization study of the ore is vital. In this regard, characterization study of as-received iron ore sample has to be done in terms of particle size analysis, elemental composition analysis, mineral phase analysis & their distribution, and magnetic susceptibility study.

Dwari et al. (2013) performed a magnetic separation study on lean grade siliceous magnetite ore. However, the prior characterization studies on lean grade iron ore sample include size-wise Fe analysis and reflected light microscopic studies. The analysis indicates (Table 2.1) that the distribution of Fe is almost uniform in the particle size fractions of -10+6 to -1+0.850 mm, after that the content of Fe upsurges and maximum extent was attained at a particle size fraction of 0.1 mm. Further, the microscopic studies (Fig. 2.1) of polished sections indicate that the sample (hand specimen) generally comprises Fe bearing mineral phases such as goethite (FeO), magnetite (Fe_3O_4), and hematite (Fe_2O_3) along with gangue mineral phases (carbonates and silicates). Liberation studies on particle size fractions show (Fig. 2.2) that Fe_3O_4 mineral grains have shown the optimal liberation under 0.1 mm size fraction. Therefore, from all these characterization studies it was concluded

that the beneficiation study can be carried out using magnetic separation technique because the selected iron ore is Fe_3O_4 in nature.

Table 2.1: Size-wise Fe distribution at dissimilar particle size fractions.

Particle size fractions (mm)	Wt. (%)	Fe (%)
-10+6	15.17	42.50
-6+3	13.75	43.60
-3+2	17.55	41.55
-2+1	9.34	40.58
-1+0.850	5.20	41.53
-0.850+0.500	7.29	42.34
-0.500+0.300	3.36	44.70
-0.300+0.210	6.62	47.46
-0.210+0.100	7.19	47.00
-0.100	14.53	48.00
Head	100	43.76
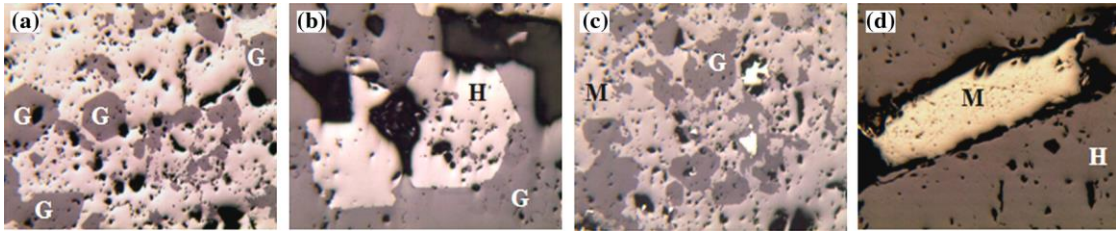
Fig. 2.1: Photomicrographs of hand specimen: (a) Gangue minerals (G) with in the hematite (H), (b) hematite mineral within the gangue minerals, (c) the gangue minerals contained microscopic magnetite (M) grains, and the G was encapsulated within the H, and (d) Magnetite inside the hematite is of lath shape (Dwari et al. 2013).
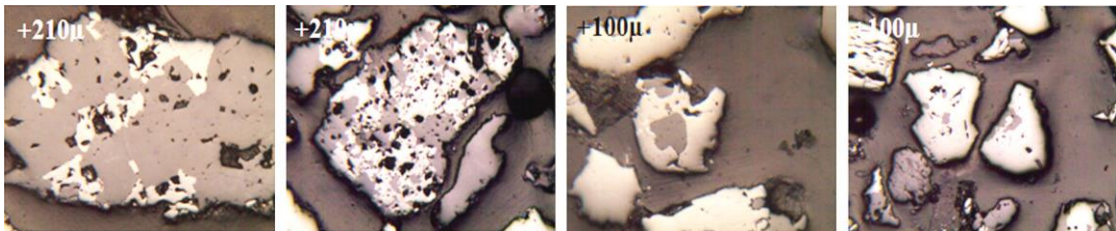
Fig. 2.2: Photomicrographs of categorized size fractions which shows the optimal liberation can happen under 0.1 mm size fraction (Dwari et al. 2013).

The same author Dwari et al. (2014) conducted another investigation employing magnetic separation technology to separate siliceous iron ore of lower grade. Whereas, the characterization/mineralogy study with the aid of XRD (Fig. 2.3) and OM (Fig. 2.4), revealed that the head (as-received) sample contains chief Fe bearing mineral phases such as goethite (G), magnetite (M), and hematite (H) along with kaolinite (K) and quartz (Q) as gangue mineral phases. Also, according to a quantifiable mineralogical study, the sample has about 7.69 % of magnetite accompanied by goethite (40.94 %), hematite (34.97 %), and quartz (9.67 %) phase, which makes the ore suitable for processing using magnetic separation technique. Hence, from the characterization studies it was concluded that, initially, the sample could be exposed to LIMS (to remove magnetite first), followed by the WHIMS of LIMS's tailings to achieve the best recovery of Fe values from the sample.
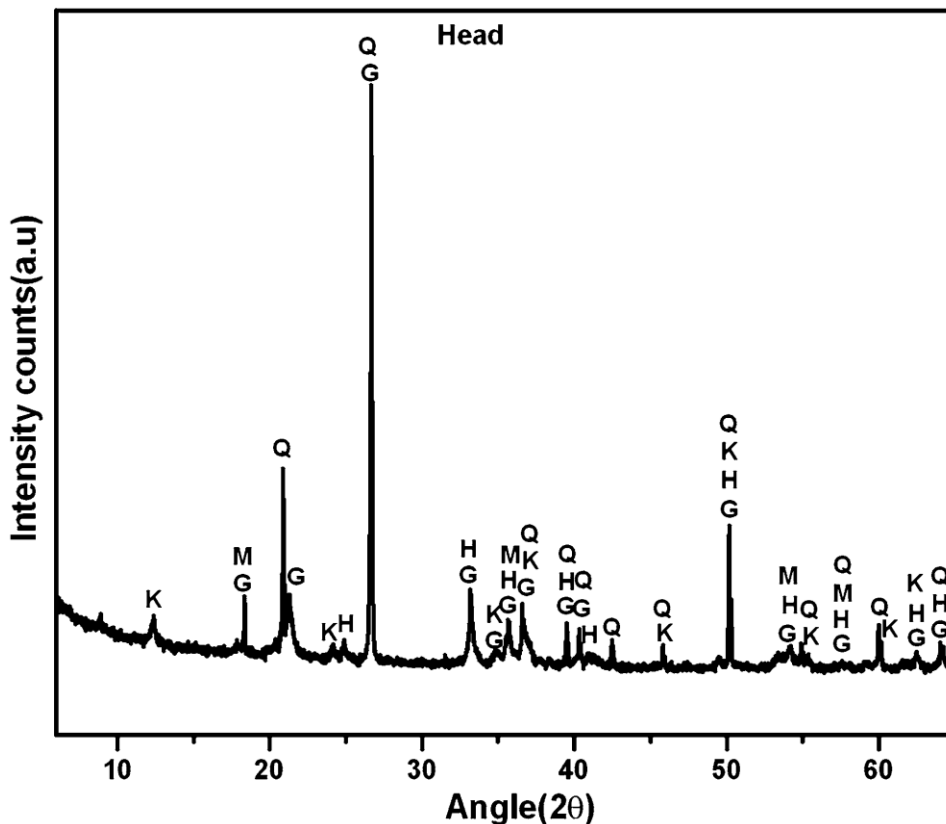
Fig. 2.3: Head (as-received) sample's XRD pattern (Dwari et al. 2014).
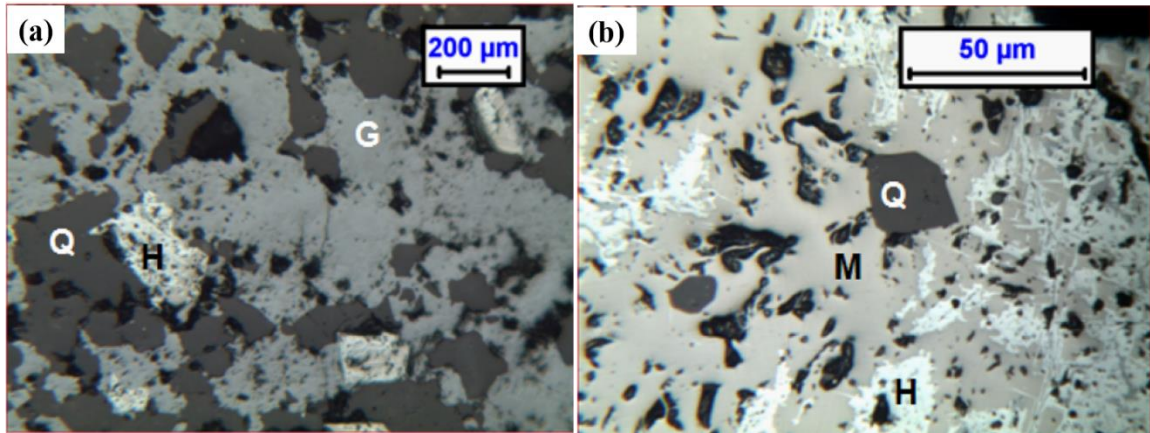
Fig. 2.4: Reflected light photomicrographs: (a) Goethite, quartz, and hematite are all closely associated with one another. Also, the shape, as well as size of silicates, differ widely, and (b) Reveals the presence of hematite and silicate inside the magnetite (Dwari et al. 2014).

Jena et al. (2015) used a flow sheet that included hydrocyclone as well as magnetic separation technology to conduct a beneficiation investigation on bulk (as-received) Fe ore slimes from Barsua mines, India. Initially, the characterization study on the slime sample indicates that 46.4 % of material is below 45 µm assayed 53.4 % of Fe. Also, the existence of goethite and hematite as chief Fe-bearing mineral phases along with kaolinite mineral as the main gangue phase was indicated by the XRD study (Fig. 2.5 (a)). Whereas the presence of quartz was in minor amount as silicate phase, hence the peaks related to quartz phase were not be detected, but during the SEM-EDS study (Fig. 2.5 (b)) the quartz was detected. Also, similar mineral types were witnessed in the particle size fractions of below 45 µm. Hence from these characterization studies, it was concluded that the iron ore slimes should be treated with hydrocyclone to separate the associated SiO_2 and Al_2O_3 bearing gangue mineral particles from the finer particle size fractions. In addition, WHIMS was used to recover lost iron values in the slimes of hydrocyclone underflow products. Since the Fe-bearing minerals have relatively different magnetic susceptibility than that of associated gangue mineral phases which leads to attaining an appropriate Fe grade and recovery %.
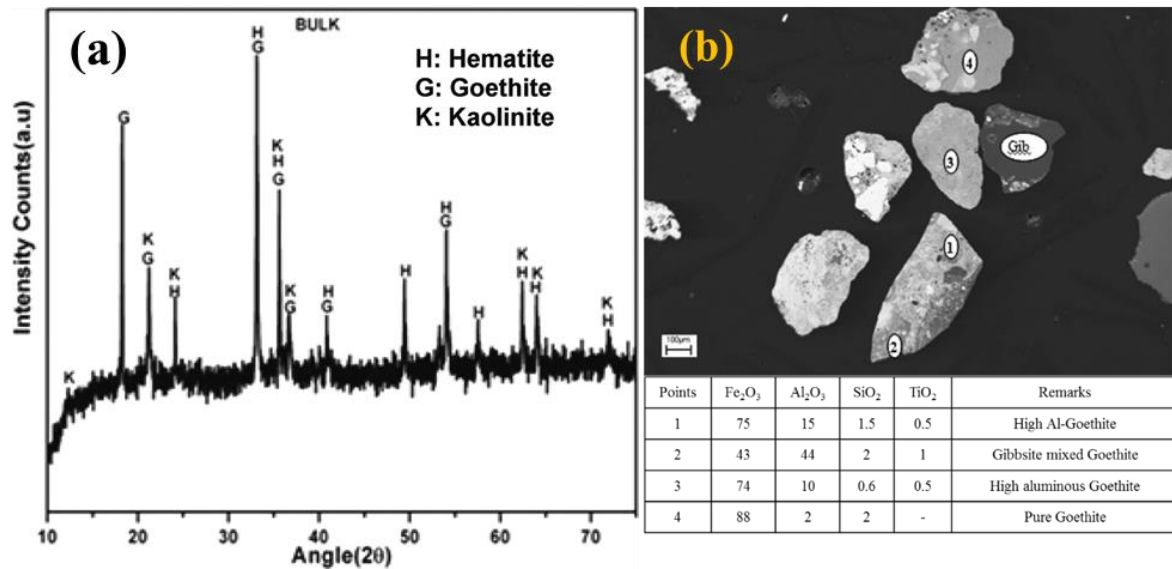
Fig. 2.5: (a) Iron ore slime's XRD pattern, and (b) Iron ore slime back-scattered electron picture with EDS point analysis (Jena et al. 2015)

Likewise, a similar study conducted by Rao et al. (2016) on the recovery of iron values from hematite fines (slime) via hydrocyclone, followed by magnetic separation results in producing pellet grade concentrate. At first, the characterization studies such as size-wise elemental distribution, XRD, and the microscopic study was carried out which reveals the nature of the sample. Fig. 2.6 shows the dissemination of Fe at coarser particle size fractions, whereas SiO_2 and Al_2O_3 at finer particle size fractions. The XRD study (Fig. 2.7) indicates that the Al_2O_3 is in the form of Kaolinite ($Al_2Si_2O_5(OH)_4$) and iron is in the oxide form (Fe_2O_3). In addition, the microscopic study (Fig. 2.8) shows the occurrence of Fe-bearing minerals in the form of goethite and hematite, whereas the gangue minerals were ferruginous clay, quartz, and pseudo ore. So, based on the characterization studies, it was concluded that desliming is required to eliminate the fine particles of Al_2O_3 and SiO_2 using hydrocyclone. Then, the hydrocyclone underflow products were exposed to WHIMS to achieve pellet grade concentrate.
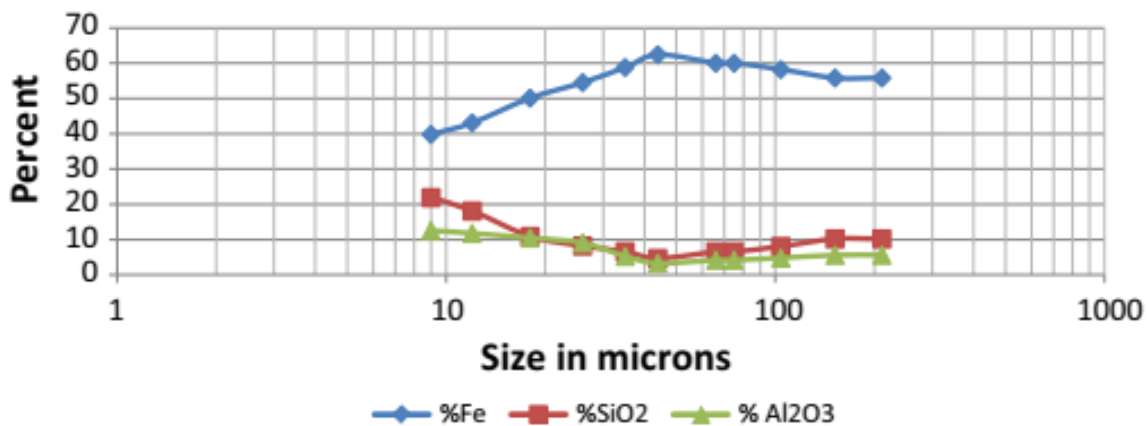
Fig. 2.6: Distribution of Fe, SiO$_2$, and Al$_2$O$_3$ in various particle size fractions of as-received slime sample (Rao et al. 2016).
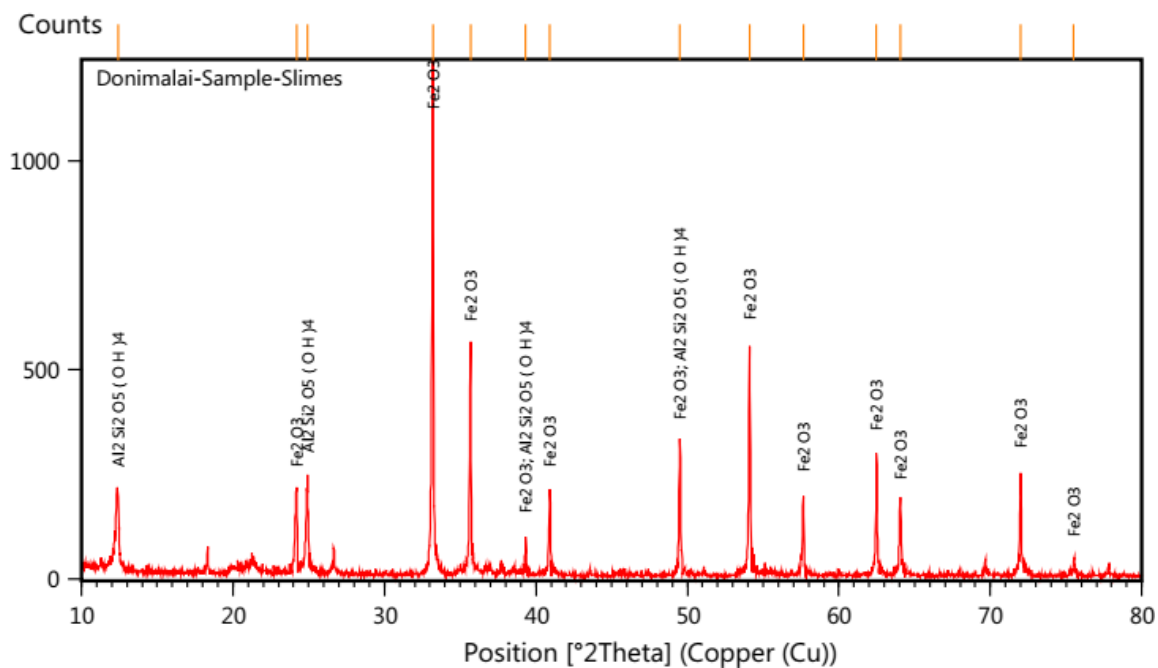
Fig. 2.7: As- received slime sample's XRD pattern (Rao et al. 2016).
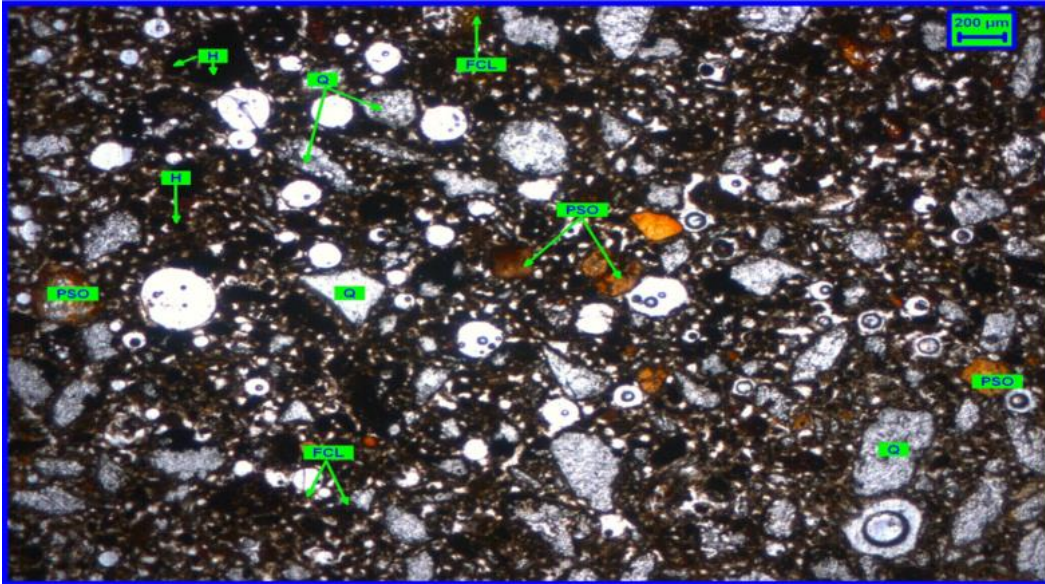
Fig. 2.8: Photomicrograph under transmitted light mode displays the dissemination of Ferruginous Clay (FCL), Hematite (H), irregular-shaped Quartz (Q), and Pseudo Ore (PSO) in as-received slimes (Rao et al. 2016).

Yu et al. (2017) carried out a magnetizing roasting (roasting with bitumite) method followed by LIMS of carbonate-bearing Fe ore of lower grade. Primarily, the XRD pattern (Fig. 2.9 (a)) of sample indicates the chief Fe-bearing minerals as siderite, hematite, and magnetite, whereas quartz and chlorite were gangue minerals. In addition, an optical microscopy study (Fig. 2.9 (b)) reveals the presence of finely associated hematite in magnetite along with gangue minerals. Therefore, from characterization studies (XRD and OM study) it was found that due to the existence of weakly magnetic iron minerals (hematite and siderite) in the sample. The application of LIMS could not be an effective method for the separation of valuable minerals. Hence, the Fe ore fines of low grade were magnetized by magnetizing roasting to make weak magnetic Fe bearing minerals acceptable for the separation using LIMS. In addition, the magnetic characteristic of as-received/raw and roasted ore was investigated using VSM. It was observed from Fig. 2.10 (a), the saturation magnetization was improved from 9 to 37 emu/g when the as-received ore was exposed to magnetizing roasting. This increased saturation magnetization indicates that the maximum amount of hematite phase was transformed to magnetite phase and

facilitates the effective separation using LIMS. In addition, the XRD pattern (Fig. 2.10 (b)) of roasted ore confirms the transformation of siderite as well as hematite phase into magnetite phase as compared with raw/as-received ore (Fig. 2.9 (a)). Therefore, from this available literature (Yu et al. 2017) it was found that through prior characterization studies, the suitability of the ore for magnetic separation study was justified.
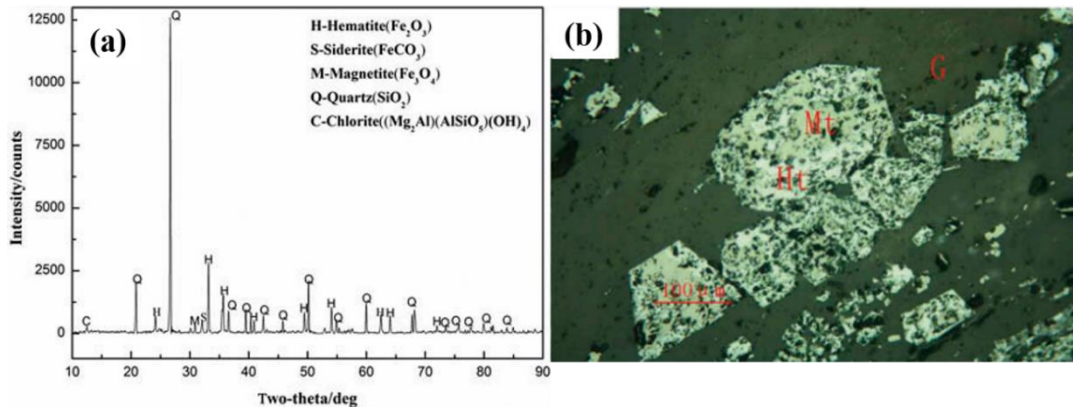
Fig. 2.9: (a) Fe ore (lower grade) sample's XRD pattern, (b) Microscopy images of iron ore (lower grade) sample; magnetite (Mt), hematite (Ht), and gangue (G) (Yu et al. 2017).
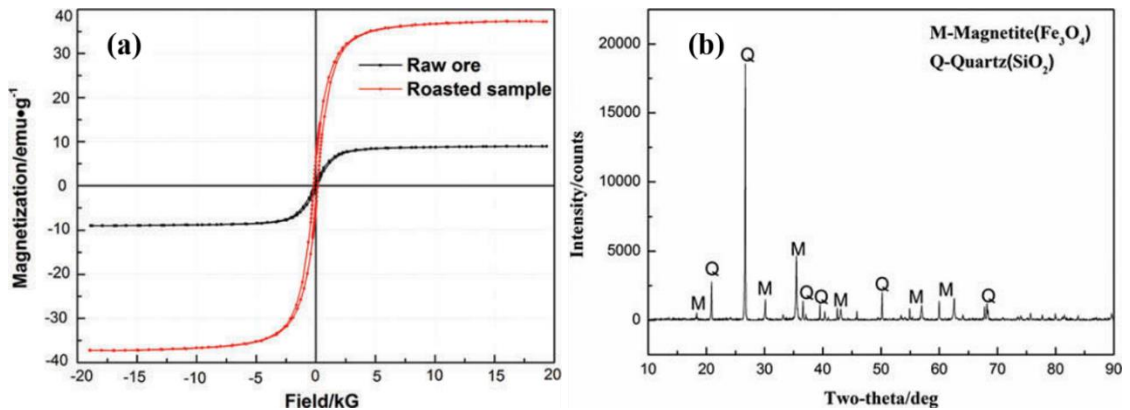
Fig. 2.10: (a) Hysteresis curve of raw and roasted ore, and (b) XRD pattern of roasted ore sample (Yu et al. 2017).

In addition, another similar study conducted by the same author (Yu et al. 2017a) on the up-gradation of hematite ore (low grade) comprising of carbonate-bearing minerals through magnetization roasting (roasting with bituminous coal) followed by magnetic separation. Initially, the XRD pattern (Fig. 2.11) of raw ore indicated the existence of

hematite and quartz phase structures. Whereas, other Fe-bearing minerals such as siderite as well as magnetite were not seen in the XRD study because of their minor content. Meanwhile, the Fe phase analysis of raw ore shows the dissemination of Fe in the form of iron sulfide minerals (0.29%), hematite (64.76%), carbonate (6.45%, primarily occur in ankerite and siderite), magnetite (27.29%), and iron silicate minerals (0.42%). Therefore, from the primary characterization study, it was concluded that the hematite ore (lower grade) comprising carbonate minerals can be upgraded through magnetic separation. Since the magnetic susceptibility, as well as saturation magnetization of hematite ore (low grade), was improved because of the selective transformation of siderite and hematite phase into magnetite phase via magnetization roasting technique. The effectiveness of magnetization roasting in improving the saturation magnetization as well as magnetic susceptibility of hematite ore was indicated in Fig. 2.12 (A) i.e., 8.9 emu/g (raw ore) to 37.3 emu/g (roasted product). As mentioned, this increase in saturation and susceptibility of hematite ore was because of the phase transformation of siderite and hematite into magnetite via magnetization roasting. The XRD pattern of the roasted sample at different temperatures was shown in Fig. 2.12 (B). It is clear to see that (Fig. 2.12 (B)) the maximum amount of hematite (Fe_2O_3) was converted to magnetite (Fe_3O_4) after roasting of raw ore, which justifies the suitability of ore for beneficiation through the magnetic separation process.
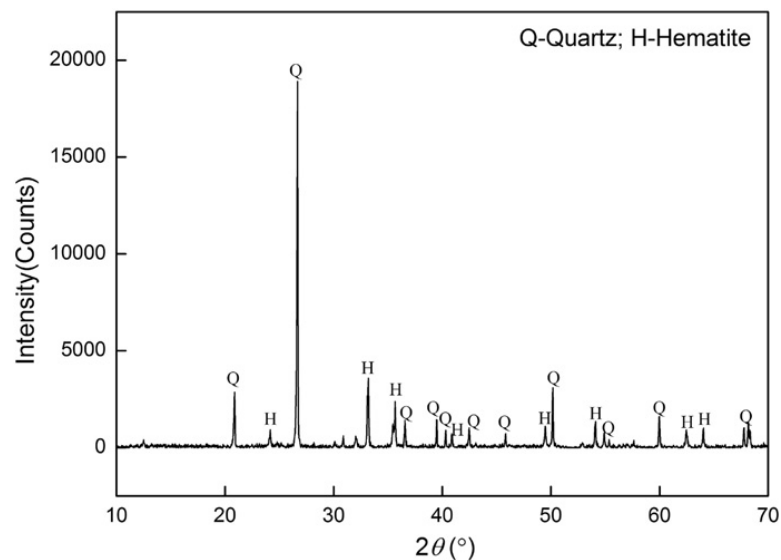
Fig. 2.11: XRD pattern of raw ore (Yu et al. 2017a).

24
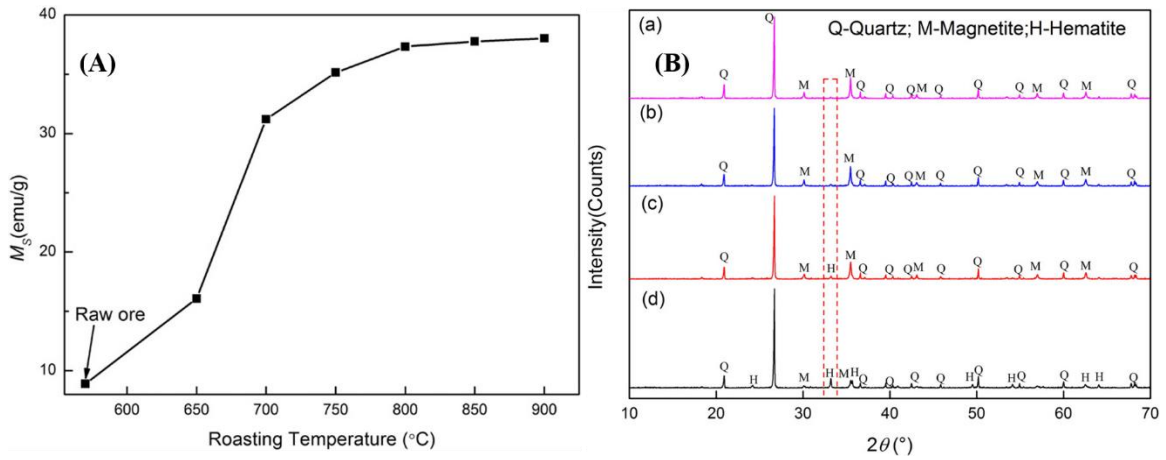
Fig. 2.12: (A) Roasting temperature effect on magnetic susceptibility of roasted samples, and (B) XRD patterns of ore roasted at various temperature; (a) 900 °C, (b) 800 °C, (c) 750 °C, and (d) 650 °C (Yu et al. 2017a).

Equally, the importance of particle magnetic susceptibility in magnetic separation was studied by Dahlin and Rule (1993). In their study, it was found that when two equal-sized particles of unlike magnetic susceptibilities are opened to an equivalent magnetic field, the magnetic forces created on both the particles will be unlike and allow the effective parting of these particles. Additionally, the magnetic susceptibility study in terms of magnetization versus applied magnetic field strength on paramagnetic minerals in comparison with diamagnetic and ferromagnetic minerals was investigated (Jiles 2015; Jordens et al. 2014; Waters et al. 2007). Since the specific magnetic behavior of a mineral has been analyzed by seeing the material magnetization versus applied magnetic field strength. The results indicated that paramagnetic materials show (Fig. 2.13) linear increase in magnetization as applied magnetic field strength increases due to the alignment of magnetic dipoles which are present in the sample (Jordens et al. 2014; Waters et al. 2007). On the other hand, the diamagnetic mineral has shown the negative linear behavior of magnetization as the applied field strength increases. This is due to the repulsion of diamagnetic minerals along the applied magnetic field lines (Jiles 2015; Waters et al. 2007). Whereas, in the case of ferromagnetic material, even at low applied field there was a swift rise in magnetization till it approaches magnetic saturation, at which time increased field strength has no influence on magnetization (Jordens et al. 2014; Waters et al. 2007).
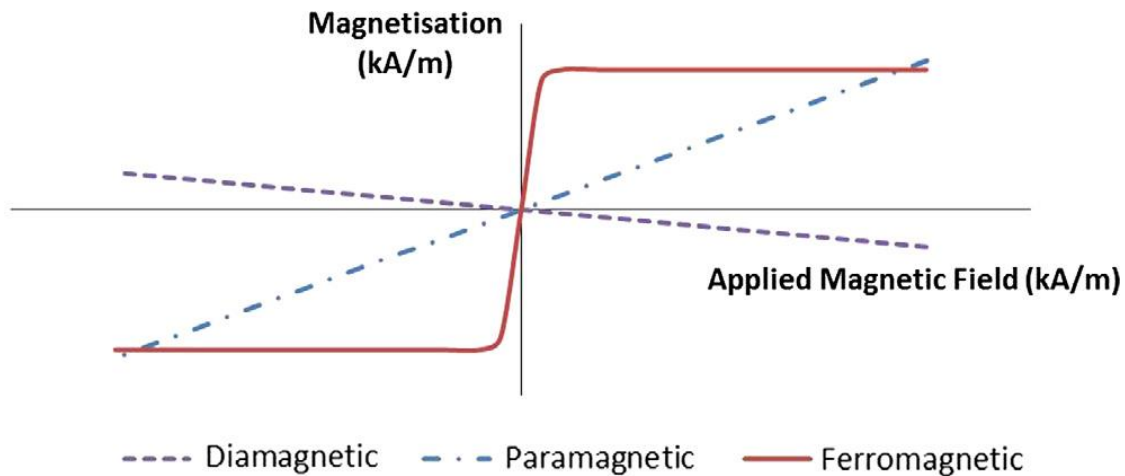
Fig. 2.13: Hysteresis curve for various materials (Waters et al. 2007).

Similarly, Tripathy et al. (2017a) investigated the magnetization property of as-received low grade hematite ore sample (Odisha, India) in their magnetic separation study. The result (Fig. 2.14 (a)) shows the magnetic characteristic of the sample (associated with jasper and hematite minerals) in terms of magnetization versus applied field strength. As seen in Fig. 2.14 (a), hematite displays a minor ferromagnetic trend with a significantly lower saturation magnetization. Since the paramagnetic property of the mineral (hematite) accounts for the lower saturation remanence value. Also, the decreased saturation magnetization value at 1.5 T (Fig. 2.14 (a)) is owing to the combination of jasper and hematite minerals, which reduces the value.

Another similar study was conducted by Tripathy et al. (2016) on the processing of ferruginous chromite ores (Sukinda chromite mines, India). It was observed from Fig. 2.14 (b), the higher grade mineral ore (Sample A) showed high magnetization value because of the large amount of paramagnetic mineral phase (FeO) associated with a small amount of quartz mineral (diamagnetic) as compared to ore of lower grade (Sample B).

26
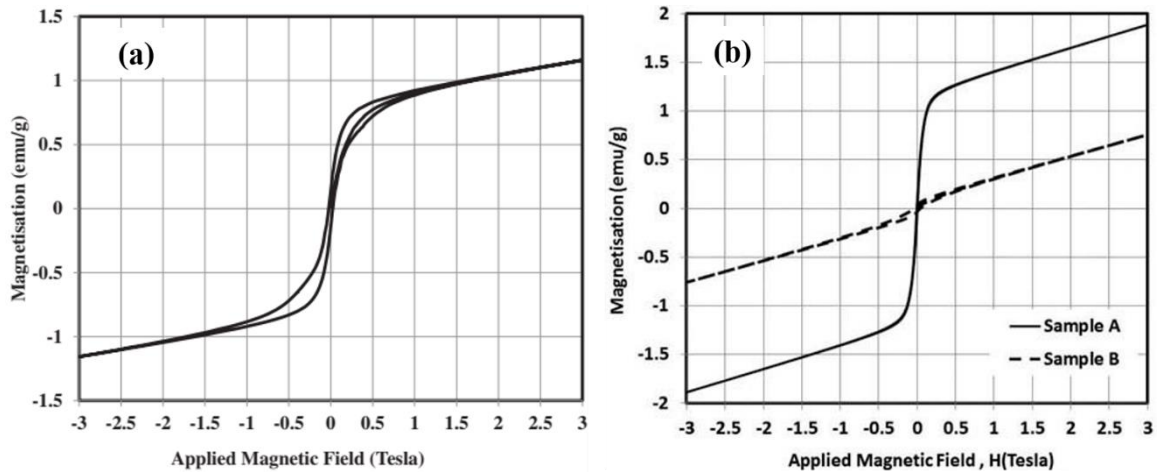
Fig. 2.14: Hysteresis curve (a) hematite ore of lower grade (Tripathy et al. 2017a), and (b) ferruginous chromite ore (Tripathy et al. 2016).

2.2 Permanent Roll Magnetic Separator (PRMS)

2.2.1 Brief description

The concept of a PRMS comprising of mild steel discs sandwiched between permanent magnet disks was first proposed in 1965 (Andreachi and palasvirta 1965). However, the advancement of these machines has taken place after the emergence of permanent rare-earth magnet materials. Then, a patent (Yaniv 1981) by E.L. Bateman Ltd became the beginning of the successful production of a wide range of roll separators. Originally, permanent magnets of samarium-cobalt (Sm-Co) were used, but, when neodymium (NdFeB) magnets become commercially accessible, they swiftly replace the samarium-cobalt (Sm-Co) magnets (Svoboda 2004). In addition, the PRMS is a major driver of advancement in dry paramagnetic mineral separation at high capacity and reduced operating costs. Also, the PRMS can now be used for medium to weak magnetic materials, because of the increasing accessibility of permanent magnetic materials (rare-earth) and their decreasing cost. Furthermore, the PRMS is generally more effective, selective, and easily attuned to feed variants depending upon the necessity. The highly efficient separators are successful not only with standard particle size fractions but also with materials including smaller size fractions (<75μm) (Arvidson 1999).

2.2.2 Effect of design specification

Many modifications have been done in the designing of PRMS to increase its separation ability. Wells and Rowson (1992) investigated PRMS performance by varying magnetic roller diameters. It was recorded that, the particle's resident time in the magnetic field and field depth increases as the roller diameter increases which provides good separation efficiency. Arvidson and Norrgran (2014) suggested that variation in magnet-to-steel disk width ratio escalates the magnetic force value due to the high concentration of magnetic field lines. Also, Svoboda (2004) reported that by maintaining a proper roller-belt assembly, the particles enter the magnetic region with even horizontal velocity and will have less rebound. This increases paramagnetic particles selectivity during the separation process. These aspects contribute to attaining a better separation and have considerably low mass as well as size than that needed in IRMS (Svoboda 2004; Svoboda and Fujita 2003).

The study made by Orhan and Gülsoy (2004) focuses on the effects of different magnet-steel configurations (Fig. 2.15 (a)) on the rejection of Fe-bearing minerals as impurities from the feed sample (feldspar). The difference in magnetic flux values for unlike roll design was displayed in Fig. 2.15 (b). From Fig. 2.15 (b), it was found that the maximum flux density on the surface of the roller was witnessed in the configuration 12:3 ratio. Also, they focus on the separation performance of Fe-bearing impurities from feldspar sample using different roll designs. From their study, it was concluded that, for the particle size fractions -0.5+0.075 and -1+0.075 mm, concentrate Fe_2O_3 content decreases in such a way that 12:3 > 8:2 > 4:1 magnet-steel configurations (Fig. 2.16 (a)). Whereas, in the size fraction -2+0.075 mm, concentrate Fe_2O_3 content shows opposite order (12:3 < 8:2 < 4:1 magnet-steel configurations). A similar relationship holds for the removal recovery of Fe_2O_3 (Fig. 2.16 (b)) for all the particle size fractions but in the opposite order. These results reveal that removal recovery of Fe_2O_3 and concentrate Fe_2O_3 is considerably get effected by the magnet-steel configurations in the concentration of feldspar sample. In addition, it was also concluded that the uppermost magnetic flux value does not give the best separation results for all the particle size fractions. The coarser size

fractions get separated effectively by high magnetic flux and magnet-steel configurations (width ratios). However, the dissemination of close particle size fractions results in efficient separation through magnetic separators rather than the wide range of particle size distribution (Orhan and Gülsoy 2004).
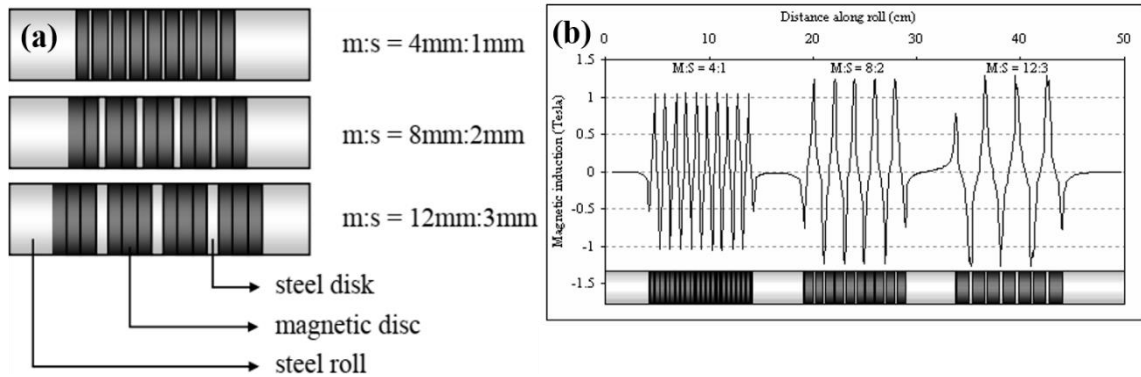
Fig. 2.15: (a) Magnet-to-steel disk configurations, and (b) Variation in magnetic flux throughout the magnetic roll length for dissimilar magnet-steel configurations (Orhan and Gülsoy 2004).
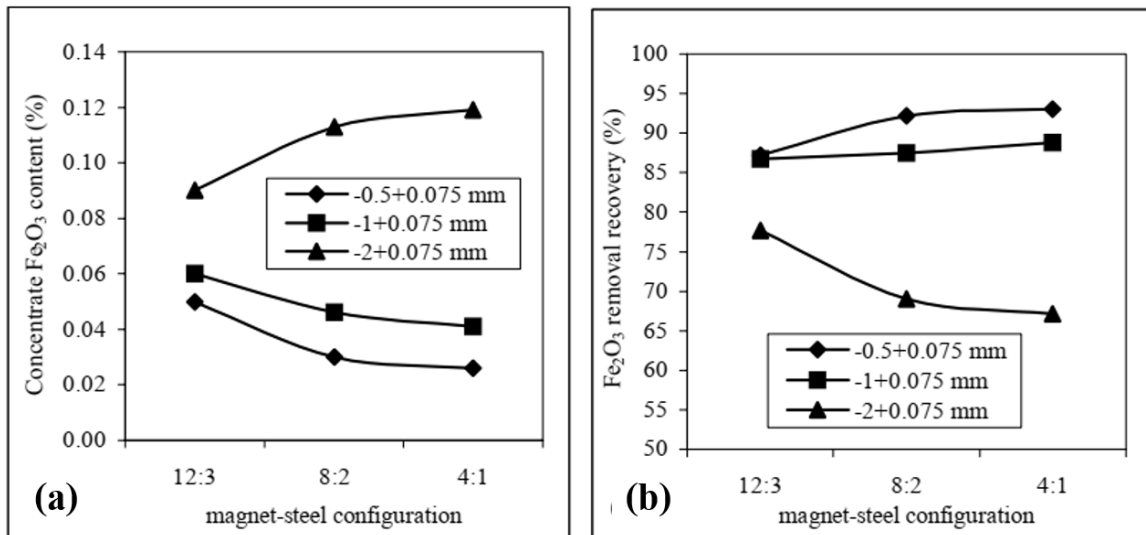
Fig. 2.16: (a) Percentage of concentrate Fe_2O_3 contents, and (b) Percentage removal recovery of Fe_2O_3, gained at unlike magnet-steel configurations (Orhan and Gülsoy 2004).

Tripathy et al. (2017a) conducted a study on Fe ore of lower grade using two unlike magnetic rollers (1.6 T and 1.2 T) operated at different roller speeds (100-400 rpm at 50 rpm increment) with a constant feed rate (0.2 ton/h) and splitter position (37˚). The results indicate (Fig. 2.17 (a)) that the magnetic product grade was augmented to 49.5 % Fe from 35.9 % Fe using a high-intensity magnetic roller (1.6 T) at 250 rpm. Whereas in lower intensity magnetic roller (1.2 T) the improvement in Fe content was only up to 42.6 % for the same roller speed 250 rpm. This decrease in product grade at lower intensity roll (1.2 T) compared to higher intensity roll (1.6 T) was because of the low magnetic field value (1.2 T) on the surface of roll which makes it unable to pick up para-magnetic minerals. In addition, the highest grade of 49.5 % Fe (Fig. 2.17 (a)), and separation efficiency of 40 % (Fig. 2.17 (b)) were reported at a roller speed of 250 rpm for a magnetic roll of 1.6 T field strength. While the yield (Fig. 2.17 (b)) of the magnetic product was in decreasing order with an upsurge in the speed of the roll. Also, the magnetic product grade was increased with an upsurge in the speed of roll i.e., up to 250 rpm (Fig. 2.17 (a)), which also mirrored in terms of high separation output (Fig. 2.17 (b)). Then, further, increase in roll speed over 250 rpm there was a decrease in product quality (Fig. 2.17 (a)). Since the domination of centrifugal force increases on ore particles at higher roll speed (over 250 rpm) which leads to decreased product quality.
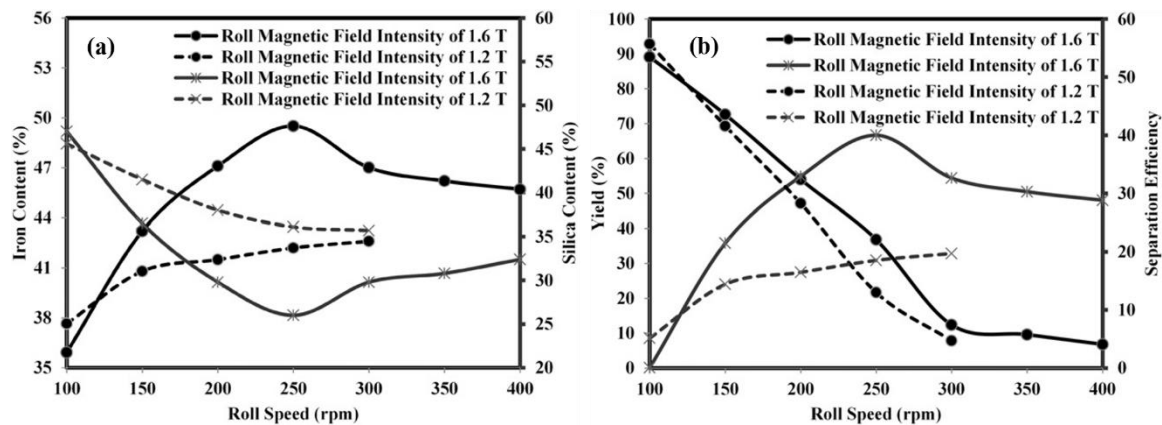
Fig. 2.17: (a) Roll speed effect on Fe and SiO_2 content, and (b) Roll speed effect on yield % and efficiency of separation (Tripathy et al. 2017a).

2.2.3 Mineral separation

Many authors have analyzed the influence of different operating parameters on the grade and recovery of magnetically separated products. In that contrast, the effect of particle size on the separation of minerals in RERMS under different roll speeds and splitter position was carried out by Ibrahim et al. (2017); Tripathy et al. (2015); Gehauf (2004). The effect of size of the particle in a given magnetic field was explained in terms of the trajectory of the particle, and reporting of a particle to the product bins as shown in Fig. 2.18. It was observed from Fig. 2.18, the magnetic particles that are firmly adhered to a surface of the magnetic roll are often stuck to the roller surface till they are free from the influence of the magnetic field. Whereas, the feebly adhered magnetic particles deflected by the given magnetic field and causing them to deviate from their typical path. When this happens, the big, feebly adhered magnetic particles and the tiny, non-magnetic particles were get overlapped, which affects the grade and recovery of final products (Ibrahim et al. 2017; Tripathy et al. 2015; Gehauf 2004).
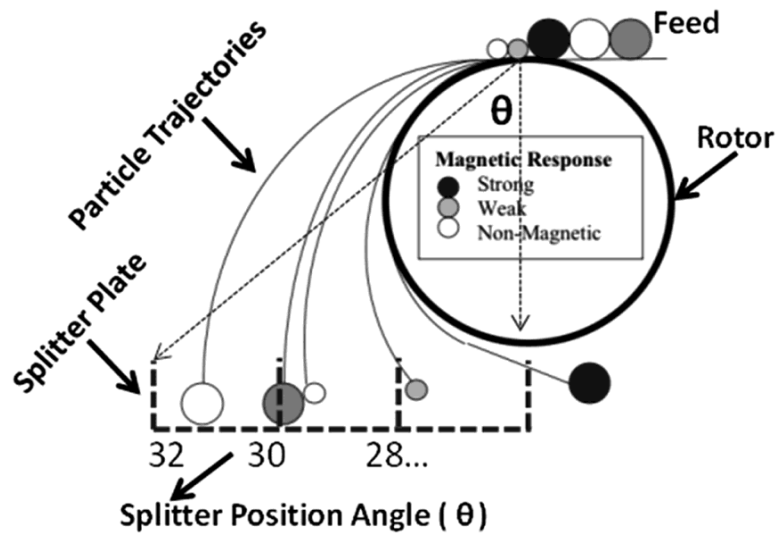
Fig. 2.18: Trajectories of various particle size fractions having different magnetic concentrations (Ibrahim et al. 2017).

A separation study of iron ore of lower grade was performed by Dwari et al. (2014) on a reduced size fraction of below 1 mm using PRMS. Where the operating parameters such as feed rate, roller speed, belt thickness, and splitter position were kept constant. The

results suggested that the feed of 44.3 % Fe was increased up to 60.2% Fe with the recovery of 30.05% Fe. Also, the XRD study (Fig. 2.19 (a), (b), (c)) of processed products in comparison with the head (as-received) sample (Fig. 2.19 (d)) confirms the enrichment of Fe content in the magnetic concentrate products. The XRD study of concentrate product (Fig. 2.19 (a)) indicates the Fe-bearing mineral phases such as goethite (G), hematite (H), and magnetite (M). Whereas the presence of kaolinite (K) and quartz (Q) along with Fe bearing phases were shown in middling fractions (Fig. 2.19 (b)). In addition, the occurrence of much higher gangue mineral phases (kaolinite and quartz) was noticed in the tailings fraction (Fig. 2.19 (c)) as compared to magnetic and middling fractions.
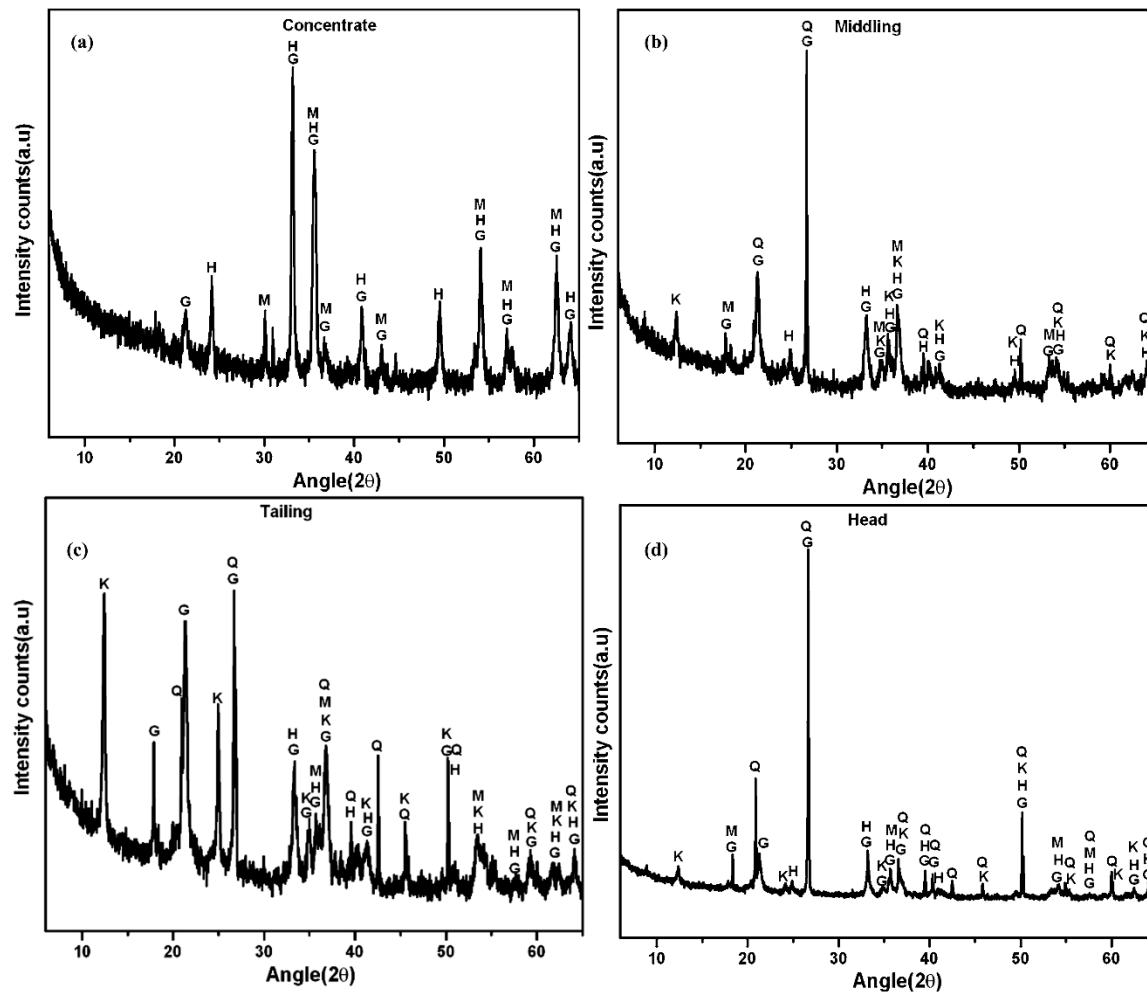
Fig. 2.19: XRD pattern of (a) Magnetic concentrate (b) magnetic middling (c) tailing, and (d) head (as-received) sample (Dwari et al. 2014).

32

Likewise, another similar study was conducted by the same author Dwari et al. (2013) on dry magnetic separation (PRMS) for a feed size range of -1+0.3 mm and -0.3 mm, by keeping feed rate, roll speed, belt thickness, and splitter position constant. The results indicated (Table 2.2) that the iron ore fines assaying 43.8% Fe were upgraded more than 50% Fe and an average of 85% Fe recovery was obtained at the magnetic product.

Table 2.2: Magnetic separation study on bulk (as-received) samples.

As-received	Product	Wt. %	Fe %	Fe recovery %
-1+0.3 mm	Magnetic	68.34	51.94	88.0
	Middling	9.04	23.32	5.2
	Non-magnetic	22.62	12.15	6.8
	Head	100	40.35	100
-0.3 mm	Magnetic	86.30	50.96	95.3
	Middling	4.10	19.83	1.8
	Non-magnetic	9.60	13.86	2.9
	Head	100	46.13	100

Also, the PRMS is used as an alternative unit for improving the product grade by discarding the iron-bearing/magnetic minerals as a gangue from the valuables.

Tripathy et al. (2016) carried out the separation study for two dissimilar chromite specimens (Sample A and Sample B) from the Sukinda region, India using RERMS. The existence of possible composition of chromite samples was shown in Table 2.3. The study reveals (Table 2.4) that, for Sample A, reduction in yield % was 92.9%-30.8% when the roller speed increases from 150-350 rpm, respectively, where the feed rate is 0.2 tph. However, for Sample B, the reduction in yield % was 98.5%-47.3% for the same roller speed and feed rate condition as that of Sample A. Also, the corresponding improvement/decrement in the grade of products for Sample A and B was represented through Cr_2O_3 and SiO_2 % as shown in Table 2.4 at different operating conditions.

Table 2.3: Compositional study of chromite samples.

Samples	SiO_2	Al_2O_3	Cr_2O_3	Fe	MgO	CaO	LOI	Cr:Fe
Sample A	4.3	9.5	50.6	11.1	12.7	3.2	2.5	3.09
Sample B	9.7	11.6	34.7	18.3	8.0	2.7	5.5	1.29

Table 2.4: Results of RERMS for different operating conditions.

Feed rate tph	Roll speed rpm	Product	Sample A				Sample B			
			P	Q	R	S	P	Q	R	S
0.1	150	M	95.0	50.4	4.1	3.05	98.9	34.7	9.5	1.29
		NM	5.0	53.9	6.5	4.17	1.1	32.3	22.4	1.94
	250	M	87.1	50.1	4.2	3.00	95.0	34.4	9.6	1.26
		NM	12.9	54.0	4.5	3.91	5.0	41.2	12.0	1.99
	350	M	36.8	42.4	4.4	2.05	55.7	39.3	7.9	1.78
		NM	63.2	55.3	4.2	4.00	44.3	28.9	11.9	0.88
0.2	150	M	92.9	50.3	4.1	3.04	98.5	34.8	9.5	1.29
		NM	7.1	53.6	6.3	4.00	1.5	30.0	22.5	1.80
	250	M	84.9	49.9	4.2	2.99	92.9	34.4	9.5	1.25
		NM	15.1	54.3	4.8	3.79	7.1	39.4	11.9	2.04
	350	M	30.8	37.2	5.7	1.75	47.3	43.6	7.5	1.97
		NM	69.2	56.5	3.6	3.99	52.7	26.7	11.7	0.86
0.3	150	M	88.7	50.2	4.0	3.01	93.8	34.8	9.0	1.26
		NM	11.3	53.7	6.2	3.93	6.2	33.5	19.5	1.96
	250	M	82.6	49.9	4.1	2.97	88.6	34.0	9.4	1.23
		NM	17.4	53.8	4.9	3.81	11.4	40.3	11.6	1.89
	350	M	25.9	36.1	4.1	1.65	32.9	42.1	7.4	1.96
		NM	74.1	55.6	4.3	3.86	67.1	31.1	10.8	1.05

Legend: P- Yield %; Q- Cr_2O_3 %; R- SiO_2 %; S- Cr:Fe ratio; M- Magneics; NM- Non-magnetics

Likewise, another similar study conducted by the same author Tripathy et al. (2015a) used RERMS by changing roller speed (150, 250, and 350 rpm) and feed rate (0.10 and 0.15 ton/h) to separate iron-bearing gangue from ferruginous chromite fines. The result shows (Table 2.5) that by removing iron-bearing minerals, the RERMS has improved the chromium to iron ratio of 2.6 from 1.6 with a yield of 13.9 % (at 250 rpm roll speed and 0.10 th^{-1} feed rate).

Table 2.5: Results of RERMS for various operating conditions.

Feed rate t/h	Roll speed rpm	Product	Weight %	Assay value %			Cr:Fe ratio
				Cr_2O_3	Fe	SiO_2	
0.1	150	Magnetics	98.1	43.9	18.1	3.4	1.7
		Non-magnetics	1.9	18.6	8.7	22.1	1.5
	250	Magnetics	86.1	43.3	19.0	3.3	1.5
		Non-magnetics	13.9	44	11.6	6.4	2.6
	350	Magnetics	59.6	43.8	20.5	2.7	1.4

		Non-magnetics	40.4	42.8	14.2	5.2	2.1
	150	Magnetics	99.1	43.6	18.1	3.6	1.6
		Non-magnetics	0.9	26.9	6.6	18.5	1.5
0.15	250	Magnetics	83.1	44.4	19.1	2.9	1.6
		Non-magnetics	16.9	38.8	12.5	8.0	2.1
	350	Magnetics	55.4	45.6	20.0	2.7	1.5
		Non-magnetics	44.6	40.7	15.4	5.0	1.8

Alp (2009) in their study investigated the magnetic separation technology using PRMS under fixed operating conditions (5°splitter angle, 50 g/m and 60 rpm). In their work, the outcomes of various particle size fractions were considered to yield the grade and recovery results for the size fraction of +0.075 mm (Table 2.6). The results revealed that B_2O_3 of 41.3 % concentrate was achieved with a recovery of 96.7 % from the feed assay of 30.7% B_2O_3. So, which satisfies the commercial acceptance grade of colemanite concentrates which should contain ≥40 weight % B_2O_3. Also, Fig. 2.20 indicates the results of cumulative grade and recovery of various oversize particle fractions.

Table 2.6: Magnetic separation results (combined) on the colemanite ore.

Product	Mass wt. %	Colemanite content wt. %	B_2O_3 content wt. %	B_2O_3 distribution %
Concentrate	71.6	81.26	41.29	96.76
Tails	28.4	6.95	3.53	3.24
Head	100	60.54	30.76	100
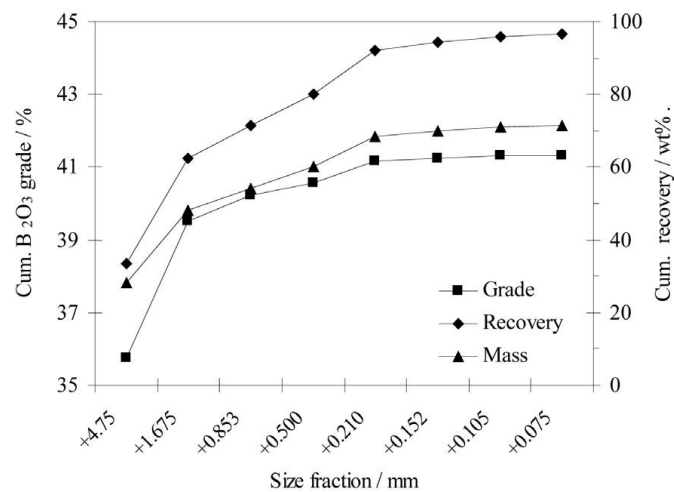
Fig. 2.20: Combined results of magnetic separation test (Alp 2009).

Ozdemir et al. (2011) studied the influence of magnetic separation on trona ore (the basis for Na_2CO_3) using RERMS. The study involves a two-stage magnetic separation process as shown in Fig. 2.21. The results indicated (Table 2.7) that, magnetic separation of single-stage greatly enhanced the grade of trona for all particle size fractions. Furthermore, second stage magnetic separation of first stage non-magnetic concentrate further enriched the trona grade. Also, from the study, it was concluded that the recovery of trona was reduced to 87.8 % for fines than that of coarser particle size fractions i.e., 94.8 % recovery as shown in Table 2.7.
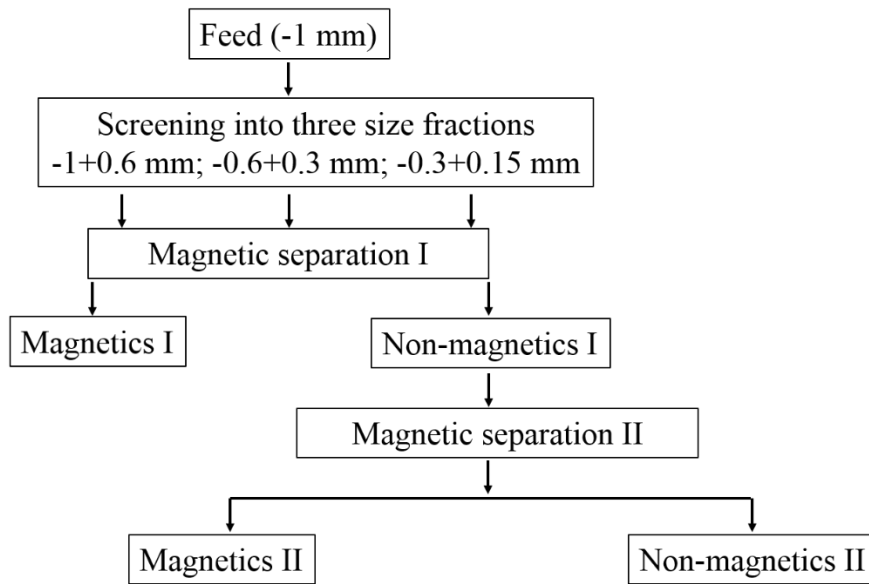
Fig. 2.21: Magnetic separation flowsheet of trona ore (Ozdemir et al. 2011).

Table 2.7: Magnetic separation results for unlike particle size fractions.

Products	-1+0.6 mm			-0.6+0.3 mm			-0.3+0.15 mm		
	F	M	NM	F	M	NM	F	M	NM
Stage I									
Weight %	100	16.3	83.7	100	15.5	84.5	100	15.8	84.2
Insoluble content %	19.6	79.4	7.9	19.9	74.5	9.9	15.9	55.6	8.6
Total grade %	80.4	20.6	92.1	80.1	25.5	90.1	84.1	44.4	91.4
Total recovery %	100	4.2	95.8	100	4.9	95.1	100	8.4	91.6
Stage II									
Weight %	83.7	1.6	82.1	84.5	2.4	82.1	84.2	4.6	79.6
Insoluble content %	7.9	43.1	7.2	9.9	45.7	8.9	8.6	29.4	7.3
Total grade %	92.1	56.9	92.8	19.1	54.3	91.1	91.4	70.6	92.7

Total recovery %	100	1.2	98.8	100	1.7	98.3	100	4.1	95.9
Overall									
Weight %	100	17.9	82.1	100	17.9	82.1	100	20.4	79.6
Insoluble content %	19.6	76.2	7.2	19.9	70.6	8.9	15.9	49.6	7.4
Total grade %	80.4	23.8	92.8	80.1	29.4	91.1	84	50.4	92.7
Total recovery %	100	5.2	94.8	100	6.6	93.4	100	12.2	87.8

Operating parameters: feed rate = 0.018-0.024 tph; splitter angle = 90-92° (coarsest size fraction) and 95-98° (intermediate and fine-size fractions) and roll speed = 30-40% of maximum voltage setting.
Legend: F- Feed; M- Magnetics; NM- Non-magnetics

Bhagat et al. (2006) investigated the influence of feed particle size and belt speed to separate the refractory grade bauxite by removing the paramagnetic minerals (goethite, hematite, and rutile) using PRMS (Fig. 2.22). The results indicated that, at a 6 rpm belt speed, improved non-magnetics grade along with the best yield was achieved as compared to 3 and 9 rpm belt speed. Hence, based on the optimum result of 6 rpm belt speed, the influence of different particle size fractions was studied (Table 2.8). The best results found that an optimum particle size of -690+350 μm and belt speed of 6 rpm could reduce the level of impurity needed for the development of the required material specification.

Feed
↓
Dry magnetic separation
↓
Magnetics   Non-magnetics
↓
Dry magnetic separation
↓
Magnetics   Non-magnetics
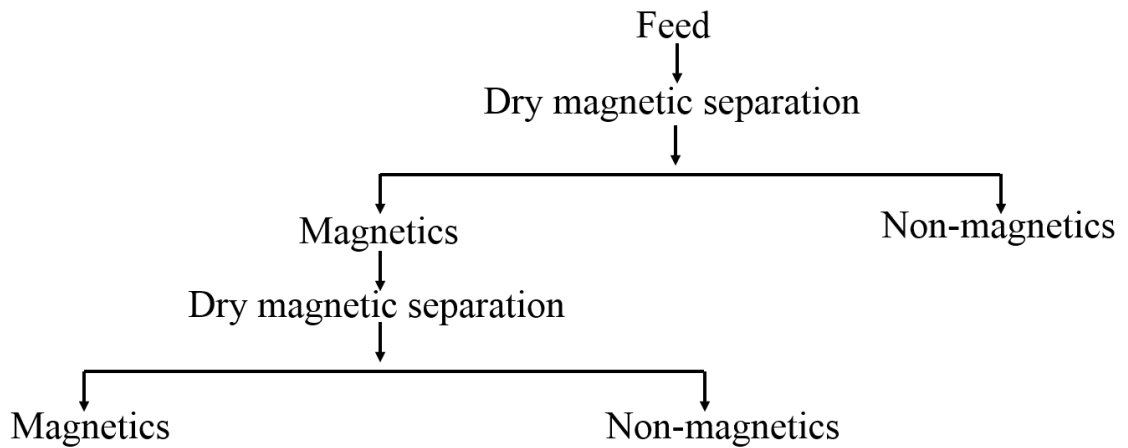
Fig. 2.22: Magnetic separation process flow chart (Bhagat et al. 2006).

Table 2.8: Effect of bauxite ore size fractions at optimum belt speed 6 rpm in PRMS.

Products	Weight %	Assay weight %		Distribution weight %	
		Fe_2O_3	TiO_2	Fe_2O_3	TiO_2
Test I: -2000+690 µm					
Non-magnetic I	78.2	2.15	6.03	54.7	73.7
Non-magnetic II	9.4	3.45	7.13	10.5	10.5
Magnetic	12.4	8.62	8.18	34.8	15.8
Head	100	3.08	6.40	100	100
Test II: -690+350 µm					
Non-magnetic I	50.5	1.52	5.16	23.3	35.7
Non-magnetic II	9.5	3.75	5.16	10.7	6.7
Magnetic	40.0	5.46	10.55	66.0	57.6
Head	100	3.31	7.31	100	100
Test III: -350+210 µm					
Non-magnetic I	20.5	1.62	6.04	9.0	14.5
Non-magnetic II	41.6	3.58	8.03	40.4	39.4
Magnetic	37.9	4.91	10.37	50.6	46.2
Head	100	3.68	8.51	100	100

Separation of Fe-bearing mineral impurities, when the nepheline syenite samples were treated magnetically using RERMS was investigated by Ibrahim et al. (2002). From their study, it was found that there was a reduction in Fe_2O_3 content from 6 to 0.24 % for the Abu-Khrug sample and 5.3 to 0.28 % for the El-Kahfa sample, when the samples were subjected to a belt speed of 4 m/min, a magnetic field of 1.45 T and feed rate of 12 kg/h. However, the obtained concentrates meet the global specifications for fiber as well as amber glass production and ceramic industries (Ibrahim et al. 2002).

A study (Stamboliadis and Kailis 2004) on calcite removal from the bauxite ore of the Greece region was explored using a PRMS. The results revealed that the size fractions up to 30 mm of bauxite mineral can be parted as a magnetic fraction using PRMS. However, the magnetic fraction of each particle size was produced by subjecting the non-magnetic fractions to multiple times magnetic separation process. Moreover, in each pass, the feed rate, as well as roller speed, was reduced. Likewise, a study was conducted by (Herskovitch and Lin 1996) to remove Fe_2O_3 impurity from perlite (volcanic glass) through optimized variables such as roll speed and feed rate by using PRMS. The obtained result indicates that the Fe_2O_3 content has reduced to < 0.7 % for particle size < 1 mm after three

stages of separation. The separated perlite is used for making the quality glass product. Similarly, Babu et al. (2009) carried out a study to produce ilmenite concentrate by separating mineral impurities from Teri sand of Tamil Nadu region through dry separation technique using PRMS. Here, the pre concentrated sample from the spiral concentrator was used as a feed for PRMS. A similar type of application was reported by Goolsby and Moore (1997), where the effect of belt type as well as belt thickness was considered along with the speed of roll in the removal of Fluid Catalytic Cracking (FCC) powder.

Similarly, Grieco et al. (2014) studied the magnetic separation of braunite mineral particles from metamorphic deposits, Turkey using PRMS. The results showed that about 13 % MnO enhancement was observed in a composite feed of -10+1 mm size faction. Also, they have revealed that the pre-sizing of braunite ore into various size fractions does not contribute to magnetic separation efficiency in comparison with composite feed. Moreover, here, the influence of operating parameters (splitter position, feed rate, and roller speed) was not varied to determine the particle size-based optimum separation.

2.2.4 Coal separation

A study on lignite coal sample via pyrolysis as a pretreatment process and followed by the separation using a PRMS was reported. From the study, it has been concluded that the effective separation was achieved at a roller speed, splitter angle and feed rate of 40 rpm, 100° and 50 g/min, respectively for coarser size fractions. Whereas, for other than coarser size fractions the splitter angle of 96° was considered. Table 2.9 summarized the obtained results under the above-mentioned operating conditions (Koca et al. 2000).

Similarly, the beneficiation of lean-grade semi-coked lignite was studied by Yildinm et al. (1996) using RERMS. The obtained results show that a significant reduction in the level of sulfur was achieved from 2.49% to 0.39% under the optimal set of operating parameters. The key parameters of the system are splitter position, particle size, feed rate, and roll speed were varied.

Table 2.9: Summarized results of PRMS.

Particle size mm	Products	Ash %	Total Sulphur %	Combined recovery %		Reduction in Sulphur %		LCV Kcal/kg
				P	Q	P	Q	
-1.7+1.5	A	32.85	1.01	84.19	47.79	53.19	80.63	5112
	B	75.73	2.21	15.81	8.97	---	---	1132
	C	47.51	1.42	100	56.76	---	---	3751
-1.0+0.5	A	32.77	0.96	87.44	47.81			5194
	B	81.17	2.23	12.56	6.87	---	---	905
	C	49.18	1.39	100	54.68	---	---	3740
-0.5+0.25	A	22.67	0.88	80.71	46.09			6106
	B	78.25	1.97	19.29	11.02	---	---	997
	C	48.13	1.38	100	57.11	---	---	3763

Legend: A- Clean coal; B-Tailing; C-Feed; P-According to experiment; Q-According to head sample; LCV- Low calorific value.

The study conducted by Çelik (2002) on carbonization process followed by magnetic separation of coal (lower-ranked) using RERMS was reported. The reported results conclude that the optimized conditions of both carbonization and magnetic separation process leads to reduction in sulfur content up to 0.41% from 2.09% and the ash content of 14.2% from 39.49%. Where the optimum condition of PRMS was Front splitter 80˚; feed rate 155 g/min; back splitter 100˚; size fraction -3+0.1 mm (Çelik 2002). Likewise, research conducted by Saeid et al. (1993) on the desulphurization of coal from the UK intended to remove pyrite by using a PRMS. The results concluded that from the coal fraction of -500 + 106 μm the removal of ash could be up to 40% of ash could be removed along with a maximum of 10% sulfur content (Saeid et al. 1993). Also, a separate study of macerals from lignite mines (South Dakota) was conducted by Order et al. (2003) using air jig and dry PRMS. The obtained result indicates that the products with distinct magnetic susceptibility depending on their content of maceral might be separated using PRMS. Also, the ash content could be dropped to 12.3% in the PRMS from coal having the ash content of 35.6% which was pre-concentrated in an air jig (Order et al. 2003).

2.2.5 Waste utilization and processing

The application of RERMS to improve the effectiveness of the FCC system through the efficient removal of deactivated (spent) catalysts from the process was attempted by Leaper

et al. (2002). The obtained results found that the effective separation is hopeful for the size fraction up to 90 µm, but the particle size fraction less than 90 µm was inefficient. Since, the supremacy of drag force over finer particle size fractions as compared to magnetic force, makes the separation of fines difficult (Leaper et al. 2002).

Similarly, the use of dry magnetic separation technique to beneficiate a charge chrome slag (-8 mm particle size) assayed 9.3% Cr_2O_3 using PRMS was reported (Shen and Forssberg 2003; Das et al. 1997). In their study, two stages of magnetic separation were used i.e., 0.1 and 0.08 T of magnetic field for initial and cleaning step, respectively. The results show that the produced concentrate has the best Cr_2O_3 content and yield i.e., 57.1 and 1.5 %, respectively. Likewise, the application of dry magnetic separation for the removal of metal from the incineration residue (bottom ash) was investigated by Schmelzer (1995). The obtained results show that the magnetic fraction comprising 20 to 30 % Fe was obtained from high ash material after the dry magnetic separation process.

Equally, the separation of Fe-bearing mineral impurities from the fly ash (lignite) produced from the power plant of Turkey was studied using RERMS (Özdemir and Çelik 2002). The study reveals that the magnetic product assayed 35.1 % Fe was separated by classifying the feed (11.03% Fe) into two size fractions (+106 and -106 µm) followed by the magnetic separation process. Further, the non-magnetics were subjected to subsequent cleaning to gain a carbon with low ash content.

2.3 Finite Element Method Magnetics (FEMM)

The goal of this section is to give a brief description of the earlier work done by various researchers using FEMM software.

Masoumi and Wang (2016) investigate a magnetic levitation characteristic-based RMS. In their study, the RMS was provided with levitating magnets which were stacked together by various magnet arrangements. The FEMM was used to investigate the generated magnetic field by different RMS magnet (NdFeB grade 42) configurations and the resulting field strength. As shown in Fig. 2.23 (a), (b), and (c) the quantification of the magnetic field along the line 'd' at a distance 'd_1', is crucial for predicting the power output through generated magnetic flux densities (Fig. 2.24 (a) and (b)). The result shows (Fig.

2.24 (a) and (b)) that, around 0.3 and 0.22 T was the normal flux density generated for the magnet with like poles and magnet with unlike poles facing each other, respectively. In addition, the variation in the magnetic field of around 0.1 T between the magnets and retains a higher value than the other arrangement (magnet with unlike poles facing each other), where the field value varies significantly among the magnets and reaches zero in the mid-portion (Fig. 2.24 (b)). In particular, the magnet stack with like poles of the magnet facing each other produced a higher field value than that of unlike poles of the magnet facing each other.
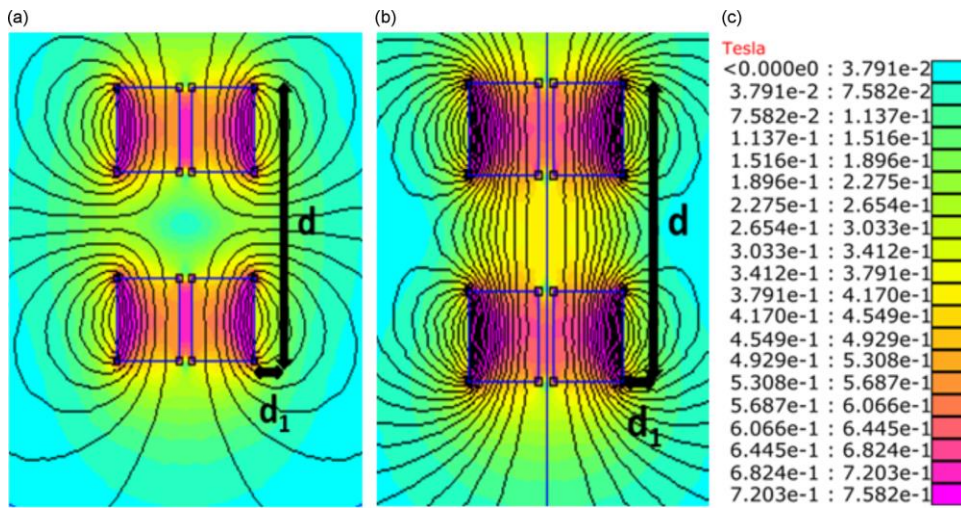
Fig 2.23: (a) Like poles of the magnet facing each other, (b) unlike poles of the magnet facing each other (d=82.55 mm. & d_1=5.08 mm), and (c) Magnetic field scale (Masoumi and Wang 2016).
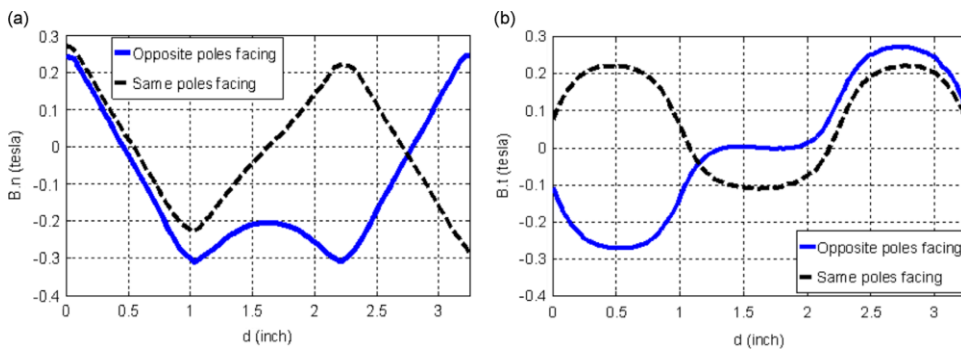
Fig. 2.24: (a) Normal, and (b) Tangential magnetic flux density (Masoumi and Wang 2016).

Furthermore, the influence of unlike materials for pole pieces, which results in the variation of normal magnetic flux density was also studied by Masoumi and Wang (2016). The result shows that (Fig. 2.25), in terms of enhancing magnetic field intensity, there was no discernible difference across metals with varying permeability. As a result, 1018 carbon steel was selected as a material for the pole piece, since it is cost-effective. In addition, the influence of the thickness of pole pieces on the distribution and strength of magnetic field lines was simulated and results were displayed in Fig. 2.26 (a), (b), (c), and (d). In each case (Fig. 2.27 (a), (b), and (c)), throughout line 'd', the normal magnetic flux density turns stronger as the thickness of the pole piece decreases. Moreover, as the pole piece becomes thinner, more force is necessary to combine the magnets (NdFeB grade 42).
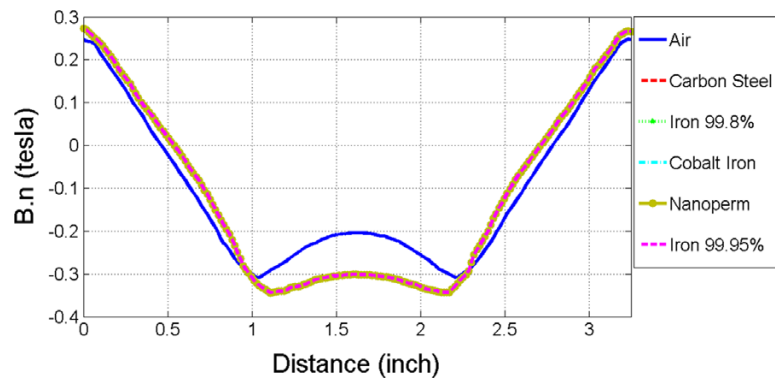
Fig. 2.25: Normal magnetic flux density for dissimilar material as pole piece (Masoumi and Wang 2016).
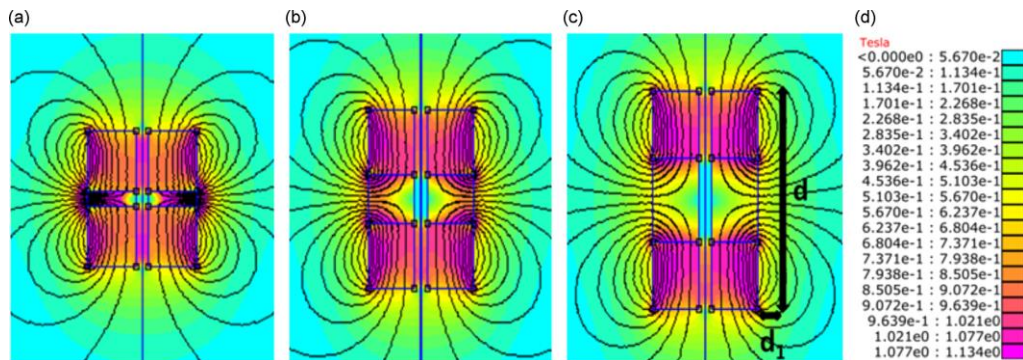
Fig. 2.26: Simulated magnetic field results for various distance of magnet: (a) d=57.15 mm & d_1=5.08 mm, (b) d=69.85 mm & d_1=5.08 mm, (c) d=82.55 mm & d_1=5.08 mm, and (d) Scale of magnetic field (Masoumi and Wang 2016).
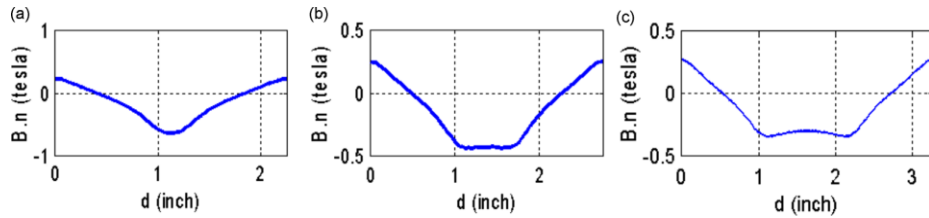
Fig. 2.27: Normal flux density throughout the line d: (a) d=57.15 mm & d_1=5.08 mm (b) d=69.85 mm & d_1=5.08 mm (c) d=82.55 mm & d_1=5.08 mm (Masoumi and Wang 2016).

Tušek et al. (2010) illustrated a magnetic refrigerator of the rotary type, in which the operating principle was based on rotary type movement of AMRs provided with a material that is magneto-caloric. The permanent magnets of NdFeB 40 grade were used to produce the required magnetic field. The analysis of produced magnetic field/flux in the magnetic structure was conducted using FEMM software. The results show that (Fig. 2.28), flux density in the air gap where magneto-caloric material was projected to magnetize of around 0.98 T. Also, the flux density of 0.05 T was found in the place where the material (magneto-caloric) was projected to demagnetize. This indicates that both the magnet as well as steel were at an appropriate distance from the projected area of demagnetization to offer suitable lower flux density values. Moreover, the findings (Fig. 2.28) gained from the FEMM software and measurement, shows the high level of agreement, and endorse the suitability of FEMM software for predicting the field value produced by the structures of the magnetic circuit.
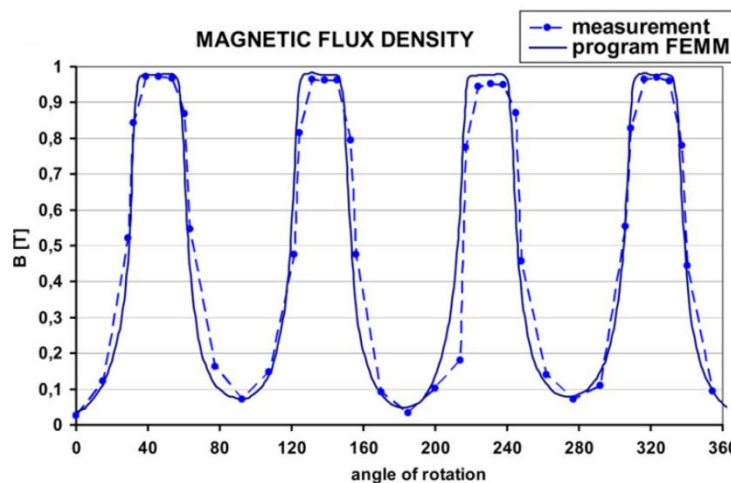
Fig. 2.28: Distribution of flux density in AMR (Tušek et al. 2010).

Similarly, Akbar and Awang (2014) were proposed a new flywheel energy storage device in which the permanent magnets were installed in specified mountings to create a flywheel. Here, the FEMM was used to examine the device performance metrics such as energy reinforcement and discharge elongation %, concerning magnet geometry. The results showed that the magnet geometry should be wide enough to offer long magnetic field interaction instead of strong interaction. Also, the boundary of the magnetized part was extended to offer longer time interaction, because the device rotated at high velocity.

2.4 Artificial Neural Network (ANN)

In this section, the application of ANN modelling for the prediction analyses of required output (grade and recovery) in the magnetic separation process was briefed from the available literature.

Hosseini and Samanipour (2015) attempted the prediction analysis of the final concentrate grade of the magnetic separation process through the FANN algorithm using the ANN method. Fig. 2.29 shows that the input layer provided with five neurons corresponds to particle size (d_{80}), iron (Fe), iron oxide (FeO), phosphor (P) and sulfur (S) percentages of a run of mine (ROM) used as network inputs. Whereas the output layer provided with four neurons corresponds to Fe, FeO, P, and S amount present in the final concentrate as network output. Fig. 2.30 (a), (b), (c) and (d) shows the plot containing predicted data versus actual/process data. The correlation coefficient (R^2) obtained from the testing tests for P, Fe, S, and FeO % was around 0.90, 0.96, 0.94, and 0.96 predictions, respectively. From the obtained results, it was found that a higher R^2 value for the final Fe concentrate grade endorse the suitability of the ANN model for the prediction analysis.
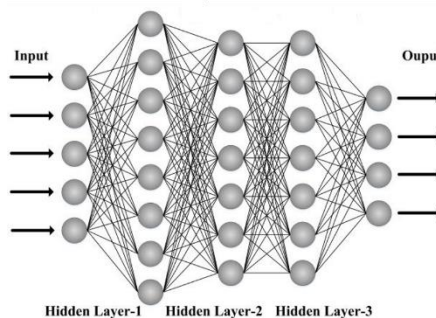
Fig. 2.29: Multilayer perceptron neural network model (Hosseini and Samanipour 2015).
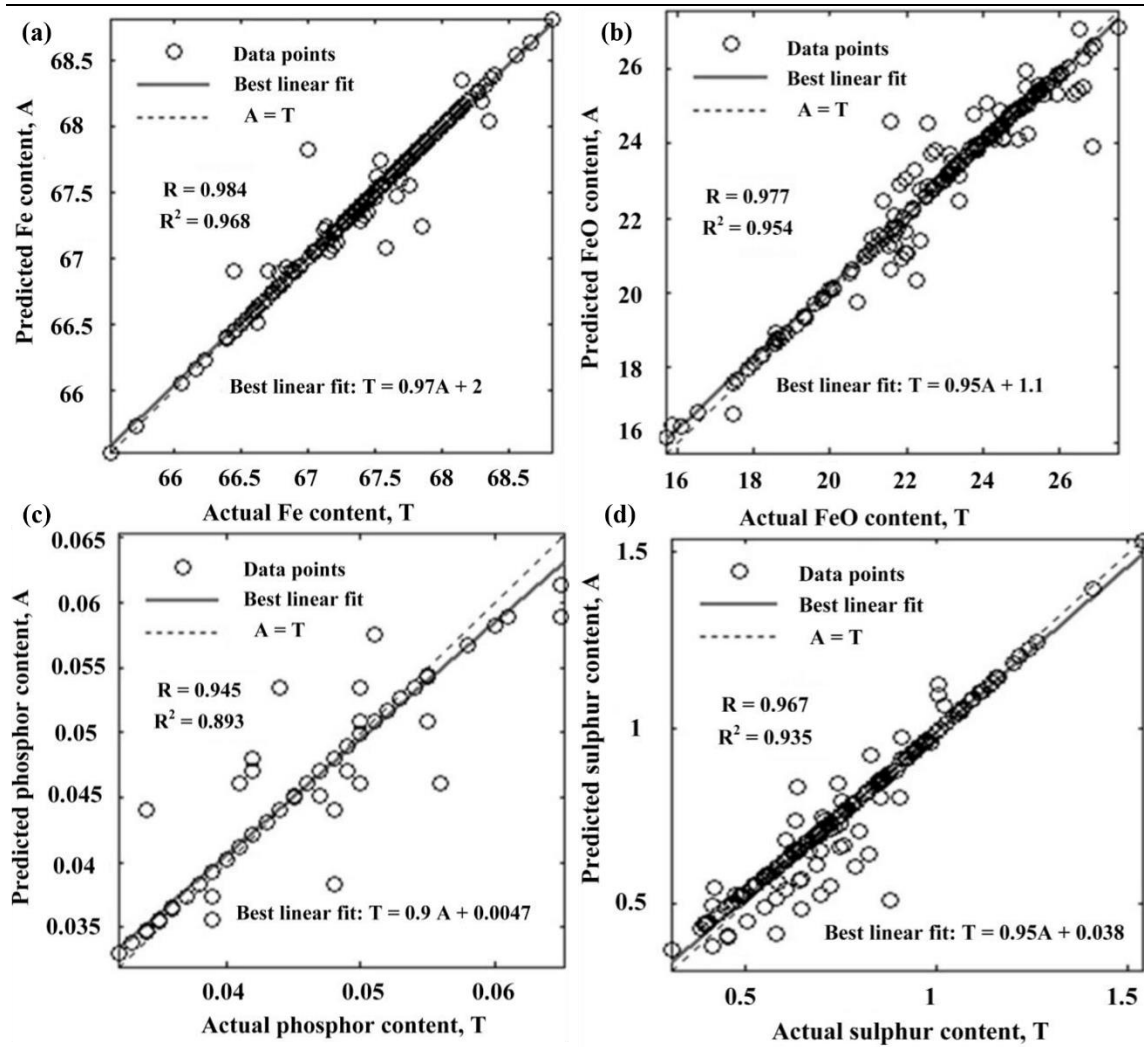
Fig. 2.30: Linear regression (a) predicted versus actual Fe content, (b) predicted versus actual FeO content, (c) predicted versus actual P content, and (d) predicted versus actual S content (Hosseini and Samanipour 2015).

Singh (2009) preferred the ANN method to model the roll magnetic separation process through a connectionist approach. The database was developed using input parameters (splitter position, magnetic field/flux intensity, roll speed, and particle size) and output parameters (Fe recovery and wt. recovery) to establish a relationship between them (Fig. 2.31). The obtained regression coefficient (R^2) of ANN among the predicted and measured data was 0.89 for Fe recovery and 0.94 for wt. recovery as represented in Fig.

2.32 (a) and (b). Hence, the developed ANN model was found satisfactory in predicting the efficiency of the separation process with altered ore properties.
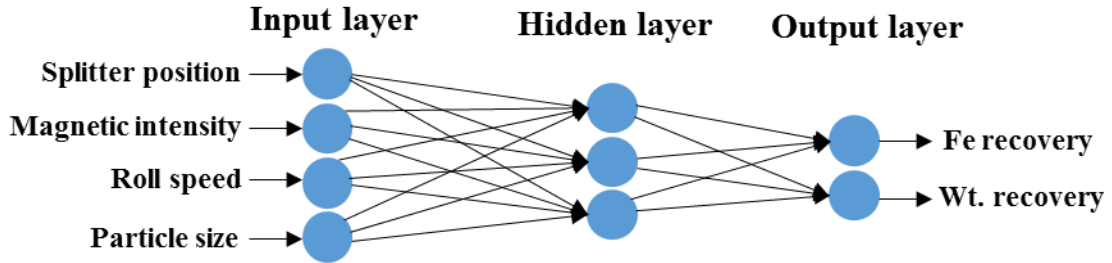
Fig. 2.31: Neural network (Singh 2009)
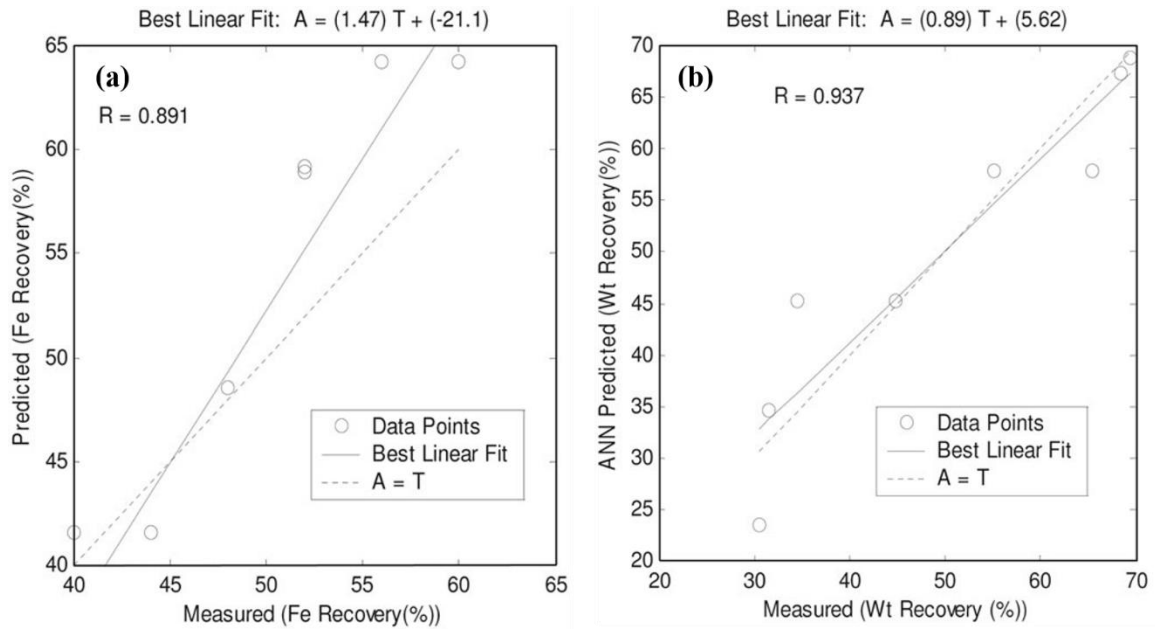
Fig. 2.32: Predicted and measured data for (a) Fe recovery %, and (b) Wt. recovery % (Singh 2009).

Paledi et al. (2021) investigated the competence of ANN in predicting the selectivity index (SI) as well as separation efficiency (SE) of the magnetic separation process. In their study, S %, Fe %, 80 % passing size, and FeO % in a mill as well as cobber feed and plant capacity were taken as network inputs. The outcomes of ANN modelling using backpropagation algorithm (BPA) were displayed in Fig. 2.33 (a), (b), (c) and (d)

reveals that the determination coefficient (R^2) of training, as well as testing stage, found satisfactory. In addition, the neural network performance was further improved through the use of a genetic algorithm (GA) to optimize biases as well as weights of the network. The results (Fig. 2.34 (a), (b), (c), and (d)) of the developed GA-ANN model was found better and effective in output prediction as compared to the BPA-ANN model.
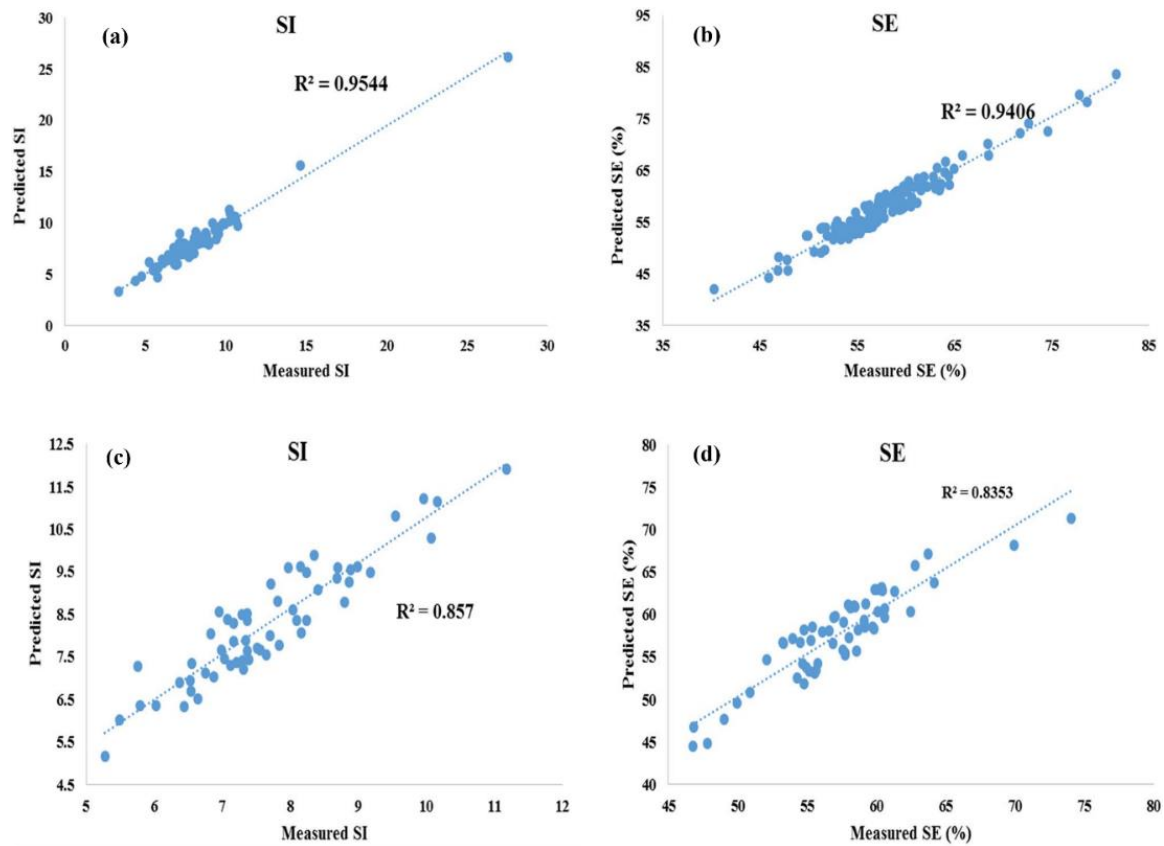
Fig. 2.33: Predicted versus measured data for BPA-ANN (a) &(b) training stage, and (c) & (d) testing stage (Paledi et al. 2021).
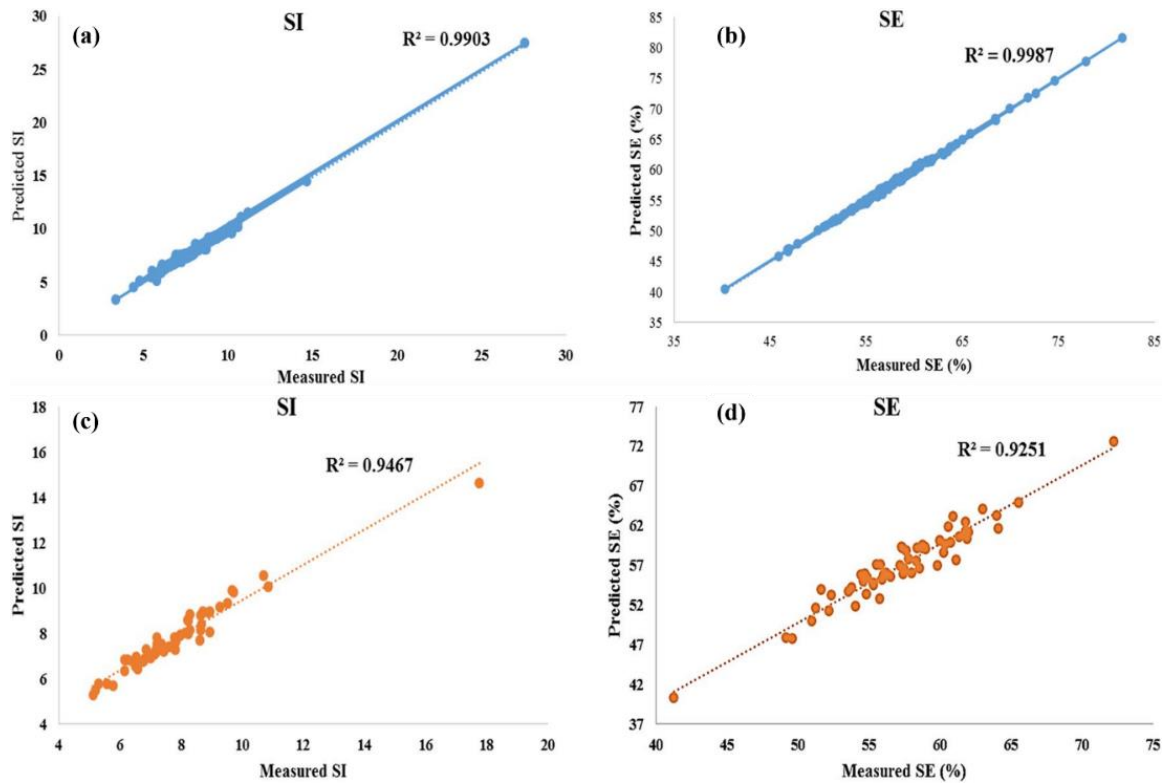
Fig. 2.34: Predicted versus measured data for GA-ANN (a) & (b) training stage, and (c) & (d) testing stage (Paledi et al. 2021).

Tripathy et al. (2020) presented an ANN model with a feed-forward algorithm for the prediction of IRMS performance while beneficiating the iron ore of lower grade. Key variables of IRMS operation such as particle size, applied current, feed rate, splitter position, and speed of rotor were treated as network inputs. However, the separation performance of IRMS was predicted based on Fe, SiO_2, Fe recovery, and SiO_2 rejection percentage of the magnetic product were treated as network outputs. The obtained results (Fig. 2.35 (a), (b), (c), and (d)) of ANN modelling shows the correlation coefficient, $R^2 > 0.95$ during training as well as testing phase, which found the established model was efficient in output prediction.
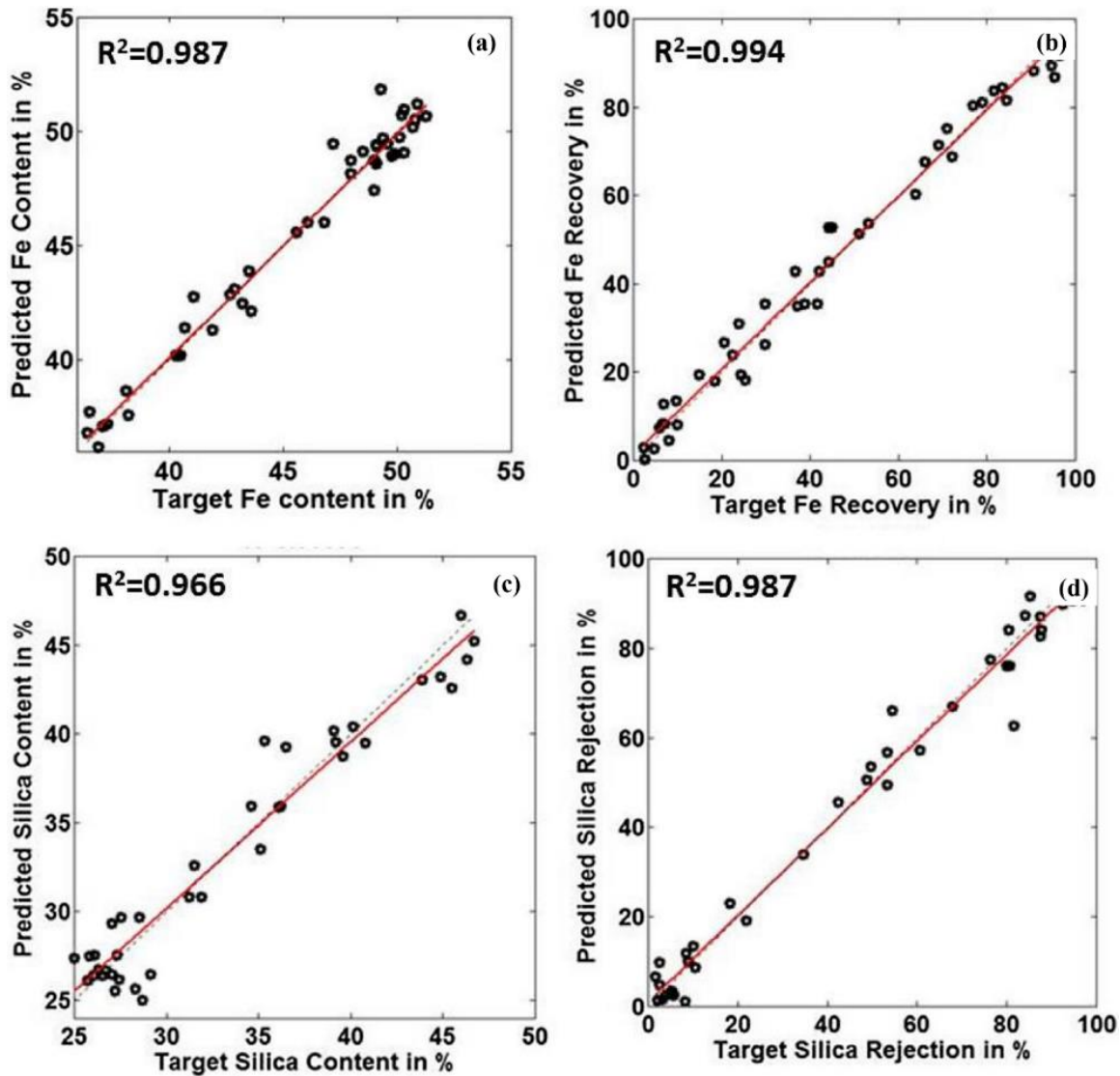
Fig. 2.35: Prediction analysis of (a) Fe %, (b) Fe recovery %, (c) SiO_2 %, and (d) SiO_2 rejection % (Tripathy et al. 2020).

2.5 Optimization method

This section was briefed about the optimization approach applied to iron ore beneficiation through Taguchi and ANOVA method.

2.5.1 Taguchi method

A study conducted by Altiner (2020) on the roasting of goethite ore (low grade, assayed 17.60% Fe, Hatay Province, Turkey) using horse residue followed by magnetic separation

(WHIMS). The roasting parameters were considered at three levels (Table 2.10) and were considered based on Taguchi L_9 experimental design (Table 2.10) with corresponding response variables (Fe grade and recovery). Finally, the concentrate of Fe ore assaying a grade of 62.12 % Fe and a recovery of 56.93 % was achieved by using WHIMS (the applied magnetic field was 0.5 T) under the roasting conditions of the experiment no. 5 as shown in Table 2.10. Also, the magnetic product with a grade of 50.57 % Fe and a recovery of 88.04 % was achieved under the roasting conditions of experiment no. 3 (Table 2.10). Moreover, the experimented and predicted results of the magnetic product's Fe grade and recovery were in good correlation with a regression coefficient of 0.99 and 0.94, respectively, as shown in Fig. 2.36. Therefore, it was concluded that the Taguchi method was appropriate for assessing the impact of roasting variables on the magnetic susceptibility of Fe ores, which in turn affects the magnetic separation results in terms of Fe grade and recovery %.

Table 2.10: Roasting parameters and Taguchi based L_9 experimental design.

Parameters			Symbol	Level 1	Level 2	Level 3
Roasting temperature (˚C)			A	400	500	600
Reducing agent/sample ratio			B	0.04	0.08	0.12
Roasting time (min)			C	10	20	30
Experiment No.	A	B	C	Fe %	Recovery %	
1	400	0.04	10	54.35	47.77	
2	400	0.08	20	49.90	70.69	
3	400	0.12	30	50.57	88.04	
4	500	0.04	20	52.92	49.06	
5	500	0.08	30	62.12	56.93	
6	500	0.12	10	61.63	62.49	
7	600	0.04	30	50.64	50.80	
8	600	0.08	10	58.97	69.94	
9	600	0.12	20	49.56	73.18	
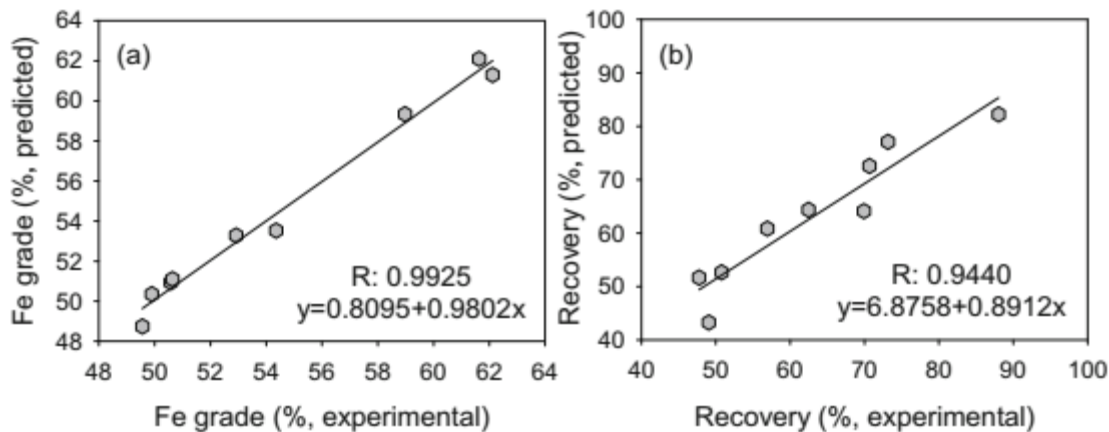
Fig. 2.36: Experimented versus predicted results of the magnetic product (a) Fe grade %, and (b) Fe recovery % (Altiner 2020).

Rath et al. (2016) illustrated the reduction roasting followed by magnetic separation (LIMS and WHIMS) of Fe ore assayed 57% Fe (Karnataka mines, India). The effects of various parameters were investigated and then optimized using the Taguchi approach. The L_{16} orthogonal array was used to achieve the reduction roasting experiments (Four-level) in the muffle furnace. The considered parameters in muffle furnace roasting were reductant concentration, roasting time, and roasting temperature with corresponding Fe grade and recovery as the response variables. Whereas, L_9 orthogonal arrays were employed to achieve the reduction roasting experiments (Three-level) in the microwave roasting. Here, ore particle size, the concentration of charcoal, and roasting time were considered as parameters with corresponding Fe grade and recovery as the response variables. Fig. 2.37 and 2.38 show the marginal means of S/N ratios which were plotted upon each parameter at various levels. The results show that, under optimized conditions, the furnace roasting method produced a Fe concentrate having 64% Fe and 90% wt. recovery at reductant concentration of 4%, roasting time of 90 min, and roasting temperature of 1050° C (Fig. 2.37). Whereas, microwave roasting method produced a Fe concentrate having 63% Fe content and 85% wt. recovery at a particle size of -2 mm, charcoal concentration of 6% and roasting time of 4 min as shown in Fig. 2.38. Hence, in comparison with muffle furnace roasting, it was concluded that microwave roasting has a remarkable possibility to yield a

similar good roasted product in a considerably shorter period and facilitates good magnetic separation.
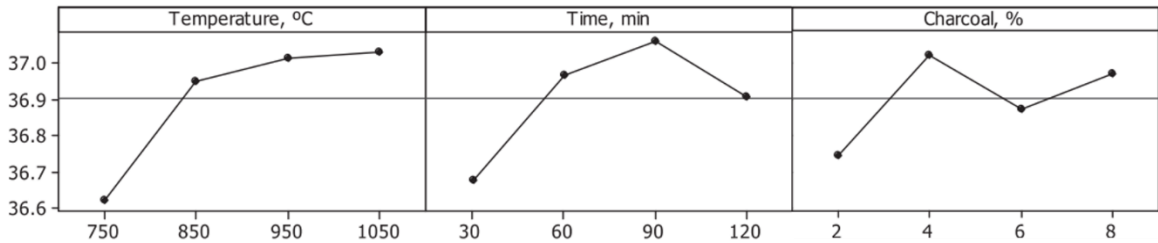
Fig. 2.37: Main effects plot of muffle furnace roasting parameters (Rath et al. 2016).
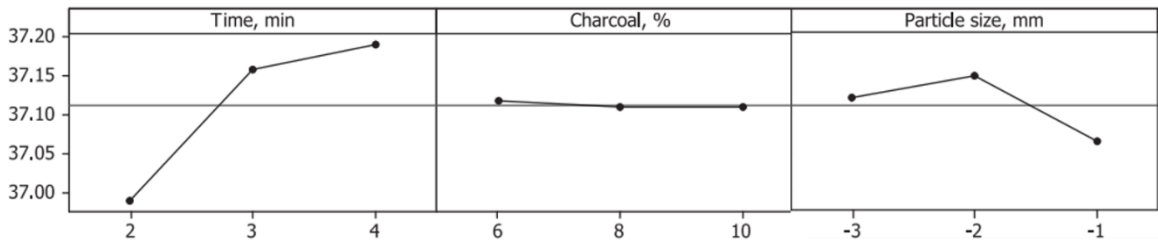
Fig. 2.38: Main effects plot of microwave roasting parameters (Rath et al. 2016).

Another study attempted by (Rath et al. 2016a) on the beneficiation of Fe ore slimes (Barsua mines, India) assayed 56.2 % Fe through reduction roasting (cow dung as reductant) followed by magnetic separation (LIMS) technique. The roasting experiments were carried out using Taguchi L_9 experimental design with three levels and factors as shown in Table 2.11. Whereas the response variables were magnetic product's Fe grade and recovery which was produced from LIMS. Also, the interaction effects of considered variables on Fe grade and recovery were analyzed via contour plot as depicted in Fig. 2.39 (a), (b), (c), and (d). Fig. 2.39 (a) depicted that the maximum Fe grade was attained at ~900 °C temperature and time of 45–70 minutes. Whereas, ~700 °C temperature and time of 55–70 minutes show the best recovery (Fig. 2.39 (b)). Similarly, Fig. 2.39 (c) shows the conjunction of high reductant-to-feed ratio and temperature of ~0.75 and ~900 °C, respectively prefer the maximum Fe grade. While, regardless of the reductant-to-feed ratio, the maximum recovery was achieved at 700–750 °C temperature (Fig. 2.39 (d)). Even though the contour plots have given the sign of better regions of the process to gain the best product, the impact of each parameter was analyzed through S/N ratios of each run.

Therefore, according to the design, the optimal overall experimental condition was 0.25 (reductant-to-feed ratio), 700 °C (temperature), and 90 minutes (time) as shown in Fig. 2.40. However, based on the obtained results, it is possible to gain a concentrate of 64.3% Fe with a recovery of 66.2% from the iron ore assayed 56.2 % Fe.

Table 2.11: Experimental parameters and their levels.

Factors	Symbol	Level 1	Level 2	Level 3
Reductant to feed ratio	A	0.25	0.5	0.75
Temperature (° C)	B	700	800	900
Time (min)	C	30	60	90
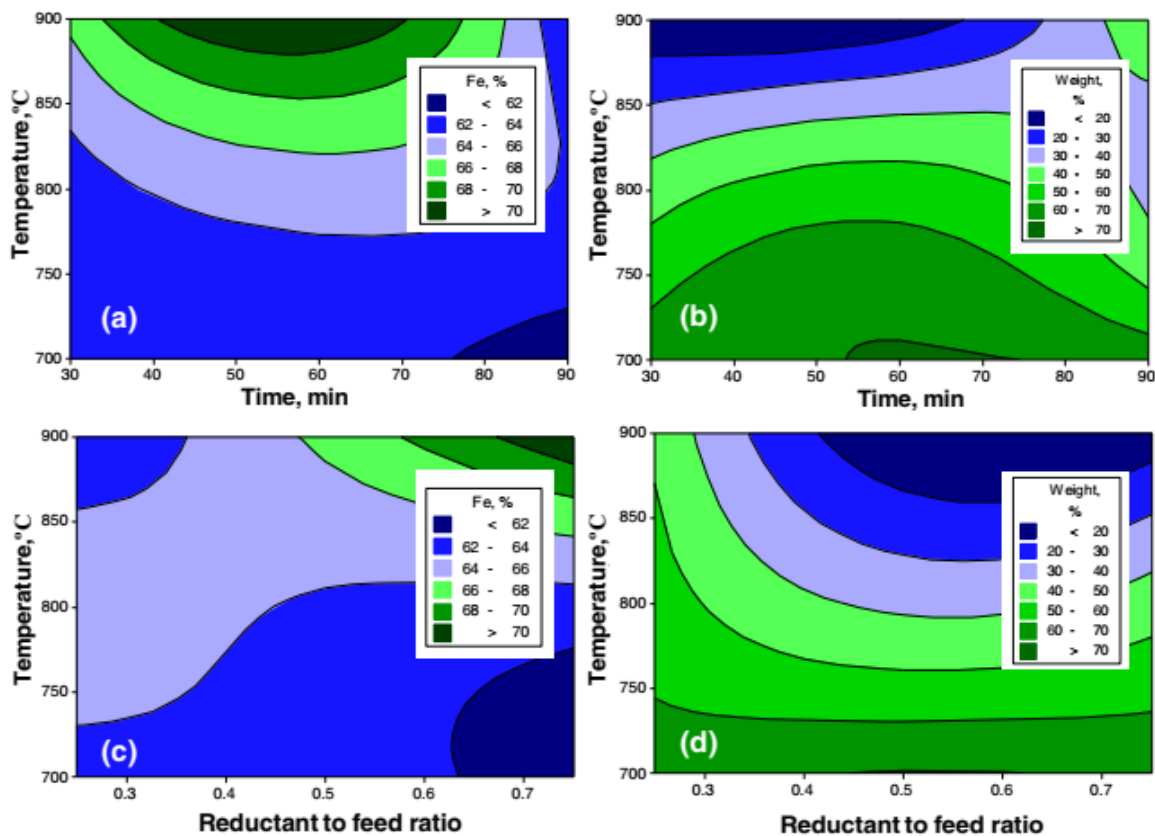
Fig. 2.39: Contour plots illustrate the variation of (a) Fe grade, (b) Fe recovery concerning temperature and time, (c) Fe grade, and (d) Fe recovery concerning temperature and reductant-to-feed ratio (Rath et al. 2016a).
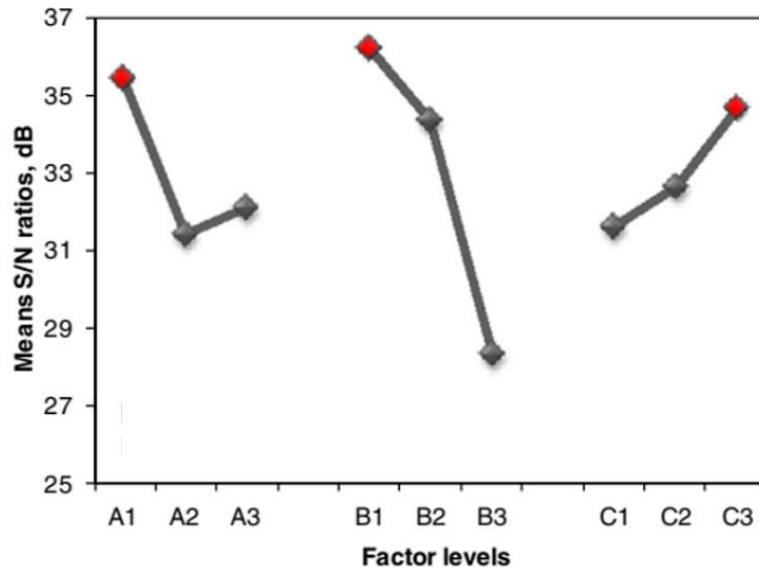
Fig. 2.40: Main effects plot of roasting parameters (Rath et al. 2016a).

Likewise, the beneficiation of low grade iron ore from different regions through reduction roasting followed by magnetic separation was reported in many studies (Rath et al. 2018, 2018a, Ray et al. 2018). However, in all these studies roasting experiments were optimized through the Taguchi approach for different variables and levels by using different reductants. The reductants such as biomass briquette (Rath et al. 2018), blast furnace flue dust (Rath et al. 2018a), and Coal (Ray et al. 2018).

2.5.2 ANOVA method

Altiner (2019) studied the performance of magnetic separator after conducting microwave roasting using DOE statistical modeling. The effect of variables such as microwave power (A), exposure time (B), and magnetic field strength (C) on Fe recovery was examined using ANOVA analysis. In ANOVA analysis, the F-Value (Table 2.12) was utilized to obtain significant and non-significant variables affecting the data set. Results showed that the F-value (highest to lowest) for the Fe recovery were: exposure time > magnetic field strength > microwave power, respectively. The obtained regression coefficient (R^2) value for the study was 0.8807, which provides a better possible fit of the prediction model with the experimental data sets.

Table 2.12: ANOVA analysis for Fe recovery.

Variance source	Sum of squares (SS)	Mean squares (MS)	F-value
Main effects			
A	0.003	0.003	0.02
B	2.875	2.875	13.71
C	1.884	1.884	8.99
Square effects			
A^2	1.288	1.288	6.15
B^2	0.235	0.235	1.12
C^2	0.212	0.212	1.01
2-way interactions			
AB	0.462	0.462	2.20
AC	0.176	0.176	0.84
BC	0.552	0.552	2.63

Similarly, Angadi et al. (2012) studied the influence of particle size (X_1), applied magnetic field (X_2), and wash water rate (X_3) in the particle separation process using WHIMS. The significance of variables based on F- value was carried out using the ANOVA method for both product yield and grade (Table 2.13). The order of significance of the main variables on the product yield and grade were as follows $X_1 > X_2 > X_3$. Whereas the interaction between $X_1 X_3$ and $X_2 X_3$ was insignificant for the same. The corresponding R^2 value for both product yield and recovery was 0.95 and 0.97, respectively. The obtained R^2 value (closer to 1) indicates the close relationship between the prediction model and experimental data sets, as shown in Fig. 2.41.

Table 2.13: ANOVA analysis for yield and grade.

Source	Yield		grade	
	F- value	P- value	F- value	P- value
X_1	1017.66	19	3794.47	19
X_2	267.83	19	2322.47	19
X_3	38.11	19	20.88	19
$X_1 X_2$	11.963	6.39	311.23	6.39
$X_1 X_3$	1.159	6.39	2.35	6.39
$X_2 X_3$	0.588	6.39	1.58	6.39
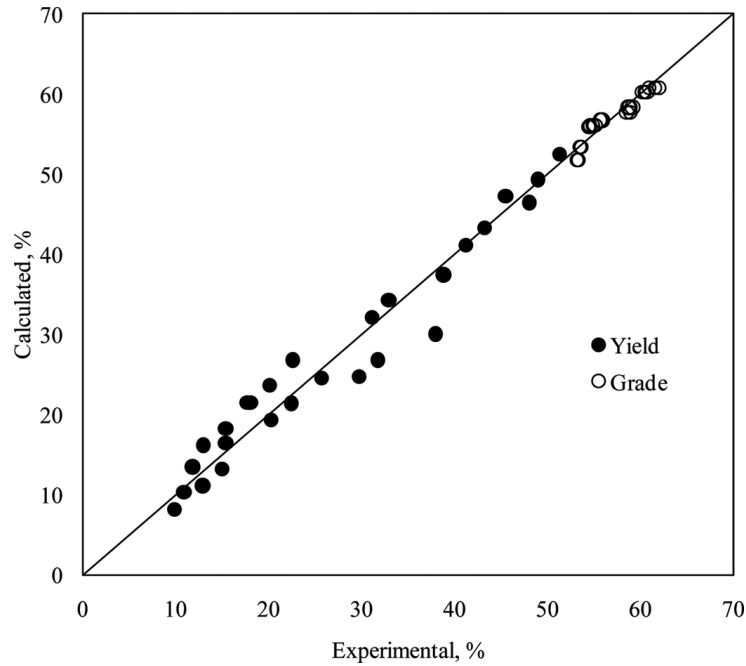
Fig. 2.41: Comparison of experimental and predicted values (Angadi et al. 2012).

A study illustrated by Rayapudi and Dhawan (2019) on the beneficiation of microwave treated followed by low-intensity magnetic separation (WHIMS) of banded magnetite quartzite iron ore (Fe 41%). The statistical design with three factors, namely, microwave power (A), residence time (B), and particle size (C) has been pursued. Whereas the temperature attained, iron grade, recovery, and yield were recorded as responses. The significance of factors based on F-value was studied through ANOVA, as shown in Table 2.14. In addition, the regression coefficient (R^2) was 90% which shows the close agreement between the prediction model and experimental data sets.

Table 2.14: ANOVA for temperature, grade, yield, and recovery.

Source	Temperature	Grade	Yield	Recovery
	F- value	F- value	F- value	F- value
A	2.89	3.30	4.87	0.44
B	0.86	0.81	5.97	0.33
C	3.72	1.52	2.75	0.91
AB	1.25	1.63	8.14	0.11
AC	2.41	1.64	0.01	2.72
BC	0.55	0.04	0.036	0.082
A^2	0.940	0.40	0.039	0.085

B^2	0.001	0.24	8.69	8.93
C^2	3.34	2.85	19.0	0.44
R^2	0.73	0.72	0.90	0.74
Significance	C >A >B	A >C >B	B >A >C	C >A >B

Likewise, Hamzeh Amiri (2019) investigated the effects of factors on Fe grade and Fe recovery. In their study, the design of experiments (DOE) was utilized to model the experimental results of WHIMS experiments. The factors such as magnetic field intensity, rotor speed, and feed water flowrate were considered as the input variables. The ANOVA of the developed models (Table 2.15) showed the fitted models were significant at a 95% confidence level. Also, the regression coefficient (R^2) predicted results for Fe recovery and Fe grade were 0.91 and 0.69 %, respectively, as shown in Fig. 2.42. The high R^2 value indicates the best fit of the model to Fe recovery (0.91) response than compared to Fe grade (0.69).

Table 2.15: ANOVA of selected factorial models.

Source	F- value	P- value
Fe grade	71.94	< 0.0001
Fe recovery	49.90	< 0.0001
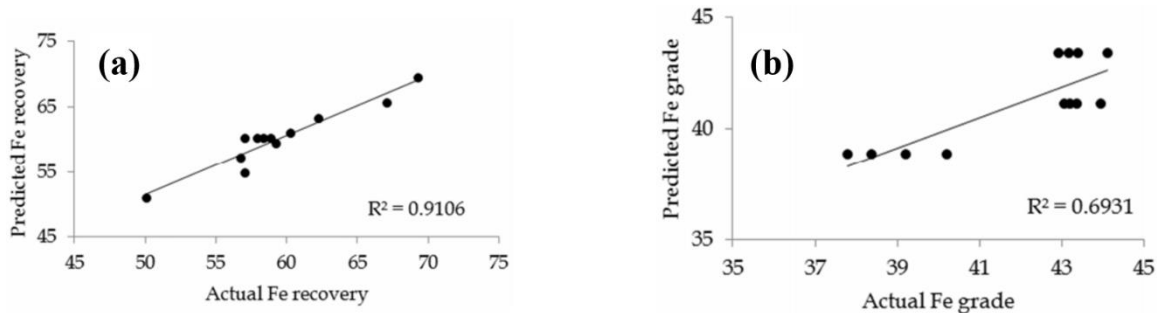
Fig. 2.42: Predicted versus actual values (a) Fe recovery %, and (b) Fe grade % (Hamzeh Amiri 2019).

Correspondingly, Bhoja et al. (2021) investigated the two types of ferruginous manganese ore samples through a dry magnetic separation process. The effect of three variables, namely, roller speed (A), feed rate (B), and splitter position (C) on Mn grade %, Mn: Fe ratio, and Mn recovery %, were studied through the DOE. However, the variables' significance was studied through ANOVA, as shown in Table 2.16. In the case of samples

1 and 2, roll speed was found to be the most significant variable which affected the grade, recovery, and Mn: Fe ratio, the interactional effect between roll speed and splitter position was more pronounced for binary interactions than the other interaction (between feed rate and splitter position).

Table 2.16: Significance of parameters affecting individual response.

Sample	Response	Grade	Recovery	Mn:Fe ratio
	Primary effect	A >B	A	A >B
Sample 1	Binary interactive effect	---	AC >BC	---
	Ternary interactive effect	---	ABC	---
Sample 2	Primary effect	A	A	A

2.6 Research gap from the literature survey

Although several studies were conducted on the PRMS, no work was carried out on the FEMM analysis of the magnetic roller (the active part of PRMS) and design of PRMS. Also, the magnetic roller configurations (magnet-to-steel thickness ratios) were directly chosen without any scientific validation. In addition, the design calculations in terms of power requirement for newly designed lab-scale PRMS were not done. Furthermore, the influence of PRMS operating parameters on the beneficiation of paramagnetic (hematite) ore without any roasting technique was not optimized statistically (using Taguchi and ANOVA method) for optimum operation of PRMS.

2.7 Objectives of the research work

- The characterization studies on as-received iron ore sample followed by the FEMM analysis of magnetic roller for different magnet-to-steel disk thickness ratios.
- Validation of obtained FEMM data through prediction analysis using ANN modelling technique.
- Fabrication of optimized magnetic roller and development of new lab-scale PRMS.
- Design calculations of newly developed/fabricated lab-scale PRMS and evaluation of separation performance.
- Optimization of operating parameters for the processing of low grade iron ore using DOE.

CHAPTER 3

METHODOLOGY

This chapter summarizes the detailed description of characterization studies, parameters considered in the FEMM analysis of magnetic roller, prediction analysis of FEMM data using ANN, experimental procedure for magnetic separation, and optimization of selected operating parameters of newly developed lab-scale PRMS through DOE (Taguchi and ANOVA methods)

3.1 Characterization studies

The effectiveness of the present work lies in the characterization of iron ore samples. Since the characterization of the ore is essential for process selection and pilot/lab-scale tests (Srivastava et al. 2001). Here, the iron ore (hematite) sample was received from Chiria and Kiriburu mines, India. The representative samples for characterization studies such as size distribution analysis, chemical composition analysis, XRD study, magnetic susceptibility study, and OM study was selected through coning and quartering technique.

3.1.1 Sampling

A sampling of any kind of ore is carried out by using a quadrant divider (Fig. 3.1(b)). Sampling is a technique of extracting a representative sample from a vast quantity of a given sample using a variety of methods. As illustrated in Fig. 3.1, the sampling process was carried out using coning and quartering method. Coning and quartering is a sample reduction technique in which the sample is reduced to half of its prior value (quantity) with each iteration. This procedure works well with any amount of material. Making a pile of material (conical form shape) (Fig. 3.1 (a)), settled at its natural angle of repose, is one of the steps involved in this process. The cone has to be radial symmetry. It is then flattened into a round disc by using a spatula and quartered using a Quadrant Divider (Fig. 3.1 (c)). The remaining material is rejected, once a quarter of opposite quadrants have been taken (Fig. 3.1 (d)). This procedure is repeated until the appropriate sample quantity has been reached.
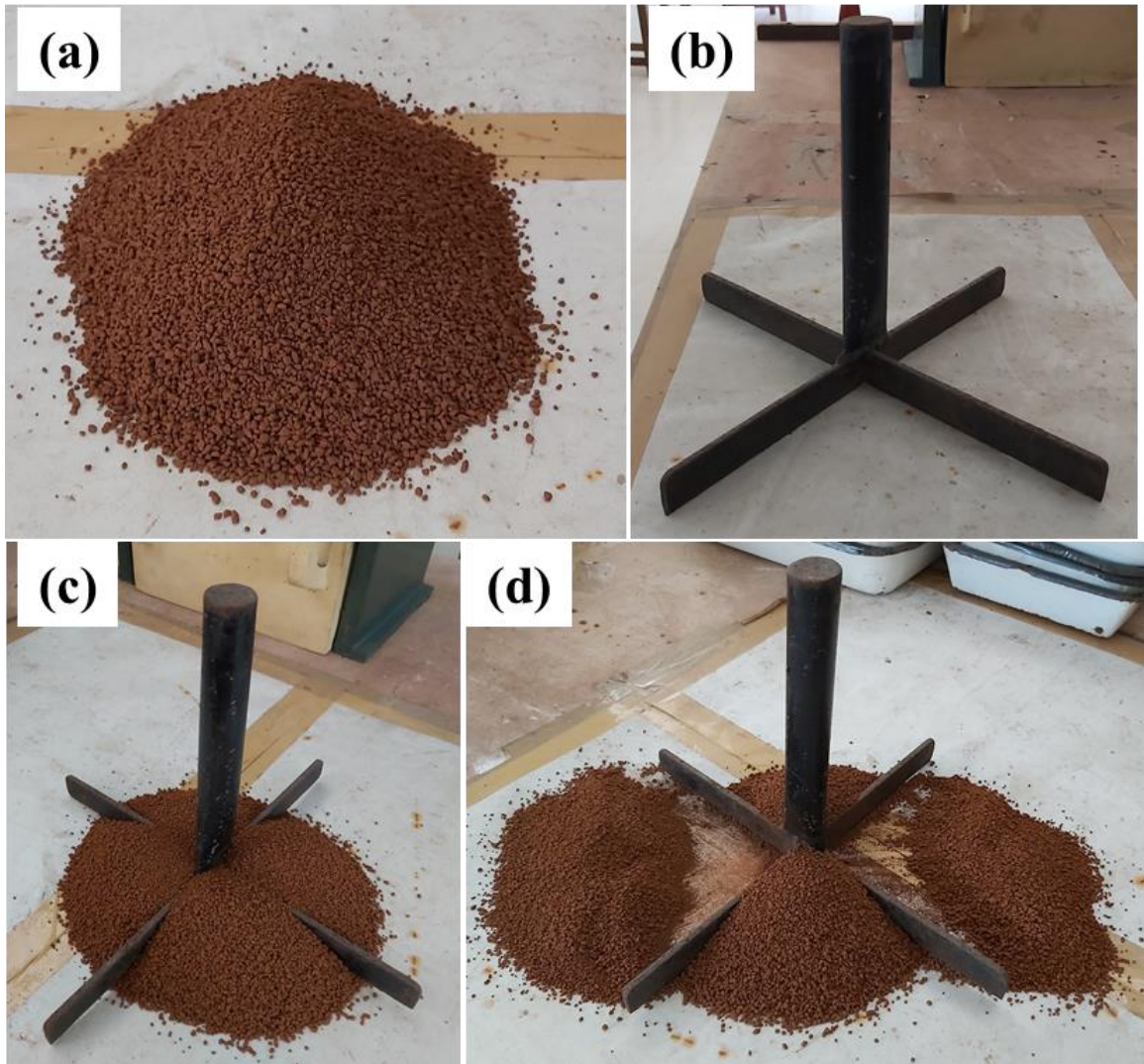
Fig. 3.1: (a) Making a pile of material (b) Quadrant divider (c) Quartered using the quadrant divider, and (d) Quarter of opposite quadrants will be taken.

3.1.2 Particle size distribution analysis

The size distribution of the as-received ore (Chiria and Kiriburu mines) samples was analyzed using Ro-Tap sieve shaker with standard test sieves to determine the percentage of various particle size fractions distributed within the samples. The sieve shaker used in the present study was shown in Fig. 3.2.

Fig. 3.2: (a) Ro-Tap sieve shaker, and (b) Ro-Tap sieve shaker with standard test sieves.

3.1.3 Wet chemical analysis

The chemical composition analysis was carried out on all the size fractions (including as-received and processed ore samples) using wet chemical analysis to determine the percentage of Fe, SiO_2, and Al_2O_3 present in the samples. The detailed procedure/methodology involved in the wet chemical analysis for the determination of Fe, $SiO_{2,}$ and Al_2O_3 was shown in Fig. 3.3, 3.4, and 3.5, respectively.
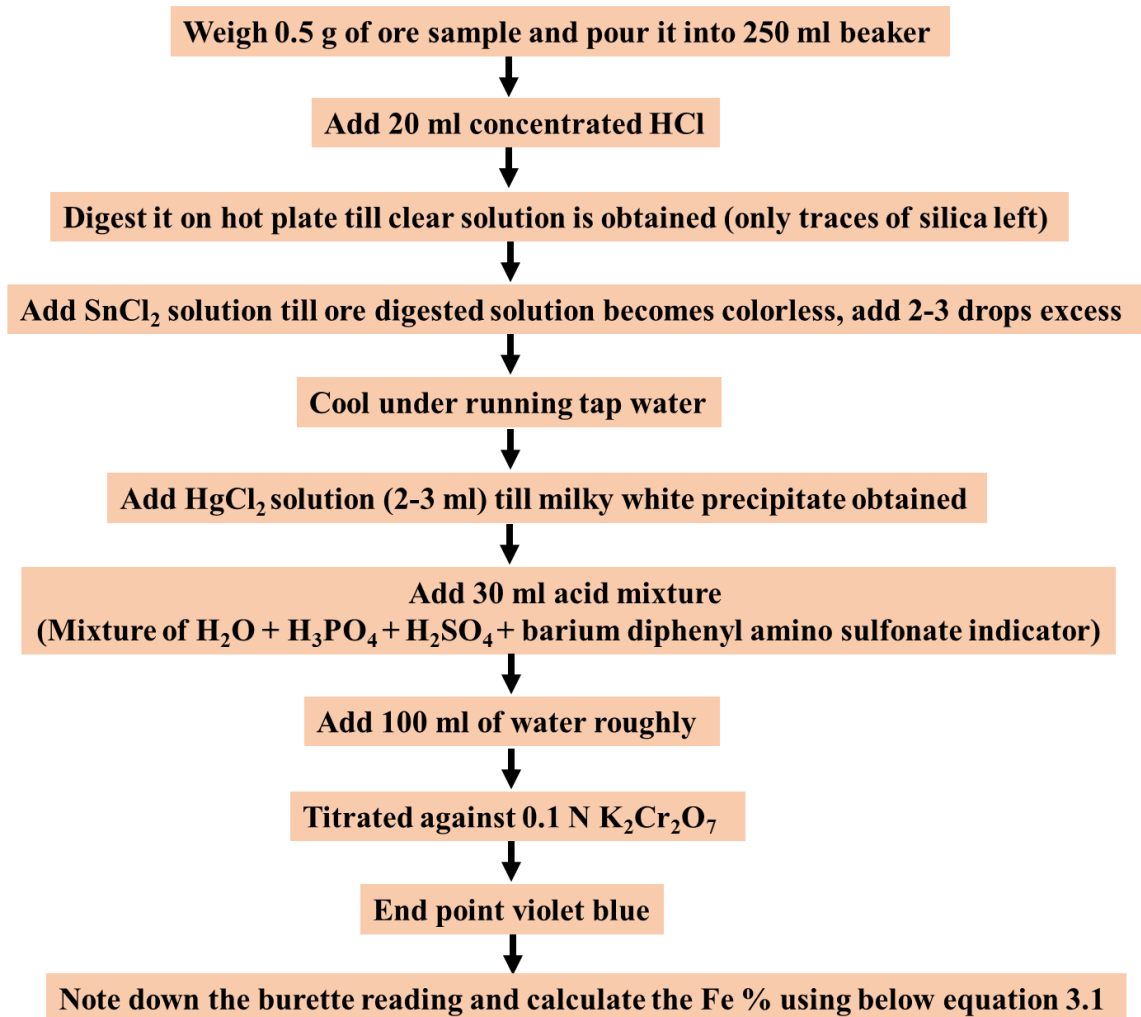
Fig. 3.3: Wet chemical analysis procedure for the determination of Fe %.

$$\text{Fe \%} = \frac{X}{\text{Sample weight}} \times \frac{N}{1000} \times 55.85 \times 100. \qquad (3.1)$$

Where,

'X' ml = Burette reading

N= Normality of $K_2Cr_2O_7$

55.85 = Equivalent weight of Fe

1000 = for 1 liter

Weigh 1 g of ore sample and pour it into 250 ml beaker.

↓

Add 30-40 ml concentrated HCl and digest it on hot plate.

↓

Add 2-3 drops of concentrated HNO_3 which results in appearance of brown fumes.

↓

After brown fumes disappears, add 7-10 ml $HClO_4$, allowed to bake till crystal forms.

↓

Dilute the formed crystals with 1:1 HCl and heat.

↓

After heating, filter the solution with whatman filter paper (40 no.).

↓

Properly wash the beaker with distilled water and transfer the washings to filter paper.

↓

Properly wash the filter paper with 1:1 HCl and hot water, alternatively. Collect the filtrate in 250 ml standard volumetric flask. In the meantime, take the empty weight of platinum crucible (W_1).

↓

After complete filtration, transfer the filter paper into the platinum crucible and ignite the filter paper by keeping platinum crucible into the muffle furnace at 906 °C for 25 minutes.

↓

After 25 minutes in muffle furnace take the crucible out, allow it to cool and weigh the crucible with burnt filter paper (W_2).

↓

Wet the burnt filter paper with 2-3 drops of water + 2 drops of conc. H_2SO_4 + up to ¾th crucible of HF.

↓

Keep the platinum crucible on the hot plate till all the things get evaporated.

↓

After evaporation, again keep the crucible in muffle furnace at 906 °C about 25 minutes.

↓

After 25 minutes, take the crucible out, allow it to cool and weigh the crucible (W_3).

↓

Calculate SiO_2 % using below equation 3.2.

Fig. 3.4: Wet chemical analysis procedure for the determination of SiO_2 %.

SiO_2 % = (W_2-W_3) × 100. (3.2)

Up-to 7th step same procedure will be followed as that of SiO2 determination. Whereas, the collected filtrate in the 8th step was make up to 250 ml in standard volumetric flask.

↓

Then, pipette out 25 ml of filtrate from 250 ml standard volumetric flask and transfer it in to 250 ml beaker.

↓

Add 15 ml of 10 % NaOH solution.

↓

Add 4-5 g of unhydrous Na2CO3.

↓

Boil the solution and filter the solution into 500 ml conical flask by using whatman 2A no. filter paper.

↓

Add 2 drops of methyl red indicator to get yellowish color.

↓

Add 1:1 HCl into conical flask till yellowish color turns into pink.

↓

Add 5 ml of 0.01 M EDTA.

↓

Add 1 spoon of ammonium acetate till solution converts into original yellowish color and boil the solution, then cool completely.

↓

Add 2 drops of xylon orange indicator (yellow orange solution should obtain).

↓

Titrate against 0.01 M standard zinc solution.

↓

End point wine red (dark red).

↓

Note down the burette reading and calculate the Al2O3 % using below equation 3.3.

Fig. 3.5: Wet chemical analysis procedure for the determination of Al_2O_3 %.

Al_2O_3 % = 'X' ml × 0.51.   (3.3)

Where, 'X' ml = 5 – Burette reading

3.1.4 Density measurement

Density measurement was carried out on each particle size fraction through a standard pycnometer test (Fig. 3.6) according to the following equation (3.4)

$$\text{Density of particle } (\rho_P) = \frac{\text{Mass of particle } (m_P)}{\text{Volume of particle } (V_P)} \text{ (g/cm}^3). \qquad (3.4)$$

As shown in Fig. 3.6,

Q_1 = Empty bottle (g)

Q_2 = Bottle + 1/3rd Sample (g)

Q_3 = Bottle + 1/3rd sample + Rest of the bottle volume is filled with water (g)

Q_4 = Bottle + Entire bottle volume is completely filled with water (g)

Where, $m_p = Q_2 - Q_1$ (g). $\qquad$ (3.5)

However, the calculation for volume of particle (V_P) is as follows:

Mass of water (m_w) = $Q_3 - Q_2$ (g). $\qquad$ (3.6)

$$\text{Volume of water } (V_w) = \frac{\text{Mass of water } (m_w)}{\text{Density of water } (\rho_w)} \text{ (cm}^3). \qquad (3.7)$$

V_P = Empty bottle volume - V_w (cm^3). $\qquad$ (3.8)

But, Empty bottle volume = Volume of water completely filled in the bottle (V_o)

$$V_o = \frac{\text{Mass of water } (Q_4 - Q_1)}{\rho_w} \text{ (cm}^3). \qquad (3.9)$$

Substitute equation (3.9) in (3.8) to get V_P.

Then, Substitute for V_P and m_P in equation (3.4) to get ρ_P.
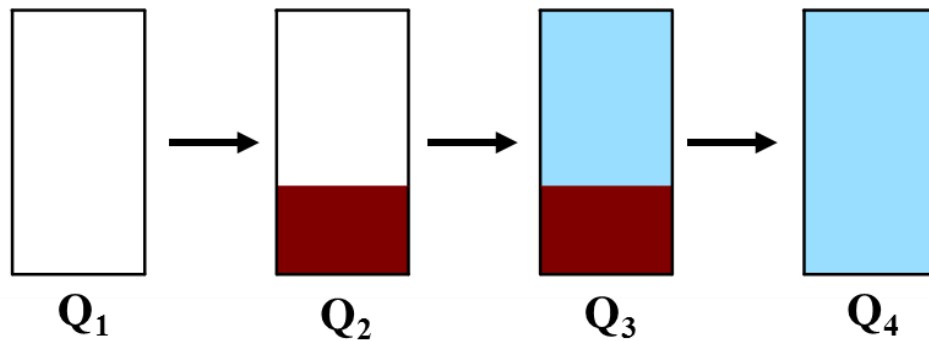
Fig. 3.6: Steps involved in density measurement.

3.1.5 XRD study

The mineral phases present in the ore samples were analyzed through an XRD study by using PANalytical multi-purpose high-resolution XRD (Model: Empyrean) with a scanning range and scanning speed of 10-90 degrees and 0.06 degree/sec, respectively as shown in Fig. 3.7.

Fig. 3.7: XRD machine.

3.1.6 Magnetic susceptibility study

The magnetic susceptibility of the ore samples at room temperature was measured using a SQUID magnetometer (Make: Quantum Designs, Model: MPMS 3-111) as shown in Fig. 3.8 at IISc, Bangalore, where the applied magnetic field value was up to 5 T.
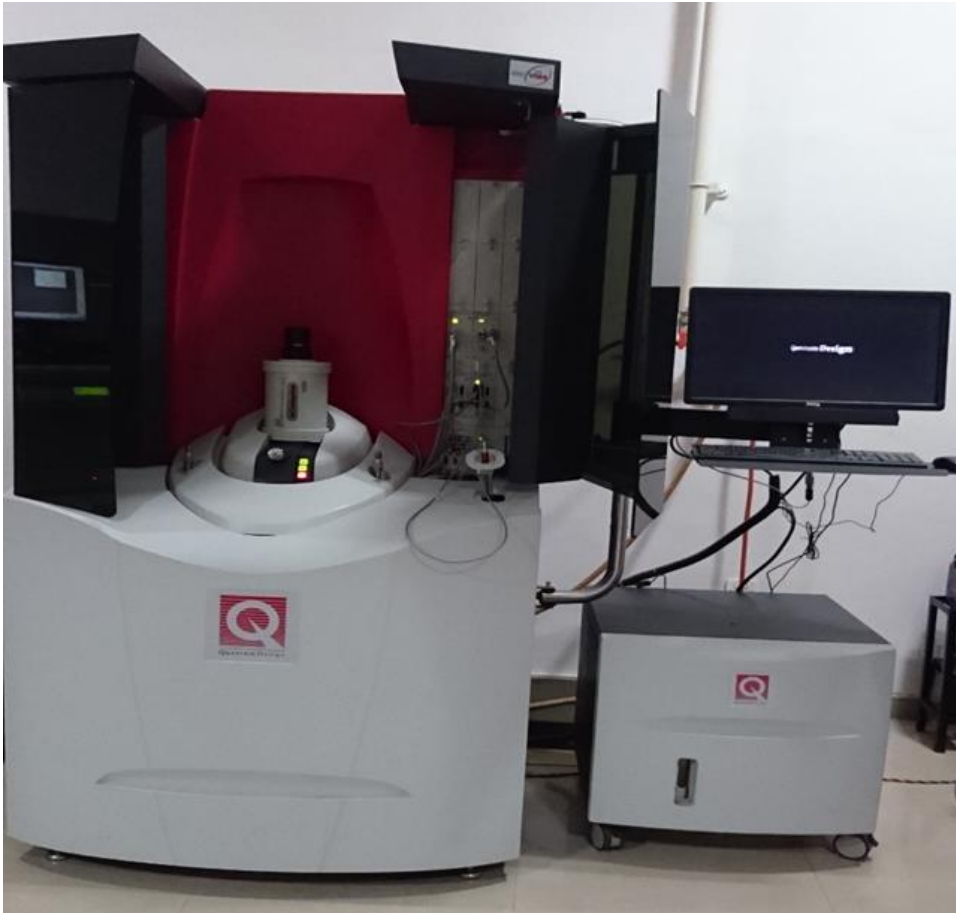
Fig. 3.8: SQUID magnetometer.

3.1.7 Optical microscopy study

The mode of association and distribution of mineral phases existent in the ore samples was identified in the microscopy study using an optical microscope (Make: Carl Zeiss, Model: Axio Vert.A1) under reflected mode at 20x magnification as shown in Fig. 3.9. Moreover, for the microscopy study, the polished specimens were prepared using epoxy resin mount for respective size fractions. The details of sample preparation for the OM study were explained in the subsequent section 3.1.7.1

Fig. 3.9: Optical microscope interfaced with a computer.

3.1.7.1 Sample/Specimen preparation for optical microscopy study

The steps involved in the preparation of a sample for the OM study was shown in Fig. 3.10. For preparing the sample, 5 g of iron ore was added to 4 g of resin and 2 g of hardener. Then, the mixture is thoroughly mixed and poured into a rubber mould (Fig. 3.10 (a)). Later the mould was kept in the air-tight oven for 8 hours at a temperature of 40-60 ˚C. After that, the dried mould (Fig. 3.10 (b)) was taken out followed by polishing of the dried sample (Fig. 3.10 (c)) on grinding/polishing wheel equipment (Fig. 3.10 (d)). The grinding wheel has the flexibility of changing the abrasive sandpapers during polishing operations (Fig. 3.10 (e)) to get the required surface finish for viewing the mode of distribution of various mineral phases present in the sample. However, the appearance of the hematite mineral in the ore is luster metallic grey (dull to bright). Whereas, the gangue (earthy appearance - dull/non-reflective) is the material that surrounds or is closely mixed with a hematite mineral.
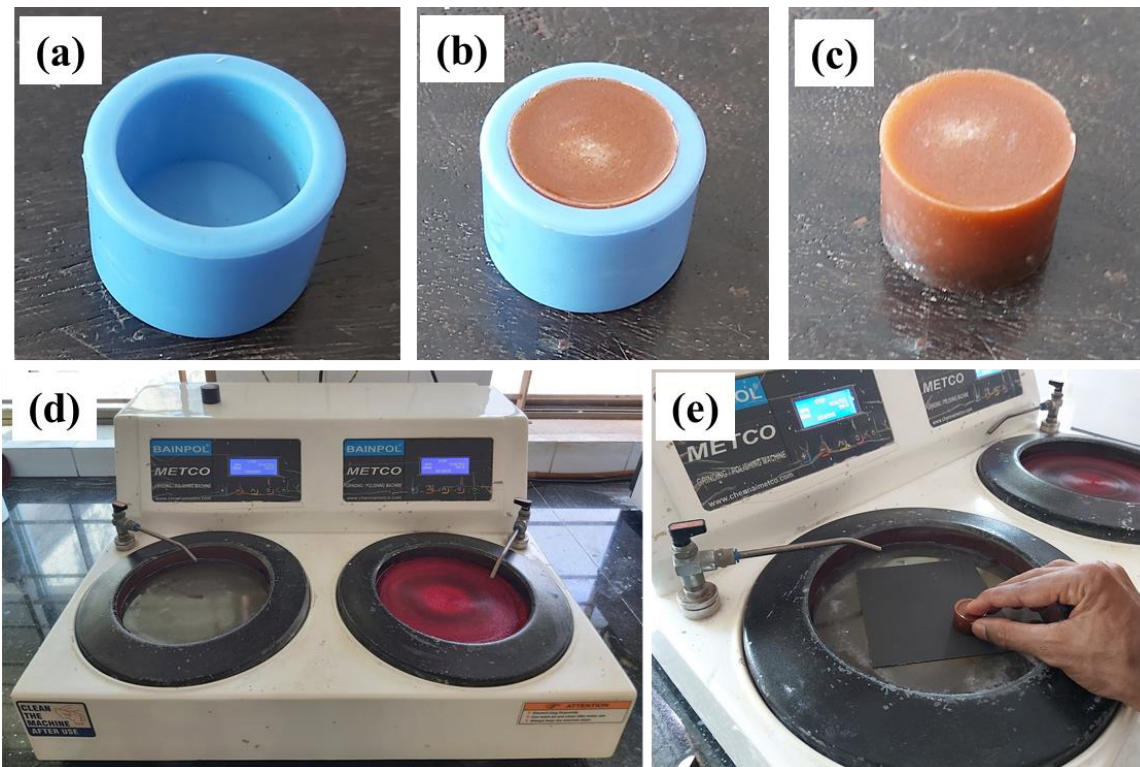
Fig. 3.10: (a) Rubber mould (b) Dried sample in the rubber mould (c) Dried sample (d) Grinding/polishing wheel equipment, and (e) Polishing operation on sandpaper.

3.2 Optimization of magnetic roller based on FEMM analysis

The selection of a suitable magnet-to-steel disk thickness ratio for the design of an optimized magnetic roller is a critical parameter. Therefore, the characterization study of ore sample followed by FEMM analysis of different magnet-to-steel disk thickness ratios was conducted via FEMM-2D software (David 2014). Since, before the fabrication of magnetic roller, the effects of unlike magnet-to-steel disk thickness ratio on the generation of flux lines and magnetic field around the magnetic roller have to be analyzed. The FEMM analysis results help to obtain the optimum magnet (NdFeB grade 52) to steel (SAE1010) disk thickness ratio which is responsible for the optimized magnetism configurations of the magnetic roller.

In FEMM-2D software, a three-dimensional magnetic roller was simplified into two-dimensional axis-symmetric problems to know the distribution of the magnetic field

over the magnetic roller for different magnet-to-steel disk thickness ratios. The boundary conditions can be set on any line and a user can also control the parameters of the mesh (Al-Sharif et al. 2010). Besides, the FEMM uses the discretization (finite element) method to resolve Maxwell's equations numerically over a generated mesh. It provides a graphical user interface to describe the problem by dividing the plane into regions and then describing the properties of each region (Al-Sharif et al. 2010).

3.2.1 Parameters considered in the magnetic roller optimization corresponding to FEMM analysis

The schematic diagram of a magnetic roller having magnet and steel disk stack along with a wrapped belt around the roller and particles of different sizes on the belt surface were shown in Fig. 3.11. The magnetic roller comprises steel disks (SAE 1010) sandwiched between permanent magnet disks (NdFeB grade 52) with the same poles facing each other and having axial magnetization. Further, the FEMM analyses were performed on three different magnetic rollers having magnet-to-steel disk thickness ratios 5 mm: 5 mm, 5 mm: 2.5 mm, and 5 mm: 1.25 mm. Whereas the outer and inner diameter of magnet and steel disks were kept as same 90 mm and 6 mm, respectively. Also, the 2D model analysis of the magnetic roller was carried out under asymptotic boundary conditions to closely approximate the unbounded solution, since the magnetic roller was considered in free space and surrounded by air as a fluid medium. Furthermore, a triangular meshing (Appendix-I) and the density plot mode were used to get color contours in the solution region (Parmar et al. 2018; David 2014). Moreover, the nonlinear B-H relationship of NdFeB grade 52 magnet and SAE 1010 steel (David 2014) which were used in the FEMM analysis was shown in Fig. 3.12. This provides a critical piece of information regarding the response of a material to an external magnetic field. The difference in the B-H curve represents the ability of a material to retain its magnetization even when the applied magnetic field is shut off.
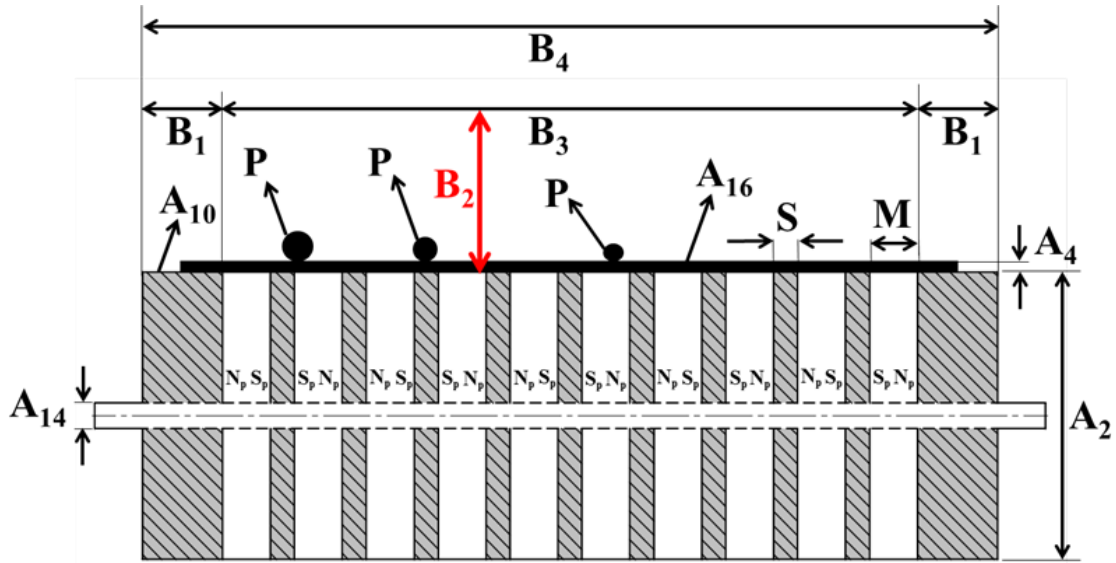
Fig. 3.11: The schematic representation of magnetic roller provided with magnet and steel disk arrangement. The thick black line represents the belt wrapped around the magnetic roller, and 'P' represents the particle on the belt surface with different diameters/sizes.
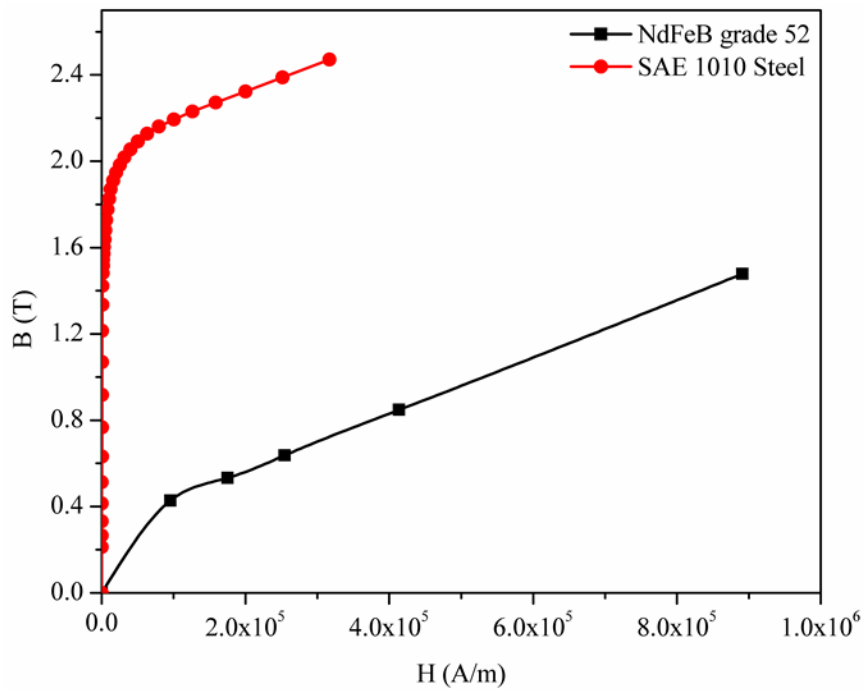
Fig. 3.12: Nonlinear B-H curve of NdFeB grade 52 magnet and SAE 1010 steel.

3.3 Prediction analysis of FEMM data through ANN modelling technique

In the present study, the obtained FEMM data for magnetic flux density of three unlike magnetic rollers having M: S ratio of 5 mm: 5 mm, 5 mm: 2.5 mm, and 5 mm: 1.25 mm consists of 10,000 data sets (Appendix-II). The validation of obtained FEMM data was done via prediction analysis using ANN in MATLAB 19. Since the ANN provides a better statistical model for large data sets having a complex relationship between input and output parameters (Panda and Tripathy 2014; Jorjani et al. 2009). The ANN model utilizes 70%, 15%, and 15% analytical data for training, validation, and testing of the model, respectively. For each ANN model, Regression-value (R-value) was obtained for training, validation, testing, and overall. However, the R-value represents the correlation between FEMM and predicted data (Shanmugam et al. 2020). So, to obtain a higher R-value, the feed-forward backpropagation network technique was used, which reduces the error rate by fine-tuning of predicted value thereby increasing the accuracy of the ANN model. Thus, the ANN modelling was used to do the prediction analysis by considering the feed-forward backpropagation network. Moreover, the design of the ANN model consists of different hidden layers which were determined by the trial and error method. Fig. 3.13 shows the optimum ANN model developed with input, hidden layer (provided with forty-five neurons), and an output layer for predicting the nonlinear relationship between input parameters (B_3) and output parameters (distributed magnetic field/flux density on the magnetic roller surface (i.e., $B_2=0$) along the line B_3 as shown in Fig. 3.11). Furthermore the additional information about the developed ANN model was briefed in Table AP-I of Appendix-III. Additionally, the ANN prediction model was validated through a normal probability plot and histogram, which was developed for the residuals obtained from the ANN prediction model.
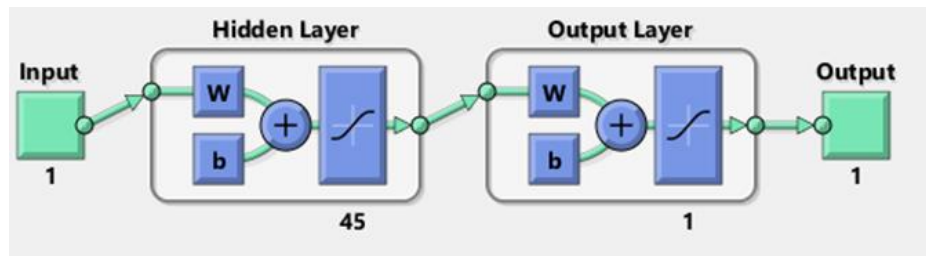
Fig. 3.13: ANN model (W: Weight and b: bias).

3.4 Experimental procedure for magnetic separation using newly fabricated lab-scale PRMS

Based on FEMM analysis, the optimized magnet-to-steel disk thickness ratio has been chosen and the magnetic roller was designed and fabricated accordingly. Then, the fabricated magnetic roller was used to develop lab-scale PRMS. After the fabrication of PRMS, the Lakeshore (Model: 410) gauss meter was used to measure the active magnetic field on the magnetic roller surface (Fig. 1.4) and at a suitable distance (B_2) from the roller surface. Then the separation ability of fabricated lab-scale PRMS was demonstrated for the particle size fraction (Chiria mines ore sample) having the lowest Fe content. Furthermore, the optimum separation of paramagnetic minerals (Kiriburu mines ore sample) was carried out through optimization of PRMS operating parameters using the DOE approach.

Initially, the experimental setup was switched on and the speed of the magnetic roller was adjusted by using a speed knob. The feed to the PRMS was introduced onto the magnetic roller with a thin belt. As the belt carrying paramagnetic minerals (hematite ore) passes over the magnetic roller, the magnetic particles are attracted by the magnetic roller, whereas feebly magnetic and non-magnetic particles are repelled off due to the resultant action of magnetic, centrifugal, and gravitational forces. The particle separation process of PRMS is shown in Fig. 1.3 (a). The separated products (magnetic/concentrate, middling, and non-magnetic) were subjected to characterization studies to check the separation ability of the newly designed magnetic roller (the active part of PRMS).

3.5 Design of Experiments (DOE)

Minitab.v.17.1 software has been used for both the Taguchi and ANOVA methods for experimental design and results processing.

3.5.1 Taguchi method

The main reason for choosing the Taguchi method was, it is simple to implement and dedicated to process or product optimization. Also, it allows optimization of the qualitative parameter with less number of required experiments (Ranjit 1990, Taguchi 1987).

Based on initial test runs, and outcomes of previously reported studies as discussed in the literature review chapter, the three operating parameters have been selected for

investigation such as feed rate (kg/h), roller/roll speed (rpm), and belt thickness (mm). An experimental plan was prepared based on the L_{27} orthogonal array which was designed to use openly following Taguchi methodology. For the construction of the experimental array, the selected operating parameters were varied at three levels as given in Table 3.1. Table 3.2 shows the L_{27} experimental design with three parameters at three levels. The main objective of parametric variation of selected operating parameters was to identify the values at which product of highest Fe grade and Fe recovery % could be attained. To achieve the highest Fe grade and Fe recovery %, Taguchi recommends a kind of parameter optimization that is, "Larger is better" [the goal is to maximize the response (Fe grade and Fe recovery %)]. For a "Larger is better" optimization, the corresponding signal-to-noise ratio relation was shown in the equation (1.15).

Table 3.1: Selected parameters and their variation levels.

Parameters	Feed Rate (ton/h)	Roller Speed (rpm)	Belt thickness (mm)
Notation	A	B	C
Level 1	0.04	80	0.50
Level 2	0.08	160	0.75
Level 3	0.12	240	1.00

Table 3.2: Experimental conditions as per Taguchi L_{27} statistical design.

Experiment No.	Feed rate (ton/h)	Roller speed (rpm)	Belt thickness (mm)
1	0.04	80	0.50
2	0.04	80	0.75
3	0.04	80	1.00
4	0.04	160	0.50
5	0.04	160	0.75
6	0.04	160	1.00
7	0.04	240	0.50

8	0.04	240	0.75
9	0.04	240	1.00
10	0.08	80	0.50
11	0.08	80	0.75
12	0.08	80	1.00
13	0.08	160	0.50
14	0.08	160	0.75
15	0.08	160	1.00
16	0.08	240	0.50
17	0.08	240	0.75
18	0.08	240	1.00
19	0.12	80	0.50
20	0.12	80	0.75
21	0.12	80	1.00
22	0.12	160	0.50
23	0.12	160	0.75
24	0.12	160	1.00
25	0.12	240	0.50
26	0.12	240	0.75
27	0.12	240	1.00

3.5.2 Analysis of Variance (ANOVA) method

The main reason for choosing ANOVA was, which gives statically analyzed results regarding the degree to which the selected parameters influence the response and the level of importance of the parameter at 95% confidence level (Yunus and Alsoufi 2016). The Fisher's value 'F' (F test), and the probability of significance 'P' (P test), were used to govern the importance of selected parameters on multiple response characteristics. For a higher F-value or lower P-value, the corresponding operating parameter has a major impact on the response characteristics (Yunus and Alsoufi 2016, Pawar and Palhade 2015).

CHAPTER 4

RESULTS AND DISCUSSION

This chapter illustrated the characterization of the ore (as-received and processed) samples and the effectiveness of FEMM analysis in designing of optimized magnetic roller (the active part of PRMS) through suitable magnet-to-steel disk configuration. Also, the accuracy of obtained FEMM data was statically verified through ANN modelling technique. Further, the design calculations of newly developed PRMS were included. Then, the magnetic separation performance of the newly designed PRMS was addressed. Finally, the effect of PRMS operating parameters on the processing of paramagnetic ore through DOE and evaluation of separated products through characterization studies was reported.

4.1 Characterization studies

The as-received (head) iron ore sample received from Chiria mines, India assayed 54.18% Fe, 11.22% SiO_2, and 5.96% Al_2O_3. The particle size and wet chemical analysis of corresponding size fractions were listed in Table 4.1. It was observed from Table 4.1, the particle size fraction of -150+105 µm has the lowest Fe content (51.24% Fe) with maximum weight % of ore sample (22.55%) retained. The percentage of Fe in the size fraction -150+105µm was decreased by an amount of 7.69 % from +500µm due to the distribution of low Fe content and the segregation of SiO_2 and Al_2O_3 in the reduced size fractions (Rao et al. 2016) which resulted in lower density values, as indicated in Table 4.1. Whereas, at the finest size fractions (-105+90 µm and -90 µm), the presence of Fe values in the ore sample has increased corresponding to the increase in the density values (Table 4.1). This indicates the good amount of liberation of the iron-bearing phase (hematite) (Dwari et al. 2013, 2014). The size fraction with the lowest Fe content that is, -150+105µm was selected for further XRD, magnetic susceptibility, and microscopy study. The XRD study confirmed the presence of hematite (Fe_2O_3) is an iron-bearing mineral along with the gangue mineral phases (quartz and kaolinite) as shown in Fig. 4.1. Similarly, the existence of the above-stated mineral phases at the corresponding angle (2Θ) was reported in the available literature (Yu et al. 2017; Rivera et al. 2016). Additionally, the magnetization property of size fraction -150+105µm was measured by using a SQUID

magnetometer and the corresponding hysteresis curve was shown in Fig. 4.2. It was found that from Fig. 4.2, the saturation magnetization value of the sample was 3.9 emu/g at a magnetic field strength of 9 kOe (0.9 Tesla). This linear positive increase in magnetization value along with lower magnetic saturation (3.8 emu/g) as the applied magnetic field strength increases, shows the paramagnetic nature of hematite mineral along with the other gangue mineral phase in the sample (Tripathy et al. 2016; Jordens et al. 2014; Waters et al. 2007). Also, the presence of Fe and gangue minerals in the form of hematite and alumina-associated silica phase were further confirmed from the microscopy study and shown in Fig. 4.3 (a) and (b). However, Fig. 4.3 (a) and (b) show the optical microscopy study, which was carried out at two different locations on the surface of the specimen (-150+105μm head sample) under constant magnification (20x). Moreover, the microscopy study reveals that the hematite and gangue phases are freely associated with each other. Hence, the Fe grade of the ore can be improved by subjecting the ore to the magnetic separation test.

Table 4.1: Particle size and elemental composition analysis of different size fractions.

Sl. No.	Particle size μm	Weight % retained	Cumulative weight % retained	Density g/cm^3	Element %		
					Fe	SiO$_2$	Al$_2$O$_3$
1	+500	9.41	9.41	3.83	58.93	7.24	2.24
2	-500+420	12.86	22.27	3.75	57.93	8.45	2.30
3	-420+300	14.38	36.65	3.72	57.37	8.32	2.36
4	-300+150	16.27	52.92	3.57	54.84	9.38	2.49
5	-150+105	22.55	75.47	3.41	51.24	10.20	2.98
6	-105+90	11.75	87.22	3.55	54.69	9.33	2.54
7	-90	12.78	100	3.62	55.69	9.40	2.52
	Head	100		3.63	54.81	11.22	5.96
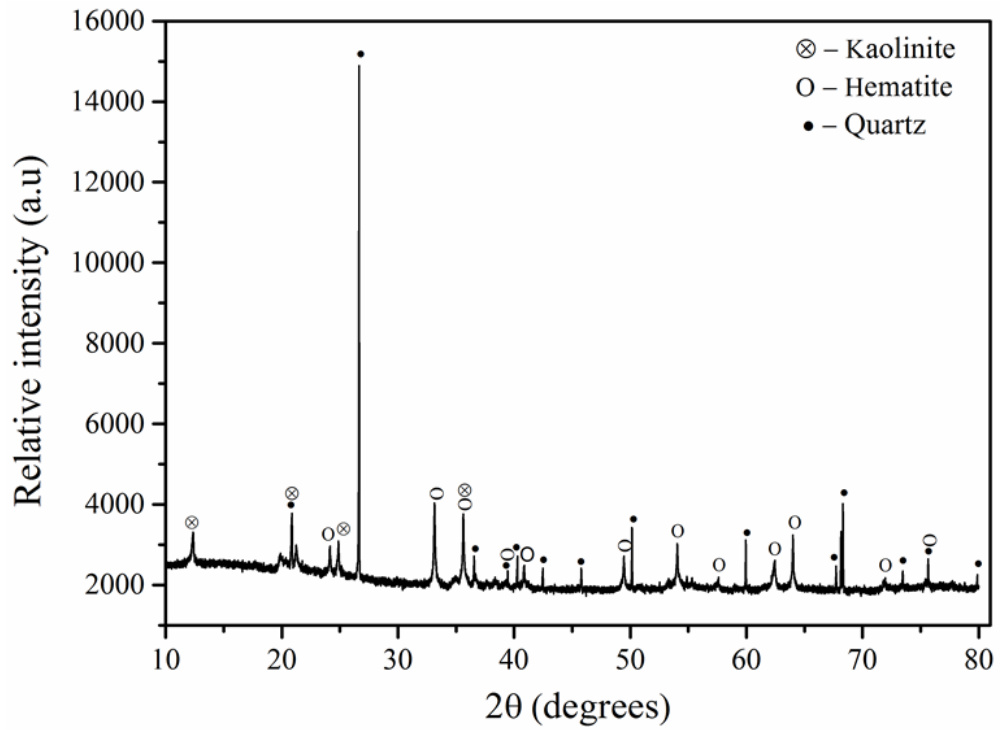
Fig. 4.1: XRD pattern of powdered iron ore sample (-150+105µm).
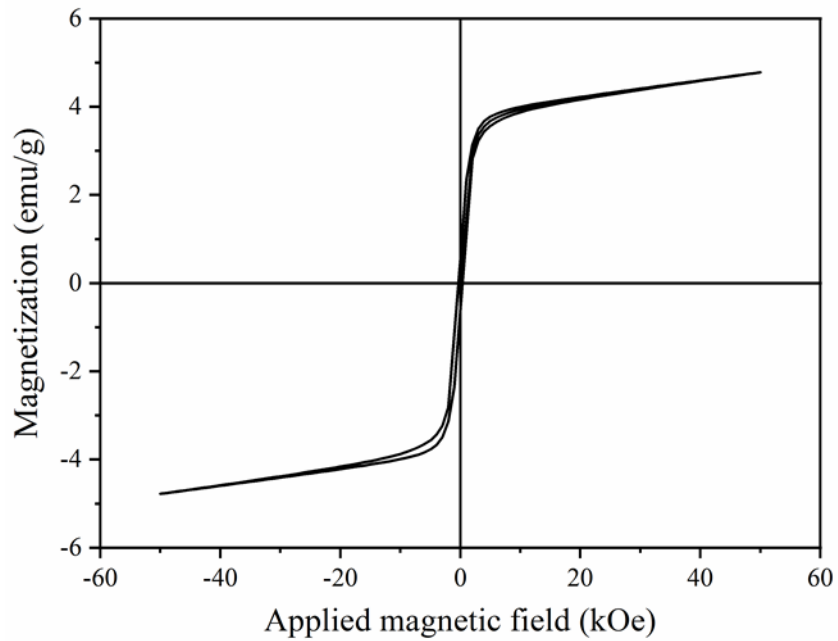
Fig. 4.2: Hysteresis curve for the powdered iron ore sample (-150+105µm).
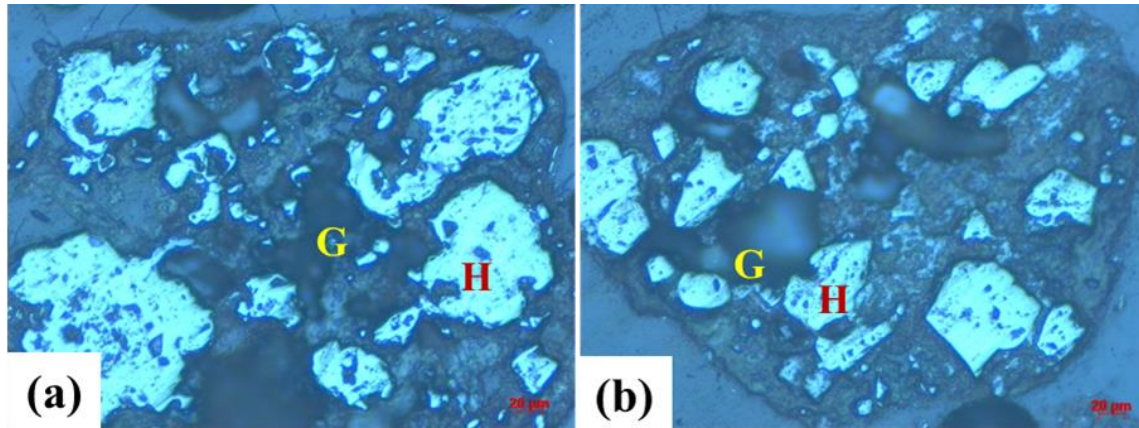
Fig. 4.3: Photomicrographs [(a), and (b)] of iron ore sample (-150+105µm) indicated the presence of hematite (H) along with the alumina associated silica gangue mineral (G) phase.

4.2 Design and fabrication of lab scale PRMS based on FEMM and prediction analysis of magnetic roller

4.2.1 Numerical analysis of magnetic roller using FEMM

Here, the modelling and simulation of a magnetic roller were executed using the discretization method (finite element method) via FEMM-2D software. The first stage was to develop a 2D model of the magnetic roller as shown in Fig. 4.4 (a), (c), and (e), which are corresponded to magnet-to-steel disk thickness ratio of 5 mm: 5 mm, 5 mm: 2.5 mm, and 5 mm: 1.25 mm. Also, the simulated results of 2D models correspond to Fig. 4.4 (a), (c), and (e) were shown in Fig. 4.4 (b), (d), and (f), respectively, which are symmetrical about the z-axis (horizontal axis), and the r-axis represents the vertical axis. Moreover, each simulation result depicts the field lines and the magnetic field/flux density in the area of a semi-circle centered at the origin with a radius of 100 mm in the r-z plane. Although Fig. 4.4 (b), (d), and (f) do show similar contour plots, they are not exact matches. This can be noticed by looking at the distribution of the flux lines around the magnetic roller.
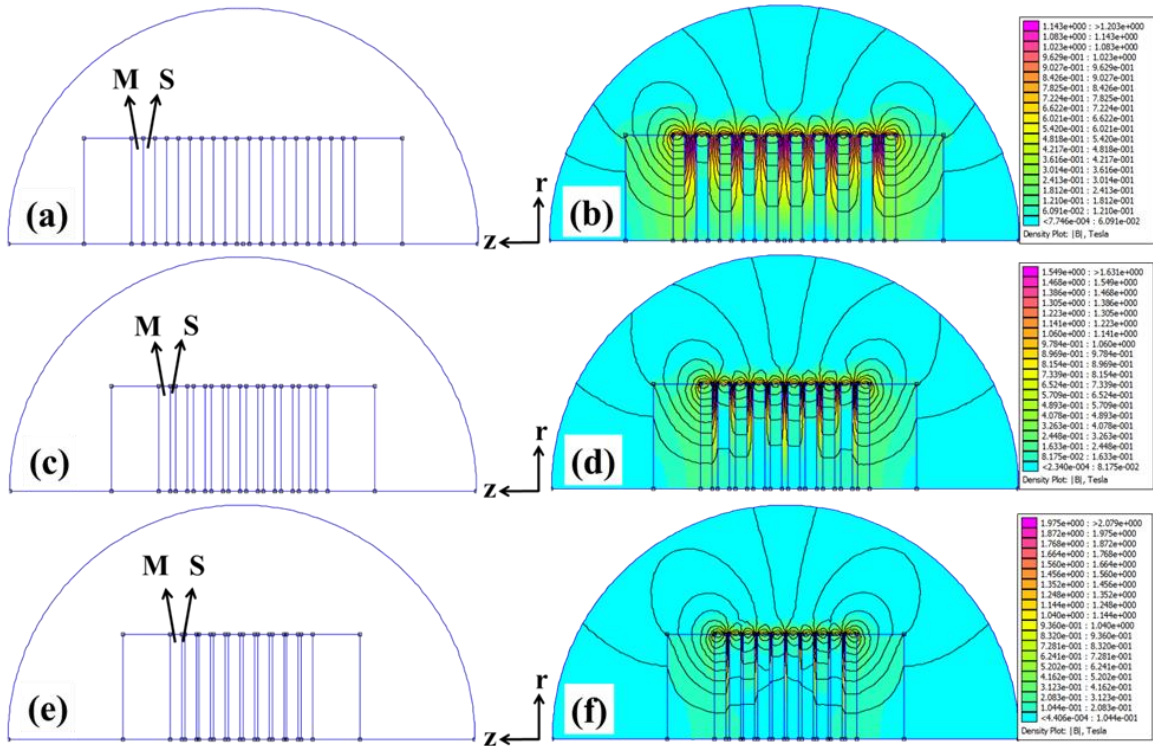
Fig. 4.4: FEMM-2D models & simulated results of magnetic roller for different M:S ratios - (a) & (b) M:S=5 mm: 5 mm, (c) & (d) M:S=5 mm: 2.5 mm, and (e) & (f) M:S=5 mm: 1.25 mm, respectively.

In Fig. 4.4 (b), (d), and (f), the distribution of magnetic field/flux lines around the magnetic roller for different magnet-to-steel disk thickness ratios was seen. Meanwhile, to have a good vision of the magnetic field intensity on the surface of the magnetic roller, Fig. 4.4 (b), (d), and (f) were magnified and shown in Fig. 4.5 (a), (c), and (e). Here, B_3 represents the effective length of the magnetic roller at a height of B_2, and B_2 represents the variable distance from the magnetic roller surface in the transverse/radial direction. Therefore, the quantification of the magnetic field passing through line B_3 at $B_2=0$ mm (i.e., on the magnetic roller surface) is critical for predicting the magnetic force acting on the ore particles to be separated. Fig. 4.5 (b), (d), and (f) represents the fluctuations in magnetic field intensity along the effective length of the magnetic roller through line B_3 at $B_2=0$ mm. In Fig. 4.5 (b), (d), and (f), 'i' represents magnetic field value at the interleaved position of magnet and steel disk, 'm' and 's' represents lowest magnetic field value at the

mid-portion of magnet disk and steel disk thickness. Furthermore, through the simulation of unlike cases the highest magnetic field ensues at the narrow region, that is, at the interleaved position between the magnet and steel disk (indicated by 'i', 2.07 T- 2.47 T for M: S=5 mm: 5 mm, 2.04 T- 2.59 T for M: S=5 mm: 2.5 mm and 1.98 T- 2.61 T for M: S=5 mm: 1.25 mm) as shown in Fig. 4.5 (b), (d) and (f). However, the occurrence of maximum magnetic field value at the interleaved position between the magnet and steel disks is due to the concentration of the magnetic flow lines at the edges of the steel disks rather than away from its edges (Svoboda 2004). Whereas the lowest magnetic field value was observed at the mid-portion of magnet disk thickness as shown in Fig. 4.5 (d) and (f) [indicated by 'm', 0.89 T for M: S=5 mm: 2.5 mm and 0.79 T for M: S=5 mm: 1.25 mm]. Also, it can be seen from Fig. 4.5 (b) in comparison with Fig. 4.5 (d) and (f), found that the magnetic field at the mid-portion of the magnet disk thickness (indicated by 'm', 0.90 T for M: S=5 mm: 5 mm) is more than that of the magnetic field at the mid-portion of the steel disk thickness (indicated by 's') because the saturation magnetization of the thicker steel disk is much greater than that of the permanent magnet disk.

Meanwhile, a steel disk with a larger thickness leads to the distribution of total magnetic field/flux throughout the steel disk thickness and results in a broader peak with a relatively low intensity of around (indicated by s) 0.6 T- 0.75 T for M: S=5 mm: 5 mm and 0.89 T- 1.13 T for M: S=5 mm: 2.5 mm as shown in Fig. 4.5 (b) and (d). Whereas a smaller thickness of the steel disk results in the concentration of the magnetic field/flux into a sharp peak giving the high intensity of around (indicated by s) 1.29 T- 1.57 T for M: S=5 mm: 1.25 mm as shown in Fig. 4.5 (f). These occurrences of variation in peak and intensity level are due to the magnetic flow lines that have to pass through the steel disk thickness, smaller the steel disk thickness, higher magnetic flow lines were passed through the steel disk thickness results in the concentration of the magnetic field/flux into a sharp peak giving high intensity. While for larger steel disk thickness, the lower magnetic flow lines were passed through steel disk thickness, resulting in the concentration of the magnetic field/flux into a broader peak and giving low intensity. Hence, there is a sheer field gradient throughout the gap due to dissimilar intensity levels (Chakravorty 1989). Also, the

minimum active magnetic field/flux over the magnetic roller surface should be 0.80 T which is required to attract the hematite grains for the separation (Tripathy et al. 2017a). So, from the simulation results (Fig. 4.5 (b), (d) and (f)) it is clear that, the magnetic roller with M: S= 5 mm: 2.5 mm configuration having the optimum magnetic field/flux on the magnetic roller surface is of the order 0.89 T- 2.59 T (Fig. 4.5 (d)).
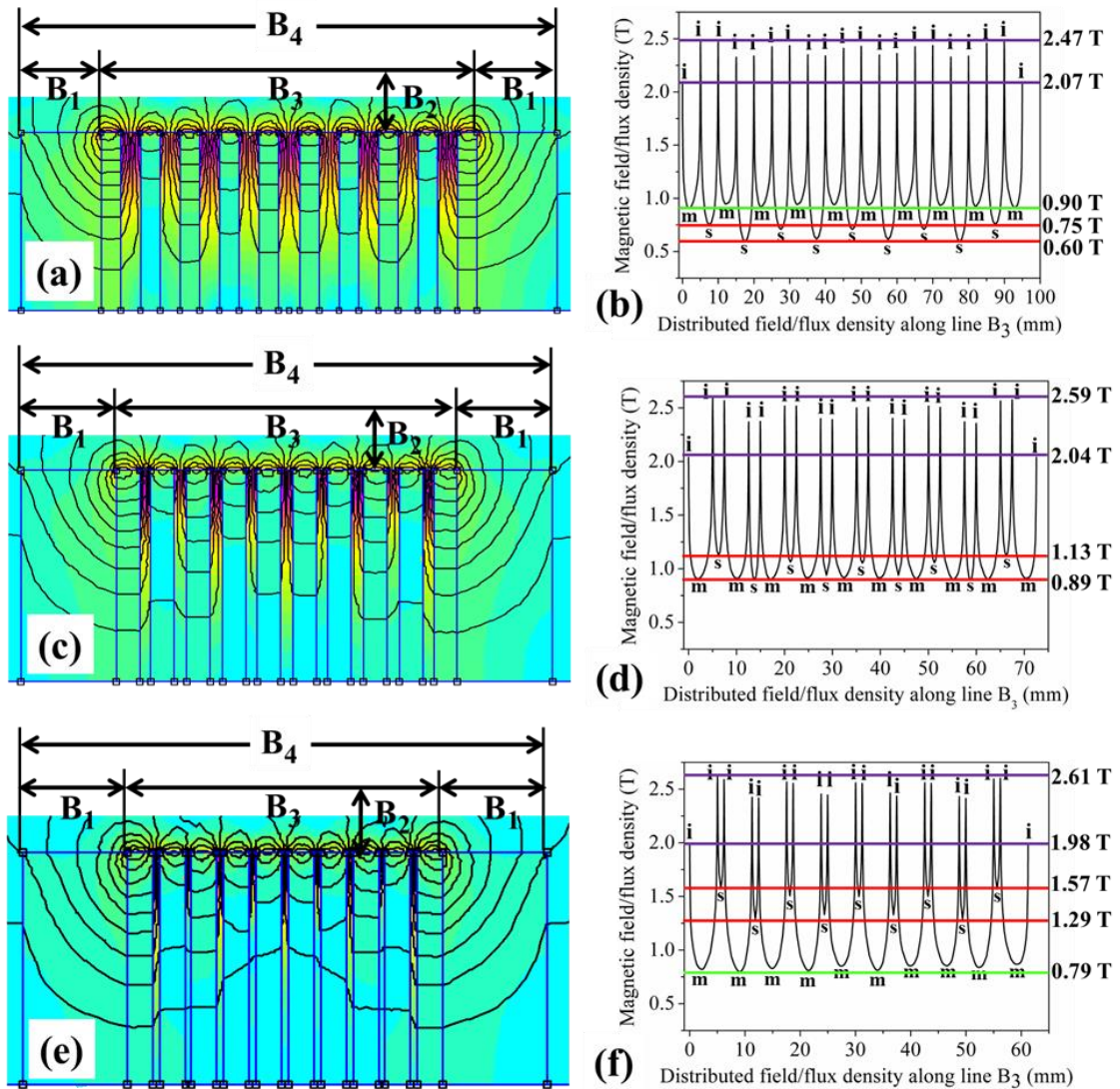
Fig. 4.5: Magnified simulated results & variations in magnetic field/flux density values on the surface of magnetic roller (i.e., at B_2= 0 mm) along B_3 line for different M: S ratios- (a) & (b) M:S=5 mm: 5 mm, (c) & (d) M:S=5 mm: 2.5 mm, and (e) & (f) M:S=5 mm: 1.25 mm, respectively.

Moreover, the magnetic force is directly proportional to the force index (the product of the magnetic field and its gradient) as mentioned in the equation. (1.1) (Svoboda 2004). In the case of the permanent magnetic roller, B and B∇B (force index) are calculated (Appendix-IV) by using equations (4.1) and (4.2) (Kopp 1984).

$$B = B_o \exp\left(\frac{-z}{t}\right). \tag{4.1}$$

$$B\nabla B = \frac{B_o{}^2}{t} \exp\left(\frac{-2z}{t}\right). \tag{4.2}$$

Additionally, Fig. 4.6 (a) and (b) shows the force index and magnetic force v/s various distance from the magnetic roller surface in the transverse direction (B_2) respectively. The force index and magnetic force were calculated by considering the minimum magnetic field value obtained on the roller surface (i.e., 0.60 T for M: S=5 mm: 5 mm, 0.89 T for M: S=5 mm: 2.5 mm, and 0.79 T for M: S= 5 mm: 1.25 mm as shown in Fig. 4.5 (b), (d) and (f)).

Here, the maximum force index (product of magnetic field and its gradient) value occurs in the magnet-to-steel disk thickness ratio is in the order of 5 mm: 1.25 mm>5 mm: 2.5 mm>5 mm: 5 mm on the magnetic roller surface (that is, at B_2=0 mm) as shown in Fig. 4.6 (a). This is due to the decrease in the flow of magnetic field lines through the steel disk as the thickness of the steel disk increases, and follows the order of 5 mm>2.5 mm>1.25 mm. Moreover, as B_2 increases, there is a steep decrease in the force index value was occurred in the M: S ratio and follows the order of 5 mm: 1.25 mm>5 mm: 2.5 mm>5 mm: 5 mm. This results in a dramatic drop of the magnetic force, but the rate of decrease is much smaller for thicker steel disks (Alp 2009; Svoboda 2004) as shown in Fig. 4.6 (a) and (b). This dramatic drop in force index and magnetic force value is due to the sharp decrease in the long reach of magnetic field lines in the transverse direction (B_2) from the magnetic roller surface. As the steel disk thickness reduces, the sudden drop in force index and magnetic force value from the magnetic roller surface in the transverse direction increases, and follows the order of 1.25 mm>2.5 mm>5 mm. Furthermore, beyond B_2= 1.25 mm, the magnitude of the magnetic force acting on the ore particles is comparatively high in the case of M: S= 5 mm: 2.5 mm ratio as shown in Fig. 4.6 (b). This is due to the effect of steel disk thickness in the M: S ratio, because if the thickness of the steel disk goes beyond a

certain optimum value, the magnet disk does not succeed in saturating the steel disk, which results in a decrease in the long reach of magnetic field lines from the roller surface in the transverse direction (Svoboda 2004). Hence, based on all the factors, M: S= 5 mm: 2.5 mm ratio was considered for the fabrication of an optimized magnetic roller. Even though, the FEMM result has proved that, the M: S= 5 mm: 2.5 mm ratio was optimum for the fabrication of an optimized magnetic roller. The obtained FEMM results (for M: S ratio of 5 mm: 5 mm, 5 mm: 2.5 mm, and 5 mm: 1.25 mm) need to be validated via prediction analysis using ANN, to ensure that the obtained FEMM data was statistically accurate and valid.
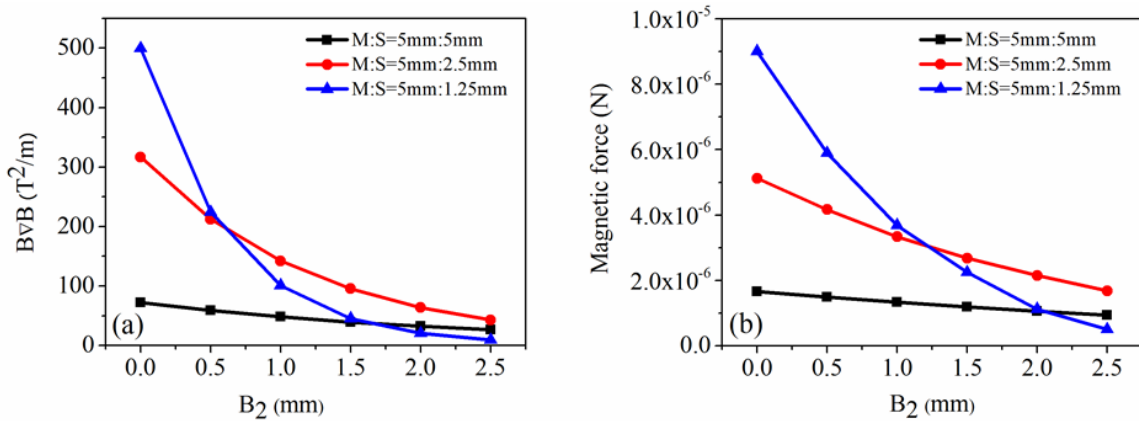
Fig. 4.6: (a) Change in B∇B (force index) as a function of B$_2$ for different M: S ratios, and (b) Change in magnetic force as a function of B$_2$ for different M: S ratios.

4.2.2 Prediction analysis of FEMM data

Here, the prediction analysis of distributed magnetic field/flux density on the magnetic roller surface (i.e., B$_2$=0) along the line B$_3$ for three different magnetic rollers using the ANN modeling technique was illustrated. The ANN database was developed using input parameters (B$_3$) and output parameters (magnetic field on the magnetic roller surface (i.e., B$_2$=0) along the line B$_3$) to establish relationship between them. The outcomes of ANN modelling using feed forward backpropagation network were displayed in Fig. 4.7 (a), (b), and (c) which shows the plot containing predicted versus actual/simulated magnetic field value. It was found that from Fig. 4.7 (a), (b), and (c), the higher values of the model is

systematically under-predicting in all the cases (M: S= 5 mm: 5 mm, 5 mm: 2.5 mm, and 5 mm: 1.25 mm). Since, there is a sudden change (linear increase and decrease) in the magnetic field value at the interleaved position between magnet and steel disc along the effective length of magnetic roller (B_3) surface as shown in Fig. 4.5 (b), (d), and (f). This sudden rise and fall in the magnetic field value of magnetic roller configurations (M: S=5 mm: 5 mm, 5 mm: 2.5 mm and 5 mm: 1.25 mm) has caused slight inaccurate data fit (of around 5 %) with the back propagation algorithm of ANN model provided with forty-five neurons as shown in Fig. 4.7 (a), (b), and (c), respectively. Although, nearly a five percent of the dataset has not been fitted well with the developed prediction model. The validation R-value obtained for three different M: S ratios were nearer to maximum value i.e., 1 (such as 5 mm: 5 mm, 5 mm: 2.5 mm and 5 mm: 1.25 mm was 0.96723, 0.96529 and 0.95976, respectively), which shows that the developed model was valid and accurate. In addition, the higher overall R-value of each ANN model indicates that the feed-forward backpropagation network with forty-five neurons provides the highest correlation between analytical data and prediction data (Information regarding weight and bias values of each ANN model is shown in Appendix-V). Although the ANN model itself provides the validation for each M: S ratio, the normal probability plot, and histogram were further utilized to revalidate the prediction analysis results of the ANN model. Hence, Fig. 4.8 and 4.9 show the normal probability plot and histogram developed using residuals obtained from the ANN model of 5 mm: 5 mm, 5 mm: 2.5 mm, and 5 mm: 1.25 mm M: S ratio. However, Fig. 4.8 shows that the errors are randomly distributed and more than 95 % of the residuals are close to the normal line, which indicates that the errors are independent of each other (Çelik and Tan 2005; Hsu et al. 1977). Also, Fig. 4.8 shows that the vertical spread of the data around the normal line appears to be fairly constant, which satisfies the condition of homoscedasticity (Aznarte et al. 2011). In addition, from Fig. 4.9, it was clear that the residuals from the ANN model are normally distributed for three different conditions of the M: S ratio (John and Draper 1980). Furthermore, Fig. 4.8 and 4.9 shows that the mean error for residuals obtained from the ANN model of three different M: S ratios was less than 0.01 (such as 5 mm: 5 mm, 5 mm: 2.5 mm, and 5 mm: 1.25 mm was

0.00096, 0.0088 and 0.0024, respectively) (John and Draper 1980). This represents that the mean error was approximately close to zero. Therefore, from Fig. 4.8 and 4.9, it was found that the condition of normality, independence, homoscedasticity, and zero mean of errors was satisfactory for the residual analysis of the ANN model. Thus, the developed ANN model for three different conditions of the M: S ratio fits the data well. So, from the results, it was clear that the mathematical equation (for 'overall' condition) developed between the input parameter (B_3) and output parameter (distributed magnetic flux density on the magnetic roller surface (i.e., B_2=0) along the line B_3) will provide a valid and accurate prediction analysis of magnetic flux density, as shown in Fig. 4.7 (a), (b) and (c). Hence, the results of ANN model along with the normal probability plot and histogram validation represents that the FEMM results obtained for three different conditions of M: S ratio was statistically accurate and valid.
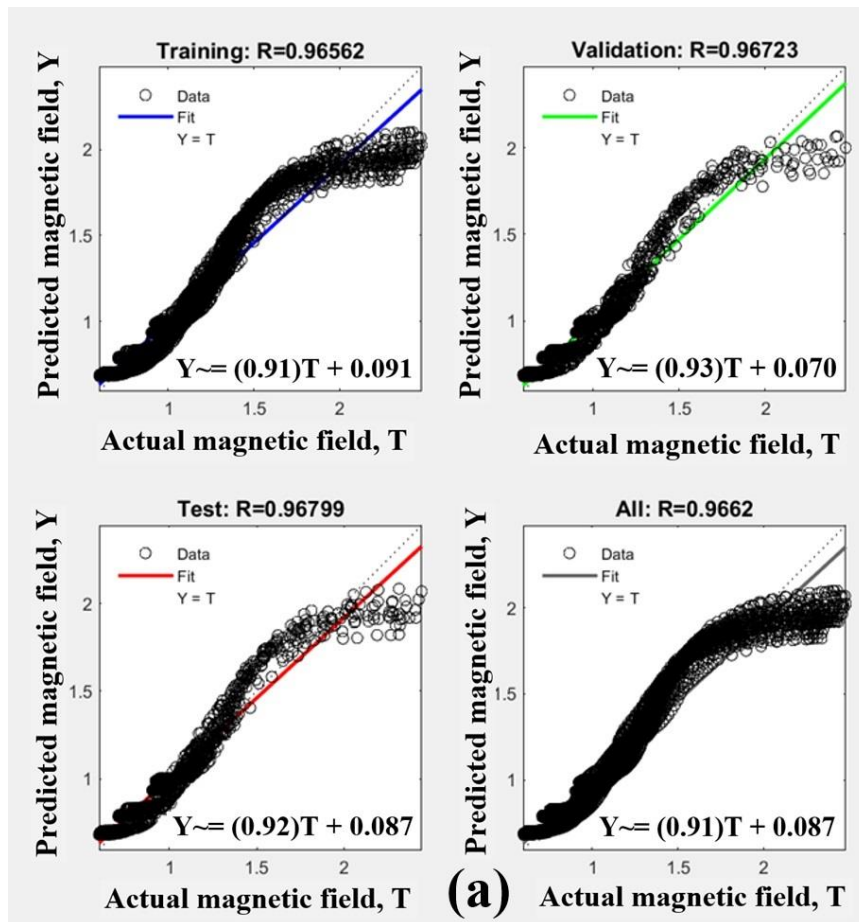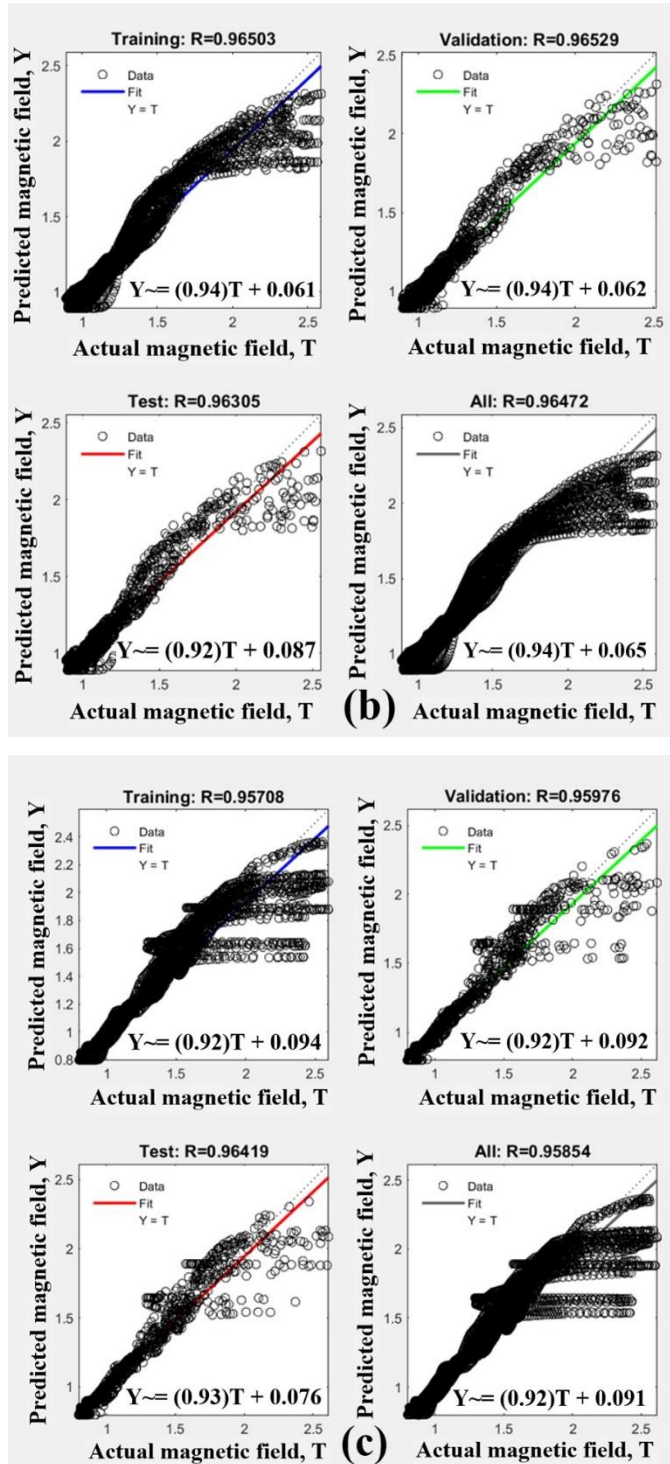
Fig. 4.7: Predicted versus simulated magnetic field/flux density on the magnetic roller surface (i.e., $B_2=0$) along the line B_3 for different M:S ratios – (a) M:S= 5 mm: 5 mm, (b) M:S= 5 mm: 2.5 mm, and (c) M:S= 5 mm: 1.25 mm.
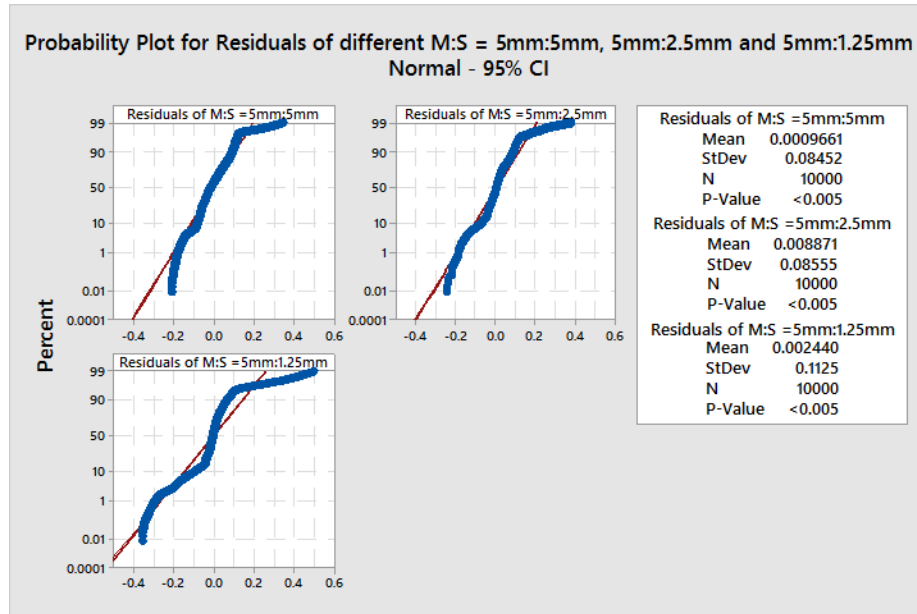
Fig. 4.8: Probability plot of residuals obtained from ANN model for different M:S = 5 mm: 5 mm, 5 mm: 2.5 mm, and 5 mm: 1.25 mm.
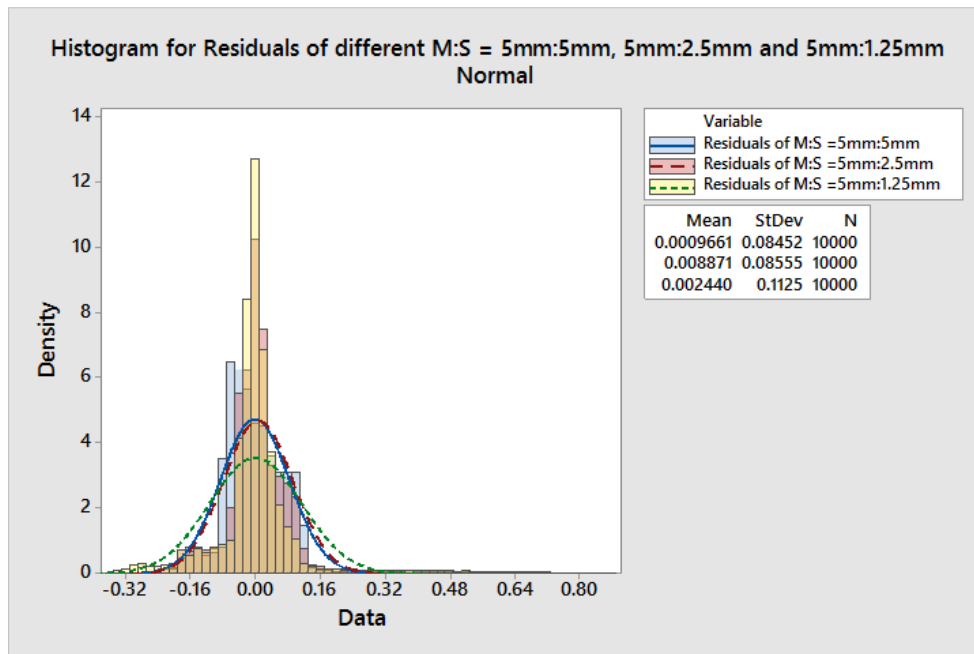
Fig. 4.9: Histogram of residuals obtained from ANN model for different M:S = 5 mm: 5 mm (blue line), 5 mm: 2.5 mm (red line) and 5 mm: 1.25 mm (green line).

4.2.3 Design description of fabricated lab-scale PRMS

The magnetic roller of 90 mm diameter was fabricated by using an optimized magnet-to-steel disk thickness ratio of 5 mm: 2.5 mm. Since, for larger magnetic roller diameter, particles residence time in the magnetic field and field depth increases which results in better separation with zero heat generation during the separation process (Wells and Rowson 1992). However, the magnetic roller was fabricated in such a way that, the magnet disk (NdFeB grade 52) was interleaved with the steel disk (SAE 1010) [Fig. 4.10 (a) and (b)]. In addition, the fabricated optimized magnetic roller was used in the lab-scale PRMS as shown in Fig. 4.11 and 4.12. The lab-scale PRMS consists of a hopper and electromagnetic vibratory feeder, which controls the uniform flow of feed material onto the belt drive. The belt drive was connected by two rollers. The roller which is connected to the motor is a magnetic roller (Fig. 4.10 (a) and (b)) and the other one is a support roller (Fig. 4.10 (c) and (d)). Moreover, the roller-belt assembly was designed in such a way that there is no rebound or dispersion of particles when they entered the magnetic zone and all particles go into the magnetic zone with the uniform horizontal velocity. Therefore, these factors help to achieve sharp separation. Also, the separated products (magnetic, middling, and non-magnetic) were get collected in three collection bins, which are parted from the fixed splitters as shown in Fig. 4.11. In addition, with suitable equations, power requirements, and belt tensions were calculated.
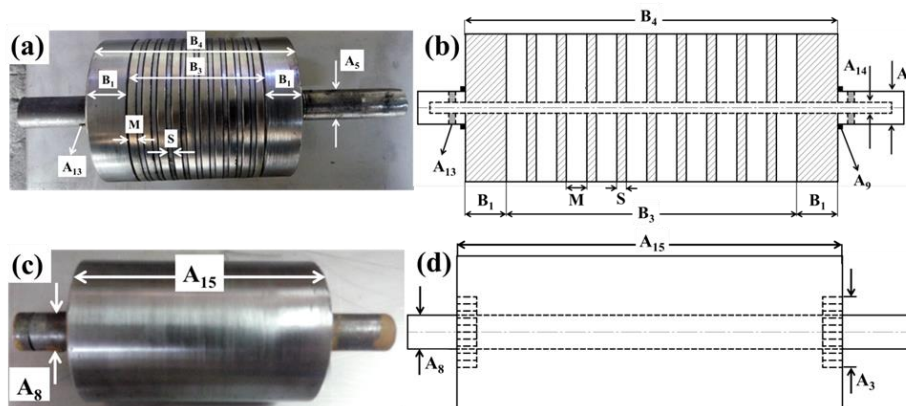
Fig. 4.10: (a) Optimized magnetic roller, (b) 2D model of optimized magnetic roller with geometric details, (c) Support roller, and (d) 2D model of support roller with geometric details.
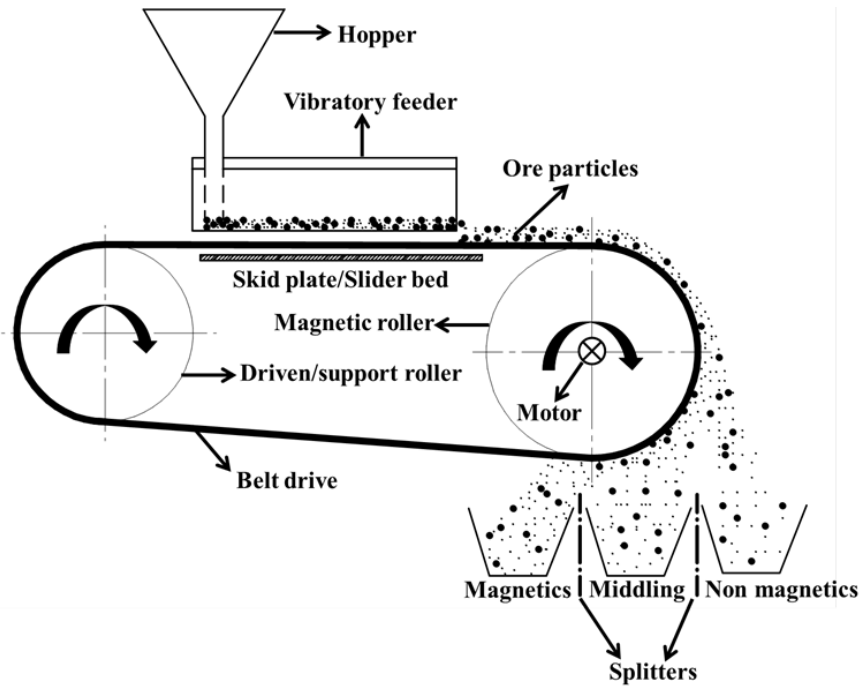
Fig. 4.11: Line diagram for the separation principle of fabricated lab-scale PRMS.
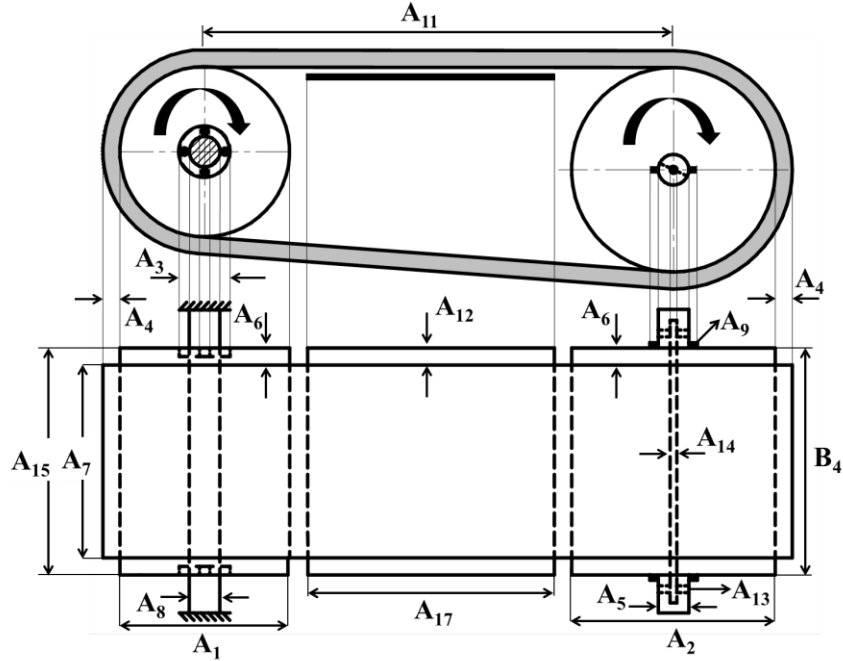
Fig. 4.12: 2D representation of fabricated lab-scale PRMS.

4.2.4 Power requirements

The calculations are based on hematite ore sample having an average material density that is, $M_d = 3410$ kg/m³, and $W_1 = L_1 = 0.110$m, $A_2 = 0.09$m, $A_1 = 0.075$m, $A_{11} = 0.245$m for different roller speed (n= 60, 120, 180 and 240 rpm) and belt thickness ($A_4 = 0.5, 0.75$ and 1 mm).

All calculation methods presume that the belt is packed consistently along the length and that the load outspreads to within a slight distance 'x' of the edge of the belt (Yardley 2008) as shown in Fig. 4.13 (a). To calculate the required power to run the PRMS, it is required to compute effective belt tension (T_e), given by equation (4.3) (Dunlop 2009) and shown in Fig. 4.13 (b).
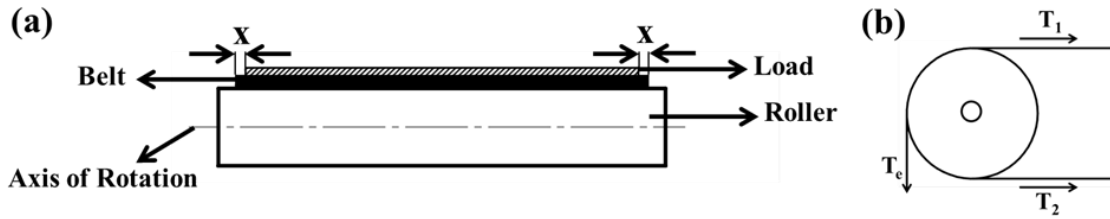
Fig. 4.13: (a) Loaded belt drive, and (b) Plain drive.

$$T_e = f_o \times 2W_l^2 \times L_l \times M_d \times 9.81 \times 10^{-3}. \tag{4.3}$$

Where, $f_o = 0.6$ for slider bed operation (Dunlop 2009).

By considering the belt thickness for a given driver/magnetic roller, the velocity of the belt (v) is calculated by equation (4.4) (Bhandari 2003).

$$v = \frac{\pi(A_2 + A_4)n}{60} \text{ since the magnetic roller } (A_2) \text{ is the larger roller (Bhandari 2003).} \tag{4.4}$$

Thus, the required motor power (P_m) to run the PRMS is stated in equation (4.5) (Yardley 2008).

$$P_m = T_e \times v. \tag{4.5}$$

Also, for running the PRMS, an electric motor is used to turn the magnetic roller. So, the selected motor should satisfy the smallest power required for the driver head. Therefore, for minimum motor power (P_{min}), equation (4.6) (Derikvand 2015) is applied:

$$P_{min} = \frac{P_m}{\eta}. \tag{4.6}$$

Where, η=0.95, by considering the 5 % of motor losses (Bhandari 2003)

4.2.5 Belt tensions

The belt tensions were calculated by considering the total resistance T_e, which is the effective belt tension at the magnetic roller and is given by the equation (4.7) (Yardley 2008).

$$T_e = T_1 - T_2.\tag{4.7}$$

To determine T_1 and T_2, the supplementary relationship called Capstan equation is given by the equation (4.8) (Yardley 2008), which is used to model the belt friction.

$$\frac{T_1}{T_2} = e^{\mu\theta}.\tag{4.8}$$

Where, $\mu = 0.3$ for horizontal conveyor belt, under the bare pulley and dry condition (Dunlop 2009).

Since, $\frac{T_1}{T_2} = e^{\mu\theta}.$

Therefore, $T_1 - T_2 = T_2(e^{\mu\theta} - 1).\tag{4.9}$

Then, $\frac{T_2}{T_1 - T_2} = \frac{1}{e^{\mu\theta} - 1} = \frac{T_2}{T_e}.$

And $T_2 = \frac{T_e}{e^{\mu\theta} - 1}.\tag{4.10}$

Since both the magnetic roller (Fig. 4.10 (a) and (b)) and support roller (Fig. 4.10 (c) and (d)) are not of the same diameter, the angle of the belt wrap around the larger roller (magnetic/driver roller) (θ_L) is given by equation (4.11) (Bhandari 2003).

$$\theta_L = \pi + 2\sin^{-1}\left(\frac{A_2 - A_1}{2A_{11}}\right).\tag{4.11}$$

The angle of the belt wrap around the smaller roller (support/driven roller) (θ_s) is given by equation (4.12) (Bhandari 2003).

$$\theta_s = \pi - 2\sin^{-1}\left(\frac{A_2 - A_1}{2A_{11}}\right).\tag{4.12}$$

If the belt is used to transmit power between two rollers of unequal diameters, the belt will first slip on the roller having a smaller angle of contact, i.e., on the smaller roller. Therefore, it is necessary to take θ_s into account while designing (Bhandari 2003).

Let $K = \text{constant} = \frac{1}{e^{\mu\theta_s} - 1}.\tag{4.13}$

Therefore, from the equation (4.10) and (4.7), $T_2 = T_e \times K$ and $T_1 = T_e(K + 1)$.

The design calculations results were shown in Table 4.2 and Fig. 4.14 (a) and (b). Also, from Fig. 4.14 (a) and (b), it was observed that the belt speed and power consumption get affected substantially for the roller speeds than compared to belt thickness. As the roller speed increases, there is an appreciable increase in the belt speed and power consumption for all the belt thickness. Whereas in the case of increasing belt thickness, the belt speed and power consumption remain almost the same for all the speeds. Since, from the equations 4.4 and 4.5, it was mathematically proved that the contribution of roller speed towards the belt speed and power consumption is more as compared to belt thickness. So, to monitor the roller speed VFD (speed controller) was used. Also, initially, a belt of 0.5 mm thickness was used in the PRMS as shown in Fig. 4.15 (a) and (b). However, the fabricated lab-scale PRMS (fabrication details were given in the Appendix-VI) has the flexibility to vary the roller speed and to change the belt of different thicknesses. In addition, the calculated belt tensions T_1 and T_2 (Table 4.2) were found to be satisfactory for transmitting the power without any belt slip from the roller surface. This condition was verified through several trials run before separation tests. Moreover, before performing the separation test, the active magnetic field on the roller surface (i.e., $B_2=0$ mm) and at suitable distances from the roller surface was experimentally measured as shown in Fig. 4.16 (a). Also, from Fig. 4.16 (c), it was found that experimental and numerical value agrees well with the acceptable variations for all B_2 distances. However, there is always a fluctuation between the experimental and numerical value of around 0.1 T due to the sensitivity of the Hall sensor which is present in the axial probe as shown in Fig. 4.16 (b). The separation performance of newly fabricated PRMS was evaluated by using paramagnetic minerals (hematite ore) with a size fraction -150+105 µm (Chiria mines ore sample).

Table 4.2: Calculated results of new lab-scale PRMS.

T_e (N)	Roller Speed (rpm)	Belt thickness (mm)						θ_L (rad)	θ_s (rad)	T_1 (N)	T_2 (N)
		0.5		0.75		1					
		v (m/s)	P_{min} (W)	v (m/s)	P_{min} (W)	v (m/s)	P_{min} (W)				
53.42	60	0.284	15.97	0.285	16.02	0.285	16.02	3.20	3.08	88.57	35.15
	120	0.568	31.96	0.57	32.05	0.571	32.1				
	180	0.852	47.95	0.855	48.07	0.857	48.19				
	240	1.137	63.92	1.14	64.1	1.143	64.27				
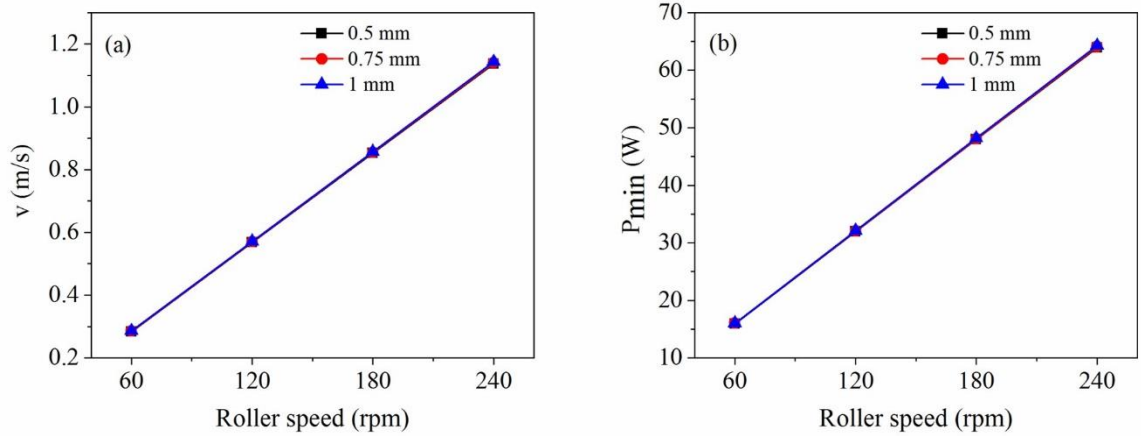
Fig. 4.14: (a) Effect on v concerning roller speed and belt thickness, and (b) Effect on P_{min} concerning roller speed and belt thickness.
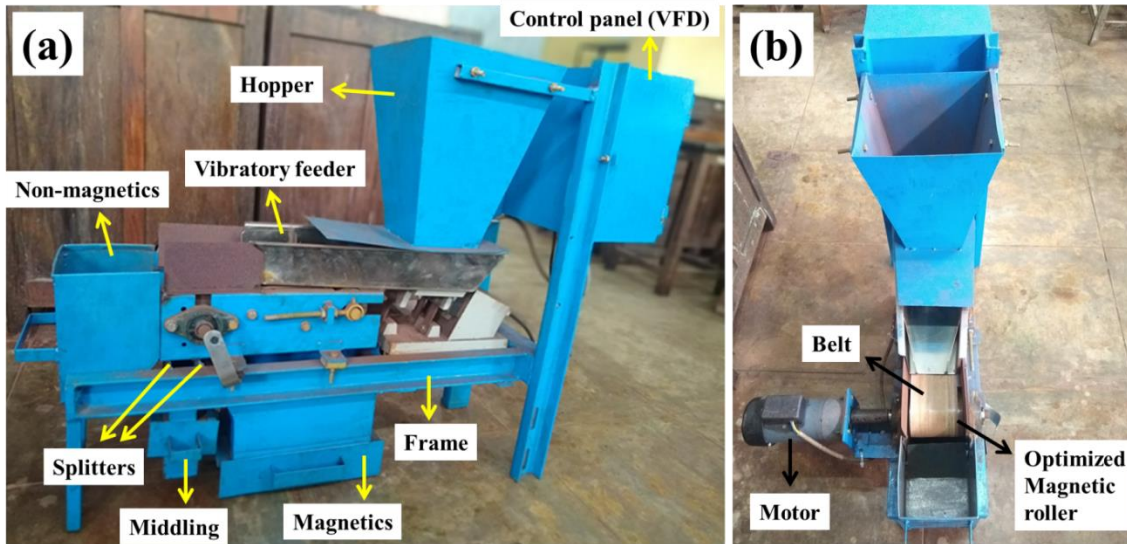
Fig. 4.15: Fabricated lab-scale permanent roll magnetic separator (a) Side view, and (b) Front view.
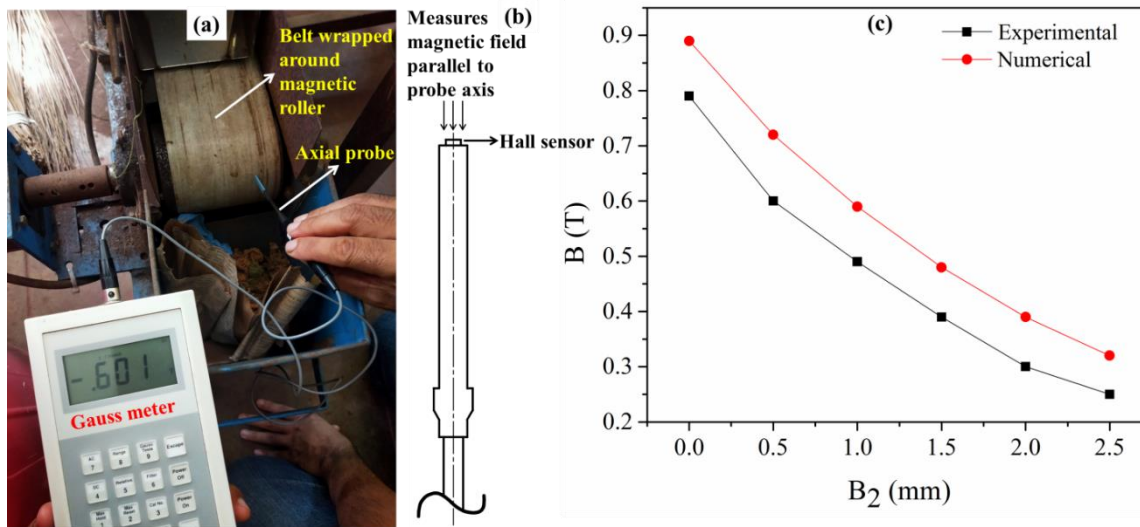
Fig. 4.16: (a) Experimental setup for magnetic field measurement on the magnetic roller surface (b) 2D representation of axial probe, and (c) Comparison of experimental and numerical magnetic field values at various B_2 distances from the magnetic roller.

4.3 Measure of separation ability of newly designed PRMS through experimental trails

The experimental trials were conducted under varying roller speeds (60, 120, 180, and 240 rpm) for different belt thicknesses (0.5, 0.75, and 1 mm). Whereas the remaining variables such as feed rate (0.05 ton/h), splitter position (90º), and particle size fraction (-150+105μm) were kept constant. In addition, the wet chemical analysis results (Fe %) of separated products were shown in Table 4.3 and Fig. 4.17 (a), (c), and (e).

Furthermore, the performance evaluation of fabricated PRMS in terms of Fe recovery out of the total Fe present in the feed was calculated using equation 4.14 (Rayapudi et al. 2019) and obtained results were tabulated in Table 4.3 and shown in Fig. 4.17 (b), (d) and (f).

$$\text{Fe Recovery \%} = \frac{(\text{Fe \%} \times \text{Weight \%})_{magnetics}}{(\text{Fe \%} \times \text{Weight \%})_{feed}} \times 100. \tag{4.14}$$

Table 4.3: Results of magnetic separation test on -150+105μm size fraction sample (assaying 51.24% Fe, 10.20% SiO_2, and 2.98% Al_2O_3) at different roller speeds and belt thicknesses with a feed rate of 0.05 ton/h.

Roller speed (rpm)	Details	Belt thickness (mm)								
		0.5			0.75			1		
		W %	Fe %	R %	W %	Fe %	R %	W %	Fe %	R %
	Ma	73.23	56.9	81.31	69.18	57.2	77.22	61.1	57.4	68.44
60	Mi	2.31	39.7	1.78	3.38	41	2.70	4.1	42.1	3.36
	Nm	24.5	35.4	16.92	27.44	37.6	20.13	34.89	41.4	28.18
	Ma	69.2	57.9	78.19	64.86	58.1	73.54	58.34	58.34	66.42
120	Mi	2.5	40.2	1.96	3.04	41.9	2.48	4.29	43.1	3.60
	Nm	28.3	36.1	19.93	32.1	39.32	24.63	37.37	42	30.63
	Ma	61.5	59.5	71.41	55.26	59.6	64.27	47.83	59.75	55.77

180	Mi	2.9	41.1	2.32	3.3	43.94	2.82	7.53	44.49	6.53
	Nm	35.6	37.9	26.33	41.44	41.34	33.43	44.64	43.42	37.82
	Ma	60.46	58.8	69.38	51.38	59.1	59.26	42.93	59.24	49.63
240	Mi	2.1	42	1.72	2.5	44.26	2.15	3.7	48.68	3.51
	Nm	37.5	39.7	29.05	46.14	42.87	38.60	53.45	44.97	46.90

Note: W % - Weight %, Fe % - Fe grade, R % - Fe Recovery %, Ma - Magnetics, Mi – Middlings, and Nm – Non-magnetics.
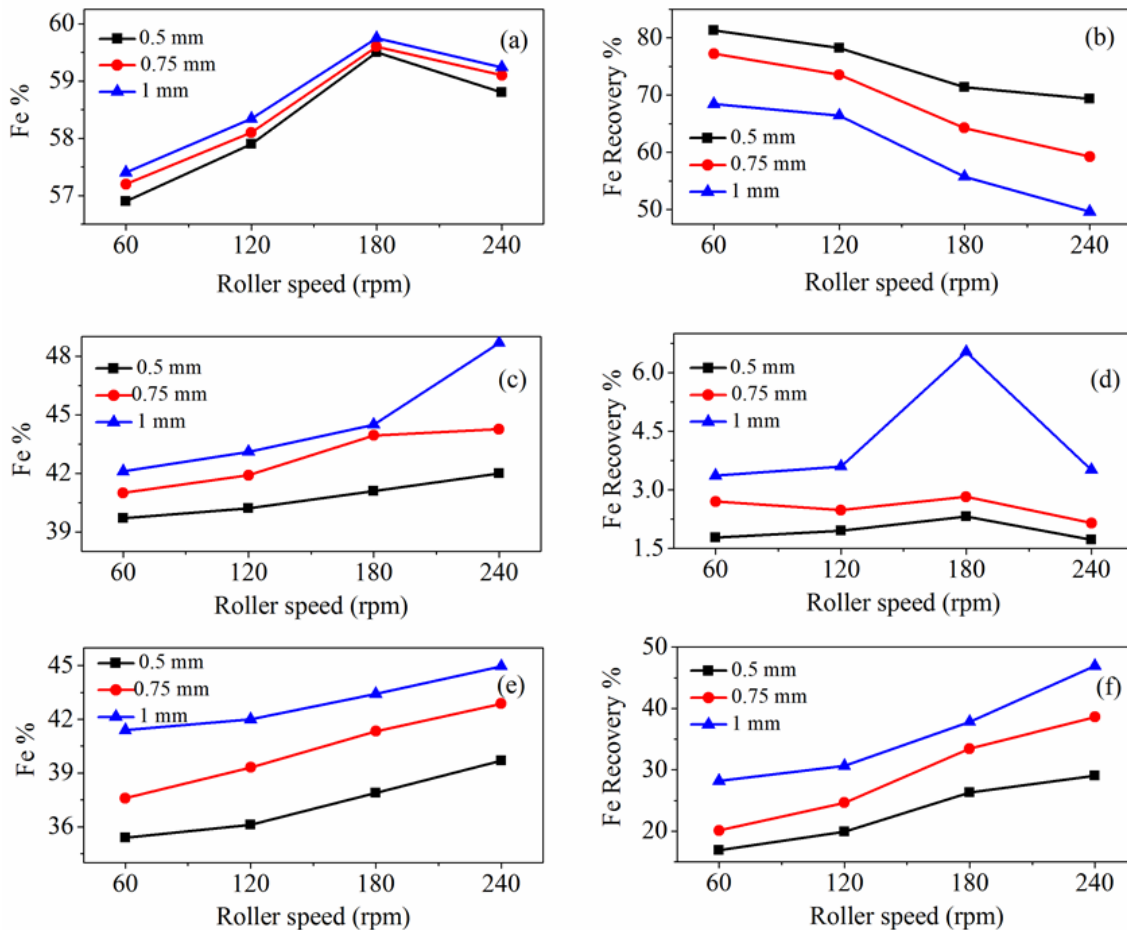
Fig. 4.17: Variation in Fe % and Fe recovery % with respect to roller speed and belt thickness (a) & (b) - Magnetics, (c) & (d) – Middlings, and (e) & (f) – Non-magnetics.

From Fig. 4.17 (a), it was found that, with an increase in roller speed of PRMS, there is an increase in Fe % of the magnetic product up to 180 rpm for all belt thicknesses (0.5, 0.75, and 1 mm). After 180 rpm (that is, at 240 rpm), the Fe % was decreased in the magnetic product (Fig. 4.17 (a)). However, the Fe % was increased in middling and non-magnetic fraction at 240 rpm for all belt thickness as shown in Fig. 4.17 (c) and (e). This is due to the domination of higher centrifugal force at the same time improper particle spacing and reduced residence time on the magnetic roller surface decreases the particle selectivity in the given magnetic field at 240rpm. This leads to throwing away of magnetic and partial magnetic particles towards the middling and non-magnetic end (Tripathy et al. 2017a; Ibrahim et al. 2002). Hence, there was a decreased Fe % in magnetic product and a corresponding increase in Fe % at the middling and non-magnetic products at 240 rpm as shown in Fig. 4.17 (a), (c), and (e).

Also, Fig. 4.17 (a) shows that, increasing belt thickness results in a very slight increase in Fe % at the magnetics fraction that is, up to 0.5 % for the corresponding roller speeds. In the case of middlings and non-magnetic fraction increase in Fe % was up to 7 % and 6% respectively, as shown in Fig. 4.17 (c) and (e). Since the amount of magnetic force acting upon the particles results from a relationship between the magnetic force from the magnetic roller and the thickness of the belt (Goolsby and Moore 1997). As the wrapped belt thickness around the magnetic roller increases, the active magnetic force available for the particle separation decreases. Therefore, when the magnetic roller rotates, only the particle with the highest magnetic property will get a stick on the belt surface by magnetic force and follows around until it passes the magnetic roller. At that point, the magnetic force vanishes and the highest magnetic content of ore particle falls into collection bins and gets collected as magnetics/concentrate (Goolsby and Moore 1997). Whereas the particle with a feeble and partial amount of magnetic content gets pulled downward by gravitational force, and the centrifugal force produced by the roller speed gives the particle momentum to overcome the magnetic force and get lost as middlings and non-magnetics (Goolsby and Moore 1997). This leads to an increase in Fe recovery % of middling and non-magnetic products concerning an increase in belt thickness as shown in Fig. 4.17 (d)

and (f). Meanwhile, the Fe recovery % of magnetic product gets reduced as the belt thickness increases, shown in Fig. 4.17 (b). Since the reduced belt thickness results in the separation of even a feeble magnetic content ore particle into a magnetic product which in turn increases the Fe recovery % of the magnetic product with reduced Fe grade. This change in the quality of the Fe grade and recovery % was accomplished by the combination of magnetic, centrifugal, and gravitational forces acting on the particle (Nakai et al. 2010; Goolsby and Moore 1997). The net resulting force is liable for the respective movement of the particle in the applied magnetic field, where the magnetic force acting on the particle must be suitably high as compared to the sum of centrifugal force and gravitational force acting on the particle (Yamamoto 2013; Svoboda and Fujita 2003) as shown in Fig. 4.18 (b).

However, in comparison with Fe grade and recovery %, the magnetic roller (M: S= 5 mm: 2.5 mm) with 0.5 mm belt thickness has given the optimum results of 59.5% and 71.41 % in the magnetics product at a roller speed of 180 rpm (Fig. 4.17 (a) and (b)). Hence, to obtain a better Fe grade and recovery %, the magnet-to-steel disk thickness ratio is an important factor that needs to be sensibly chosen before fabricating any magnetic roller. Therefore, the FEMM analysis of magnet-to-steel disk thickness ratio helps to select a suitable M: S ratio which results in an optimized magnetic roller (M: S= 5 mm: 2.5 mm) in a cost-effective way.
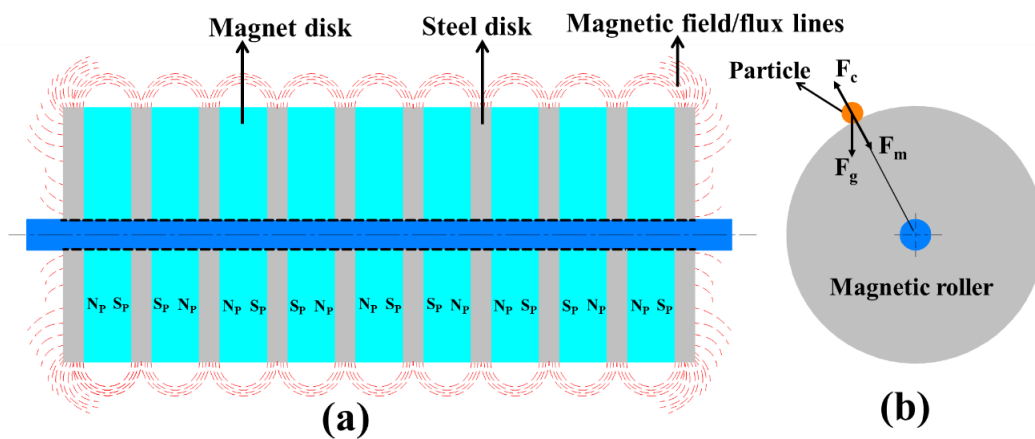
Fig. 4.18: (a) Distribution of magnetic flux lines around the magnetic roller, and (b) Distribution of forces on an ore particle in a magnetic roller.

4.3.1 Optical microscopy study of separated products

The magnetic product obtained at the experimental condition of 180 rpm roller speed and 0.5 mm belt thickness has given the better Fe grade (59.5 %) and recovery (71.41 %). Therefore, for the microscopy study, the separated products (magnetic, middling, and non-magnetic), which were gained from the same experimental condition was considered. Here, the microscopy analysis has been carried out on the specimen surface of each separated product at more than one location under constant magnification (20x).

However, the corresponding distributions of hematite and gangue mineral phases at two different locations on the specimen surface of the magnetic, middling and non-magnetic product were shown in Fig. 4.19. Therefore, Fig. 4.19 (a) & (b) shows the distribution of hematite (H) and gangue (G) mineral phases at two different locations for the magnetic specimen. Similarly, Fig. 4.19 (c) & (d), and Fig. 4.19 (e) & (f) represents the dissemination of hematite and gangue mineral phases at two different locations for the middling and non-magnetic specimen. Moreover, in the microscopy images of each separated product specimen, the bright patches indicate the hematite (H) phase, whereas, the black earthy-like appearance indicates the gangue (G) mineral phase. Furthermore, the analysis of separated products via microscopy study reveals that there is a significant distribution of hematite phase in the magnetics products (Fig. 4.19 (a) & (b)) than compared to middlings (Fig. 4.19 (c) & (d)) and non-magnetic (Fig. 4.19 (e) & (f)) products, which endorses the presence of higher Fe % in the magnetics product. Also, the presence of a significant portion of gangue minerals in the form of alumina-associated silica phase in both non-magnetic and middlings suppresses the presence of hematite phase as shown in Fig. 4.19 (e) & (f), and (c) & (d).
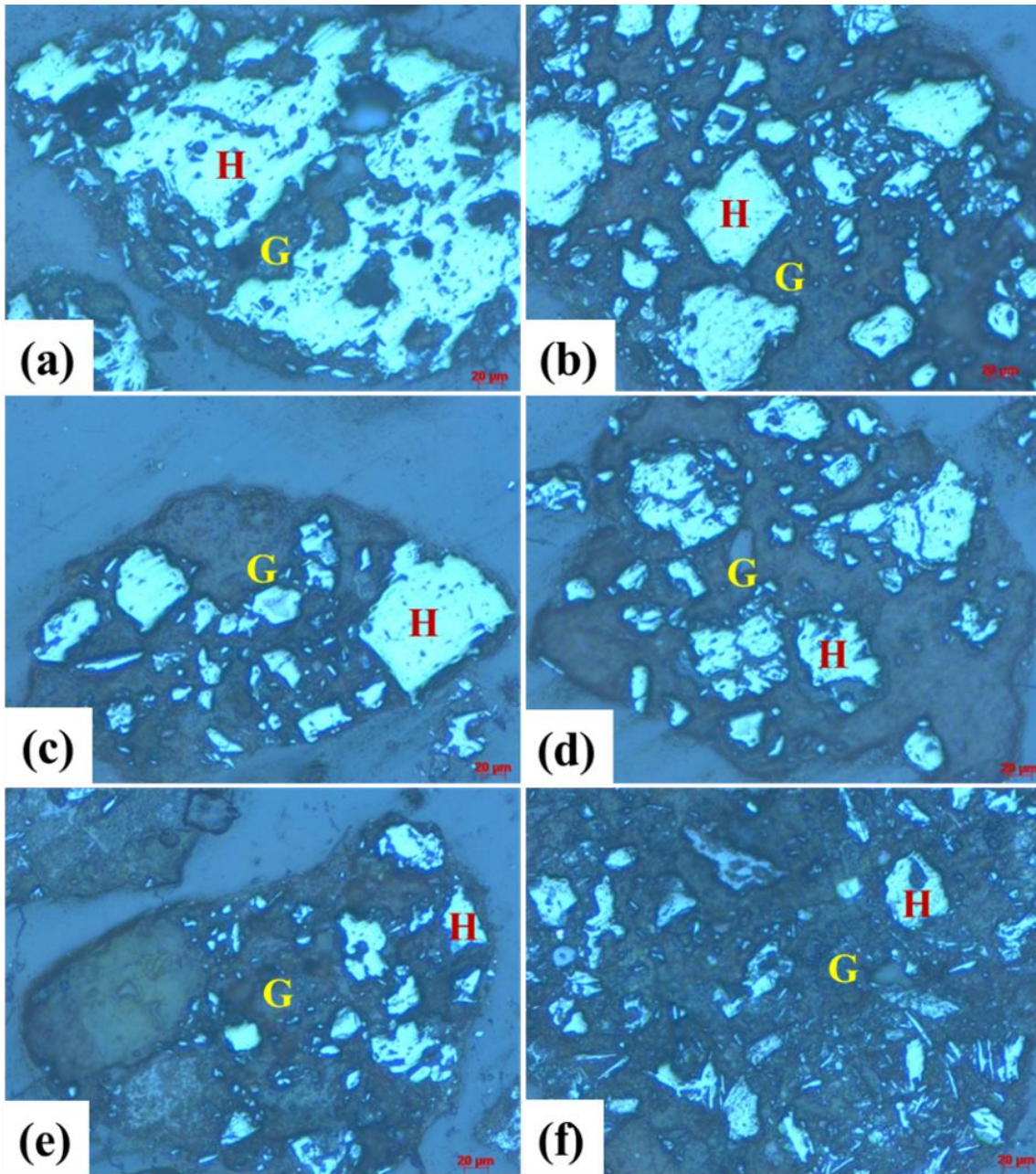
Fig. 4.19: Photomicrographs of separated products indicated the distribution of hematite (H) along with the alumina associated silica gangue mineral (G) phase - (a) & (b) distribution of H and G in magnetics, (c) & (d) distribution of H and G in middlings, and (e) & (f) distribution of H and G in non-magnetics.

4.4 Optimization of operating parameters of newly designed lab-scale PRMS

The effect of PRMS operating parameters on the processing of paramagnetic minerals (hematite ore) through an optimization technique using Taguchi-based experimental design was illustrated here. The parametric optimization of selected operating parameters of newly developed lab-scale PRMS was carried out through the beneficiation of low grade iron ore fines of size fraction -150 µm (feed) from Kiriburu mines, India. Since, characteristically, Indian iron ores are soft and fragile, by mechanized mining operations a substantial amount of fines (-150 µm) get generated. The use of these fines for metal extraction is a critical concern for better utilization of resources and pollution control (Sah and Dutta 2009, Chokshi and Dutta 2014).

4.4.1 Characterization studies on feed sample

It was observed that from Table 4.4, about 87 % of the sample includes +90 µm size fractions. Also, a decrease in size fraction results in decreased Fe content, which indicates the segregation of silica and alumina results in poor liberation of Fe at finer size fractions.

Table 4.4: Size-by-size analysis of -150 µm (feed) sample.

Particle size (µm)	Weight %	Fe %	SiO_2 %	Al_2O_3 %
-150+105	45.50	47.48	22.9	5.75
-105+90	41.49	47.63	22.21	5.99
-90+45	8.02	46.58	18.76	8.59
-45	4.99	40.29	20.35	11.05
Feed	100	46.95	22.03	6.50

Furthermore, the presence of Fe in the form of hematite; Si and Al elements in the form of quartz and aluminum silicate hydroxide (kaolinite) was confirmed from the XRD study (Fig. 4.20) and the corresponding quantification details was given in the Appendix-VII. In addition, the OM study (Fig. 4.21) endorses the distribution of hematite and gangue mineral phases (quartz and kaolinite) i.e., they were freely allied with each other without any interlocking appearance. Finally, the magnetic susceptibility study (Fig. 4.22) reveals

the specific magnetic behavior of the feed sample against the applied magnetic field strength. It was observed from Fig. 4.22 that, the linear positive increase in magnetization with a lower magnetic saturation value (2.80 emu/g at 0.8 T) against the applied field strength reveals the paramagnetic property of the ore. However, the decreased saturation magnetization value is owing to the combination of quartz and hematite minerals in the ore sample. This magnetic response of the feed sample (-150 µm) has paved the way for the improvement of Fe grade % using a high-intensity dry magnetic separator (lab-scale PRMS).
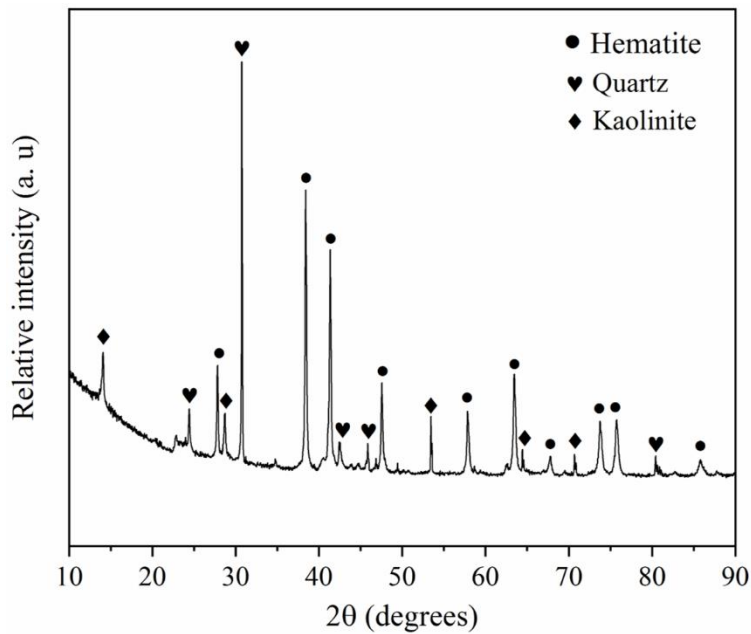
Fig. 4.20: XRD pattern of feed sample (-150 µm).
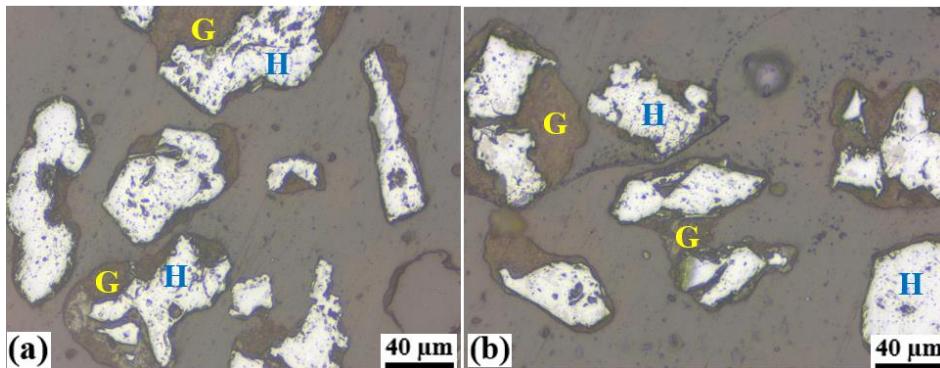
Fig. 4.21: OM images [(a) and (b), Reflected mode, 20x] of feed sample (-150 µm) at two different positions on the specimen surface. Hematite (H); alumina-associated silica (G).
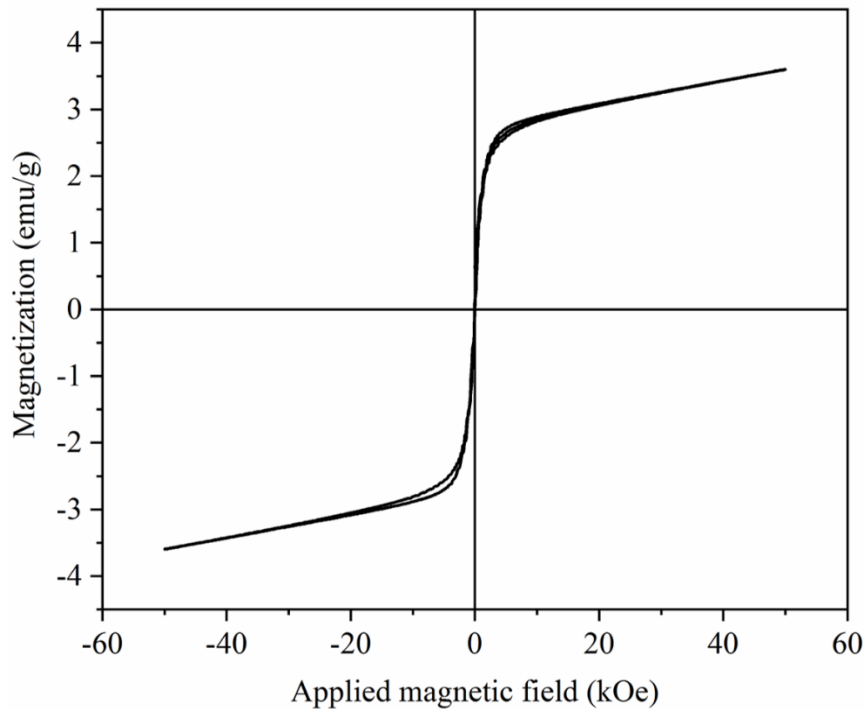
Fig. 4.22: Hysteresis curve of feed sample (-150 µm).

4.4.2 Design of Experiments (DOE)

4.4.2.1 Taguchi method

The experiments were carried out in lab-scale PRMS as per the DOE (Taguchi-based L_{27} orthogonal array). Table 4.5 summarizes the influence of selected parameters (feed rate, roller/roll speed, and belt thickness) on the Fe grade, and recovery %. Fig. 4.23 (a) to (f) and 4.24 (a) to (f) shows the interaction plot, which represents the variation of Fe grade and recovery %, respectively about feed rate, roll speed, and belt thickness. From the interaction plot (Fig. 4.23 (a)); it was clear that at 0.04 ton/h there was a very small increment in Fe grade % up to 160 rpm due to the domination of resultant magnetic force over the centrifugal and gravity force which is acting on the ore particles. However, in all other cases i.e. the interaction of feed rate concerning roll speed (Fig. 4.23 (a)) and belt thickness (Fig. 4.23 (b)) shows decreased Fe grade %. Since the feed rate regulates the mineral selectivity by providing necessary retention time and particle flow depth on the magnetic roller surface. However, an increase in feed rate results in the formation of a multilayer particle bed on the belt surface which leads to a decrease in the selectivity of the

particles at a given magnetic field. This decreased selectivity of the particles due to imperfection in the separation reduces the recovery of magnetic product at a higher feed rate as shown in Fig. 4.24 (a) and (b). Also, an increase in the feed rate has increased the friction force between the neighboring particles which reduces the quantity of magnetics at the magnetic product end due to an increase of non-magnetics, resulting in the poor quality of product and separation. Also, the roll speed (Fig. 4.23 (c) and (d)) is a sensitive parameter, which affects the spacing of particles on the belt surface and the time available for separation as the roll speed changes. The change in roll speed affects the centrifugal force acting on the particles, since, the centrifugal force is directly proportional to the square of the angular velocity of the roll, particle mass, and roller radius (Tripathy et al. 2017). Therefore, from Fig. 4.23 (c) and (d) it was observed that there was a decrease in the magnetic product grade as the roll speed increased to 240 rpm. Since, as the roll speed increases, the centrifugal force becomes more dominant along with the reduced particle residence time at the given magnetic field during the separation process, which forces the partial magnetics to pass towards middling and non-magnetic products. Also, Fig. 4.24 (c) and (d) show the better recovery of magnetic product corresponding to 80 rpm, due to the $F_m > F_c + F_g$. Similarly, Fig. 4.23 (e) and (f) indicate the effect on product grade due to the interaction of belt thickness concerning the feed rate and roll speed. From Fig. 4.23 (e) and (f), it was observed that, as the belt thickness increases, there was increased Fe grade % at the magnetic fraction. Since, during the process of separation, the intensity of magnetic force experienced by the particle mainly depends on the correlation between the magnetic force from the magnetic roller surface and the belt thickness (Goolsby and Moore 1997). As the thickness of enfolded belt around the magnetic roller increases, the effective magnetic force required for the particle separation also increases. Therefore, as the magnetic roller revolves, mostly the particle with the utmost magnetic property will adhere to the surface of the belt due to magnetic force and continue to follow around till it leaves the magnetic roller. Then at this point, the magnetic force ceases and an ore particle with the highest magnetic content drops into the collection bin and is called magnetics/concentrate which results in improved product grade and reduced recovery %

(Fig. 4.24 (e) and (f)). Whereas, the decreased belt thickness leads to the parting of weakly magnetic ore particles into a magnetic product result in reduced product grade and increased recovery percentage of the magnetic product.

Even though the interaction plots have indicated a better level of operating parameters to gain the best magnetic products, the impact of each parameter was analyzed through the S/N ratios of each experiment. Therefore, Fig. 4.25 and 4.26 show the main effect plot for S/N ratios of Fe grade and recovery %, respectively. From Fig. 4.25, it was clear that to obtain the highest Fe grade %, the optimum operating parameters for feed rate, roll speed, and belt thickness were 0.04 ton/h (A1), 80 rpm (B1), and 1 mm (C3). Also, from Fig. 4.26, to obtain the highest Fe recovery %, the optimum operating parameters for feed rate, roll speed, and belt thickness were 0.04 ton/h (A1), 80 rpm (B1), and 0.5 mm (C1). However, the highest Fe grade and Fe recovery % could not be obtained under the same optimum operating conditions. Since, Fe grade and Fe recovery % were inversely proportional to each other i.e., as the Fe grade % falls the Fe recovery % increases and vice versa (Rayapudi et al. 2019). Further to check the significance of selected operating parameters and to recognize the effect of parameters on response variables the ANOVA method was adopted based on a 95% confidence interval.

Table 4.5: Experimental results of Fe grade and Fe recovery %.

Experiment No.	Feed rate (ton/h)	Roller speed (rpm)	Belt thickness (mm)	Magnetic product	
				Fe grade %	Fe recovery %
1	0.04	80	0.50	54.6	81.13
2	0.04	80	0.75	55.66	68.40
3	0.04	80	1.00	56.19	46.22
4	0.04	160	0.50	55.14	80.10
5	0.04	160	0.75	55.46	61.30
6	0.04	160	1.00	55.94	34.95
7	0.04	240	0.50	54.1	75.57
8	0.04	240	0.75	55.19	48.80

9	0.04	240	1.00	55.78	26.32
10	0.08	80	0.50	53.8	68.88
11	0.08	80	0.75	55.42	62.33
12	0.08	80	1.00	56.1	38.49
13	0.08	160	0.50	54.1	64.20
14	0.08	160	0.75	55.23	53.82
15	0.08	160	1.00	55.63	28.36
16	0.08	240	0.50	52.9	36.25
17	0.08	240	0.75	55.1	29.17
18	0.08	240	1.00	55.66	21.66
19	0.12	80	0.50	52.5	64.63
20	0.12	80	0.75	55.29	55.02
21	0.12	80	1.00	55.94	34.85
22	0.12	160	0.50	53.02	55.10
23	0.12	160	0.75	55.11	33.35
24	0.12	160	1.00	55.38	10.83
25	0.12	240	0.50	51.96	24.09
26	0.12	240	0.75	55.08	13.09
27	0.12	240	1.00	55.22	3.32
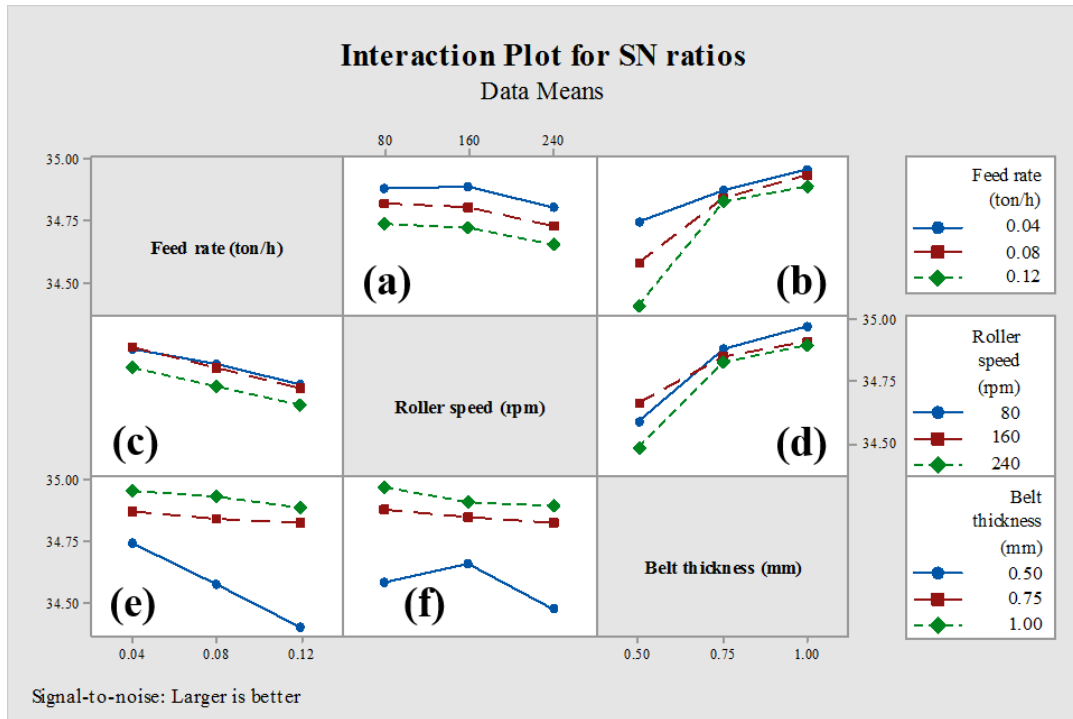
Fig. 4.23: Interaction plot for Fe grade %.
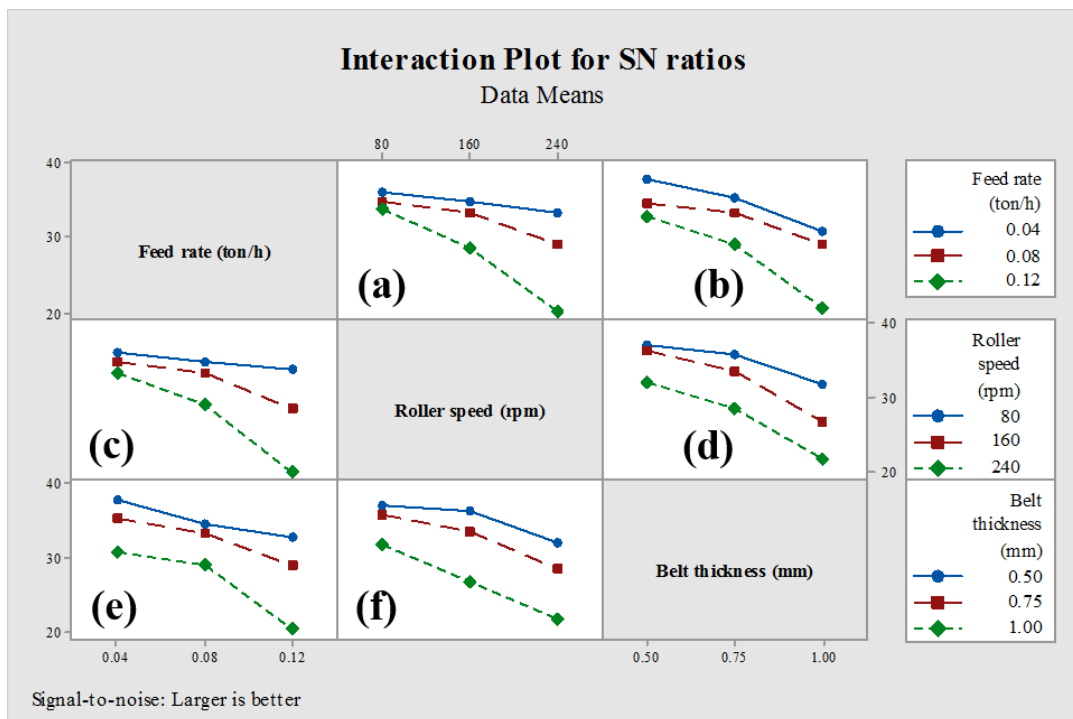
Fig. 4.24: Interaction plot for Fe recovery %.
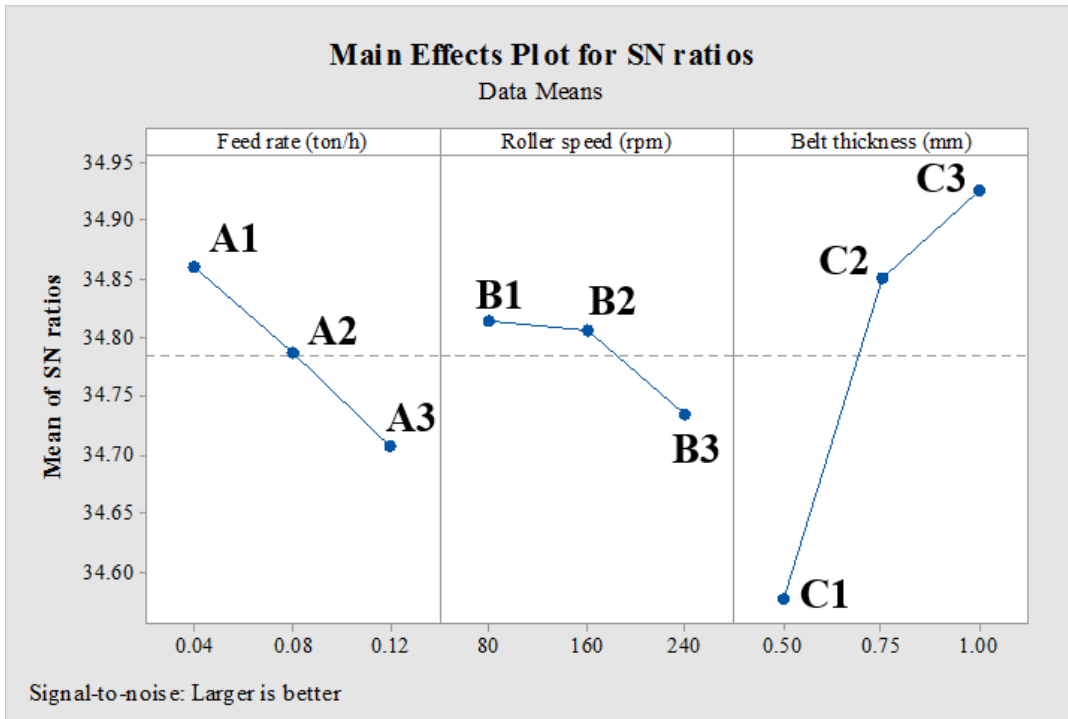
Fig. 4.25: Main effects plot for Fe grade %.
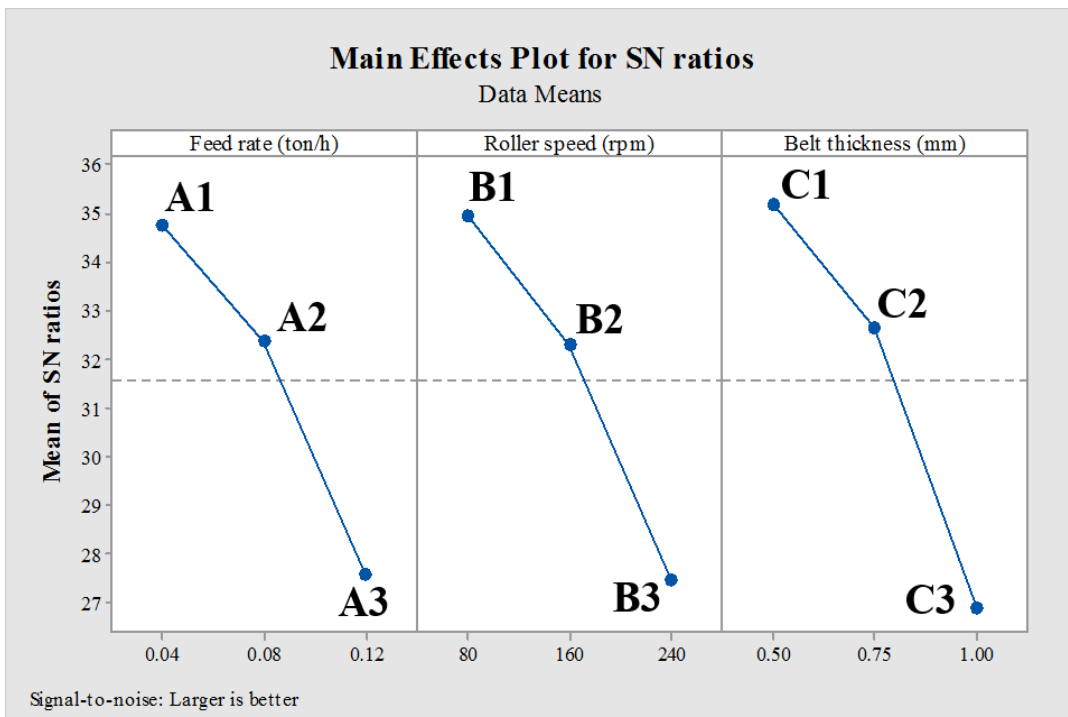
Fig. 4.26: Main effects plot for Fe recovery %.

4.4.2.2 ANOVA method

The significance of the parameter was statistically analyzed by using ANOVA. Tables 4.6 and 4.7 represent the ANOVA results for Fe grade and Fe recovery %. The results show the significance level of operating parameters affecting the response variable. From Table 4.6 and 4.7, the adjusted sum of squares (Adj SS), adjusted Mean Squared Errors (Adj MS), and Fisher's value (F-value) was more for belt thickness as compared to feed rate and roll speed. This shows that the belt thickness is the most significant parameter for Fe grade and Fe recovery %. Also, in Table 4.6 and 4.7, the Probability of significance value (P-value) for all the parameters was <0.05 which shows the developed ANOVA model is valid.

Table 4.6: ANOVA for Fe grade %.

Source	Degrees of Freedom	Adj SS	Adj MS	F-Value	P-Value
Feed rate	2	4.073	2.036	9.40	0.001
Roll speed	2	1.361	0.680	3.14	0.065
Belt thickness	2	23.894	11.947	55.15	0.000

Table 4.7: ANOVA for Fe recovery %.

Source	Degrees of Freedom	Adj SS	Adj MS	F-Value	P-Value
Feed rate	2	2903	1451.54	28.06	0.000
Roll speed	2	3284	1641.90	31.76	0.000
Belt thickness	2	5224	2611.81	50.49	0.000

4.4.3 Validation of developed statistical (ANOVA) model

Based on the experimental results, the statistical model for Fe grade and recovery % was developed using ANOVA methodology. It was seen that the regression coefficient of the developed statistical model for Fe grade and Fe recovery % was 87.13 and 91.69%, respectively. Although the high value of the regression coefficient shows that the developed model was accurate, further validation of the developed statistical model was carried out using a normal probability plot. Fig. 4.27 and 4.28 show the normal probability

plot of Fe grade and recovery %, respectively. However, from Fig. 4.27 and 4.28, it was found that the predicted values almost form a straight line. This shows that the predicted value of both (Fe grade and recovery %) the model was normally distributed and independent of each other, which indicates that the developed statistical model of Fe grade and recovery % was valid and accurate. Moreover, the closeness in regression coefficient and normal probability plot shows the highest correlation between experimental and predicted results.
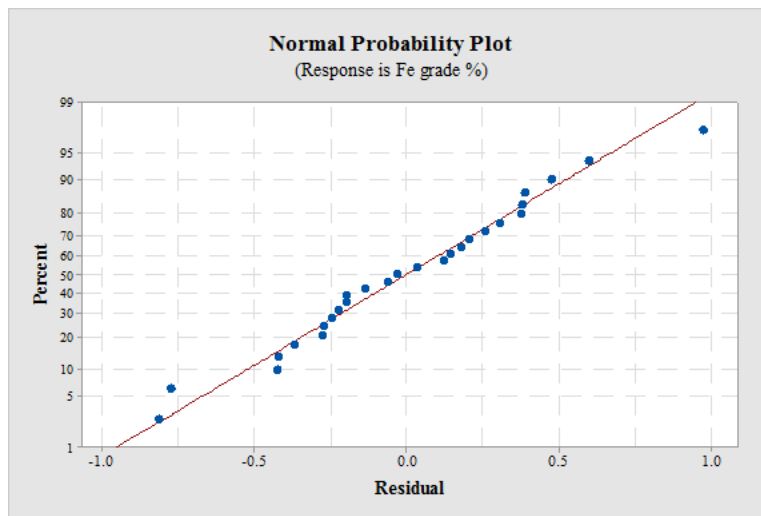
Fig. 4.27: Normal probability plot for Fe grade %.
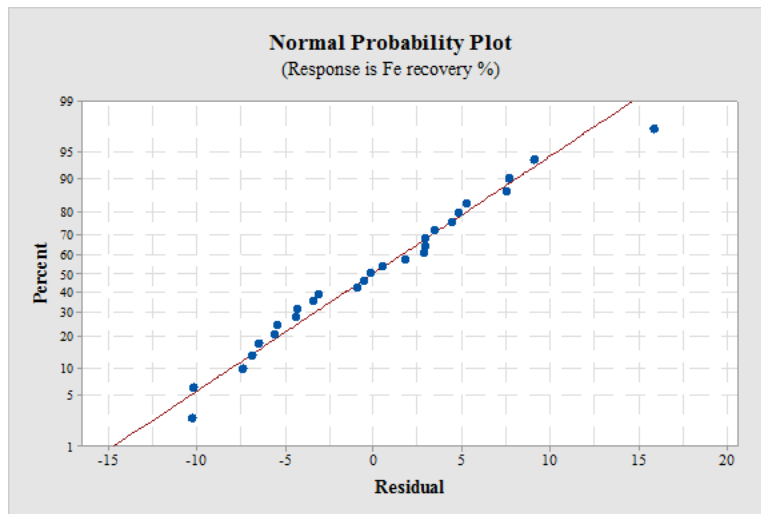
Fig. 4.28: Normal probability plot for Fe recovery %.

4.4.4 Confirmation test/Model validation test

The discussion made in the previous section 4.4.2.1 along with Fig. 4.27 and 4.28 it was clear that the optimized condition for Fe grade % was feed rate (A1), roll speed (B1), and belt thickness (C3) was set at 0.04 ton/h, 80 rpm, and 1 mm, respectively. Whereas the optimized condition for Fe recovery % was feed rate (A1), roll speed (B1), and belt thickness (C1) was set at 0.04 ton/h, 80 rpm, and 0.5 mm, respectively. The confirmation tests were carried out for these optimized conditions (A1-B1-C3 and A1-B1-C1) and were correlated with the predicted results for validation.

Tables 4.8 and 4.9 show the average value of five experimental trails obtained for optimal setting of Fe grade and recovery % compared with the predicted results. Also, Tables 4.8 and 4.9 indicate the closeness between the predicted and experimental results in terms of error %. Meanwhile, the indicated closeness of the results (predicted and experimental results) endorses the statistical relationship between the response variable (Fe grade and recovery %) and selected parameters (feed rate, roll speed, and belt thickness) were in good agreement.

Table 4.8: Confirmation test and predicted results of Fe grade %.

Response	Optimal combination of parameters		Error %
	Predicted (A1-B1-C3)	Experimental (A1-B1-C3)	
Fe grade %	56.41	56.17	0.42

Table 4.9: Confirmation test and predicted results of Fe recovery %.

Response	Optimal combination of parameters		Error %
	Predicted (A1-B1-C1)	Experimental (A1-B1-C1)	
Fe recovery %	86.57	81.94	5.65

4.4.5 Evaluation of separated products (magnetic, middling, and non-magnetic) through characterization studies

The comparison of Tables 4.8 and 4.9 shows that A1-B1-C3 and A1-B1-C1 are optimal setting parameters for Fe grade and recovery %. However, in both optimal setting

parameters, the belt thickness (i.e., C3 and C1) is the most influencing parameter for Fe grade and recovery %. Also, from Table 4.5, it was found that the difference in Fe grade % between Experiment No. 3 (A1-B1-C3) and Experiment No. 1 (A1-B1-C1) was less i.e., 1.59%. Whereas, the difference in Fe recovery % between Experiment No. 3 and Experiment No. 1 was significantly high i.e., 35.80%. Therefore, in conjunction with Fe grade and recovery %, the separated products which were obtained under the optimized condition of A1-B1-C1 were found to be better and taken into account for the evaluation through XRD, OM, and magnetic susceptibility study.

The XRD analysis of separated products was shown in Fig. 4.29. By comparing the magnetic product with middling and non-magnetic products (Fig. 4.29) it is clear that the hematite peak intensity of the magnetic product was increased while the peak intensity of gangue mineral phases was approximately disappeared. This increased peak intensity indicates the supremacy of the hematite phase in the magnetic products due to the closer dissociation of gangue minerals after the magnetic separation (Liu et al. 2019; Omran et al. 2014). In addition, based on the peak intensity (Fig. 4.29), the semi quantitative analysis of mineral phases present in the separated products was performed. The approximate % of mineral phases present in the separated products was calculated from the refined data and shown in Table 4.10. The results shows that, the abundance of hematite phase in the separated products follows the order of magnetics > middlings > non-magnetics. Whereas the dominance of gangue mineral phases in the separated products follows the reverse order i.e., non-magnetics > middlings > magnetics.

Moreover, based on the confirmation from the XRD study, the distribution of the iron-bearing mineral phase in the separated products was observed under OM. Fig. 4.30 shows the analysis of the separated product via the OM study. From Fig. 4.30 (a) and (b) (magnetic), it was found that there is major dissemination of hematite phase in the magnetic product as compared to middling (Fig. 4.30 (c) and (d)) and non-magnetic (Fig. 4. 30 (e) and (f)) products. This indicates the existence of a higher % of Fe in the magnetic product. Whereas, in both non-magnetic and middlings the existence of a major portion of gangue

in the form of alumina-associated silica mineral phase quashes the occurrence of hematite phase. Hence, both non-magnetic and middling products consist of lower Fe %.

Also, the variation in magnetic properties of separated products corresponding to the applied magnetic field is shown in Fig. 4.31. From Fig. 4.31, it was found that the hysteresis loop shows the linear affirmative increase in saturation magnetization value (6.3 emu/g) for the magnetic product. The increase in saturation magnetization value is due to the occurrence of high Fe content in the magnetic product compared to middling and non-magnetic products. Therefore, as expected, the hysteresis loop for middling and non-magnetic shows a decrease in saturation magnetization value of 3.6 and 1.8 emu/g, respectively.

All these results indicate that the magnetic separation under optimized parametric condition (A1-B1-C1) using newly designed lab-scale PRMS effectively facilitates the improvement in Fe content of low grade hematite ore with the best recovery. Since the evaluation of separated products through characterization studies indicates the notable improvement of the iron-bearing mineral phase in the magnetic products.
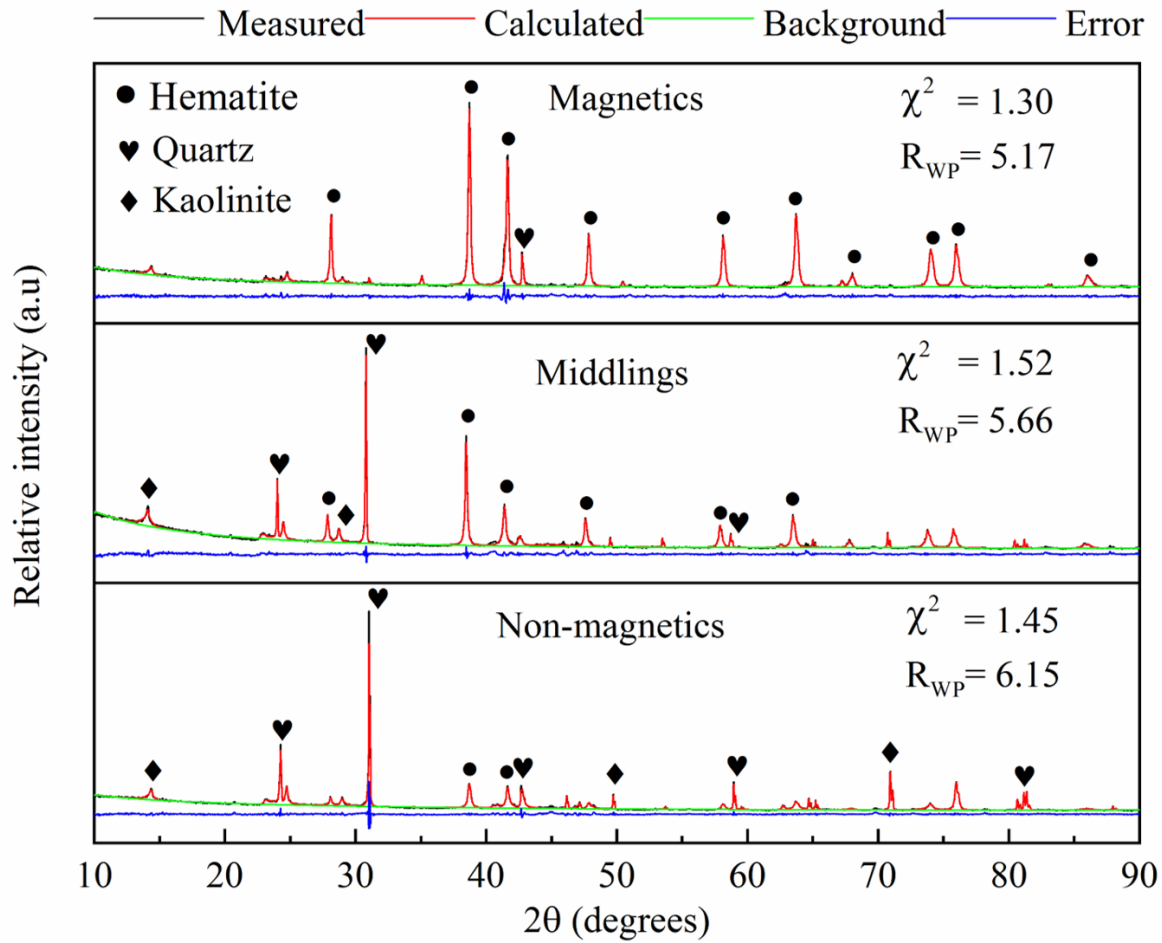
Fig. 4.29: XRD pattern of separated products.

Table 4.10: Semi quantitative analysis of separated products.

Separated products	Hematite (%)	Quartz (%)	Kaolinite (%)
Magnetic	65	17	18
Middling	42	35	23
Non-magnetic	10	79	11
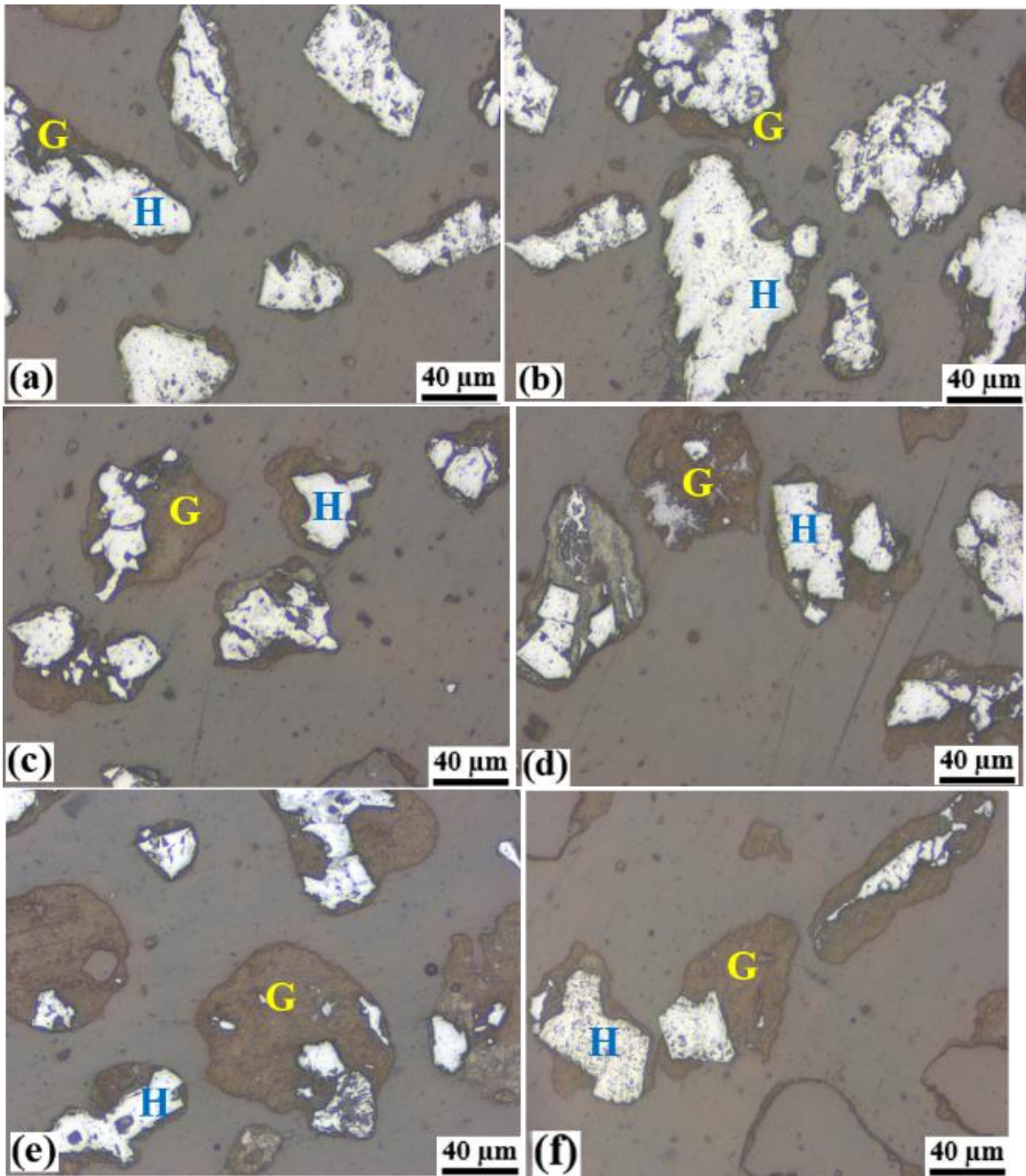
Fig. 4.30: OM images (Reflected mode, 20x) of separated products at two dissimilar positions on the surface of specimen (a) & (b)- magnetic product, (c) & (d)- middling product, and (e) & (f)- non-magnetic product.
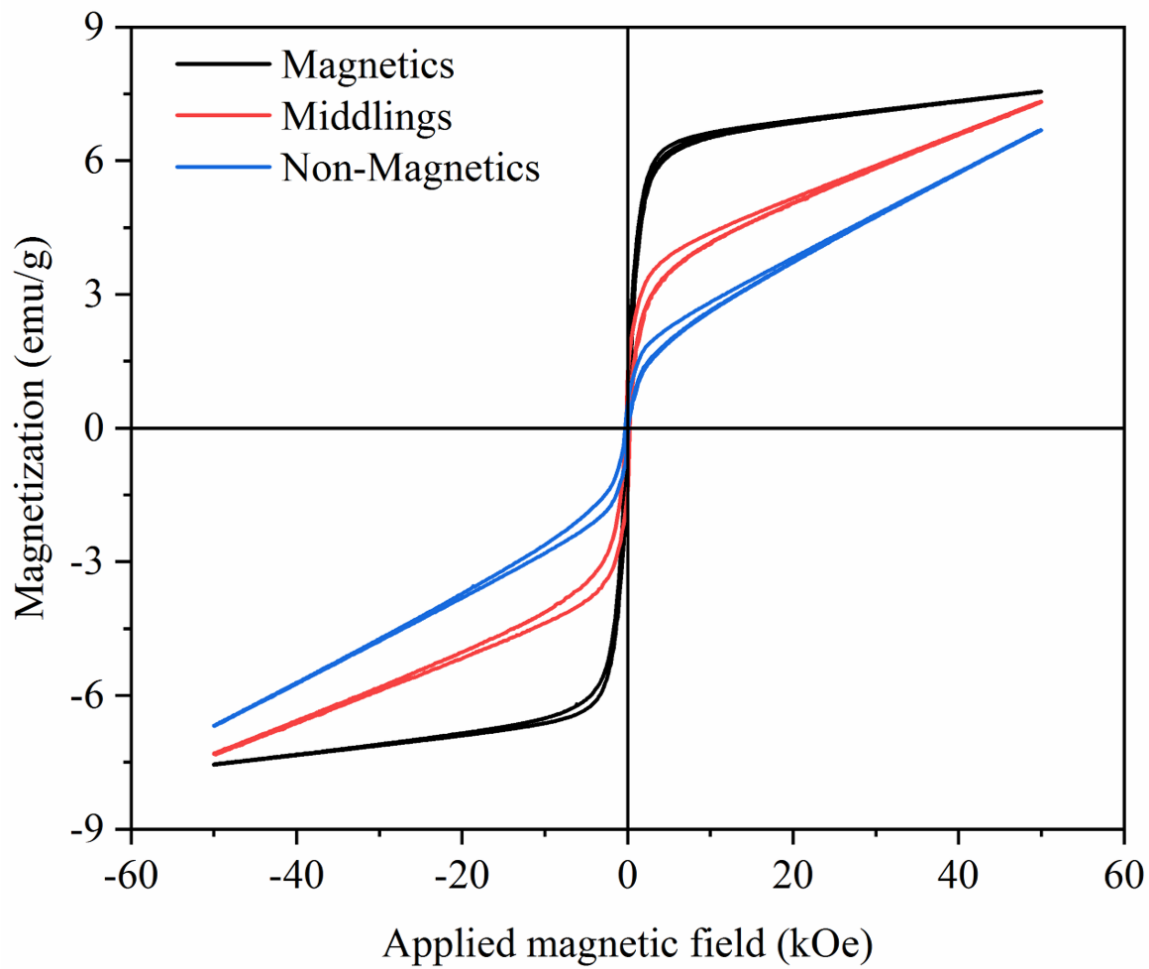
Fig. 4.31: Hysteresis curve of separated products.

CHAPTER 5

CONCLUSIONS AND SCOPE OF FUTURE WORK

5.1 Conclusions

In the present work, based on the investigations carried out in terms of samples characterization, numerical approach, and its validation for designing of an optimized magnetic roller, development of new lab-scale PRMS, and optimization of its operating parameters, the following conclusions have been drawn.

- Here, the new lab-scale PRMS was developed using an optimized magnetic roller to overcome the drawbacks of water and power consumption in mineral processing to improve the Fe content of lower grade iron ore samples. Since PRMS involves a dry separation process under a permanent magnetic field.

- The characterization studies of as-received samples in terms of XRD and OM study reveal the presence of hematite as Fe bearing mineral phase along with associated gangue mineral phases (quartz and kaolinite). Additionally, the magnetic susceptibility study confirms the paramagnetic nature of the samples in terms of linear positive increase in magnetization along with lower magnetic saturation against the applied magnetic field strength.

- The FEMM analysis indicates that, the M: S ratio of 5 mm: 2.5 mm was found effective as compared to 5 mm: 5 mm and 5 mm: 1.25 mm M: S ratios. Since its rate of decrease in force index and magnetic force value in B_2 direction is comparatively less.

- ANN modelling and validation of FEMM data clearly shows that the feed-forward backpropagation network was an optimal model for the prediction analysis of FEMM data. The experimental approach shows the fabricated PRMS using an optimized magnetic roller (M: S=5 mm: 2.5 mm) was suitable for processing of paramagnetic minerals ≤1500 μm because of the better magnetism configuration (i.e., 0.89 to 2.59 T from the roller surface).

- In DOE, the experimental and statistical results indicate that Fe grade and recovery % are majorly get affected by belt thickness compared to roller speed and feed rate. Since the F-test value for belt thickness is highest compared to feed rate and roller speed.

- The closeness of confirmation test results (56.17% and 81.94%) and predicted results (56.41% and 86.57%) for Fe grade and recovery % respectively, endorses that the obtained result was accurate and valid.

- The quality assessment of optimized (A1-B1-C1) separated products through XRD, OM, and magnetic susceptibility study confirms that the magnetic product contains high Fe content compared to the middling and non-magnetic products.

- Finally, the optimum operating parameters of new lab-scale PRMS gives a maximum Fe grade of 56.17 % at A1-B1-C3 (0.04 ton/h, 80 rpm and 1 mm) and maximum recovery of 81.94 % at A1-B1-C1 (0.04 ton/h, 80 rpm, and 0.5 mm) from a feed assay of 46.95% Fe.

5.2 Scope of future work

- The effect of magnet-to-steel disk thickness ratio on magnetism configurations using different grade and type magnetic materials for different M: S ratios will be investigated using the FEMM approach.

- Experimental investigations can be carried out on lead-zinc ore (Khetri deposit, India) to separate the magnetic impurities (biotite group minerals), by doing so, the ore quality will get improved. Since, from the preliminary study, the presence of biotite group minerals in the lead-zinc ore was confirmed. Also, the use of magnetic separation technology for the enrichment of lead-zinc ore has nowhere been reported.

- Experimental investigations can be carried out for desulfurization and deashing of low-rank lignite coals from various parts of India such as Tamil Nadu, Puducherry, Kerala, Gujarat, Rajasthan, and Jammu & Kashmir. Since the previous study done by Celik and Yildirim (2000) on lignite coal (Turkey) by considering the process route involving low-temperature carbonization followed by dry magnetic

separation shows that a good amount of desulfurization and deashing was achieved. Therefore, a systematic study on lignitic coals from various parts of India should be studied using newly designed lab-scale PRMS.

LIST OF PUBLICATIONS

1. **Mohanraj G. T**., Krishneindu P., Choudhary, R. P., Meena S. S., Yusuf S. M., **M R Rahman** (2019). "Mineralogical studies of low grade iron ore from Bellary-Hospet region, India." *AIPC*, 2087(1), 020012, Impact Factor- 0.40 (SCOPUS).

2. **Mohanraj, G. T.**, **Rahman, M. R.,** Joladarashi, S., Hanumanthappa, H., Shanmugam, B. K., Vardhan, H., & Rabbani, S. A. (2021). "Design and fabrication of optimized magnetic roller for permanent roll magnetic separator (PRMS): Finite element method magnetics (FEMM) approach." *Advanced Powder Technology*, 32(2), 546-564, Elsevier, Impact Factor - 4.83 (SCIE).

3. **Mohanraj, G. T., Rahman, M. R.,** Arya, S. B., Barman, R., Krishnendu, P., & Meena, S. S. (2021). "Characterization study and recovery of copper from low grade copper ore through hydrometallurgical route." *Advanced Powder Technology*, 33(1), 103382, Elsevier, Impact Factor - 4.83 (SCIE),

4. **Mohanraj, G. T.,** Joladarashi, S., Hanumanthappa, H., Shanmugam, B. K., Vardhan, H., Gajanan M Naik., Devadas Bhat, P., & **Rahman, M. R.** "Numerical Approach for Optimization of Magnetic Roller and Evaluating the Performance of Permanent Magnet Roller Separator through Design of Experiment" *Alexandria Engineering Journal*, Elsevier (Revision submitted), Impact Factor – 3.73 (SCIE).

REFERENCES

Akbar, A. R., and Awang, M. (2014). "Performance prediction of inertial auto-reinforce magnetic flywheel energy storage device using finite element magnetic modeling." *Appl. Mech. Mater.*, 663, 169–174.

Al-Sharif, L., Taifour, S., and Kilani, M. (2010). "Simulation and verification of the axial force of a linear permanent magnet synchronous actuator." *Int. J. Appl. Electromagn. Mech.,*32, 249-265.

Alp, I. (2009). "Application of magnetic separation technology for the processing of a colemanite ore." *J. South. African Inst. Min. Metall.*, 109(2), 139–145.

Altiner, M. (2019). "Upgrading of iron ores using microwave assisted magnetic separation followed by dephosphorization leaching." *Can. Metall. Q.*, 58(4), 445–455.

Altiner, M. (2020). "Roasting of a Low-Grade Goethite Ore Using Horse Residue and Its Beneficiation by Magnetic Separation." *Mining, Metall. Explor.*, 37(4), 1357–1365.

Andreachi, J. R., and Palasvirta, O. E. (1965). "Magnetic separators." *Candian Patent Number 711911*.

Angadi, S. I., Jeon, H. S., Mohanthy, A., Prakash, S., and Das, B. (2012). "Analysis of Wet High-Intensity Magnetic Separation of Low-Grade Indian Iron Ore using Statistical Technique." *Sep. Sci. Technol.*, 47(8), 1129–1138.

Arvidson, B. R. (1999). "Advances in rare earth magnetic drum separators for heavy minerals sand processing." *SAIMM Heavy Minerals Conference*, Durban, South Africa., 121-124.

Arvidson, B. R., and Norrgran, D. (2014). "Magnetic separation." *Miner. Process. Extr. Metall. 100 Years Innov.*, 223–233.

Aznarte, J. L., Molina, D., Sánchez, A. M., and Benítez, J. M. (2011). "A test for the homoscedasticity of the residuals in fuzzy rule-based forecasters." *Appl. Intell.*, 34(3), 386–393.

Babu, N., Vasumathi, N., and Rao, R. B. (2009). "Recovery of Ilmenite and Other Heavy Minerals from Teri Sands (Red Sands) of Tamil Nadu, India." *J. Miner. Mater. Charact. Eng.*, 8(2), 149–159.

Baltzis, K. B. (2010). "The finite element method magnetics (FEMM) freeware package: May it serve as an educational tool in teaching electromagnetics." *Educ. Inf. Technol.*, 15(1), 19–36.

Bhagat, R. P., Banerjee, B., Saha, P., and Mukherjee, B. C. (2006). "Dry Magnetic Separation of Bauxite Ore." *Proc. Int. Semin. Miner. Process. Technol. Indo-Korean Work. Resour. Recycl.*, 328–333.

Bhandari, V. B. (2003). *"Design of Machine Elements."* 8th ed., Tata McGraw Hill.

Bhoja, S. K., Tripathy, S. K., Murthy, Y. R., Ghosh, T. K., Raghu Kumar, C., and Chakraborty, D. P. (2021). "Influence of mineralogy on the dry magnetic separation of ferruginous manganese ore-a comparative study." *Minerals*, 11(2), 1–20.

Çelik, M. S. (2002). "Dry cleaning of low-rank coals by low temperature carbonization and magnetic separation." *Coal Prep.*, 22(6), 311–322.

Çelik, S., and Tan, Ö. (2005). "Determination of preconsolidation pressure with artificial neural network." *Civ. Eng. Environ. Sci.*, 22(4), 217–231.

Chakravorty,N. (1989). *"Magnetic Separation."* avilable at http://eprints.nmlindia.org/4662/1/11-_N_Chakravorty.PDF

Chaurasia, R. C., and Nikkam, S. (2017). "Application of artificial neural network to study the performance of multi-gravity separator (MGS) treating iron ore fines." *Part. Sci. Technol.*, 35(1), 93–102.

Chokshi, Y., and Dutta, S. K. (2014). "Processing of Low Grade Iron Ore Fines and Utilisation by Pelletization." *Iron Ore Pelletization*, 58(192), 1–5.

Corte, C. da, Bergmann, C., and Woollacott, L. (2019). "Improving the separation efficiency of Southern African haematite from slimes through selective flocculation

coupled with magnetic separation." *J. South. African Inst. Min. Metall.*, 119(11), 963–972.

Dahlin, D. C., and Rule, A. R. (1993). *"Magnetic susceptibility of minerals in high magnetic fields." Report of investigation (United states. Bureau of mines)*, Vol. 9449.

David, M. (2014). *"Finite Element Method Magnetics : ComputationalMagneticsLinks."*

Dean, R. S., and Davis, C. W. (1941). "Magnetic Separation of Ores." *US Bureau of Mines Bulletin 425,* Washington D.C., pp. 417.

Deosarkar, M. P., and Sathe, V. S. (2012). "Predicting effective viscosity of magnetite ore slurries by using artificial neural network." *Powder Technol.*, 219, 264–270.

Derikvand, Z. (2015). "Design of a drive for a belt conveyor system." *Thesis,* Czech Technical University, Prague

Dorofki, M., Elshafie, A.H., Jaafar, O., Karim, O.A. and Mastura, S. (2012). "Comparison of artificial neural network transfer functions abilities to simulate extreme runoff data." *Int. Proc. Chem. Biol. Environ. Eng.,* 33, 39-44.

Dunlop, F. (2009). "*Conveyor Handbook.*" Conveyor Belting in Australia.

Dwari, R. K., Rao, D. S., and Reddy, P. S. R. (2013). "Magnetic separation studies for a low grade siliceous iron ore sample." *Int. J. Min. Sci. Technol.*, 23(1), 1–5.

Dwari, R. K., Rao, D. S., and Reddy, P. S. R. (2014). "Mineralogical and Beneficiation Studies of a Low Grade Iron Ore Sample." *J. Inst. Eng. Ser. D*, 95(2), 115–123.

Das, B., Mohanty, J. K., Reddy, P. S. R.,and Ansari, M. I. (1997). *"Characterisation and beneficiation studies of charge chrome slag." Scand. J. Metall.*, 26(4), 153-157.

Fraas, F. (1973). *"Alternating current matrix-type magnetic separator." US Bureau of Mines Report of Investigations*, Vol. 7746.

Ge, W., Encinas, A., Araujo, E., and Song, S. (2017). "Magnetic matrices used in high gradient magnetic separation (HGMS): A review." *Results Phys.*, 7, 4278–4286.

Gehauf, R. (2004). "A practical guide on selecting and optimizing rare earth magnetic separators. " *SME Annual Meeting*, Denver,USA.

Goolsby, T. L., and Moore, H. F. (1997). "Development of FCC catalyst magnetic separation." *Sep. Sci. Technol.*, 32(1–4), 655–668.

Grieco, G., Kastrati, S., and Pedrotti, M. (2014). "Magnetic enrichment of braunite-rich manganese ore at different grain sizes." *Miner. Process. Extr. Metall. Rev.*, 35(4), 257–265.

Hamzeh Amiri, S. (2019). "Investigation of Efficiency of Magnetic Separation Methods for Processing of Low-Grade Iron Pigments Ore (RED Ochre)." *Int. J. Miner. Process. Extr. Metall.*, 4(1), 18.

Hanumanthappa, H., Vardhan, H., Mandela, G. R., Kaza, M., Sah, R., and Shanmugam, B. K. (2020). "A comparative study on a newly designed ball mill and the conventional ball mill performance with respect to the particle size distribution and recirculating load at the discharge end." *Miner. Eng.*, 145, 106091.

Herskovitch, D., and Lin, I. J. (1996). "Upgrading of raw perlite by a dry magnetic technique" *Miner. Eng. Res. Cent.*, 7(3), 145–161.

Hosseini, S. H., and Samanipour, M. (2015). "Prediction of final concentrate grade using artificial neural networks from Gol-E-Gohar iron ore plant." *Proc. 24th Int. Min. Congr. Turkey, IMCET*, 3(3), 783–787.

Hsu, D. A. (1977). "Tests for Variance Shift at an Unknown Time Point." *Appl. Statist.*, 26(3), 279-284.

Ibrahim, S. S., Farahat, M. M., and Boulos, T. R. (2017). "Optimizing the performance of the RER magnetic separator for upgrading silica sands." *Part. Sci. Technol.*, 35(1), 21–28.

Ibrahim, S. S., Mohamed, H. A., and Boulos, T. R. (2002). "Dry Magnetic Separation of Nepheline Syenite Ores." *Physicochem. Probl. Miner. Process.*, 36(1), 173–183.

IBM (2018). *"Indian Minerals Yearbook 2017 (Part- III: Mineral Reviews)."* 56th edition:

IRON ORE.

Jena, S. K., Sahoo, H., Rath, S. S., Rao, D. S., Das, S. K., and Das, B. (2015). "Characterization and processing of iron ore slimes for recovery of iron values." *Miner. Process. Extr. Metall. Rev.*, 36(3), 174–182.

Jiles, D. (2015). *"Introduction to magnetism and magnetic materials."* CRC press.

John, J. A., and Draper, N. R. (1980). "An Alternative Family of Transformations." *Appl. Stat.*, 29(2), 190-197.

Jordens, A., Sheridan, R. S., Rowson, N. A., and Waters, K. E. (2014). "Processing a rare earth mineral deposit using gravity and magnetic separation." *Miner. Eng.*, 62, 9–18.

Jorjani, E., Asadollahi Poorali, H., Sam, A., Chehreh Chelgani, S., Mesroghli, S., and Shayestehfar, M. R. (2009). "Prediction of coal response to froth flotation based on coal analysis using regression and artificial neural network." *Miner. Eng.*, 22(11), 970–976.

Kamran Haghighi, H., Moradkhani, D. and Salarirad, M.M. (2013). "Modeling of synergetic effect of LIX 984N and D2EHPA on separation of iron and zinc using artificial neural network." *Trans. Indian Inst. Met.,* 67(3), 331-341.

Koca, H., Koca, S., and Kockar, O. M. (2000). "Upgrading of Kutahya region lignites by mild pyrolysis and high intensity dry magnetic separation." *Miner. Eng.*, 13(6), 657–661.

Kopp, J. (1984). "Permanent Magnet Disk Separators." *IEEE Trans. Magn.*, 20(5), 1204–1206.

Leaper, M. C., Kingman, S. W., and Seville, J. P. K. (2002). "Application of permanent dry high intensity magnetic separation for the processing of spent FCC catalyst." *Magn. Electr. Sep.*, 11(3), 141–153.

Liu, Y., Jiang, T., Liu, C., Huang, W., Wang, J., and Xue, X. (2019). "Effect of microwave pre-treatment on the magnetic properties of Ludwigite and its implications on magnetic separation." *Metall. Res. Technol.*, 116(1), 107-115.

Makhula, M. J., Falcon, R. M. S., Bergmann, C. P., and Bada, S. O. (2016). "Statistical analysis and concentration of iron ore using Longi LGS 500 WHIMS." *Int. J. Min. Sci. Technol.*, 26(5), 769–775.

Masoumi, M., and Wang, Y. (2016). "Repulsive magnetic levitation-based ocean wave energy harvester with variable resonance: Modeling, simulation and experiment." *J. Sound Vib.*, 381, 192–205.

Moghadassi, A., Parvizian, F., and Hosseini, S. M. (2009) "A new approach based on artificial neural networks for prediction of high pressure vapour-liquid equilibrium." *Aust. J. Basic Appl. Sci.*, 3, 1851.

Naik, G. M., Anjan, B. N., Badiger, R. I., Bellubbi, S., and Kumar Mishra, D. (2021). "An investigation on effects of wire-EDT machining parameters on surface roughness of INCONEL 718." *Mater. Today Proc.*, 35, 474–477.

Nakai, Y., Mishima, F., Akiyama, Y., and Nishijima, S. (2010). "Development of high gradient magnetic separation system under dry condition." *Phys. C Supercond. its Appl.*, 470(20), 1812–1817.

Norrgran, D. A., and Mankosa, M. J. (2006). "Selection and sizing of magnetic concentreating equipment: plant design/layout." *SME Mining Engineers Handbook*, 1069-1093.

Nunna, V., Hapugoda, S., Eswarappa, S. G., Raparla, S. K., Kumar, R., and Nanda, N. K. (2019). "Beneficiation of Low-grade Iron Ore Fines by Using a Circulating-type Air Classifier." *Miner. Process. Extr. Metall. Rev.*, 40(5), 356–367.

Omran, M., Fabritius, T., Elmahdy, A. M., Abdel-Khalek, N. A., El-Aref, M., and Elmanawi, A. E. H. (2014). "Effect of microwave pre-treatment on the magnetic properties of iron ore and its implications on magnetic separation." *Sep. Purif. Technol.*, 136, 223–232.

Order, R. R., Weinstein, R. S., and Snoby, R. J. (2003). "Combined air jig and dry magnetic

separator for cleaning coal." *Twentieth Annul International Pittsburgh Coal Conference*, Pittsburgh, 15-19.

Orhan, E., and Gülsoy, O. (2004). "Importance of magnet-steel configuration in dry high intensity permanent magnetic rolls : theoretical and practical approach." *Physicochem. Probl. Miner. Process.*, 38, 301–306.

Ozcan, O., and Celik, I. B. (2016). "Beneficiation routes for upgrading iron ore tailings with a teetered bed separator." *Sep. Sci. Technol.*, 51(17), 2844–2855.

Özdemir, O., and Çelik, M. S. (2002). "Characterization and recovery of lignitic fly ash byproducts from the Tuncbilek power station." *Can. Metall. Q.*, 41(2), 143–150.

Ozdemir, O., Gupta, V., Miller, J. D., Çinar, M., and Çelik, M. S. (2011). "Production of trona concentrates using high-intensity dry magnetic separation followed by flotation." *Miner. Metall. Process.*, 28(2), 55–61.

Paledi, U., Allahkarami, E., Rezai, B., and Aslani, M. R. (2021). "Selectivity index and separation efficiency prediction in industrial magnetic separation process using a hybrid neural genetic algorithm." *SN Appl. Sci.*, 3(3). 1-10.

Panda, L., Banerjee, P. K., Biswal, S. K., Venugopal, R., and Mandre, N. R. (2014). "Artificial neural network approach to assess selective flocculation on hematite and kaolinite." *Int. J. Miner. Metall. Mater.*, 21(7), 637–646.

Panda, L., and Tripathy, S. K. (2014). "Performance prediction of gravity concentrator by using artificial neural network-a case study." *Int. J. Min. Sci. Technol.*, 24(4), 461–465.

Parmar, S., Ramani, V., Upadhyay, R. V., and Parekh, K. (2018). "Design and development of large radial clearance static and dynamic magnetic fluid seal." *Vacuum*, 156, 325–333.

Pawar, K., and Palhade, R. D. (2015). "Multi-objective Optimization of CNC Turning Process Parameters for High Speed Steel (M2) Using Taguchi and ANOVA Method." *Int. J. Hybrid Inf. Technol.*, 8(4), 67–80.

Ranjit, K., R. (1990). "*A Primer on the Taguchi Method.* ", Copyright by Van Nostrand

Reinhold-USA

Rao, G. V., Markandeya, R., and Sharma, S. K. (2016). "Recovery of Iron Values from Iron Ore Slimes of Donimalai Tailing Dam." *Trans. Indian Inst. Met.*, 69(1), 143–150.

Rath, S. S., Dhawan, N., Rao, D. S., Das, B., and Mishra, B. K. (2016). "Beneficiation studies of a difficult to treat iron ore using conventional and microwave roasting." *Powder Technol.*, 301, 1016–1024.

Rath, S. S., Rao, D. S., and Mishra, B. K. (2016a). "A novel approach for reduction roasting of iron ore slime using cow dung." *Int. J. Miner. Process.*, 157, 216–226.

Rath, S. S., Rao, D. S., Tripathy, A., and Biswal, S. K. (2018). "Biomass briquette as an alternative reductant for low grade iron ore resources." *Biomass and Bioenergy*, 108(November 2017), 447–454.

Rath, S. S., Rao, D. S., Tripathy, S. K., and Biswal, S. K. (2018a). "Characterization vis-á-vis utilization of blast furnace flue dust in the roast reduction of banded iron ore." *Process Saf. Environ. Prot.*, 117, 232–244.

Ray, N., Nayak, D., Dash, N., and Rath, S. S. (2018). "Utilization of low-grade banded hematite jasper ores: recovery of iron values and production of ferrosilicon." *Clean Technol. Environ. Policy*, 20(8), 1761–1771.

Rayapudi, V., and Dhawan, N. (2019). "Microwave Processing of Banded Magnetite Quartzite Ore for Iron Recovery." *Trans. Indian Inst. Met.*, 72(7), 1697–1705.

Rayapudi, V., Agrawal, S., and Dhawan, N. (2019). "Optimization of microwave carbothermal reduction for processing of banded hematite jasper ore." *Miner. Eng.*, 138, 204–214.

Rivera, O., Pavez, O., Kao, J. L., and Nazer, A. (2016). "Metallurgical characterization of kaolin from Atacama, Chile." *REM - Int. Eng. J.*, 69(4), 473–478.

Roe, L. A. (1958). "Advances in magnetic separation of ores." *Mining Engineering,* pp. 1261-1265.

Roy, S. (2009). "Recovery Improvement of Fine Iron Ore Particles by Multi Gravity Separation." *Open Miner. Process. J.*, 2(1), 17–30

Russell, A. (1992). "Magnetic separation-An ever more exacting science." *Industrial Minerals,* 294, 39- 57.

Saeid, A. M., Butcher, D. A., and Rowson, N. A. (1993). "Coal desulphurisation and ash removal in intensified magnetic fields." *Magn. Electr. Sep.*, 4(2), 107–116.

Sah, R. and Dutta, S. K. (2009). "Iron ore-coal composite pellets preparation and their smelting kinetics. " *Proc. of Int. Conf. on Advances in Theory of Ironmaking and Steelmaking,* IISC, Bangalore, pp. 93-100.

Sahoo, A., and Roy, G. K. (2007). "Artificial Neural Network approach to segregation characteristic of binary homogeneous mixtures in promoted gas-solid fluidized beds." *Powder Technol.*, 171(1), 54–62.

Schmelzer, G. (1995). "Separation of metals from waste incineration residue by application of mineral processing." *Proceedings of the XIX International Mineral Processing Congress*, USA., pp. 137-140.

Shanmugam, B. K., Vardhan, H., Raj, M. G., Kaza, M., Sah, R., and Hanumanthappa, H. (2020). "Experimentation and statistical prediction of screening performance of coal with different moisture content in the vibrating screen." *Int. J. Coal Prep. Util.*, pp. 1–14.

Shen, H., and Forssberg, E. (2003). "An overview of recovery of metals from slags." *Waste Manag.*, 23(10), 933–949.

Singh, V. (2009). "Connectionist approach for modeling the dry roll magnetic separator." *Miner. Metall. Process.*, 26(3), 127–132.

Srivastava, M. P., Pan, S. K., Prasad, N., and Mishra, B. K. (2001). "Characterization and processing of iron ore fines of Kiruburu deposit of India." *Int. J. Miner. Process.*, 61(2), 93–107.

Stamboliadis, E. T., and Kailis, G. (2004). "Removal of Limestone from Bauxite by

Magnetic Separation." *Eur. J. Miner. Process. Enviromental Prot.*, 4(2), 84–90.

Suthers, S. P., Pinto, P., Nunna, V., and Nguyen, A. V. (2019). "Experimental Study of Dry Desliming Iron Ore Tailings by Air Classification." *Miner. Process. Extr. Metall. Rev.*, 40(5), 344–355.

Svoboda, J. (2004). *"Magnetic Techniques for the Treatment of Materials."* Kluwer academic publishers, Dordrecht, London.

Svoboda, J., and Fujita, T. (2003). "Recent developments in magnetic methods of material separation." *Miner. Eng.*, 16(9), 785–792.

Taguchi, G. (1987). *"System of Experimental Design."* Vol. 1, Unipub/Kraus International. White Plains, New York.

Taguchi, G., and Konishi. (1987). "Taguchi Methods, orthogonal arrays and linear graphs, tools for quality American supplier institute." *Am. Supplier Inst.*, 8–35.

Tang, H., Qin, Y., and Qi, T. (2016). "Phosphorus Removal and Iron Recovery from High-Phosphorus Hematite Using Direct Reduction Followed by Melting Separation." *Miner. Process. Extr. Metall. Rev.*, 37(4), 236–245.

Tripathy, S. K., Banerjee, P. K., and Suresh, N. (2014). "Separation analysis of dry high intensity induced roll magnetic separator for concentration of hematite fines." *Powder Technol.*, 264, 527–535.

Tripathy, S. K., Singh, V., and Suresh, N. (2015). "Prediction of Separation Performance of Dry High Intensity Magnetic Separator for Processing of Para-Magnetic Minerals." *J. Inst. Eng. Ser. D*, 96(2), 131–142.

Tripathy, S. K., Banerjee, P. K., and Suresh, N. (2015a). "Magnetic separation studies on ferruginous chromite fine to enhance Cr:Fe ratio." *Int. J. Miner. Metall. Mater.*, 22(3), 217–224.

Tripathy, S. K., Mohanty, I., and Filippov, L. O. (2020). "Application of Artificial Neural Networks to Predict Dry Magnetic Separation of Low-Grade Hematite Fines." *Trans.*

Indian Inst. Met., 73(7), 1797–1807.

Tripathy, S. K., Murthy, Y. R., Singh, V., and Suresh, N. (2016). "Processing of Ferruginous Chromite Ore by Dry High-Intensity Magnetic Separation." *Miner. Process. Extr. Metall. Rev.*, 37(3), 196–210.

Tripathy, S. K., Banerjee, P. K., Suresh, N., Murthy, Y. R., and Singh, V. (2017). "Dry High-Intensity Magnetic Separation In Mineral Industry—A Review Of Present Status And Future Prospects." *Miner. Process. Extr. Metall. Rev.*, 38(6), 339–365.

Tripathy, S. K., Singh, V., Rama Murthy, Y., Banerjee, P. K., and Suresh, N. (2017a). "Influence of process parameters of dry high intensity magnetic separators on separation of hematite." *Int. J. Miner. Process.*, 160, 16–31.

Tušek, J., Zupan, S., Šarlah, A., Prebil, I., and Poredoš, A. (2010). "Development of a rotary magnetic refrigerator." *Int. J. Refrig.*, 33(2), 294–300.

Waters, K. E., Rowson, N. A., Greenwood, R. W., and Williams, A. J. (2007). "Characterising the effect of microwave radiation on the magnetic properties of pyrite." *Sep. Purif. Technol.*, 56(1), 9–17.

Wells, I. S., and Rowson, N. A. (1992). "Application of Rare Earth Magnets in Mineral Processing." *Magn. Electr. Sep.*, 3(2), 105–111.

Wills, B. A., and Finch, J. A. (2015). *"Wills' mineral processing technology: An introduction to the practical aspects of ore treatment and mineral recovery."* Butterworth-Heinemann.

Yamamoto, M. F. (2013). "A process and system for dry recovery of iron-ore fines and superfines in a magnetic separation unit." *WO2013/138889 A1*.

Yang, C., Li, S., Zhang, C., Bai, J., and Guo, Z. (2018). "Application Of Superconducting High Gradient Magnetic Separation Technology On Silica Extraction From Iron Ore Beneficiation Tailings." *Miner. Process. Extr. Metall. Rev.*, 39(1), 44–49.

Yaniv, I. (1981). "Magnetic separators." *South African Patent Application No., 814271.*

Yardley, E. D., and Stace, L. R. (2008). *"Belt conveying of minerals."* Woodhead Publishing Limited, Cambridge.

Yildinm, I., Yiice, H., Onal, G., and Celik, M. S. (1996). "Upgrading of low-rank semi-coked lignite by high intensity dry magnetic separator." Proceeding of changing scopes in mineral processing, Rotterdam, pp. 137-142.

Youssef, M. A., El-rahman, M. K. A., Helal, N. H., Rabiei, M. M. E., and Elsaidy, S. R. (2009). "Optimization of Shaking Table and Dry Magnetic Separation on Recovery of Egyptian Placer Cassiterite Using Experimental Design Technique." *Journal of ore dressing*, 11(22), 1.

Yu, J., Han, Y., Li, Y., Gao, P., and Sun, Y. (2017). "Separation and recovery of iron from a low-grade carbonate-bearing iron ore using magnetizing roasting followed by magnetic separation." *Sep. Sci. Technol.*, 52(10), 1768–1774.

Yu, J., Han, Y., Li, Y., and Gao, P. (2017a). "Beneficiation of an iron ore fines by magnetization roasting and magnetic separation." *Int. J. Miner. Process.*, 168, 102–108.

Yunus, M., and Alsoufi, M. S. (2016). "Multi-output optimization of tribological characteristics control factors of thermally sprayed industrial ceramic coatings using hybrid Taguchi-grey relation analysis." *Friction*, 4(3), 208–216.

FEMM-2D meshed models

1. FEMM-2D meshed model with assigned properties of M: S = 5 mm: 5 mm (Fig. I. 1 (a) and (b)), Number of nodes and elements are 7195 and 13861, respectively.

Fig. I. 1 (a): Actual scale (M: S = 5 mm: 5 mm).

Fig. I. 1 (b): Magnified scale (M: S = 5 mm: 5 mm).

2. FEMM-2D meshed model with assigned properties of M: S = 5 mm: 2.5 mm (Fig. I. 2 (a) and (b)), Number of nodes and elements are 7501 and 14486, respectively.
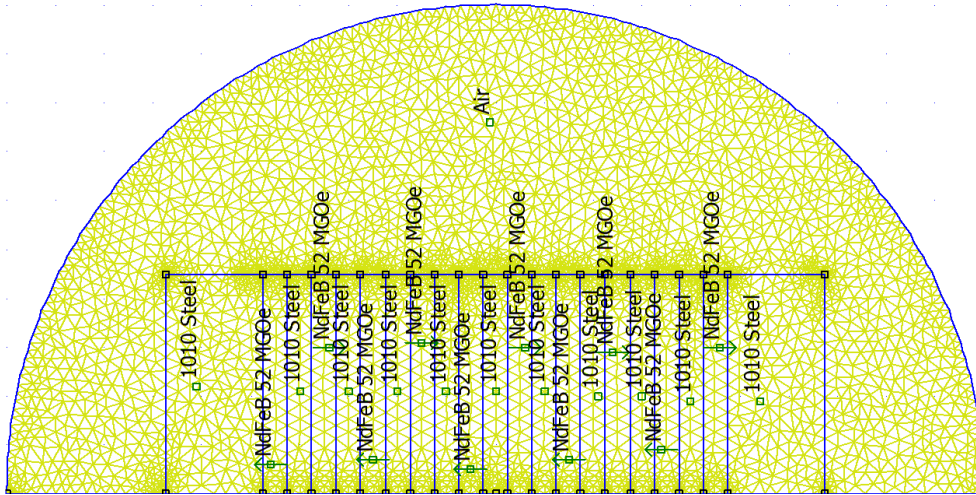

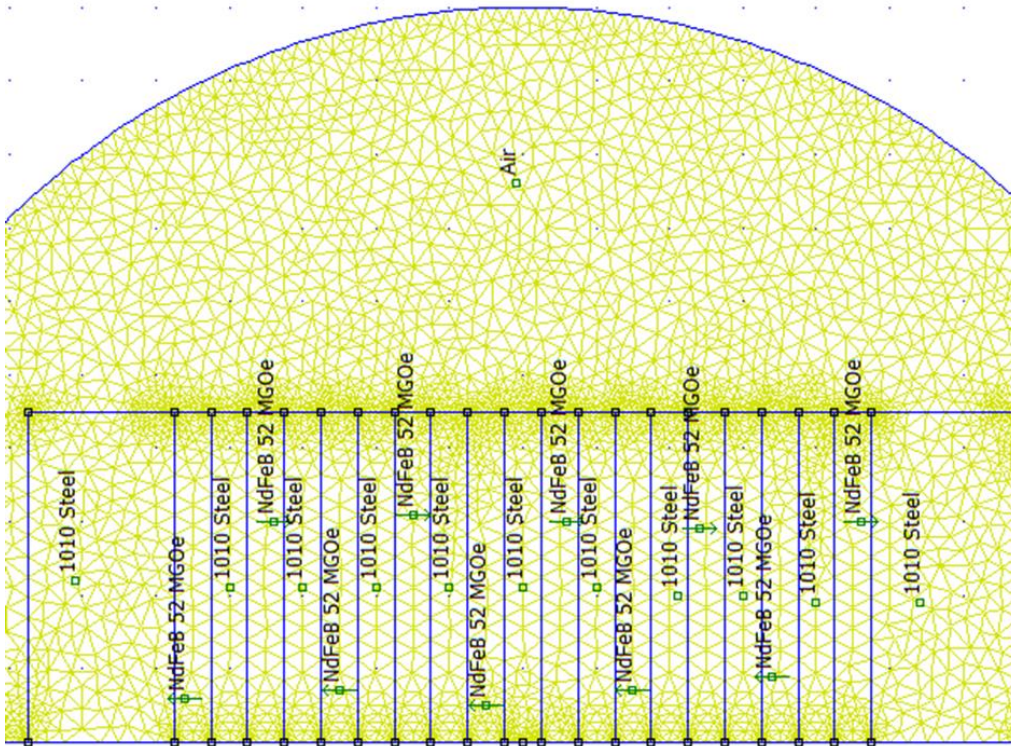Fig. I. 2 (a): Actual scale (M: S = 5 mm: 2.5 mm).

Fig. I. 2 (b): Magnified scale (M: S = 5 mm: 2.5 mm).

3. FEMM-2D meshed model with assigned properties of M: S = 5 mm: 1.25 mm (Fig. I. 3 (a) and (b)), Number of nodes and elements are 8228 and 15956, respectively.
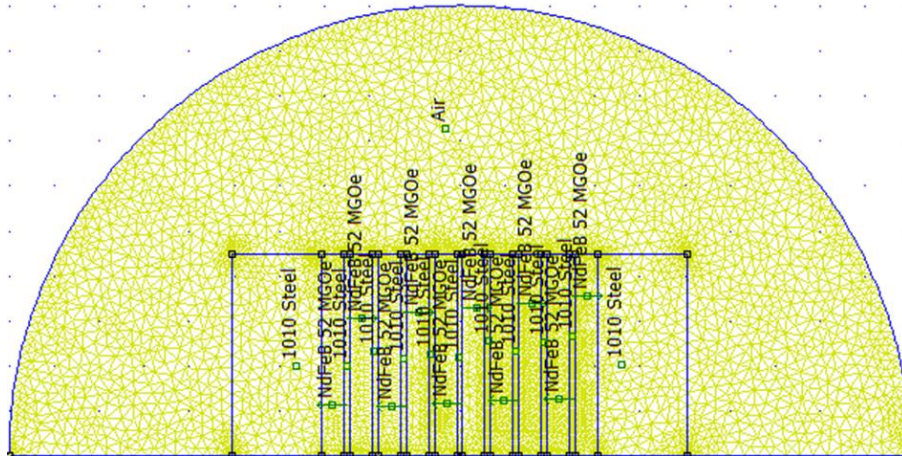

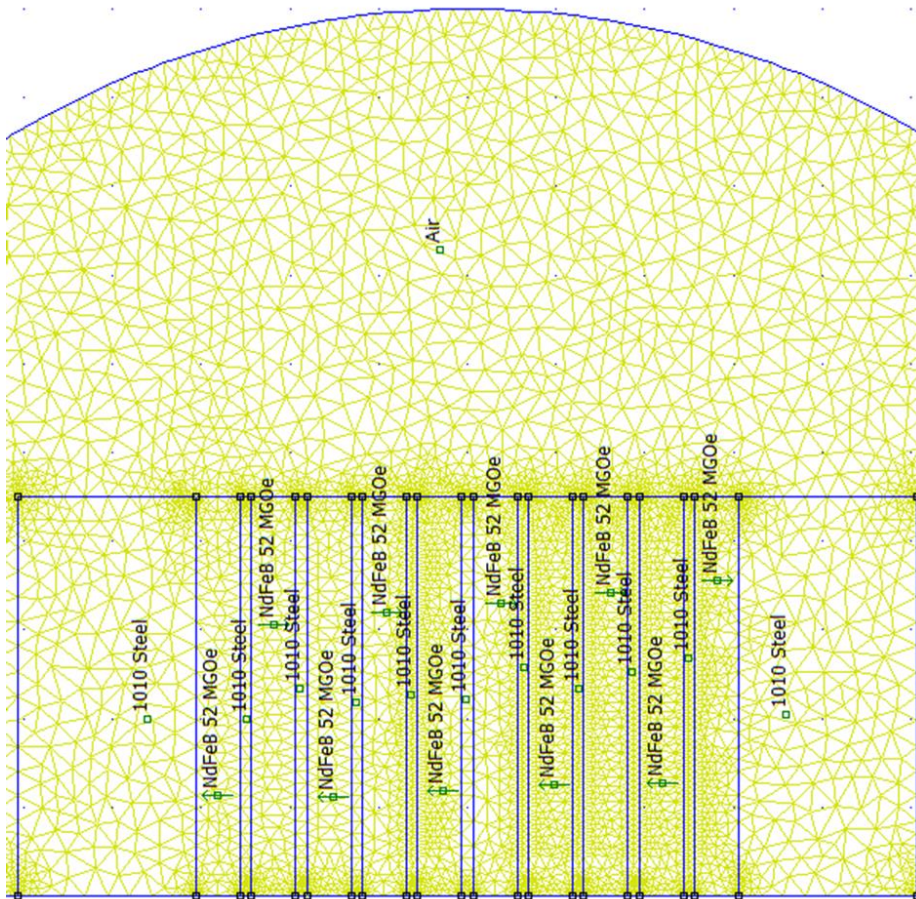Fig. I. 3 (a): Actual scale (M: S = 5 mm: 1.25 mm).

Fig. I. 3 (b): Magnified scale (M: S = 5 mm: 1.25 mm).

APPENDIX - II

Details of the data collection process in FEMM technique

The step-by-step process (Fig. S1) of the FEMM technique for data collection to analyze the M_f value of various magnetic roller configurations was described here.

```
          ┌─────────────────┐
          │  Create model   │
          └─────────────────┘
                   ↓
       ┌─────────────────────┐
       │ Set problem definition │
       └─────────────────────┘
                   ↓
          ┌─────────────┐
          │  Draw model │
          └─────────────┘
                   ↓
        ┌─────────────────┐
        │ Place block labels │
        └─────────────────┘
                   ↓
      ┌───────────────────────┐
      │ Add materials to the model │
      └───────────────────────┘
                   ↓
    ┌──────────────────────────────┐
    │ Associate properties with block labels │
    └──────────────────────────────┘
                   ↓
      ┌───────────────────────┐
      │ Create boundary conditions │
      └───────────────────────┘
                   ↓
  ┌───────────────────────────────────────┐
  │ Generate mesh and run finite element analysis (FEA) │
  └───────────────────────────────────────┘
                   ↓
      ┌───────────────────────────┐
      │ Collect, save and analysis of results │
      └───────────────────────────┘
```
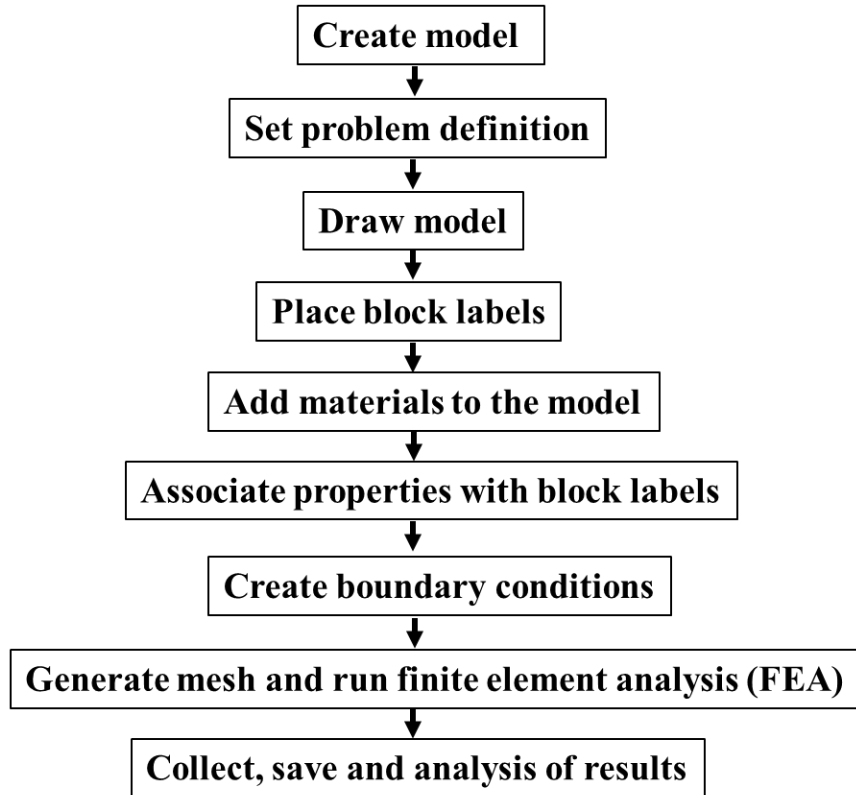
Fig. S1: Flow chart representing model construction for data collection and analysis using FEMM.

Step 1: Create model

(a) Run the FEMM 4.2 application, the default preferences will bring up a blank window with a minimal menu bar.

(b) Click 'File' on the menu bar and select 'New' from the drop list.

(c) Select 'Magnetics Problem' from the drop list and click 'OK' button.

Step 2: Set problem definition

(a) Click 'Problem' from the main menu.

(b) Set 'Problem Type' to 'Axisymmetric' from the drop list.

(c) Set 'Length Units' to 'millimeters' from the drop list.

(d) Set 'Frequency' to '0.'

(e) Accept default 'Solver Precision' as '1e-008.' ('1e-008' means 1×10^{-8})

(f) Set 'AC Solver' to 'Succ. Approx' from the drop list. ('Succ. Approx' means Successive approximation iterations).

(g) Accept remaining default settings as it is, and click 'OK' button.

Step 3: Draw model

(a) In the present work, the FEMM model consists of various blocks (NdFeB 52 magnet, SAE 1010 steel and surrounding air fluid medium).

(b) To draw the model switch to 'Nodes' mode by clicking on 'Operate on node' toolbar button in the main menu.

(c) Place 'Nodes' by defining the extent of the model requirements either by clicking mouse left button or by pressing the <TAB> key and manually entering the point co-ordinates via a popup dialog.

(d) Click 'Operate on segments' toolbar button in the main menu and connect the 'Nodes' through lines by clicking on the 'Nodes' to be connected.

Step 4: Place block labels

(a) Click 'Operate on block labels' toolbar button (concentric green circles) in the main menu.

(b) Place the block labels in the required region/block. Block labels can be placed in the same way as that node points i.e., either by clicking mouse left button or by pressing the <TAB> key.

(c) Here, the program uses block labels to associate materials and other properties with various regions/blocks in the problem geometry/model.

Step 5: Add materials to the model

(a) Click 'Properties' in the main menu.

(b) Select 'Materials Library' from the drop list

(c) Drag-and-drop the required materials (NdFeB 52 magnet material, SAE 1010 steel and Air as surrounding fluid medium) from the 'Library Materials' window to 'Model Materials' window.

(d) Add required materials (NdFeB 52 magnet material, SAE 1010 steel and Air as surrounding fluid medium) to the current model by clicking 'OK' button.

Step 6: Associate properties with block labels

(a) Right click on the block label node, the block label will turn red, denoting that it is selected.

(b) Click <SPACE> to "open" the selected block label. A dialog will pop up as 'properties for selected block' containing the properties assigned to the selected label.

(c) Set the 'Block type' to required material. If the 'Block type' has set to NdFeB 52 magnet material, then set the 'Magnetization direction' for each magnet as 270° and 90° alternatively for getting repelling magnet stack.

(d) It is usually sufficient to accept the default mesh density by clicking the 'Let Triangle choose Mesh Size' checkbox.

(e) Click on 'OK', the block label will then be labeled by the selected material name.

Step 7: Create boundary conditions

(a) Click 'Properties' in the main menu.

(b) Select 'Boundary' from the drop list. A popup dialogue 'Property definition' will appear.

(c) Click 'Add property' and set the 'Boundary condition (BC) type' to 'Mixed.'

(d) This 'Asymptotic boundary condition (Mixed)' was applied to the outer circular boundary of radius 100 mm (Fig. 10 of revised manuscript) to approximate an unbounded solution region. Here, considered 'Mixed BC parameters' are $c_1 = 0$ and $c_0 = \dfrac{n}{\mu_v \times r_o}$

Where, r_o = outer radius of the region = 100 mm, μ_v = permeability of free space/vacuum = $4\pi \times 10^{-7}$, and 'n' creates a series of circular shells that emulate the impedance of an unbounded domain = 1 (should be between 1 and 10).

Step 8: Generate mesh and run finite element analysis (FEA)

(a) Save the file.

(b) Click on the 'Run mesh generator' toolbar button (yellow mesh) in the main menu. This action generates a triangular mesh for your problem/model.

(c) Click on the 'Run analysis' toolbar button in the main menu to analyze the model.

Step 9: Collect and analysis of results

Click on the **'**View results' toolbar button in the main menu. A post-processor window will appear provided with 'FEMM output' window and black-and-white graph of magnetic field/flux lines is displayed in the solution region. The appeared 'FEMM output' window will show the number of nodes and elements required for the discretization of given problem/model to view result analysis.

Also, the post-processor window will allow you to extract many different sorts of information from the solution.

(a) In the main (post-processor) window, click 'rainbow-shaded' toolbar button. A popup window 'Dialog' will appear.

(b) Set 'Plotted value' to 'Flux density' from the drop list.

(c) Click 'Show Density Plot' checkbox and click 'OK' button. A color flux density plot of solution region along with 'FEMM output' window will appear.

In FEMM, even though the post-processor window of FEMM addresses more number of editing modes, but the present concern is limited towards 'Contour' mode.

(a) So, in the main menu of post-processor, Click 'Operation' and select 'Contours' mode from the drop list.

(b) Now, contour (thin red line) was defined on the surface of magnetic roller (Fig. S2) by clicking left mouse button at one end of magnetic roller surface which adds input node to the contour, and by clicking right mouse button to other end the desired contour get created on the magnetic roller surface. Then the obtained user-defined contour is shown in Fig. S2.

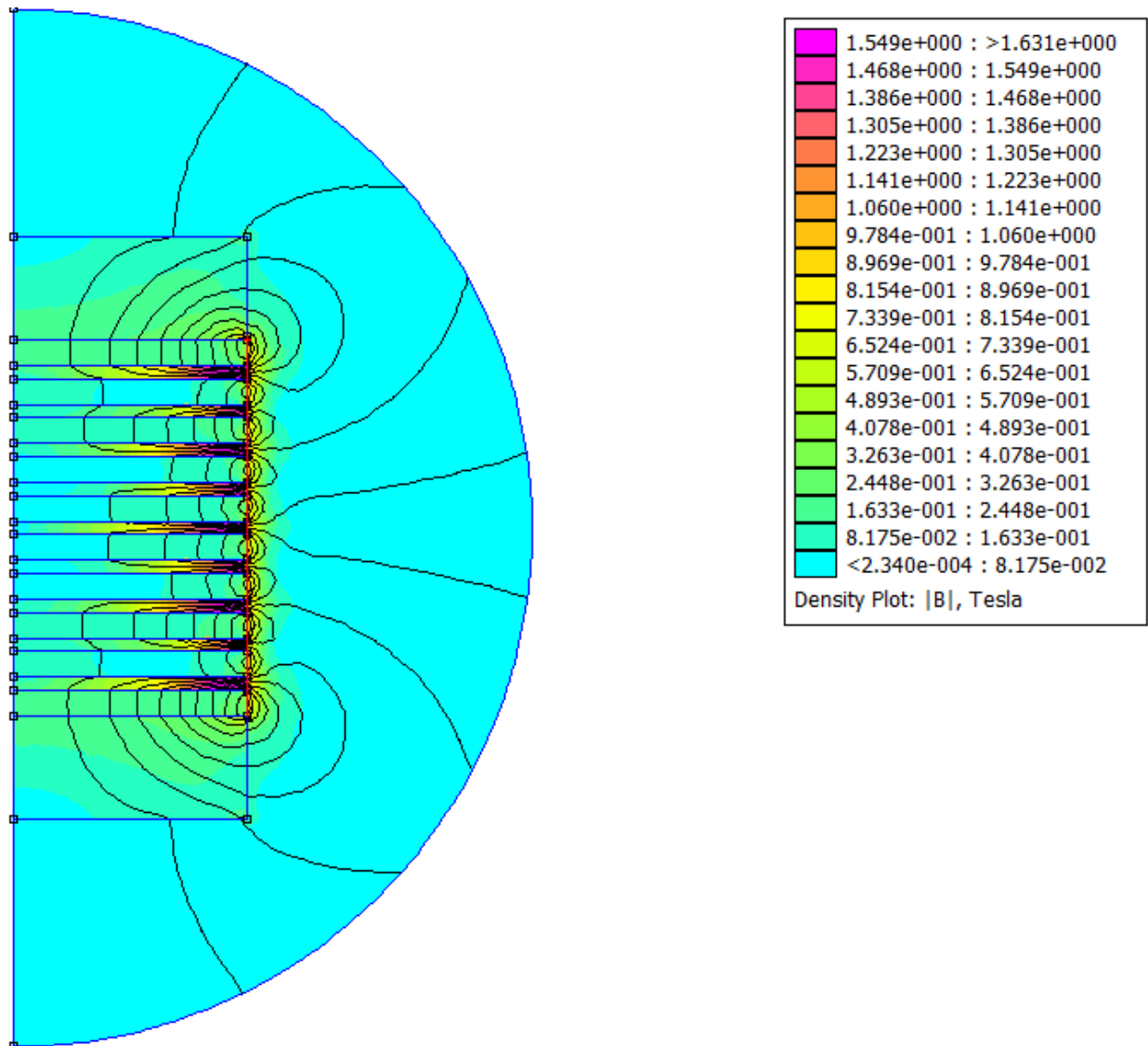| Color	Range
	1.549e+000 : >1.631e+000
	1.468e+000 : 1.549e+000
	1.386e+000 : 1.468e+000
	1.305e+000 : 1.386e+000
	1.223e+000 : 1.305e+000
	1.141e+000 : 1.223e+000
	1.060e+000 : 1.141e+000
	9.784e-001 : 1.060e+000
	8.969e-001 : 9.784e-001
	8.154e-001 : 8.969e-001
	7.339e-001 : 8.154e-001
	6.524e-001 : 7.339e-001
	5.709e-001 : 6.524e-001
	4.893e-001 : 5.709e-001
	4.078e-001 : 4.893e-001
	3.263e-001 : 4.078e-001
	2.448e-001 : 3.263e-001
	1.633e-001 : 2.448e-001
	8.175e-002 : 1.633e-001
	<2.340e-004 : 8.175e-002

Density Plot: |B|, Tesla

Fig. S2: FEMM color density plot with defined contour (thin red line) on the surface of magnetic roller.

(c) The results in terms of magnetic field/flux density value from the user-defined contour will be plotted by clicking 'Plot X-Y' mode. A pop up window 'X-Y Plot of Field Values' will appear.

(d) Set 'Plot Type' to '(magnitude of flux density)' from the drop list.

(e) Set 'Number of points in plot' as 10000.

(f) Set 'File Formatting' to 'Multicolumn text w/legend' from drop list.

(g) Click 'Write data to text file' checkbox, and Click 'OK' button.

(h) Save the file.

By doing so, the FEMM (numerical) data can be acquired for different magnetic roller configurations (M: S = 5 mm: 5 mm, 5 mm: 2.5 mm and 5 mm: 1.25 mm) in terms of magnetic field value on the surface of magnetic roller along thin red line (as shown in Fig. S2). The saved FEMM data of different magnetic roller configurations were used to do prediction analysis using ANN modelling technique.

APPENDIX – III

Information about the developed ANN model

Table AP-I: ANN model building parameters.

Parameters	Value/Condition
Number of hidden layers	1
Network type	Feed-forward back propagation network
Training function	Levenberg–Marquardt algorithm
Adaption learning function	Gradient descent with momentum weight and bias learning function
Performance function	Mean Squared Error
Transfer Function	Tan-sigmoidal
Maximum number of epochs	1000
max_fail (maximum number of validation checks before training is stopped)	1000
mu (adaptation parameter that is being used in the Levenberg - Marquardt optimization process)	0.001

- *Network type:* In the present work, the feed-forward back propagation network technique was used, which reduces the error rate by fine tuning of predicted value thereby increasing the accuracy of the ANN model. Hence, among different types of neural network, feed-forward back propagation neural network is the most commonly used which is designed with a input layer, hidden layer and output layer (Panda and Tripathy 2014; Chaurasia and Nikkam 2017; Tripathy et al. 2020; Panda et al. 2014). Since, back propagation algorithm searches for weight values that minimize the total error of the network over the set of training examples (training set). Also, back propagation consists of the repeated application of the following two passes: *(1) Forward pass:* in this step the network is activated on one example and the error of (each neuron of) the output layer is computed. *(2) Backward pass:*

144

in this step the network error is used for updating the weights. Starting at the output layer, the error is propagated backwards through the network, layer by layer. This is done by recursively computing the local gradient of each neuron. Back propagation adjusts the weights of the NN in order to minimize the network total mean squared error (Panda and Tripathy 2014; Haghighi et al. 2014).

- *Training function:* Levenberg–Marquardt algorithm was used to train the network. It is one of the best ways to improve generalization performance of network for function approximation problems. Network training function that updates weight and bias values according to *Levenberg-Marquardt* optimization. It is often the fastest backpropagation algorithm in the toolbox, and is highly recommended as a first-choice supervised algorithm, although it does require more memory than other algorithms (Haghighi et al. 2014; Chaurasia and Nikkam 2017). The *Levenberg-Marquardt algorithm* is designed to work specifically with loss functions which take the form of a sum of squared errors.

- *Activation/transfer function:* Tan-sigmoidal transfer function is commonly used in neural networks that are trained using the backpropagation algorithm which has an output in the range of -1 to +1. The results can have very small numerical differences. This function is a good tradeoff for neural networks, where speed is more important than the exact shape of the transfer function and its use was found in the available literature (Tripathy et al. 2020; Chaurasia and Nikkam 2017; Dorofki et al. 2012).

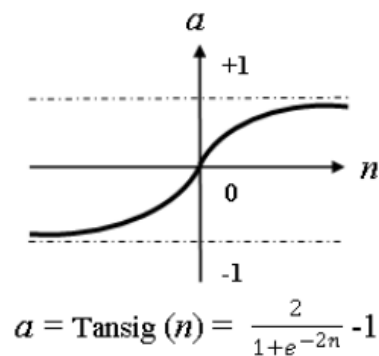$$a = \text{Tansig}(n) = \frac{2}{1+e^{-2n}} - 1$$

Fig: Tan-Sigmoid transfer function (Dorofki et al. 2012).

- ***Performance function:*** Mean squared error is used as a performance function. Since, which is a typical performance function used for training feed forward neural networks from the available literature (Panda et al. 2014; Panda and Tripathy 2014; Chaurasia and Nikkam 2017; Tripathy et al. 2020).

APPENDIX - IV

Force index and magnetic force calculation

1. Calculation of force index and magnetic force value for various M: S ratios using equations (4.1), (4.2), and (1.1).

Magnetic force is directly proportional to the force index (product of the magnetic field and its gradient) as mentioned in the equation. (1.1) (Svoboda 2004).

$$F_m = \frac{1}{\mu_o}(\chi_p - \chi_f)m_p B\nabla B. \tag{1.1}$$

Where, $\mu_o = 4\pi\times10^{-7}$Tm/A (Svoboda 2004), and χ_f = zero for air (Alp 2009).

In the case of a permanent magnetic roller, B and B∇B are calculated by using equations (4.1) and (4.2) (Kopp, 1984).

$$B = B_o\exp\left(\frac{-z}{t}\right). \tag{4.1}$$

$$B\nabla B = \frac{B_o^2}{t}\exp\left(\frac{-2z}{t}\right). \tag{4.2}$$

In addition, the density of particle $= \rho_P = \frac{m_P}{V_P}. \tag{A-1}$

For calculation assume that the particles (-150+105 µm size fractions) are spherical and have an average particle size of 127.5 µm (0.1275×10^{-3} m) diameter.

The volume of particle $= V_P = \frac{4}{3} \times \pi \times (R_P)^3$, where, R_P is the particle radius.

$V_P = \frac{4}{3} \times \pi \times (0.0637 \times 10^{-3})^3 = 1.08\times10^{-12}$ m^3, Where, $\rho_P = 3410$ kg/m^3 (Table 4.1).

Substitute for ρ_P and V_P in equation (A-1)

Therefore, $m_P = 3.6828\times10^{-9}$ kg.

Mass magnetic susceptibility of particle $= \chi_p = \dfrac{\text{Magnetization,M}_1\left(\frac{\text{Am}^2}{\text{kg}}\right)}{\text{Magnetic field strength,H}\left(\frac{\text{A}}{\text{m}}\right)}$ m^3/kg

Magnetization value for the corresponding magnetic field (B) in terms of emu/g was obtained from the magnetic susceptibility study (hysteresis curve) i.e., Fig. 4.2. However, the magnetization value of the sample varies concerning the applied magnetic field as shown in Fig. 4.2.

1.1 Force index and magnetic force value of magnetic roller having M: S ratio of 5 mm: 5 mm

Where, $t = 5$ mm (or) 5×10^{-3} m, $z = B_2$, $B_o = 0.60$ T, 1 T = 10000 Oe, $B_c = B\times10000 =$ Magnetic field in Oe, and $M_o =$ Magnetization in emu/g (Fig. 4.2).

Table AP-1: Force index results for various B_2 values (M: S=5 mm: 5 mm).

B_2 (m)	$B = B_o \exp\left(\frac{-z}{t}\right)$	$B\nabla B = \frac{B_o{}^2}{t} \exp\left(\frac{-2z}{t}\right)$
	(T)	(T^2/m)
0×10^{-3}	0.60	72.00
0.5×10^{-3}	0.54	58.94
1×10^{-3}	0.49	48.26
1.5×10^{-3}	0.44	39.51
2×10^{-3}	0.40	32.35
2.5×10^{-3}	0.36	26.48

Table AP-2: Magnetic force results for various B_2 values (M: S=5 mm: 5 mm).

B_2 (m)	B_c (Oe)	M_o (emu/g)	$M_1 = M_o\times1$ (Am^2/kg)	$H = B_C \times \frac{10^3}{4\pi}$ (A/m)	χ_p (m^3/kg)	F_m (N)
0×10^{-3}	6000	3.75	3.75	477464.82	7.85×10^{-6}	1.65×10^{-6}
0.5×10^{-3}	5400	3.70	3.75	429718.34	8.72×10^{-6}	1.50×10^{-6}
1×10^{-3}	4900	3.66	3.66	389929.61	9.38×10^{-6}	1.32×10^{-6}
1.5×10^{-3}	4400	3.60	3.60	350140.87	1.02×10^{-5}	1.18×10^{-6}
2×10^{-3}	4000	3.56	3.56	318309.88	1.11×10^{-5}	1.05×10^{-6}
2.5×10^{-3}	3600	3.48	3.48	286478.89	1.21×10^{-5}	9.38×10^{-7}

1.2 Force index and magnetic force value of magnetic roller having M: S ratio of 5 mm: 2.5 mm

Where, $t = 2.5$ mm (or) 2.5×10^{-3} m, $z = B_2$, $B_o = 0.89$ T, 1 T = 10000 Oe, $B_c = B \times 10000 =$ Magnetic field in Oe, and $M_o =$ Magnetization in emu/g (Fig. 4.2).

Table AP-3: Force index results for various B_2 values (M: S=5 mm: 2.5 mm).

B_2 (m)	$B = B_o \exp\left(\frac{-z}{t}\right)$	$B\nabla B = \frac{B_o^2}{t} \exp\left(\frac{-2z}{t}\right)$
	(T)	(T^2/m)
0×10^{-3}	0.89	316.84
0.5×10^{-3}	0.72	212.38
1×10^{-3}	0.59	142.36
1.5×10^{-3}	0.48	95.43
2×10^{-3}	0.39	63.96
2.5×10^{-3}	0.32	42.87

Table AP-4: Magnetic force results for various B_2 values (M: S=5 mm: 2.5 mm).

B_2 (m)	B_c (Oe)	M_o (emu/g)	$M_1 = M_o \times 1$ (Am^2/kg)	$H = B_C \times \frac{10^3}{4\pi}$ (A/m)	χ_p(m^3/kg)	F_m (N)
0×10^{-3}	8900	3.89	3.89	708239.49	5.49×10^{-6}	5.09×10^{-6}
0.5×10^{-3}	7200	3.82	3.82	572957.79	6.66×10^{-6}	4.14×10^{-6}
1×10^{-3}	5900	3.74	3.74	469507.08	7.96×10^{-6}	3.32×10^{-6}
1.5×10^{-3}	4800	3.65	3.65	381971.86	9.55×10^{-6}	2.67×10^{-6}
2×10^{-3}	3900	3.55	3.55	310352.13	1.14×10^{-5}	2.13×10^{-6}
2.5×10^{-3}	3200	3.40	3.40	254647.90	1.33×10^{-5}	1.67×10^{-6}

1.3 Force index and magnetic force value of magnetic roller having M: S ratio of 5 mm: 1.25 mm

Where, t = 1.25 mm (or) 1.25×10^{-3} m, z = B_2, B_o = 0.79 T, 1 T = 10000 Oe, B_c = B×10000 = Magnetic field in Oe, and M_o= Magnetization in emu/g (Fig. 4.2).

Table AP-5: Force index results for various B_2 values (M: S=5 mm: 1.25 mm).

B_2 (m)	$B = B_o \exp\left(\frac{-z}{t}\right)$ (T)	$B\nabla B = \frac{B_o{}^2}{t}\exp\left(\frac{-2z}{t}\right)$ (T^2/m)
0×10^{-3}	0.79	499.28
0.5×10^{-3}	0.52	224.34
1×10^{-3}	0.35	100.80
1.5×10^{-3}	0.23	45.29
2×10^{-3}	0.15	20.35
2.5×10^{-3}	0.10	9.14

Table AP-6: Magnetic force results for various B_2 values (M: S=5 mm: 1.25 mm).

B_2 (m)	B_c (Oe)	M_o (emu/g)	$M_1 = M_o \times 1$ (Am^2/kg)	$H = B_c \times \frac{10^3}{4\pi}$ (A/m)	χ_p(m^3/kg)	F_m (N)
0×10^{-3}	7900	3.85	3.85	628662.02	6.12×10^{-6}	8.95×10^{-6}
0.5×10^{-3}	5200	3.69	3.69	413802.85	8.91×10^{-6}	5.85×10^{-6}
1×10^{-3}	3500	3.46	3.46	278521.15	1.24×10^{-5}	3.66×10^{-6}
1.5×10^{-3}	2300	3.09	3.09	183028.18	1.68×10^{-5}	2.22×10^{-6}
2×10^{-3}	1500	2.24	2.24	119366.20	1.87×10^{-5}	1.11×10^{-6}
2.5×10^{-3}	1000	1.49	1.49	79577.47	1.87×10^{-5}	5.00×10^{-7}

APPENDIX - V

Weight and bias of developed ANN models.

Where, W_1 and b_1 are weight and bias of hidden layer

W_2 and b_2 are weight and bias of output layer

1. Weight and bias of ANN model for M: S = 5 mm: 5 mm.

$W_1 = [77.2643$
80.9211
-120.298
98.3003
108.1696
-107.521
-126.287
101.0855
100.1827
107.6693
-111.0598
122.8502
118.9611
-112.4053
113.7055
-128.0792
-107.1878
87.5858
104.7933
108.2806
119.2349
-119.4502
132.3718
108.8103
112.3655
109.136
103.1726
-115.6264
114.0755
-130.8289
115.5751
-118.3691
-110.4825

-111.5875
-101.9245
94.8398
130.4429
-115.1547
117.2263
-110.5265
-108.1372
-99.3042
121.5474
77.2745
-78.1472]

b_1 = [-78.7625 -73.2079 108.1041 -88.3675 -85.6609 85.0325 86.9108 -69.6254 -69.7362 -62.5122 64.347 -58.2298 -56.265 41.597 -41.9608 34.8489 29.031 -23.5377 -16.7113 -17.127 -5.9856 5.6541 -6.0034 5.6097 5.9284 17.1724 16.3853 -29.6809 29.6325 -33.3176 42.7536 -43.6588 -52.1464 -52.7879 -58.9209 54.9765 88.1427 -78.0574 79.8598 -87.2619 -85.4916 -89.2187 109.181 69.8982 -79.6151]^T

W_2 = [11.3776 -3.4001 11.4431 14.9544 -11.4078 -11.2573 12.6896 16.2804 -3.1759 -11.0963 -10.6756 -10.9262 11.1281 11.6683 11.4581 -14.7803 31.0231 16.6526 -10.3562 9.953 -15.2935 -31.469 -15.9327 -10.3972 10.1492 -8.9599 9.3731 33.76 15.8779 -17.4691 10.9482 10.7308 11.3037 -11.0972 9.2311 9.733 21.2566 39.3125 17.5424 10.7391 -10.9119 14.685 11.5089 3.063 10.8863]

b_2 = [21.5015]

2. Weight and bias of ANN model for M: S = 5 mm: 2.5 mm.

W_1 = [36.3597
39.1139
-230.1734
116.2965
97.8201
-274.1045
-54.9106
91.6533
102.0025
92.4729
-89.4935
55.6574

302.2128
-109.7797
118.3263
-46.6522
-113.1506
107.3377
192.8949
204.4362
21.3265
-371.1661
31.0937
26.3576
7.3572
258.0983
103.8294
-154.4645
249.1562
-52.9367
95.4639
-35.9867
-32.3149
-32.0414
-87.5944
90.5613
102.4152
-99.1637
62.0812
-300.9756
-108.701
-116.603
280.0727
39.8097
-38.5649]

b_1 = [-38.0042 -34.7923 198.9462 -99.8882 -77.7257 216.609 42.7548 -59.807 -66.3561 -54.5124 52.6726 -25.7804 -136.0839 42.6385 -52.7289 17.538 27.2663 -25.7147 -33.4627 -35.2784 -2.6878 14.4199 0.48621 0.39747 -0.2207 43.798 18.4696 -36.9404 60.5 -13.8765 35.1327 -15.8478 -14.3944 -14.5767 -51.5309 53.3687 66.7516 -64.717 48.2832 -237.9411 -86.3636 -100.1421; 242.1034 35.3301 -40.241]^T

W_2 = [27.4837 -0.92754 1.3471 1.7197 -1.9048 -1.1885 -1.0986 -9.1094 9.144 -20.9237 -20.9119 -0.94806 -1.1732 1.6606 1.7949 -2.2967 10.6147 11.2661 -7.1713 7.0694 5.587 0.6565 -56.1798 67.2861 -18.3925 -1.0453 1.8487 1.9301 1.6151 -0.85762 -1.3962 91.4203 -147.6526 54.6359 20.3692 20.3291 -21.3206 -21.2861 -1.0048 1.2906 -1.9031 1.6254 1.2106 0.96757 29.2603]

b_2 = [54.8819]

3. Weight and bias of ANN model for M: S = 5 mm: 1.25 mm.

W_1 = [99.6041
73.8183
-29.5851
312.5292
48.522
-38.4714
-31.9066
93.6361
284.13
306.5774
-91.5246
95.3577
63.6059
-68.4823
336.842
-47.5889
-76.8394
265.9675
315.8595
85.096
84.4934
-60.9685
65.6711
351.0127
45.9575
76.8366
276.2411
-304.6863
87.0341
-83.1706
60.0691

-64.8129
-331.1641
-41.9359
-83.2798
296.8568
297.1889
-89.5789
33.5699
-311.113
-72.8916
68.0868
59.7357
53.2682
-97.661]

b_1 = [-101.2851 -71.7181 23.416 -262.5975 -39.0032 30.8048 24.5698 -62.2342 -182.1207 -178.967 51.1851 -46.0869 -26.5633 28.5953 -129.1556 17.1302 20.0189 -62.0791 -55.502 -12.5981 -6.5409 0.5805 -0.62282 8.6067 2.1612 11.3189 48.2621 -71.1489 22.7273 -27.4775 23.977 -25.8713 -143.3198 -19.167 -46.3048 173.1849 190.5871 -59.9318 25.3917 -246.16 -60.2677 -56.3044 53.6919 51.3436 -99.3021]^T

W_2 = [16.7229 0.35372 92.3176 -0.62243 -52.3757 -121.1743 -24.0935 -0.39239 -0.32245 0.3181 -0.47392 -0.27032 -30.6119 -29.5738 0.55141 -0.74109 0.44502 -0.34134 0.31196 0.68014 -0.42211 30.6593 29.5295 0.55872 0.78729 -0.44492 -0.3258 -0.32218 0.67413 0.44691 -30.2864 -29.1227 -0.57576 -0.89772 0.52661 -0.32186 0.33427 -0.74081 -1.0358 0.5064 29.5099 -30.4352 0.56124 -0.64991 14.2881]

b_2 = [30.1884]

APPENDIX - VI

Fabrication of lab-scale PRMS
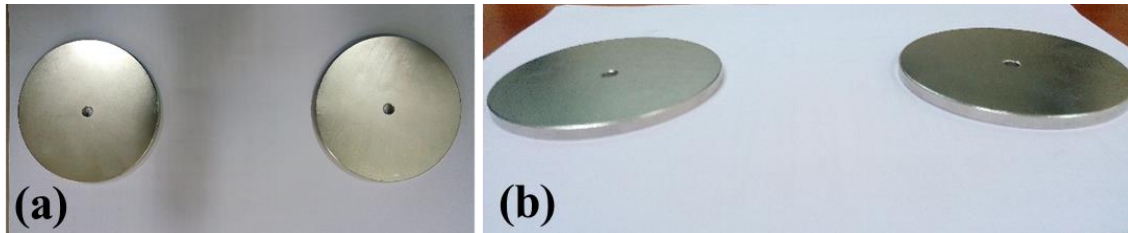
Fig. VI. 1: Magnet disks (a) Top view (b) Front view.
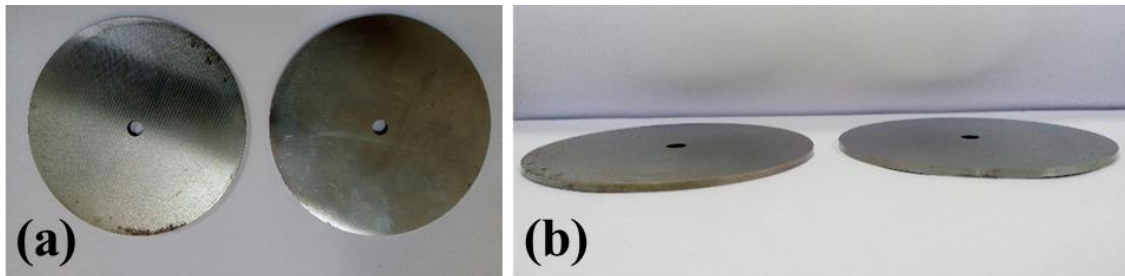
Fig. VI. 2: Steel disks (a) Top view (b) Front view.
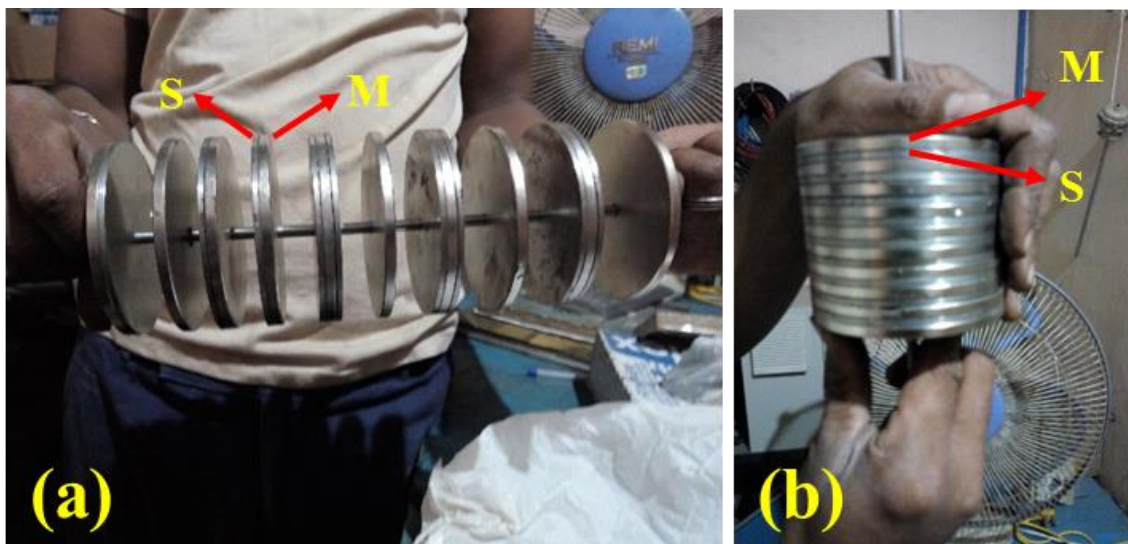
Fig. VI. 3: (a) Insertion of magnet and steel disks (b) Magnet disks interleaved with steel disks.
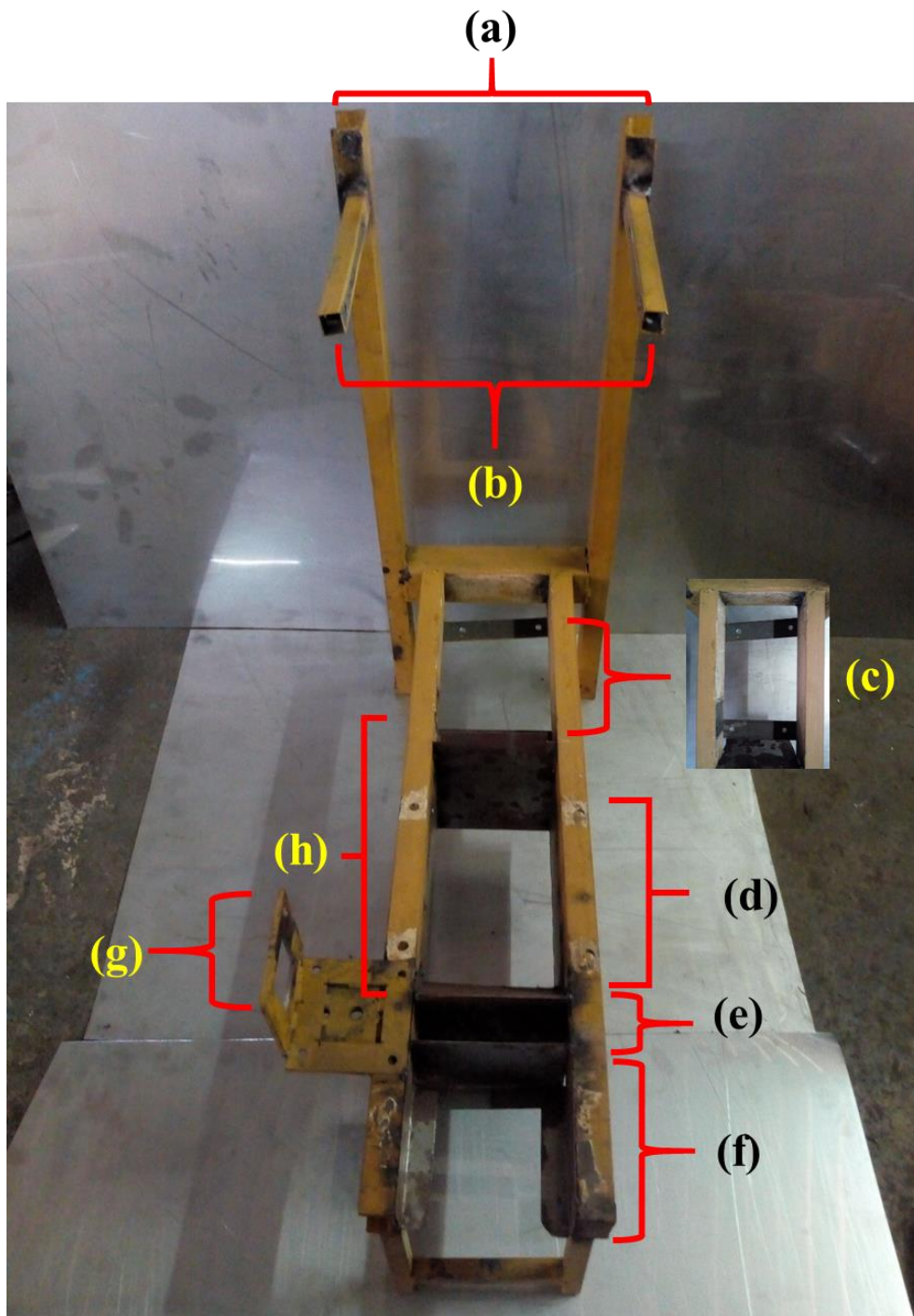
Fig. VI. 4: Cast iron frame work for the assembly of (a) Control panel (b) Hopper (c) Vibratory feeder (d) Magnetics collection bin (e) Middlings collection bin (f) Non-magnetics collection bin (f) Motor shaft (h) Roller-belt drive.
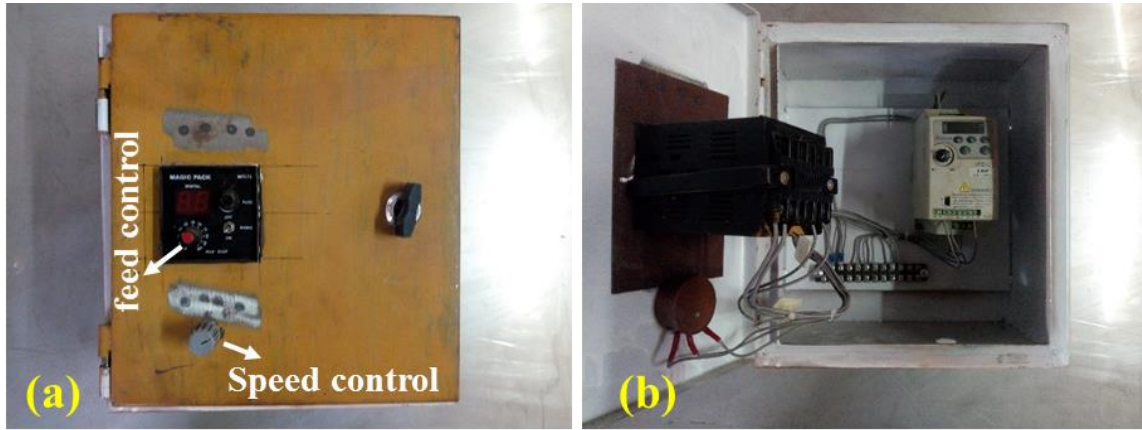
Fig. VI. 5: (a) Control panel board with speed and feed control knobs (b) Interconnection inside the panel board.
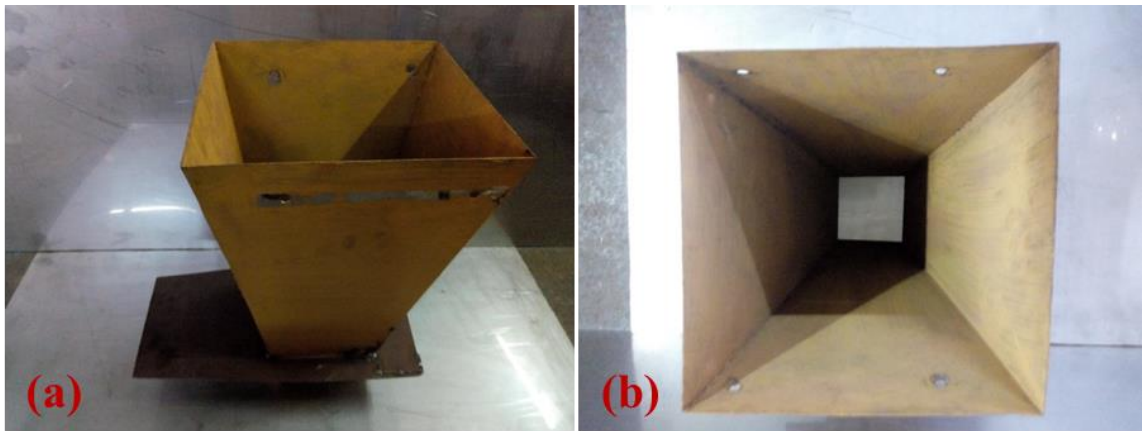
Fig. VI. 6: Hopper (a) Front view (b) Top view.
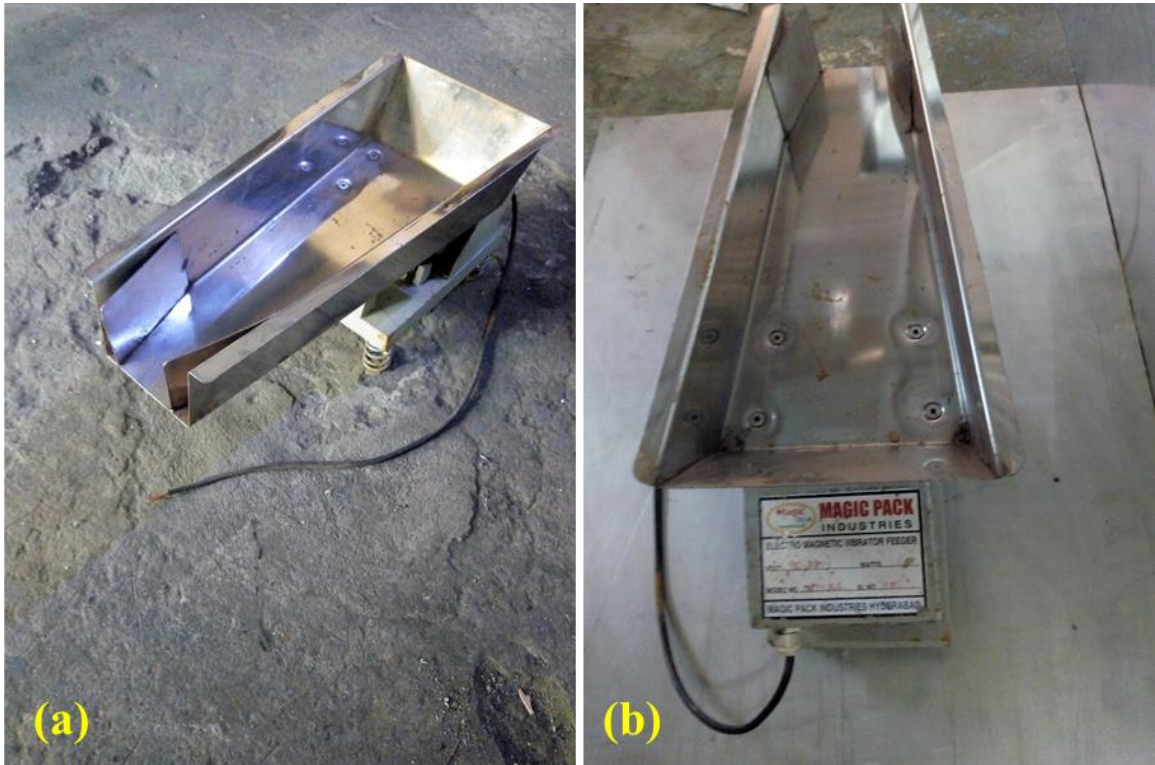
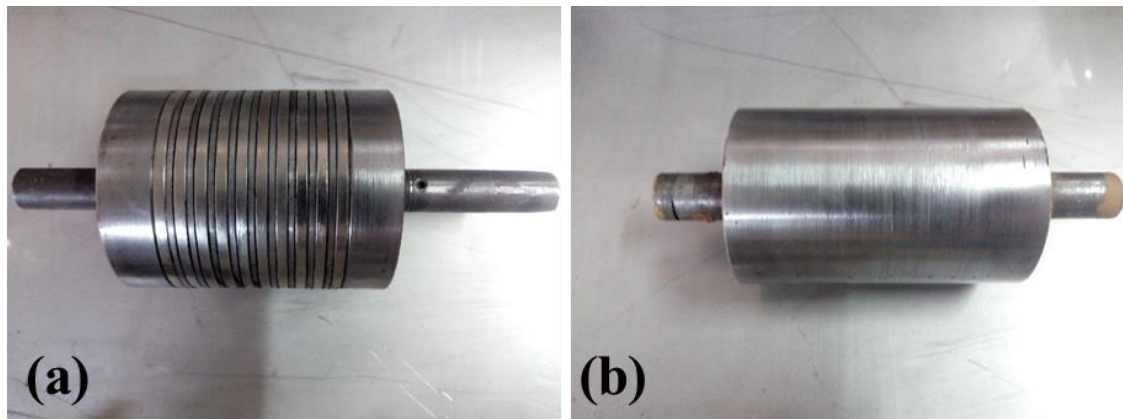Fig. VI. 7: Vibratory feeder (a) Isometric view (b) Front view.

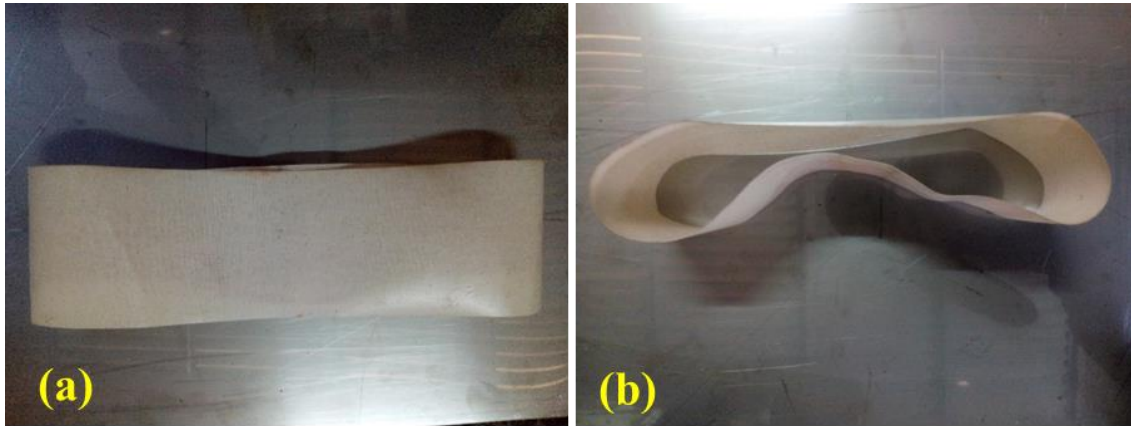Fig. VI. 8: (a) Optimized magnetic roller (b) Support roller.

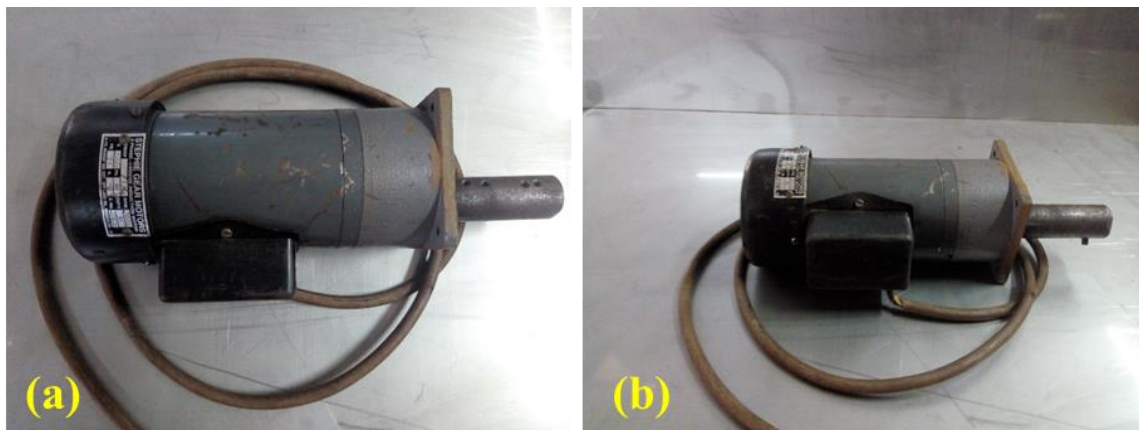Fig. VI. 9: Kevlar belt material (a) Width (b) Thickness.

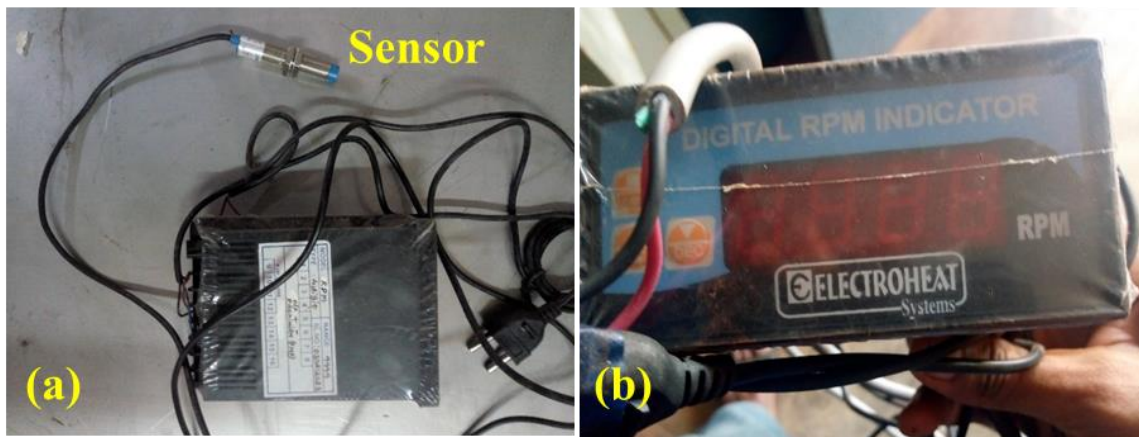Fig. VI. 10: Electric motor (a) Top view (b) Front view.

Fig. VI. 11: Digital RPM indicator provided with (a) Sensor (b) Display board.
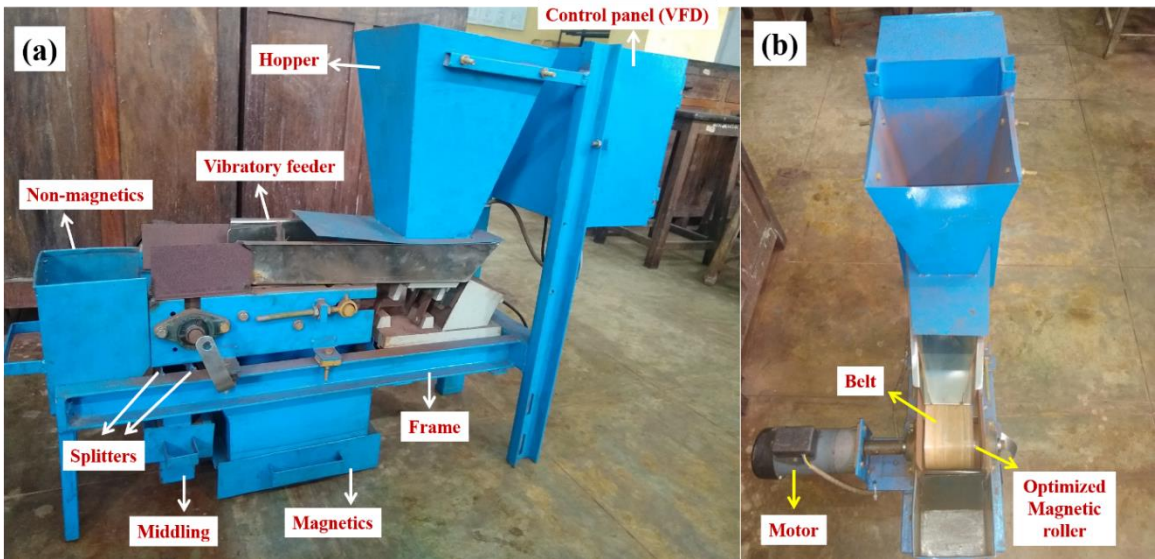
Fig. VI. 12: Newly developed lab-scale PRMS (a) Side view (b) Front view.

XRD semi quantitative analysis details

In addition, based on the peak intensity, the semi quantitative analysis of mineral phases present in the feed sample (Fig. VII. 1) and separated products (Fig. 4.29 and Table 4.10) were performed through 'default-profile-fit' refinement technique followed by 'available background' method and 'split width and shape' asymmetry type profile fit settings, using X'pert Highscore Plus software by Malvern PANalytical. The refined data of the XRD pattern shows the lower value of χ^2 (goodness of fit) and R_{WP} (Weighted-Profile R-factor), which represents the better profile fit for the estimations of mineral phases present in the feed sample and separated products. Therefore, the approximate % of mineral phases present in the feed sample (Fig. VII. 1) and separated products (Fig. 4.29 and Table 4.10) were calculated from the refined data.
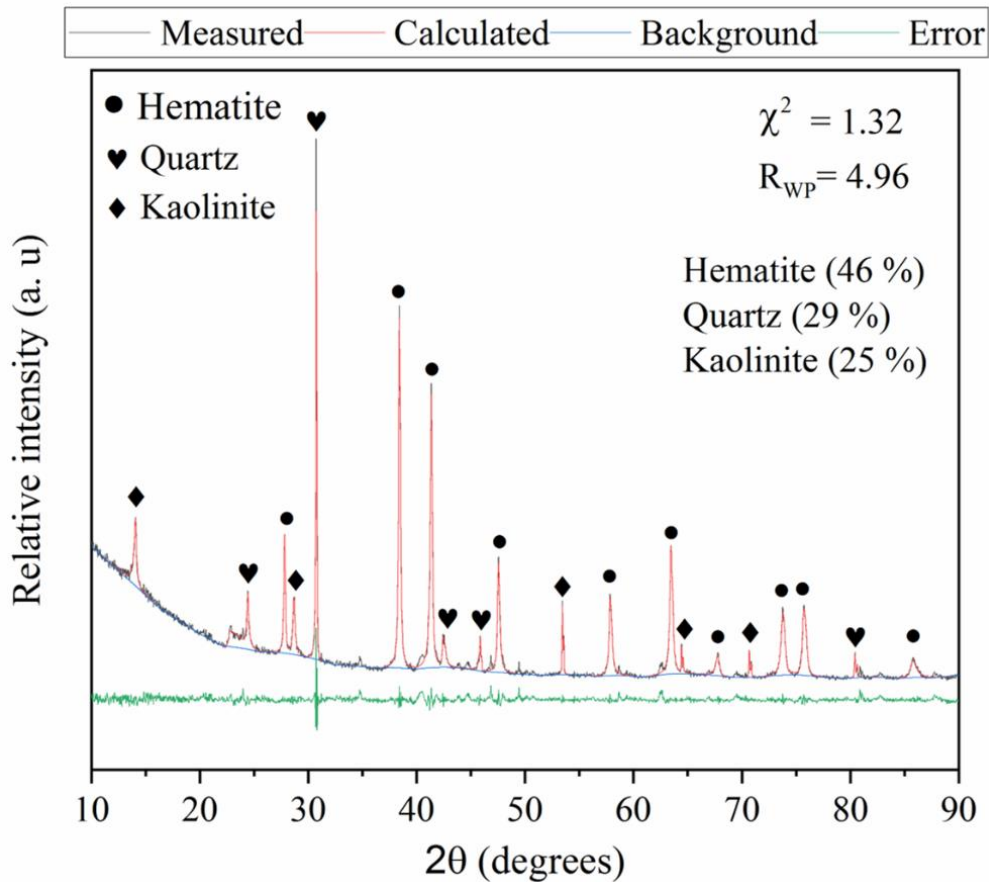

Fig. VII. 1: XRD of feed sample (-150 μm).

BIO-DATA

Name: Mohanraj G T

Father's Name: Thimmegowda G P

Mother's Name: Prameela B

Date of Birth: 04-11-1988

Nationality: Indian

Marital Status: Single

Address:

Permanent Address   **Present Address**

L. 41, 'K' Block, 2nd Stage,   Research Scholar

Ramakrishna Nagar,   Metallurgical and Materials Engg. Dept.

Mysore – 570022   NITK, Surathkal – 575025

Mobile Number: +91-9880680107

E-mail id: mohanmde09@gmail.com

Educational Qualification:

Course	Institution	University	Batch
Ph. D. (Metallurgical and Materials Engineering)	National Institute of Technology Karnataka, Surathkal	NITK	2022
M. Tech. (Design Engineering)	Jawaharlal Nehru National College Of Engineering	VTU	2012
B. E. (Industrial & Production Engineering)	Bapuji Institute of Engineering and Technology	VTU	2010